The Dissertation Committee for Lavanya Mohan Certifies that this is the approved version of the following dissertation:

Microstructure and Rheology of Soft Particle Glasses

Committee:

Roger T. Bonnecaze, Supervisor

Michel Cloitre

Thomas M. Truskett

Venkat Ganesan

Gregory J. Rodin

Microstructure and Rheology of Soft Particle Glasses

by

Lavanya Mohan, B.Tech., M.S.E.

Dissertation

Presented to the Faculty of the Graduate School of
The University of Texas at Austin
in Partial Fulfillment
of the Requirements
for the Degree of

Doctor of Philosophy

The University of Texas at Austin
December 2013

Dedication

To my dear husband Vivek, who listened to me patiently and encouraged me when things seemed difficult, cheered me when things were successful, and always supported me, and, to my loving parents, Mohan and Saraswathi, who did everything they can to help me reach here.

Acknowledgements

First, I would like to thank my advisor Dr. Roger Bonnecaze. He is an amazing research advisor, teacher and mentor. His terrific enthusiasm, tendency to celebrate even small victories along the way and strong optimism in times when I was stuck were very motivating. He truly cared for my all round development and encouraged me towards exploring other opportunities including my internship at ExxonMobil and research fellowship at ESPCI ParisTech. Despite his busy schedule, he has always been present to guide me, help me set goals and reach them.

I would like to thank Dr. Michel Cloitre, who has been an awesome mentor to me. I had wonderful discussions with him whenever he came to Austin, and I had an amazing time working under his supervision when I was at ESPCI ParisTech. He taught me how to plan and approach experiments, and how to quickly explore solutions to experimental issues. I would like to especially express my gratitude for all his help in settling down when I was in France. He was very kind and helped me with everything I needed, and always made sure I was comfortable inside and outside the lab.

I had a great time being in the company of the other members of the Bonnecaze group. I am very grateful to Jyoti Seth for all her codes which have been an asset to me, for helping me get acquainted with them and for her friendship. I would like to thank my lab mates Derek Bassett, Susana Carranza, Erin Baker, Mike Clements, Parag Katira, Erwan Chabert, Akhilesh Jain, Talha Arshad, Mark Ferraro, Ben Huntington, Meghali Chopra and Mohammad Shafiei for the lively discussions, laughs and lunches. I would also like to thank my other friends from the department for some good times, Gunja Pandav, Amanda Lanza, Thomas Lewis, Ahn Nguyen, Ying Ying Jiang and Xiaojing

Jiang. I would like to thank the members of the Matière Molle et Chimie Lab at ESPCI Paris Tech for their warm hospitality and Campus France for the EIFFEL doctoral fellowship. I would like to specially thank Charlotte Pellet for her friendship and for helping me a lot with the experiments.

I was also very fortunate to forge some other great friendships during my time here at UT which made my PhD even more enjoyable. I would like to thank Avni Jain for being a wonderful friend and my lunch companion, sharing ideas and stories inside and outside work. I would like to thank Padmini Rajagoplan, Swati Rallapalli, Shravan Gowrishankar, Harsha Kumar MC and Sucheta Arora for their wonderful friendship and all the fun filled lunches, dinners, movies, birthdays, long coffees and much more…

I would like to thank Randy Rife and Tim Guinn for all the computer support without which I would have been stuck at different points for a long time.

I would also like to thank my wonderful family for all their support, encouragement and love, my dear husband Vivek Raja, my loving parents Mohan and Saraswathi, my adoring grandparents, Kothandaraman and Jayalakshmi and my affectionate parents-in-laws, Raj Mohan and Jayalatha.

Thank you all !

Microstructure and Rheology of Soft Particle Glasses

Lavanya Mohan, Ph.D.
The University of Texas at Austin, 2013

Supervisor: Roger T. Bonnecaze

Soft particle glasses like microgels and compressed emulsions are densely packed, disordered suspensions of deformable particles. Quantitative relationships among the constituent properties and the macroscopic properties of the suspension are determined for their customized design as rheological additives. The microscopic origin of their macroscopic properties is also determined. Advanced characterization techniques like Large Amplitude Oscillatory Shear (LAOS) and microrheology are studied to use them efficiently to characterize these materials. Their microstructure and rheology are investigated through theory, simulations and experiments.

Soft particle glasses are used as rheological additives in many applications including coatings, solid inks and textured food and cosmetic products but their formulation is largely empirical. A quantitative connection between their formulation and rheology is critical to enable their rational design. Their microstructure will lead to the microscopic origin of some unique properties in common with other soft crowded materials like intracellular cytoplasm and clays. These are complex fluids and require novel techniques to characterize them. A study of these techniques is essential to efficiently interpret the observations in terms of their macroscopic properties and the microscopic dynamics involved.

Particle scale simulations of steady and oscillatory shear flow are developed to predict the nonlinear rheology and microstructure of these glasses. The origin of yielding is determined as escape of particles from their cages giving rise to a shear induced diffusion. Microrheology is studied by developing simulations of a probe particle being pulled at a constant force and the rheological information from microrheology is quantitatively connected to that from bulk rheological measurements.

Soft particle glasses develop internal stresses when quenched to a solid state by flow cessation during processing. Experiments are performed to characterize and *a priori* predict these stresses. Simulations are used to determine the particle scale mechanisms involved in the stress relaxation on flow cessation and the microstructural origin of internal stresses.

A pairwise interaction theory is developed for quiescent glasses to quantitatively predict their microstructure and elastic properties. The theory is then extended to sheared glasses to quantitatively predict their nonlinear rheology. The implementation of the pairwise theories is computationally much faster than the full three-dimensional simulations.

Table of Contents

List of Tables

List of Figures

Chapter 1: Introduction

1.1 WHY STUDY SOFT PARTICLE GLASSES?

Soft particle glasses are concentrated suspensions of soft and deformable particles which are jammed at volume fractions beyond the random close packing limit of hard spheres. They behave like weak elastic solids at low stresses but begin to flow at stresses exceeding the yield stress. Once they begin to flow, they are shear thinning; that is, their effective viscosity decreases with increase in shear rate. These unique features make them useful as rheological additives in many important industrial applications including processing of high performance coatings, solid inks, ceramic pastes, drilling muds and textured food and personal care products [Fernandez-Nieves (2011)]. Despite their wide industrial use, their formulation has been largely empirical. A quantitative bridging of the constituent properties and their macroscopic properties would enable customized design of the material to suit the requirements of its processing, use and storage. The microstructure and dynamics of biological materials such as tissues and intracellular cytoplasm [Angelini *et al.* (2011); Bursac *et al.* (2005); Trepat *et al.* (2007)], and geological materials like clays and slurries [Ancey (2007)] also resemble that of soft particle glasses.

Many interesting rheological aspects of these glasses such as yield stress, shear thinning, wall slip and history dependent phenomena like aging have been widely observed but the connection between their macroscopic behavior and microstructure is still unclear. Thus, understanding the connection between microstructure and rheology of these highly concentrated suspensions of soft particles remains an area of high importance both in terms of industrial applications and fundamental condensed soft matter physics. The purpose of this dissertation is to understand and explain the rheology of these soft particle glasses in terms of their constituent properties and the microstructural changes that occur during their deformation and flow.

1.1.1 Industrial importance of soft particle glasses

Concentrated microgel suspensions are industrially important soft particle glasses in which the constituent soft particles are swollen crosslinked polymeric particles. Microgel based additives have been used as rheological modifiers in the cosmetic industry for over 50 years. Carbopol® is a range of commercially available rheological additives based on polyacrylic microgels and are used in shampoos, hair gels, hand sanitizers, body lotions and other cosmetic products [Ketz *et al.* (1988); Lubrizol; Piau (2007)]. The yield stress nature of the soft particle glass presents high suspending ability to the product and prevents creaming and sedimentation of particulates over long periods of time that is crucial in the storage and transport of these cosmetics. The high viscosity at low shear rates allows convenient retrieval from the packaging without the product running between fingers and the shear thinning nature allows easy application on skin and scalp. Highly concentrated oil in water emulsions is another type of soft particle glass, where the constituent particles are the dispersed and compressed oil droplets. Many cosmetics like baby creams and sunscreen lotions are concentrated emulsions and thus fall under the category of industrially relevant soft particle glasses [Jager-Lezer *et al.* (1998)].

Microgel based soft particle glasses are also used as additives in the automotive coating industry [Boggs *et al.* (1996); Ishikura (1996); NipponPaints; Saatweber and Vogt-Birnbrich (1996); Wolfe (1992)]. The coating formulation has to undergo storage, pipe flow, spraying, film formation and drying. Organic solvents were initially used as the base for suspending the resins and pigments in these coatings. These solvents facilitated application of the coating and then evaporated during drying. The large amounts of volatile organic compounds (VOC's) in these coatings were not environmentally favorable and coatings with high solid content became more common and this was initially accomplished by altering the polymer molecular weight and concentration within the resins. The use of low molecular weight polymers produces coatings with low viscosities and made them suitable for spraying uniform films, but the viscosity increase at low shear during drying was insufficient and lead to sagging or running and dripping of the paint. The use of high molecular weight polymers provided high low-shear viscosity and prevented sagging but the viscosity at high shear was not low enough and presented difficulties during spraying. On the other hand, concentrated microgel glasses exhibit yield stress that improves viscosity immediately after application and prevents sagging. They are also shear thinning enough to have low viscosities during spraying and present good leveling properties. Microgel additives are also used as serigraphic ink thickeners. These inks are used in screen printing and the sharp liquid-solid transition on flow cessation which comes from the yield stress of these soft glasses is useful in maintaining the shape of the ink pattern once it is transferred to the substrate [Physical Review Focus (2000)].

Bio-compatible microgels are used as rheology modifiers in the food industry to bring the desired texture and flow behavior to various foods. Starch granules before gelatinization behave as hard spheres. They gelatinize with heat and moisture to form swollen microgel particulates and retain this nature even on cooling. At high concentrations they exhibit viscoelastic behavior [Evans and Haisman (1980); Evans and Lips (1992); Steeneken (1989)]. Starch based rheological additives are used extensively in foods like salad dressings, sauces, custards and puddings [Abbas *et al.* (2010)]. These particulate microgels can provide a texture in the mouth that mimics fats and so they have also been modified and used as additives in low-fat food products like low-fat yoghurt

[Alting *et al.* (2009)]. Concentrated glassy emulsions are abundant in food industry and include materials like mayonnaise, “spoonable” salad dressings and margarine [Friberg *et al.* (2004); McClements (2005)]. Whipped cream and ice creams are concentrated foams encountered in the food industry where the dispersed particles are essentially air bubbles.

Drilling muds are complex fluids used in drilling boreholes for oil and natural gas wells. Microgel particles are soft and deformable and can penetrate rock pores and they are used as fluid loss control agents to prevent the flow of drilling fluids into the rock pores [Fernandez-Nieves (2011)]. One of the functions of drilling muds is suspending the drill cuttings while drilling is paused and when the drilling assembly is brought in and out of the hole. Clays and polymer gels including guar gum are used as rheological additives which impart high viscosity to the mud at rest and low shear thinning viscosities when drilling begins. Concentrated microgels can be used in place of the clays and polymer gels as rheology modifiers but the right choice of constituent polymers and preparation conditions in order to make them withstand the temperature, pressure and varying salt concentrations under the earth is crucial and is an area of ongoing research.

The rheology and microstructure of a few of these industrially relevant soft particle glasses is presented in Figure 1.1-1.3. Even though soft particle glasses are widely used in various industrial applications as rheological additives and many food products fall under the category of soft particle glasses, their formulation is largely empirical [Paruta-Tuarez *et al.* (2011)]. A quantitative connection between the constituent properties like solvent viscosity and particle properties and their macroscopic rheology is lacking. The connection between the microstructure and rheology of these materials is also an open question.

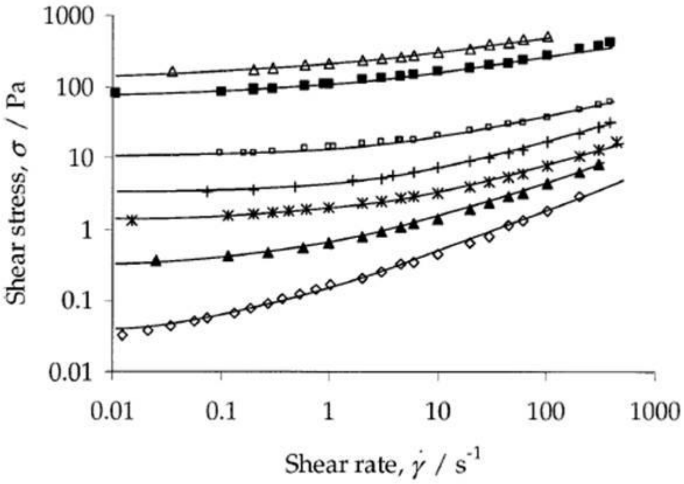

	0.045%	0.06%	0.07%	0.08%	0.10%	0.30%	1.00%
σ_0	0.03	0.300	1.25	3.0	10.00	70	115
k	0.12	0.345	0.67	1.4	3.75	40	100
n	0.60	0.550	0.50	0.5	0.45	0.35	0.3

Figure 1.1: Steady shear rheology of Carbopol from Roberts and Barnes (2001) fitted to the Herschel-Bulkley equation of form $\sigma = \sigma_0 + k\dot{\gamma}^n$.

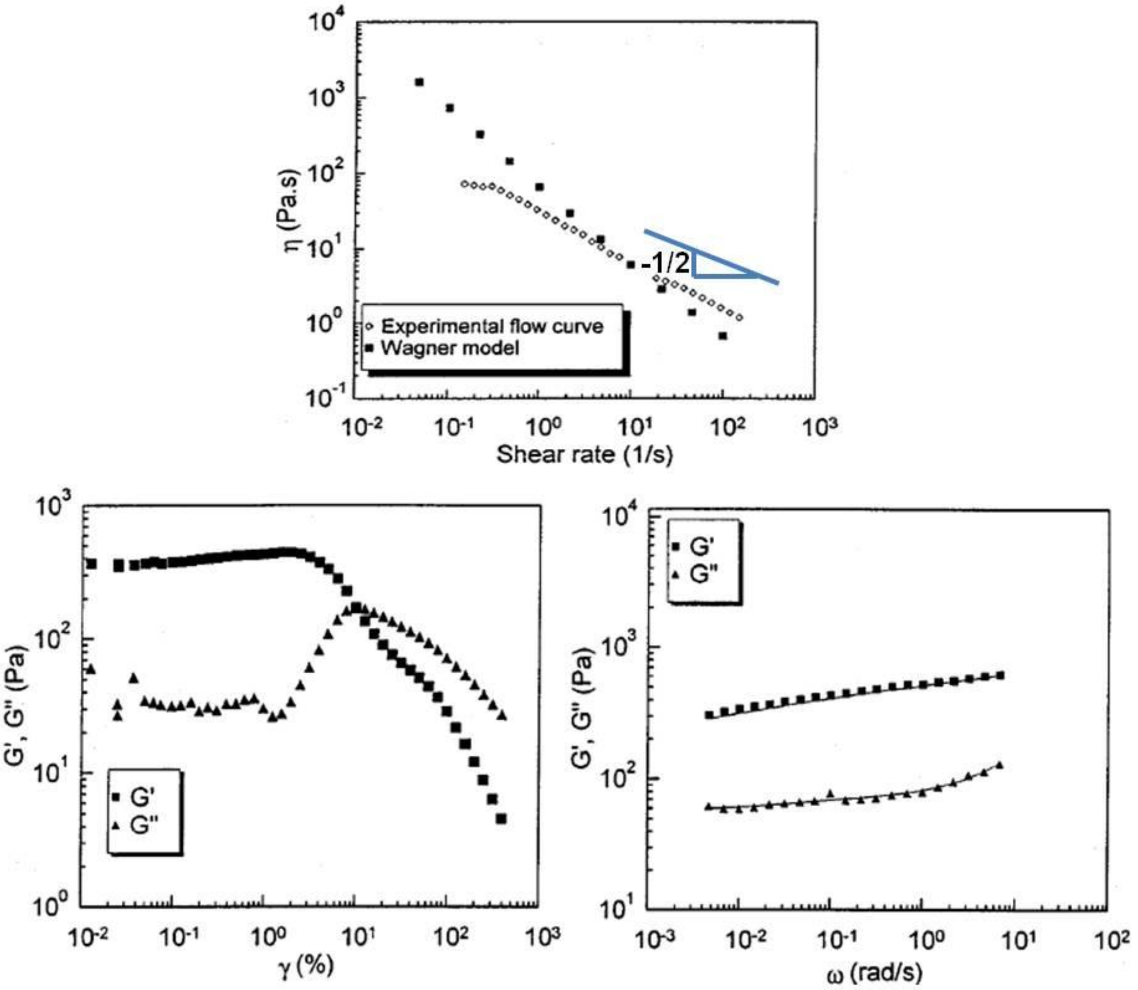

Figure 1.2: Steady and oscillatory shear rheology of commercial mayonnaise form Bower *et al.* (1999). A slope of -0.5 has been added to the steady shear flow curve on top for reference.

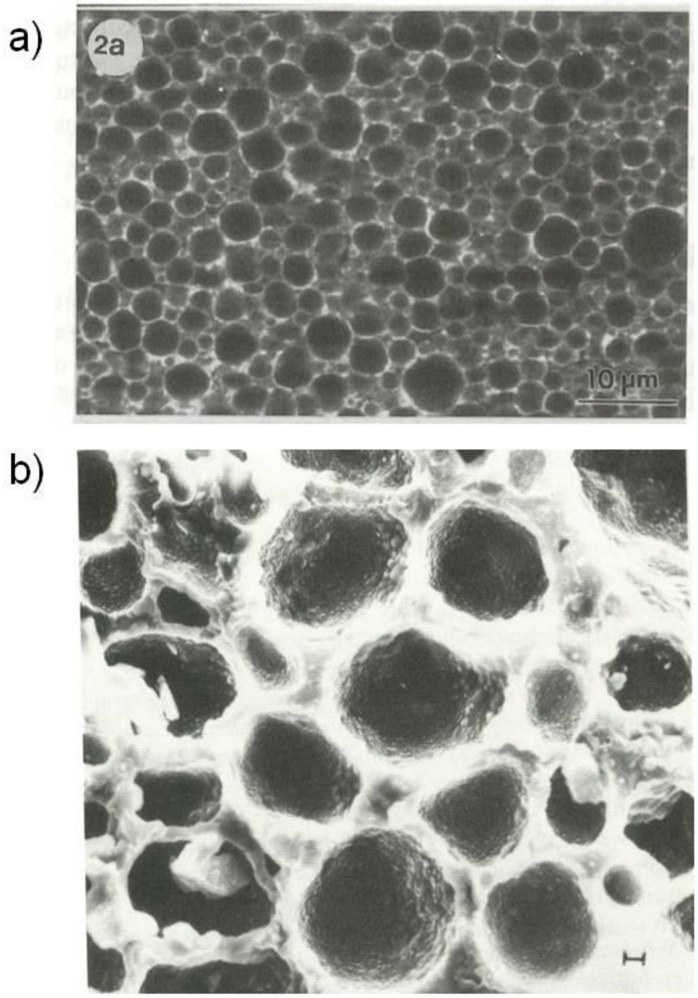

Figure 1.3: Microstructure of soft particle glasses in the food industry. (a) The microstructure of full-fat mayonnaise as visualized by CLSM (Confocal Laser Scanning Microscopy) from Dickinson and Rodríguez Patino (1999). (b) Scanning electron micrograph of whipped cream from Dickinson and Royal Society of Chemistry (Great Britain). Food Chemistry Group. (1987). The bar corresponds to 10 μm.

1.1.2 Soft particle glasses as model systems in soft condensed matter physics

The microstructure and dynamics of many other systems in biology, geology and material science resemble that of soft particle glasses. Biological materials such as tissues [Angelini *et al.* (2011); Trepat *et al.* (2007)] and intracellular cytoplasm [Bursac *et al.* (2005)] resemble crowded assemblies of soft and deformable entities. They display glassy characteristics such as aging and slow dynamics. They also exhibit a combination of solid-like and liquid-like behavior to deformation depending on the nature and duration of the stimuli. Geologically relevant systems like clays, slurries, debris and lava flows can be modeled as highly concentrated suspensions of deformable particles with vastly heterogeneous constituents in terms of size, softness and shape [Ancey (2007)]. Yield stress has been a common characteristic observed in the above mentioned concentrated geological materials.

Soft particle glasses also share some common characteristics with molecular glasses. The glass transition in molecular glasses is approached as the temperature of the material is reduced and nears the glass transition temperature while the glass transition in colloidal glasses (both hard and soft particles) is approached as the concentration (volume fraction in particular) is increased and nears the glass transition. The similarities in behavior include disorder, non-ergodicity close to glass transition, history dependent phenomena including slow dynamics and aging, yield stress and shear/temperature melting [Weitz (2011)]. Hard particle glasses also possess these similarities but the particle softness in the case of soft particle glasses provides an additional handle to study glasses of varying "fragility". In molecular glasses fragility is an indicator of how quickly the dynamics freezes as the glass approaches the glass transition temperature. Simple liquid structures tend to form more fragile glasses where the viscosity diverges steeply at glass transition similar to the case of hard spheres close to the glass transition [Angell *et* *al.* (2000)]. On the other hand, molecular glass formers with complex internal structures form strong glasses and hence molecular glasses exhibit a range of fragility. The softness of particles can be varied to mirror the varying fragilities in molecular glasses and softer particles are known to form stronger glasses [Mattsson *et al.* (2009)]. In terms of constituent particles, soft particle glasses combine the deformability of polymer coils and the impenetrability of hard spheres and provide a way to tune the interactions of the material to generate a wide range of rheological properties and form a class of important model systems in statistical and soft condensed matter physics.

1.2 BACKGROUND

1.2.1 Description of soft particle glasses

Soft particle glasses are densely packed, disordered suspensions of soft particles. The constituent soft deformable particles include a wide range of materials [Bonnecaze and Cloitre (2010)]. Figure 1.4 shows some examples of such soft particles. The size and origin of elasticity in these constituents can be widely different. Microgel particles (see figure 1.4a) are crosslinked polymeric networks swollen by a solvent. Their size can range from tens of nanometers to micrometers. The osmotic pressure difference between the gel and the solvent which gives rise to the swelling of the particles is the source of elasticity and the particle scale elasticity depends on the degree of crosslinking inside [Borrega *et al.* (1999)]. Emulsion droplets stabilized by surfactants (see figure 1.4b) are also soft and deformable yet impenetrable [Lacasse *et al.* (1996)]. The droplet sizes are usually of the order of microns for oil-in-water emulsions. The origin of elasticity here is the oil-water surface tension which resists deformation. Particles of core shell nature which have a hard interior core with a soft exterior shell form another class of soft particles [Vlassopoulos and Fytas (2010)]. They can be hard particles grafted with short polymer chains [Crassous *et al.* (2006)] (see figure 1.4c) or star polymers which are ultrasoft particles where the corona consists of long polymer chains (see figure 1.4d) [Likos (2006)]. In both cases, the deformability of the polymer exterior is the source of particle elasticity. Block copolymers (see figure 1.4e) form spherical micelles in selective solvents where the solvent-phobic ends shield themselves from the solvent by forming the core and the solvent-friendly ends form the shell or the corona of the soft particles [Buitenhuis and Forster (1997)]. Amphiphilic molecules can arrange themselves to form sheet like membranes in solution and they can form different geometries like bi-layers (see figure 1.4f) or multi-layers (see figure 1.4g) which can wrap around to form multi layered vesicles which are soft and deformable due to the flexibility of the lamellar membranes [Ramos and Cipelletti (2001)]. Foams also form soft glassy materials in which the air bubbles are the constituent soft particles and again, the air-water surface tension is the source of the elasticity of the “air particles” [Princen and Kiss (1989)].

When these soft particles are suspended in a solvent they form different phases depending on the concentration as shown in figure 1.5. Here we focus on the disordered phases formed by these particles. At very low concentration or particle volume fraction they form dilute suspensions and resemble suspensions of hard particles. As the volume fraction is increased to values greater than around 0.58 the constituent particles begin to crowd and the material exhibits glassy behavior. Each particle begins to get surrounded by a cage of other particles. The elasticity of the cage in this phase is entropic and the glasses are thermally activated which gives rise to yield stresses and elastic moduli of $O(kT)$. Now these are soft particles and are deformable and hence unlike hard particles the volume fraction can be increased beyond random close packing of hard spheres which is 0.64. In this regime the cages are tighter and the particles are compressed against each other forming flat facets at contact. The cage elasticity in this regime stems from the elastic interactions at the particle-particle contact and based on the extent of jamming this can give rise to an elastic moduli of the order of hundreds or even thousands of Pascals. The elastic contact forces are much larger than the thermal forces and thus the suspensions are athermal. The jammed soft particle suspensions in this regime are termed as soft particle glasses.

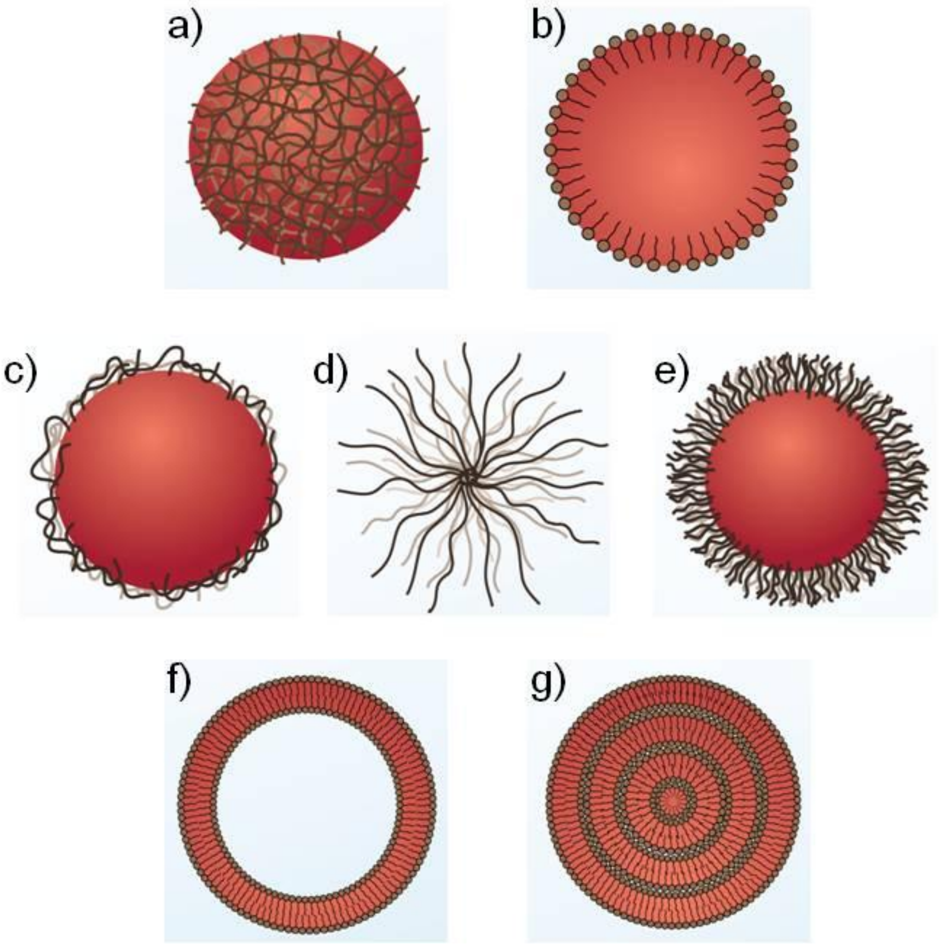

Figure 1.4: Schematic of various types of soft particles. (a) microgel particle; (b) emulsion droplet; (c) solid particle covered with adsorbed or grafted polymer chains; (d) star polymer; (e) block copolymer micelle; (f) liposome (bilayer); (g) multi-lamellar vesicle.

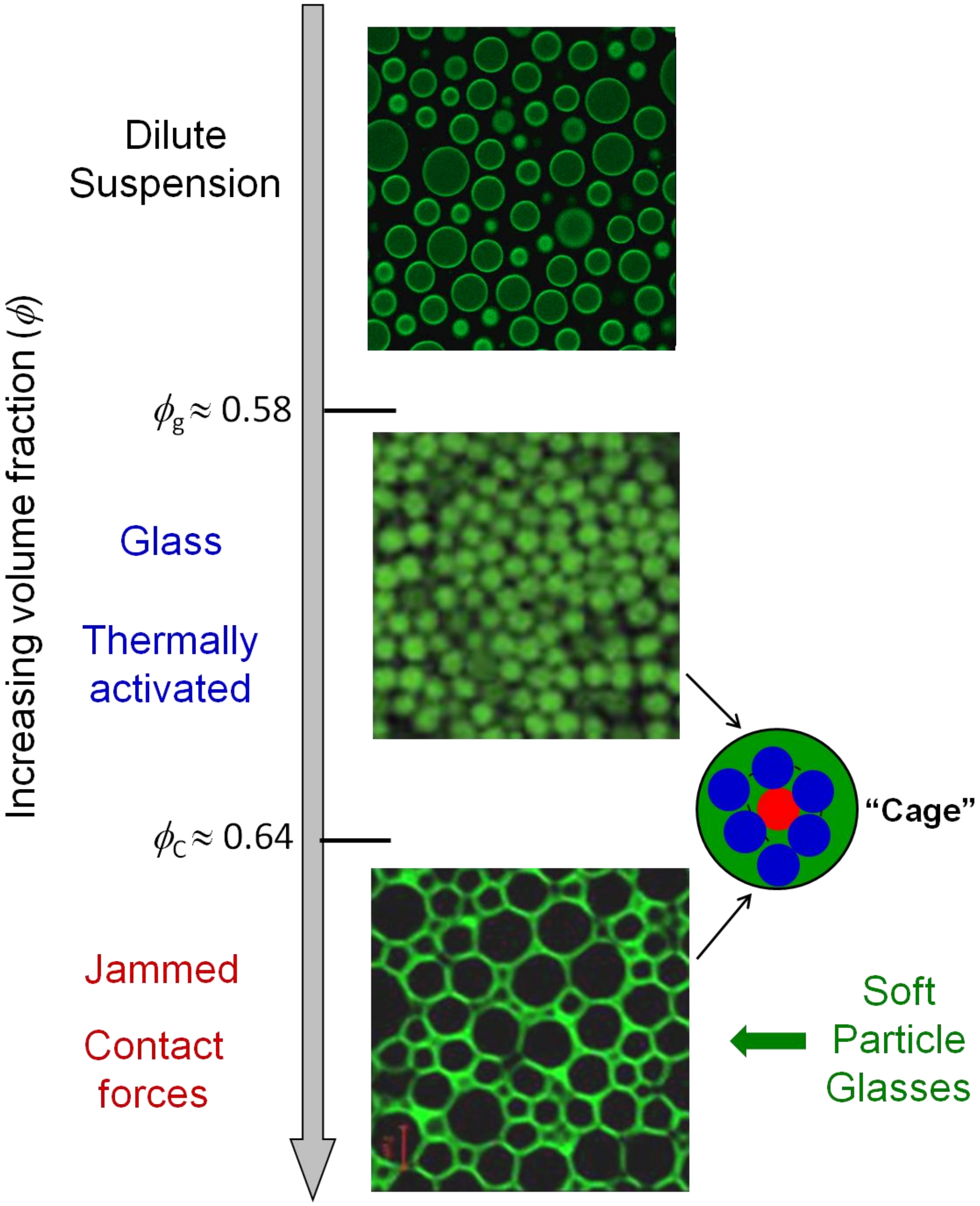

Figure 1.5: Phase diagram of disordered soft particle suspensions. Top: Confocal microscope image of a dilute silicone-oil in water emulsion ($\phi \simeq 0.35$). Center: Fluorescent micrograph of a concentrated PMMA (hard) suspension ($\phi \simeq 0.57$) from Sarangapani and Zhu (2008); Bottom: Confocal microscope image of a jammed silicone-oil in water emulsion $(\phi \simeq 0.8)$.

1.2.2 Generic microstructure and rheology of soft particle glasses

Despite the different particle sizes and sources of elasticity, these concentrated suspensions of soft particles share many common microstructural and rheological properties. Some relevant common properties are discussed below.

1.2.2.1 Microstructure

The constituent particles in soft particle glasses are compressed against one another due to their high concentration and form flat facets at contact as mentioned previously. The average separation between neighboring particles is less than twice the particle radius due to their high concentration and deformability, and this gives rise to an elastic repulsion at particle-particle contact. Each particle is trapped in a cage formed by its nearest neighbors and these cages are symmetric at rest. The cage strength depends on the elasticity of the particles themselves and the degree of compression. The generic nature of the microstructure in different soft particle glasses is shown in figure 1.6.

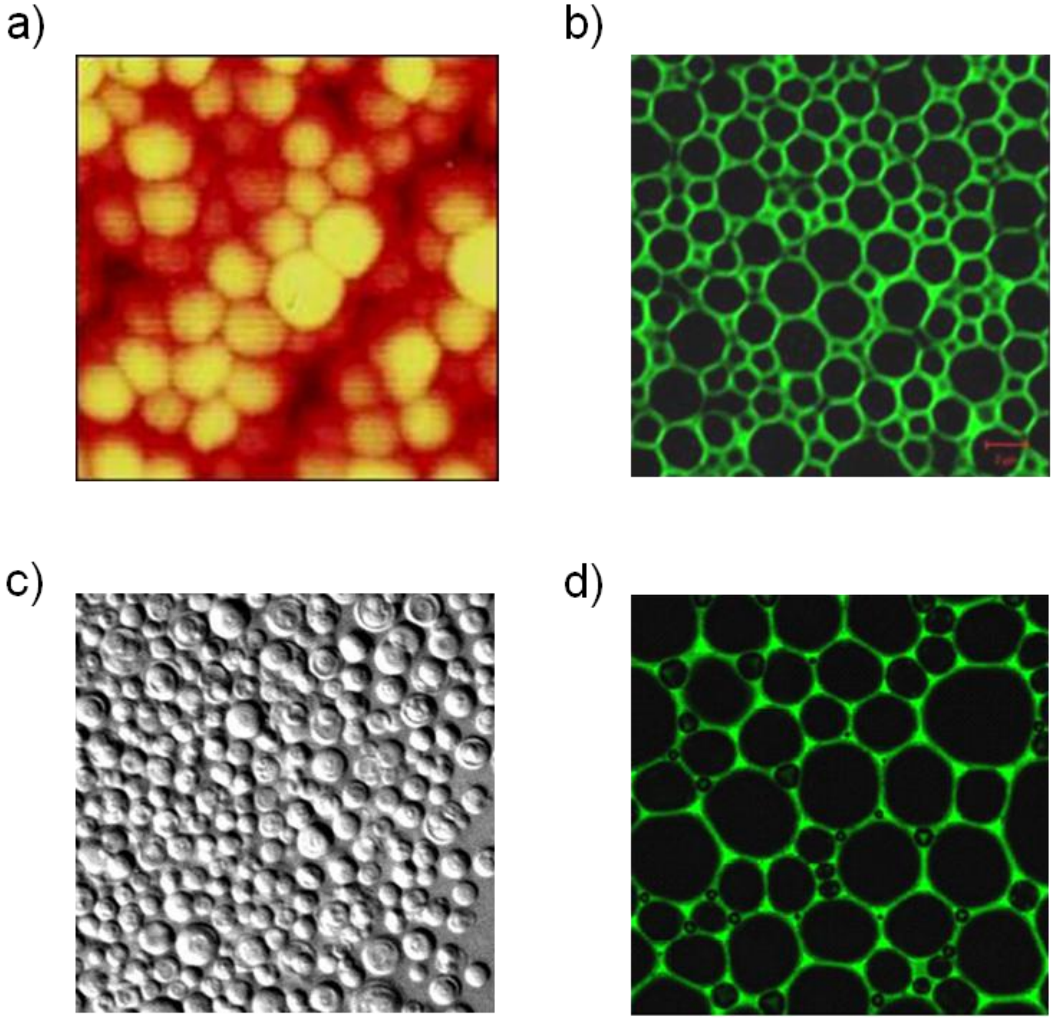

Figure 1.6: Microstructure of soft particle glasses: (a) AFM image of a concentrated microgel suspension ($d \approx 0.2\ \mu\text{m}$) from Cloitre *et al.* (2003a). (b) Confocal microscope image of a concentrated silicone-oil in water emulsion ($d \approx 2\ \mu\text{m}$) from Meeker *et al.* (2004b). (c) Optical microscope image of a multi-lamellar vesicle gel ($d \approx 5\ \mu\text{m}$) from Ramos and Cipelletti (2001). (d) Confocal microscope image of aqueous foam ($d \approx 50\ \mu\text{m}$) from Seth (2008).

1.2.2.2 Steady shear rheology

Soft particle glasses are yield stress fluids and are shear thinning at high shear rates/stresses and follow a Herschel-Bulkley type constitutive equation between shear stress (σ) and shear rate ($\dot{\gamma}$) : $\sigma = \sigma_y + k\dot{\gamma}^m$ where σ_y represents the yield stress. At low stresses, the particles are trapped inside their cages and the external stimulus is not sufficient to break them out of their cages but the soft nature of the particles allows them to compress against one another. This gives rise to local elastic deformation as allowed by the elasticity of the paste without exhibiting any macroscopic flow. As a consequence, they exhibit the phenomenon of yield stress and exhibit solid-like behavior at low stresses. At high stresses, the particles squeeze past the caging particles and break free bringing about macroscopic flow or liquid-like behavior and at this point the viscosity of the suspending fluid becomes important as well. The suspensions are shear thinning at high stress/shear rates and exhibit a universal exponent (*m* in the Herschel-Bulkley model) of around 0.5. Figure 1.7 shows the steady shear flow curves of microgels (a), compressed emulsions (b) and multi-lamellar vesicles (c). A reference slope of 0.5 is indicated in (a) and (b) and the curves with filled symbols from bottom to top indicate increasing concentration. In the case of multi-lamellar vesicles (MLV) in the study of Fujii and Richtering (2006), the radius of the MLV depends upon the preshear rate when the vesicles are formed and the main figure presents the data for a preshear of 20s^{-1} and different gap heights for shearing. The inset provides the shear thinning exponent ($m \cong$ 0.6) in the Hershel-Bulkley model for different preshear rates (vesicle sizes) and gap heights. At small gap heights and low shear rates there could be some aligned phases of lamellae forming which could lead to a deviation from the generic behavior. Soft particle glasses also exhibit non zero normal stress differences during shear [Seth *et al.* (2011)].

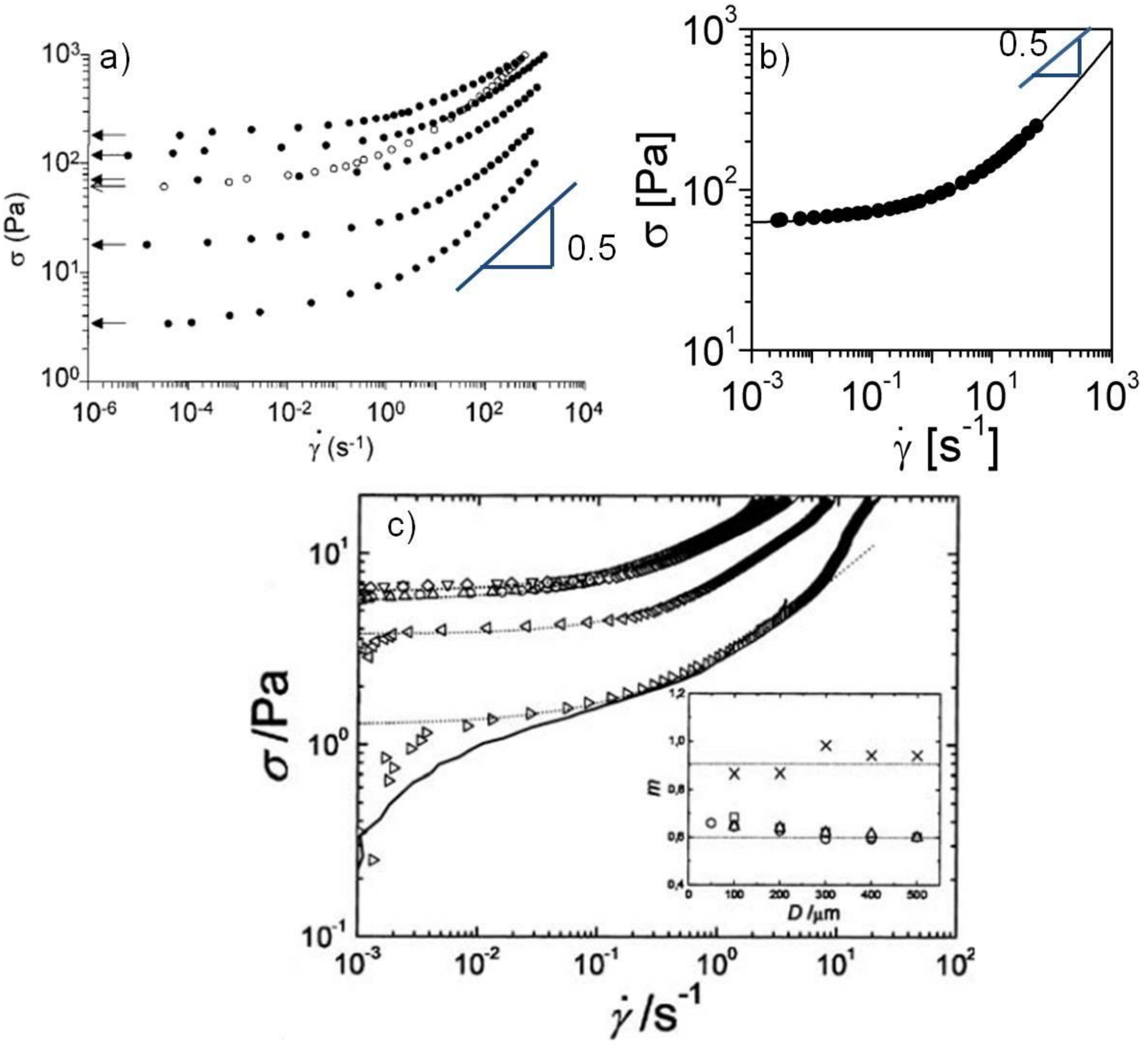

Figure 1.7: Steady shear flow curves of different soft particle glasses. (a) microgels from Cloitre *et al.* (2003b). (b) concentrated oil-in-water emulsions from Seth *et al.* (2011). (c) multi-lamellar vesicles from Fujii and Richtering (2006).

1.2.2.3 Oscillatory shear rheology

The transition of the behavior of soft particle glasses from that of an elastic solid to an elasto-plastic liquid can also be observed through oscillatory shear tests. While the steady shear flow curves present the material behavior at and above yield stress, oscillatory shear tests can provide information about the material behavior below and above the yield stress and the transition thereof. Figure 1.8 presents the results of stress-strain behavior during oscillatory shear of two different soft particle glasses: (a) microgels and (b) core-shell particles with a polystyrene (PS) core and a soft shell made of crosslinked poly(*N*-isopropylacrylamide) (PNiPAM). They exhibit linear elastic behavior at low strain amplitude and then become non-linear at large strain amplitudes with a plastic flow segment at large stresses. The viscoelastic moduli as a function of strain amplitude and frequency are presented for three different soft particle glasses in figure 1.9. The storage modulus G' is a qualitative indicator of the solid-like behavior of the material while the loss modulus G'' is a qualitative indicator of the liquid-like behavior of the material. In the linear regime (at small strain amplitudes) the storage modulus is much larger than the loss modulus indicating a solid like behavior and as strain amplitude increases the storage modulus begins to decrease and the loss modulus increases indicating more liquid like rearrangements. G'' decreases at large strain amplitudes due to shear thinning. Both storage modulus and loss modulus increase with frequency $\sim \omega^{0.5}$ at large frequencies in the linear regime.

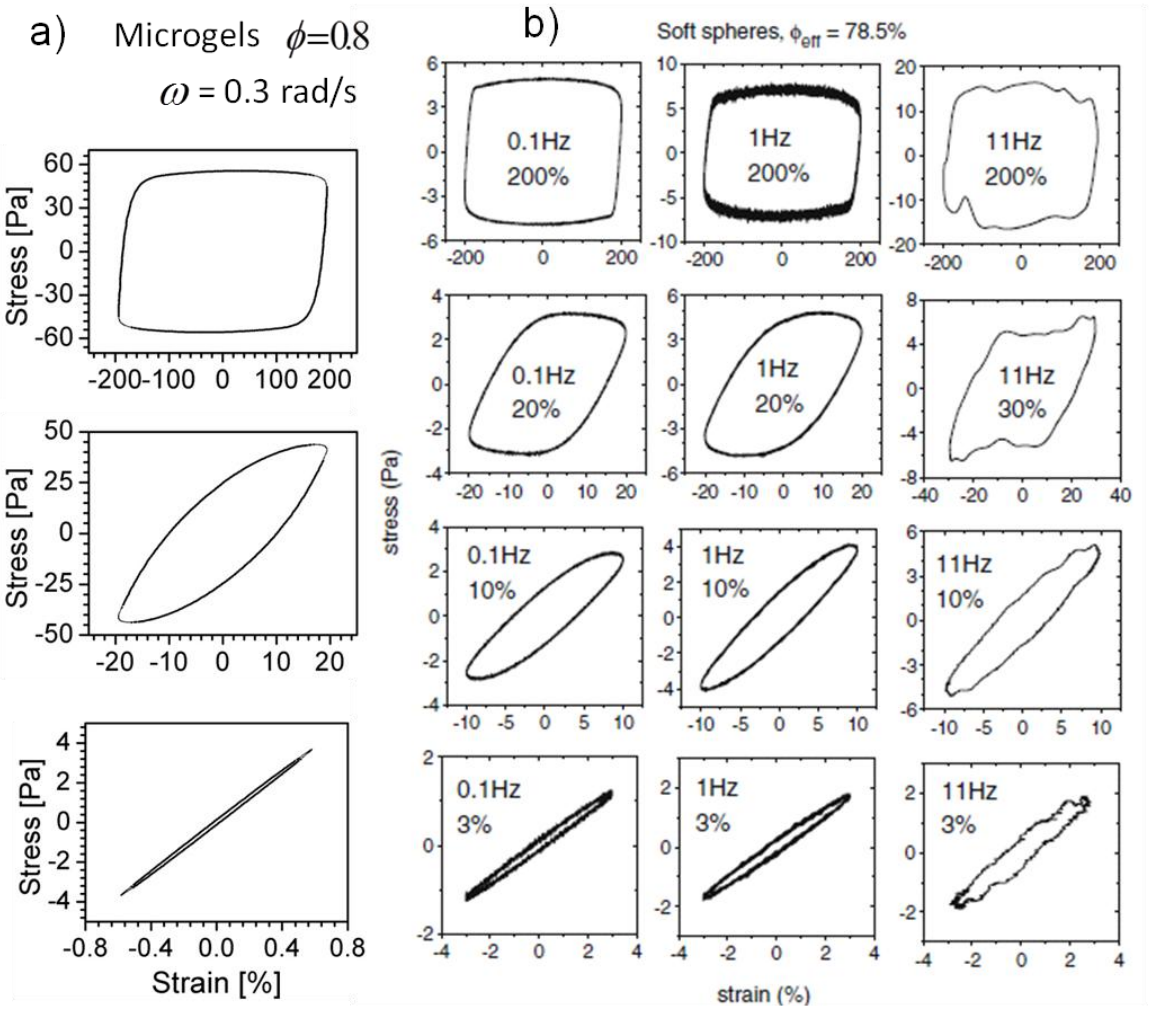

Figure 1.8: Stress-strain behavior during oscillatory shear for different soft particle glasses. (a) microgels from Mohan *et al.* (2013). (b) Core-shell particles from Le Grand and Petekidis (2008).

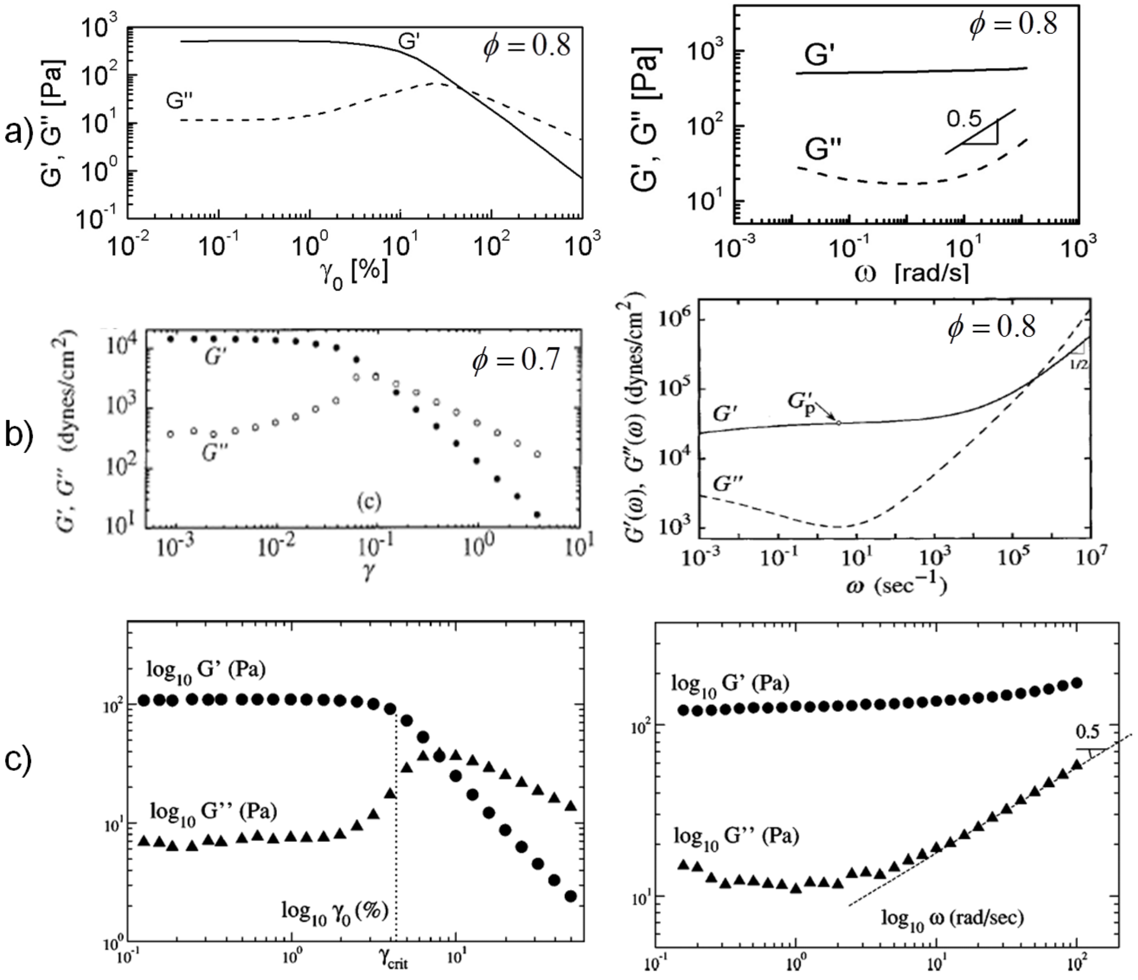

Figure 1.9: Viscoelastic moduli during strain (left) and frequency (right) sweeps for different soft particle glasses. (a) Microgels from Mohan *et al.* (2013). (b) Concentrated emulsions: strain sweep from Mason *et al.* (1996) and frequency sweep from Mason (1999). (c) silica particles with adsorbed polyethylene oxide coating from Derec *et al.* (2003).

1.2.2.4 Wall slip and other surface effects

Concentrated suspensions of both hard and soft particles are known to slip at smooth surfaces usually due to a thin lubricating layer depleted of particles near the surface Barnes (1995). The mechanism and nature of slip depends on the individual particle nature and microstructure. In the case of soft particle glasses, elastohydrodynamic interactions between the particle and the wall through the lubricating layer of solvent in between is attributed as a cause of slip. Wall slip has been observed in soft particle glasses like microgels [Meeker *et al.* (2004b); Seth *et al.* (2008)], concentrated emulsions [Pal (2000)] and foams [Denkov *et al.* (2005)]. Wall slip can affect the rheological characterization of these materials and the nature of wall slip depends not only on the smoothness of the flow surface but also on the nature of interactions between the wall surface and the constituent particles [Seth *et al.* (2012)]. Figure 1.10 shows the effect of wall slip with different wall-particle interactions for concentrated emulsions and microgels from [Seth (2008)]. At low shear rates it gives rise to apparent motion below the yield stress. The effect of slip is more predominant at low stresses and can affect the measurement of viscoelastic moduli as well. Figure 1.11 shows the effect of slip in the measurement of storage modulus for concentrated oil-in-water emulsions from [Pal (2000)]. A detailed study of the particle-wall interactions, their effect on flow mechanisms and determination of the relevant factors to control or tailor slip is an area of active interest and importance.

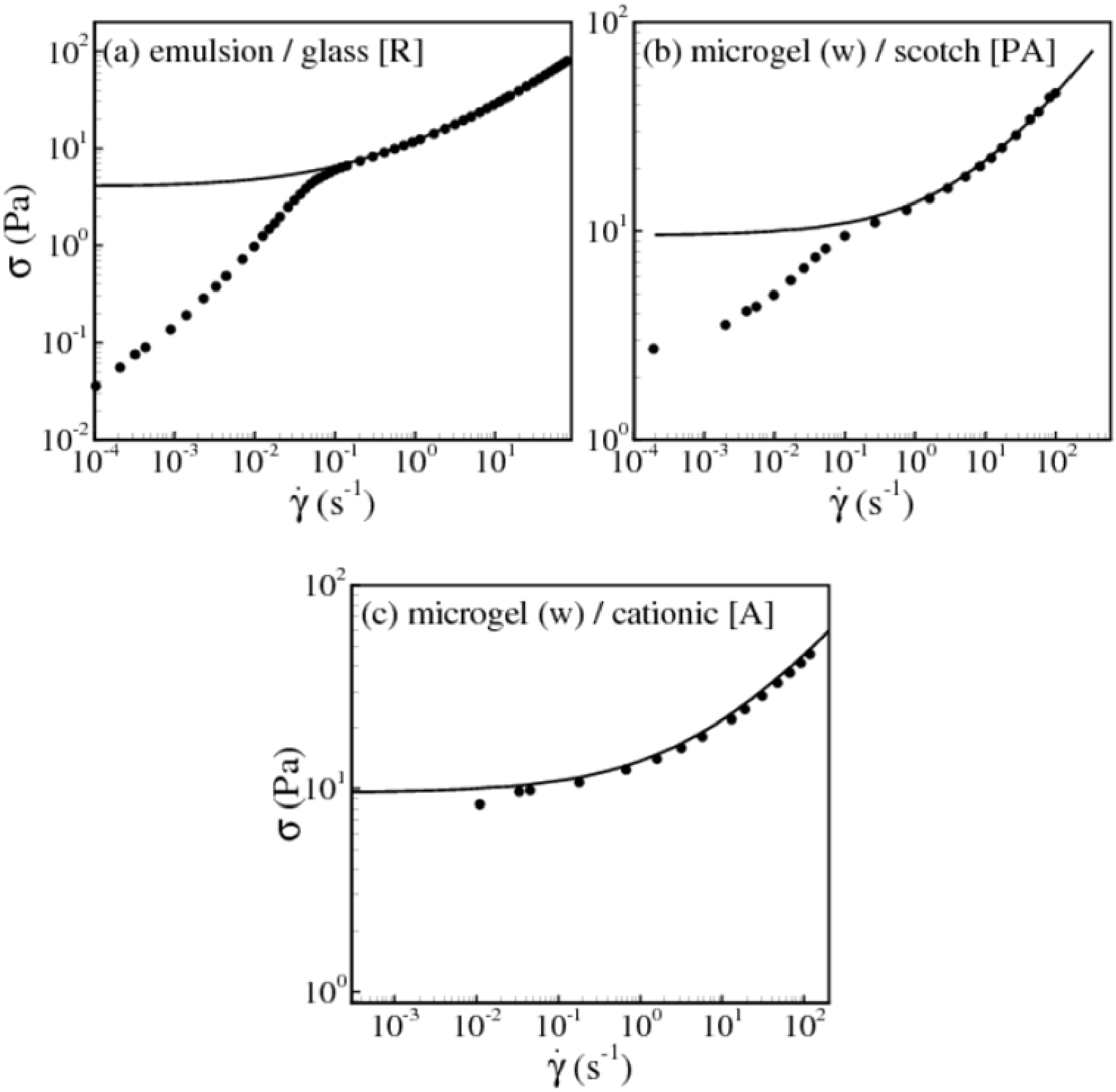

Figure 1.10: Effect of shearing surface in soft particle glasses from Seth (2008). Symbols correspond to flow curves obtained with different surfaces: (a) repulsive; (b) partially adhering and (c) attractive. The solid line corresponds to the bulk flow curves obtained using rough-rough surfaces.

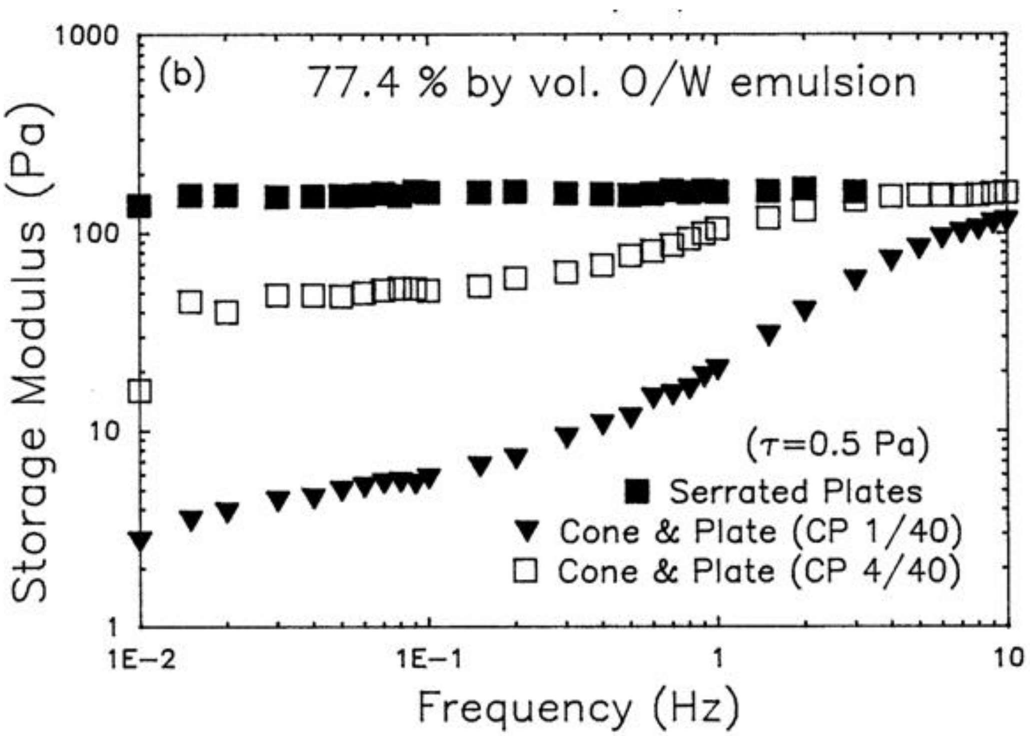

Figure 1.11: Effect of wall slip in the measurement of viscoelastic moduli in concentrated emulsions from Pal (2000).

1.2.2.5 Aging and Memory

Soft particle glasses age with time or their properties continue to evolve with time [Cloitre *et al.* (2000); Cloitre *et al.* (2003b); Lieleg *et al.* (2011); Ramos and Cipelletti (2001); Weitz (2001)]. At rest the disordered material is still out of equilibrium as the particles are kinetically trapped in a metastable, disordered configuration. The constituent particles slowly rearrange as the system tries to move towards a more stable state. Hence their microstructure and rheological properties change slowly with time and this is termed aging. Aging is monitored by tracking the evolution of properties like strain, yield stress and elastic moduli. Figure 1.12a shows aging of concentrated microgels through strain recovery after the cessation of shear. The strain continues to relax after the shear is stopped. These rearrangements also slow down further as the "stability" of the suspension increases with time which gives rise to a logarithmic strain recovery. The aging phenomenon in soft particle glasses also bears similarities with the aging in polymer [Hodge (1995)], metallic [Ruta *et al.* (2012)] and spin glasses [Jonason *et al.* (1998)].

These glasses are also known to possess memory properties. If a material is presheared in a particular direction and if a small step stress (much smaller than the yield stress) is applied in the opposite direction after aging for a time t_w, the material responds to the new step stress initially for a time comparable to t_w and then continues to trace back its old relaxation path exhibiting recollection of its flow history (see figure 1.12b). Hence these materials are also known to possess memory.

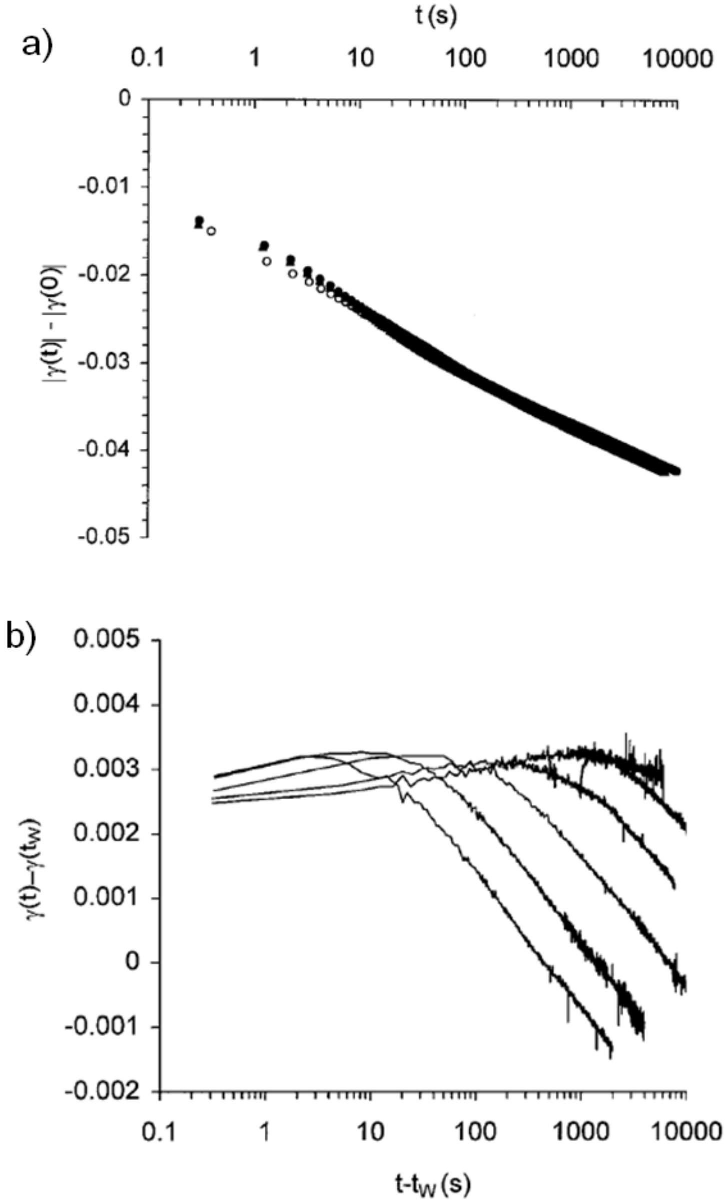

Figure 1.12: Aging and memory properties of concentrated microgel glasses from Cloitre *et al.* (2000). (a) Strain recovery on flow cessation from different preshearing stresses. (b) Strain response at different waiting times (increasing from left to right) to a small step stress.

1.3 DISSERTATION OUTLINE

Soft particle glasses possess unique rheological properties which make them useful as rheological additives in various industrial applications including high performance coatings, serigraphic inks and textured food and cosmetic products. But the design of these rheological additives is largely empirical. These glasses also serve as model systems in soft condensed matter physics by combining the deformability of polymers and impenetrability of hard spheres. They also share similarities with the rheology of biological materials like tissues and intracellular cytoplasm, and geological materials like clays and slurries. Though the unique properties of these materials like yield stress, shear thinning, wall slip and aging have been widely observed at a macroscopic level, the microscopic changes which give rise to this rheology are unknown. For my dissertation, I have investigated the rheology of these materials at a microscopic and a macroscopic scale with the goal of connecting both. I have also aimed to connect the constituent properties like solvent viscosity and particle properties like radius, contact modulus and concentration to the macroscopic properties such as osmotic pressure, viscoelastic moduli, shear and normal stresses. This provides a means to tailor the formulation of soft particle glasses to have the desired rheological properties suited to the requirements of processing, handling and storage. The outline for the rest of my dissertation is as follows.

In Chapter 2, the steady shear rheology of soft particle glasses is studied. The model developed earlier [Seth (2008)] is tested for steady shear through particle scale simulations and the macroscopic properties are compared with experiments from Dr. Clotire's lab at ESPCI ParisTech to validate the model. A connection is made between the solvent viscosity, particle concentration and particle elasticity to the macroscopic shear and normal stresses. A detailed microstructural analysis is developed and the microscopic flow mechanisms are determined. Finally, a constitutive equation for these soft particle glasses is derived from the microstructural analysis.

In Chapter 3, the model is extended to study the oscillatory shear rheology of these soft particle glasses and the simulation results are again validated with experimental results from Dr. Cloitre's lab. A connection is made between the solvent viscosity, particle concentration and particle elasticity to the macroscopic viscoelastic moduli. The origin of yielding is determined from three different scales. At the particle scale, the origin of yielding corresponds to the onset of cage escape events and the appearance of a non-negligible particle scale shear induced diffusivity. At the mesoscopic scale, yielding corresponds to the appearance of angular asymmetry in the microstructure and macroscopically yielding corresponds to the onset of non-linearity in their stress-strain behavior.

In Chapter 4, the history dependent behavior of these materials and in particular the appearance of internal stresses on flow cessation and their dependence on the flow effects before cessation are investigated. At a macroscopic scale, the stress relaxation of soft particle glasses on flow cessation was experimentally investigated by the author during a visit to ESPCI ParisTech using concentrated microgels with different constituent properties. Trapped internal stresses were observed whose magnitude depended on the shearing history and the constituent properties. Particle scale simulations are developed to understand the microscopic mechanisms behind the stress relaxation on flow cessation. A universal scaling is presented for the trapped internal stresses as a function of the initial flow conditions and the yield stress of the glass based on the insights gained from the microstructural study.

Novel experimental techniques are being developed to understand the rheology of these materials at a microscopic scale. Active microrheology is one such technique in which a probe particle is pulled through a suspension at constant force or velocity and the response of the particle is tracked to determine the local viscoelasticity of the material. This method is particularly useful for materials that are available in small volumes such as cell samples. In Chapter 5, simulations are developed to model the constant force microrheology of soft particle glasses. Local viscoelastic properties are determined and connected to the macroscopic properties computed from bulk rheology. The microstructural changes due to the forced motion of the probe particle are investigated and the findings are connected to the variation of the local viscoelastic properties.

The connection between microstructure and rheology is strongly established in chapters 2 through 5 which suggest that knowing the microstructure would enable prediction of macroscopic properties and also reveal the microscopic flow mechanism. In Chapter 6, a pairwise theory is developed to predict the microstructure and properties of quiescent soft particle glasses and the theory is tested with simulation results using three different inter-particle potentials. In Chapter 7, the theory is extended to sheared soft particle glasses and the predictions are compared with simulation results in chapter 2 and experiments from Dr. Cloitre’s lab at ESPCI ParisTech.

Finally, in Chapter 8, important conclusions from different chapters and recommendations for future work are presented.

Chapter 2: Steady Shear Rheology*

2.1 INTRODUCTION

Soft particle glasses are yield stress fluids that behave like weak elastic solids at low stresses and begin to flow at large stresses exceeding the yield stress. Unlike hard sphere glasses that have a yield stress of the order of *kT*, these materials can possess yield stresses of 10's or even 100's of Pascals because the constituent particles are packed beyond the random close packing limit and interact through elastic contacts. This unique feature of theirs makes them useful as soft rheological additives to process high performance coatings, solid inks, ceramics pastes, textured food and personal care products. Steady shear rheology of concentrated hard sphere suspensions has been investigated thoroughly [Brady (1996); Morris (2009); Stickel and Powell (2005)] through experiments [Cheng *et al.* (2002); Marshall and Zukoski (1990)], simulations [Brady and Bossis (1985); Foss and Brady (2000); Sierou and Brady (2002)] and theory [Fuchs and Cates (2002); Fuchs and Ballauff (2005)], but much of the understanding of soft particle suspensions at these volume fractions relevant in applications is empirical, and a theory connecting macroscopic flow behaviour to microstructure and particle properties remains a formidable challenge for statistical and condensed matter physics.

Mode Coupling Theory (MCT) [Fuchs and Cates (2003); Hebraud and Lequeux (1998)] and Soft Glassy Rheology (SGR) [Sollich *et al.* (1997); Sollich (1998)] are theoretical frameworks that are available in literature to explain the flow curves of these complex fluids. MCT predicts the flow curves of soft materials by modeling the cage effect as a feedback mechanism storing memory of pair densities and the advection effect as disruption. MCT has many adjustable parameters that are not universal and have to be

---

* Much of this chapter has appeared in Seth J. R., L. Mohan, C. Locatelli-Champagne, M. Cloitre and R. T. Bonnecaze, "A micromechanical model to predict the flow of soft particle glasses," Nat Mater **10**, 838-843 (2011).

determined from the static structure factor. It also requires a time scale parameter to be fit with experimental data in order to make specific predictions. The SGR model predicts the yield stress nature associated with these complex fluids and the dynamics are characterized as hops from one cage to another with the interactions coupled through an average noise temperature. This model has two adjustable parameters, the frequency of attempted hops and the background noise temperature and the directed relationship of these parameters to experimental systems is not straightforward. Other theories that have been developed in the past to explain the rheology of soft glassy materials include structural network models [Yziquel *et al.* (1999)], single stress relaxation for low frequency regime [Derec *et al.* (2001)] and activated hopping process theories [Kobelev and Schweizer (2005); Miyazaki *et al.* (2006)]. Though the models predict the flow dynamics of soft particle glasses like yielding and aging, they contain many adjustable parameters which are not directly related to the microscopic constituent properties and need to be tuned to directly match experimental data.

Here, a micromechanical 3-D model is proposed and implemented through particle scale simulations that quantitatively predicts the non-linear rheology of soft particle glasses. The microstructural changes during flow are also determined and connected to their macroscopic rheology. The shear stress and the normal stress differences depend on both the dynamic pair distribution function and the solvent-mediated elastohydrodynamic interactions among the deformed particles. The predictions, which have no adjustable parameters, are successfully validated with experiments on concentrated emulsions and polyelectrolyte microgel pastes, highlighting the universality of the flow properties of soft glasses. The results connect the macroscopic stress and shear thinning viscosity to the microscopic constituent properties like particle concentration, modulus and solvent viscosity and thus provide a framework for designing new soft additives with a desired rheological response.

The rest of the chapter is organized as follows. The model including the elastic and elastohydrodynamic interactions between particles is described in section 2.2 and the simulation technique is described in section 2.3. Steady shear rheology obtained from the particle scale simulations based on the model is presented in section 2.4. The pair distribution function and relevant spherical harmonics that describe the microstructure are calculated from particle position data and are analyzed in detail and connected to the macroscopic rheology in section 2.5. The validation of simulation results by comparison to experimental data for rheology of microgels and emulsions from Dr. Michel Cloitre's lab at ESPCI ParisTech is presented in section 2.6.

2.2 MODEL DESCRIPTION

Soft particle glasses share common features with hard-sphere glasses such as non-ergodicity and caged dynamics. However, while hard sphere colloids experience only forces due to excluded volume, soft particles at high volume fraction are compressed against each other by bulk osmotic forces and form flat facets at contact, with the average deformation depending on particle elasticity and volume fraction. The solvent forming the continuous phase is localized in thin films separating the particles.

Soft particle glasses are modeled as three dimensional packings of *N* periodically replicated non-Brownian elastic spheres (see figure 2.1*a*) dispersed in a solvent with viscosity η_s at volume fractions exceeding the random close-packing of hard spheres [Lacasse *et al.* (1996); Seth *et al.* (2006)]. The particles form flat facets at contact resulting in the relative deformation $\varepsilon_{\alpha\beta} = (R_\alpha + R_\beta - r_{\alpha\beta}) / R$ where $r_{\alpha\beta}$ is the center-to-center distance between particles α and β and $R_c = R_\alpha R_\beta / (R_\alpha + R_\beta)$ is the contact radius as shown in figure 2.1*b*. The suspension is subject to an imposed shear flow in the (*x*-*y*) plane with shear rate $\dot{\gamma}$. The resulting velocity is in the *x*-direction with *y* axis being the gradient direction. As two compressed particles move past one another, a flow of solvent develops inside the liquid films separating the facets. This generates a net positive pressure causing an additional elastic deformation of the particles, which self-consistently maintains the lubricating films and makes particle motion possible. This mechanism shares strong similarities with the elastohydrodynamic slippage of soft particles compressed against solid surfaces [Meeker *et al.* (2004a)]. The interaction between α and β is composed of a central repulsive force $\mathbf{f}_{\alpha\beta}^{e}$ associated with the elastic contact between the two particles, coupled to an elastohydrodynamic (EHD) drag force $\mathbf{f}_{\alpha\beta}^{EHD}$, due to the motion of α relative to β.

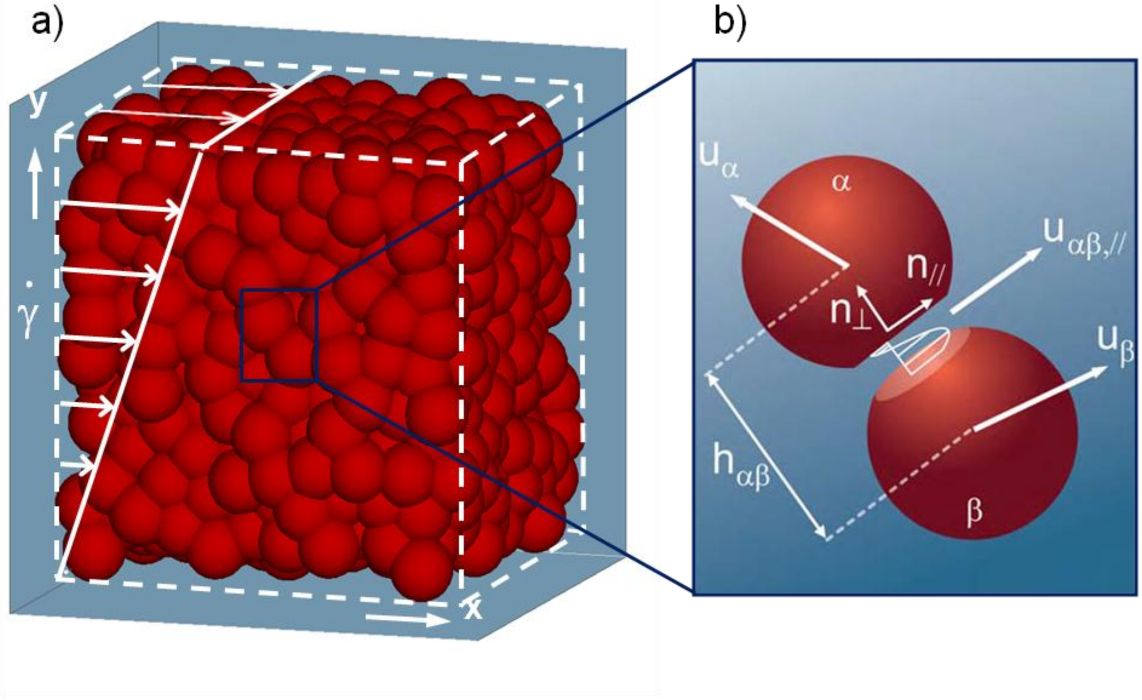

Figure 2.1: Structure and interactions of a model soft glass. (a) Typical configuration of jammed elastic spheres at $\phi = 0.8$; $\dot{\gamma}$ is the applied shear rate. (b) Schematic showing pair-wise interactions between particles α and β with radii R_α and R_β centered at $\mathbf{x}_\alpha$ and $\mathbf{x}_\beta$ and translating with velocities $\mathbf{u}_\alpha$ and $\mathbf{u}_\beta$, $r_{\alpha\beta}$ is the center-to-center distance. $h_{\alpha\beta} = R_\alpha + R_\beta - r_{\alpha\beta}$ is the overlap distance; the thickness of the lubricating film separating the facets is much smaller that the overlap distance. $u_{\alpha\beta,\|}$ is the component of the relative velocity parallel to the facets. The elastic force $\mathbf{f}_{\alpha\beta}^{e}$ and the elastohydrodynamic drag force $\mathbf{f}_{\alpha\beta}^{EHD}$ are parallel to the unit vectors normal ($\mathbf{n}_\perp$) and parallel ($\mathbf{n}_\|$) to the facets, respectively.

The elastic force $\mathbf{f}_{\alpha\beta}^{e}$ between soft particles such as elastomeric particles [Liu *et al.* (1998)], microgels [Seth *et al.* (2006); Zhang *et al.* (2009)], and emulsion droplets [Seth *et al.* (2006)] can be modelled using Hertzian-like potentials. The classical Hertz theory applies at rest and near-equilibrium [Liu *et al.* (1998)], where $\varepsilon_{\alpha\beta}$ is less than 0.1. When the glass flows at high shear-rates, $\varepsilon_{\alpha\beta}$ can be much larger and Hertz theory underestimates the contact force. A modified approximate expression† [Liu *et al.* (1998)] is used, which is valid up to $\varepsilon_{\alpha\beta} \approx 0.6$:

$$\mathbf{f}_{\alpha\beta}^{e} = {}^{4}\!/_{3}\, C E^{*} \varepsilon_{\alpha\beta}^{n} R_{c}^{2} \mathbf{n}_{\perp}, \tag{2.1}$$

where $E^{*} = E/2(1-\nu^{2})$ is the contact modulus (E : Young modulus; $\nu = 0.5$: Poisson's ratio for incompressible spheres) and $\mathbf{n}_{\perp}$ is the direction perpendicular to the particle-particle facet at contact. The values of n and C vary with the degree of compression: n = 1.5 and C = 1 for $\varepsilon_{\alpha\beta} < 0.1$; n = 3 and C = 32 for $0.1 \leq \varepsilon_{\alpha\beta} < 0.2$; n = 5 and C = 790 for $0.2 \leq \varepsilon_{\alpha\beta} < 0.6$. It is interesting to note that the elastic energy associated with the elastic contact forces is generally much larger than kT (see Supplemental Material 2.E), indicating that the origin of the dynamics resides in the elastic properties of the particles themselves [Ikeda *et al.* (2012)].

The elastohydrodynamic drag force $\mathbf{f}_{\alpha\beta}^{EHD}$ is coupled to the repulsive elastic force $\mathbf{f}_{\alpha\beta}^{e}$ because the hydrodynamic pressure in the lubricating film supports the Hertzian pressure due to $\mathbf{f}_{\alpha\beta}^{e}$. The following expression based on the solution for a single particle dragged along a smooth surface is used [Meeker *et al.* (2004a); Seth (2008)]:

---

† The coefficient presented in Seth *et al*. 2008 has been corrected and the version used in the simulations has been presented here.

$$\mathbf{f}_{\alpha\beta}^{EHD} = -\left(\eta_s C u_{\alpha\beta,||} E^* R_c^3\right)^{1/2} \varepsilon_{\alpha\beta}^{(2n+1)/4} \mathbf{n}_{||}, \tag{2.2}$$

where $u_{\alpha\beta,||}$ and $\mathbf{n}_{||}$ are the relative velocity and the direction parallel to the flat facet developed at particle-particle contact, respectively.

Each particle experiences a net elastic repulsion and an EHD drag due to all the particles in contact with it and these forces are assumed to be pairwise additive. $\mathbf{F}_\alpha^e$ and $\mathbf{F}_\alpha^{\mathrm{EHD}}$ is the sum of the contributions from all facets. The particles also experience an effective drag force due to relative motion with the solvent. Neglecting particle and fluid inertia, the sum of all forces on each particle is zero and the motion is then described by the equation: $\mathbf{u}_\alpha = d\mathbf{x}_\alpha / dt = \mathbf{u}_\alpha^\infty + M_\alpha [\mathbf{F}_\alpha^e + \mathbf{F}_\alpha^{EHD}]$ where $\mathbf{u}_\alpha^\infty$ is the velocity field due to the applied shear rate, and $M_\alpha = f_r(\phi)/6\pi\eta_s R_\alpha$ is the mobility coefficient which is that of a particle corrected by a factor $f_r(\phi)$ that accounts for its reduction at high volume fraction. The resulting equation of motion can be made dimensionless by scaling lengths, time and velocity by R, η_s/E^* and RE^*/η_s, respectively. It has the form:

$$\frac{\mathrm{d}\tilde{\mathbf{x}}_\alpha}{\mathrm{d}\tilde{t}} = \tilde{\mathbf{u}}_\alpha^\infty + \frac{f_r(\phi)}{6\pi\tilde{R}_\alpha}\left[\frac{4}{3}C\sum_\beta \varepsilon_{\alpha\beta}^n \tilde{R}_c^2 \mathbf{n}_\perp - \sum_\beta \left(C\tilde{u}_{\alpha\beta,||}\tilde{R}_c^3\right)^{1/2} \varepsilon_{\alpha\beta}^{(2n+1)/4} \mathbf{n}_{||}\right] \tag{2.3}$$

where the tilde quantities are dimensionless. The non-dimensionalized applied velocity field $\tilde{\mathbf{u}}_\alpha^\infty = \left(\dot{\gamma}\eta_s/E^*\right) y\mathbf{e}_x$ and the form of this equation shows that the dynamics is characterized solely by the dimensionless shear rate $\tilde{\dot{\gamma}} = \dot{\gamma}\eta_s / E^*$, which represents the ratio of viscous to elastic forces, and the overlap deformation $\varepsilon_{\alpha\beta}$, which depends on the volume fraction. The N coupled equations of motion were integrated numerically to determine the evolution of the spatial position and velocity of each particle.

2.3 SIMULATION TECHNIQUE

A periodically replicated random close packed configuration of hard spheres in a cubic simulation box is first generated using the compression algorithm introduced by [Lubachevsky and Stillinger (1990)]. After forming the random close-packed microstructure, the spheres are treated as deformable particles and compressed by decreasing the box size in small decrements until the desired concentration is achieved. After each decrement, the system is allowed to relax using a conjugate gradient algorithm to minimize the system energy and ensure the net contact forces and torques on each particle vanishes. The model is then implemented using a molecular dynamics-like simulation on the random packings of N elastic spheres created in the above manner. $N = 10^3$ in the simulations reported here but the results with a much larger number of spheres ($N = 10^4$) were not significantly different. The particles have a Gaussian size distribution with an average radius R and a standard deviation of 10% in order to avoid crystallization. Constant shear rate simulations were performed using the open source LAMMPS code [Plimpton (1995)] assuming Lees-Edwards boundary conditions [Rapaport (2004); Seth (2008)]. The position and the velocity of each particle were obtained by solving the N equations of motion above using the Verlet integration algorithm [Rapaport (2004)]. The mobility coefficient correction factor $f_r(\phi)$ was equal to 0.01 for these simulations but the results did not vary significantly for values of $f_r(\phi)$ less than 0.1.

The viscous, elastic and total stress tensors were computed from the Kirkwood formula [Larson (1999)]:

$$\boldsymbol{\sigma}^{V} = -\frac{1}{V}\sum_{\beta}^{N}\sum_{\alpha>\beta}^{N}\mathbf{f}_{\alpha\beta}^{EHD}(\mathbf{x}_{\alpha}-\mathbf{x}_{\beta}), \tag{2.4}$$

$$\boldsymbol{\sigma}^{e} = -\frac{1}{V} \sum_{\beta}^{N} \sum_{\alpha > \beta}^{N} \mathbf{f}_{\alpha\beta}^{e} (\mathbf{x}_{\alpha} - \mathbf{x}_{\beta}), \tag{2.5}$$

$$\boldsymbol{\sigma} = \boldsymbol{\sigma}^{V} + \boldsymbol{\sigma}^{e}, \tag{2.6}$$

where V is the box volume. The shear stress $\sigma = \boldsymbol{\sigma}_{yx}$, the first, and second normal stress differences, $N_1 = \boldsymbol{\sigma}_{xx} - \boldsymbol{\sigma}_{yy}$ and $N_2 = \boldsymbol{\sigma}_{yy} - \boldsymbol{\sigma}_{zz}$, respectively were computed from the appropriate components of the stress tensor. The simulations were performed at non-dimensional shear rates $\tilde{\dot{\gamma}} = \dot{\gamma}\eta_s / E^*$ between 10^{-9} and 10^{-4}. For every $\left(\tilde{\dot{\gamma}}, \phi\right)$ combination, σ, N_1 and N_2 were calculated at regular time intervals until steady state was reached. Steady-state values were then determined by averaging over several strain units. The results reported here were obtained by averaging over five different initial configurations of particles for each volume fraction and shear rate.

2.4 MACROSCOPIC PROPERTIES FROM SIMULATIONS

Figure 2.2 shows the simulated flow curves for volume fractions between ϕ = 0.7 and 0.9. The results are well described by the Herschel-Bulkley equation:

$$\sigma / E^* = \sigma_y / E^* + k_\sigma \tilde{\dot{\gamma}}^m, \tag{2.7}$$

with $m = 0.50 \pm 0.02$; $k_\sigma \propto G_0 / E^*$, where G_0 is the low-frequency storage modulus, which has been determined independently [Seth *et al.* (2006)]; $\sigma_y = G_0 \gamma_y$ is the yield stress, where the yield strain γ_y ranges from 0.02 to 0.04 (see figure 2.3). The shear thinning exponent $m = ½$ has been observed for soft particle suspensions very close to the jamming transition [Nordstrom *et al.* (2010); Tighe *et al.* (2010)], in compressed emulsions [Princen and Kiss (1989)], and in microgels [Cloitre *et al.* (2003b)]. Figure 2.4

shows the variations of the non-dimensional normal stress differences. They are roughly equal but opposite in magnitude $\left(N_2 \cong -N_1\right)$ indicative of a so-called film fluid [Larson (1997)]. At low shear rates, they tend to a constant value while at high shear rates they grow proportionately to $\tilde{\dot{\gamma}}^{1/2}$. In the inset of figure 2.2, we present the elastic component of the stress, $\boldsymbol{\sigma}^{e}$, which arises from the distortion of particles during rearrangements and the viscous component, $\boldsymbol{\sigma}^{v}$, due to the elastohydrodynamic drag force. The latter increases like $\boldsymbol{\sigma}^{v} \propto \tilde{\dot{\gamma}}^{2/3}$, which differs from the variation $\boldsymbol{\sigma}^{v} \propto \tilde{\dot{\gamma}}^{1/2}$ predicted for a 2-D array of emulsion droplets [Denkov *et al.* (2008); Meeker *et al.* (2004a)]. Most importantly the magnitude of $\boldsymbol{\sigma}^{e}$ is at least two orders of magnitude larger than $\boldsymbol{\sigma}^{v}$. The inset of figure 2.4b shows similar results for normal stresses. The important result here is that the rheology of soft glasses is dominated by the elastic component of the stress associated with the alteration of the structure under flow.

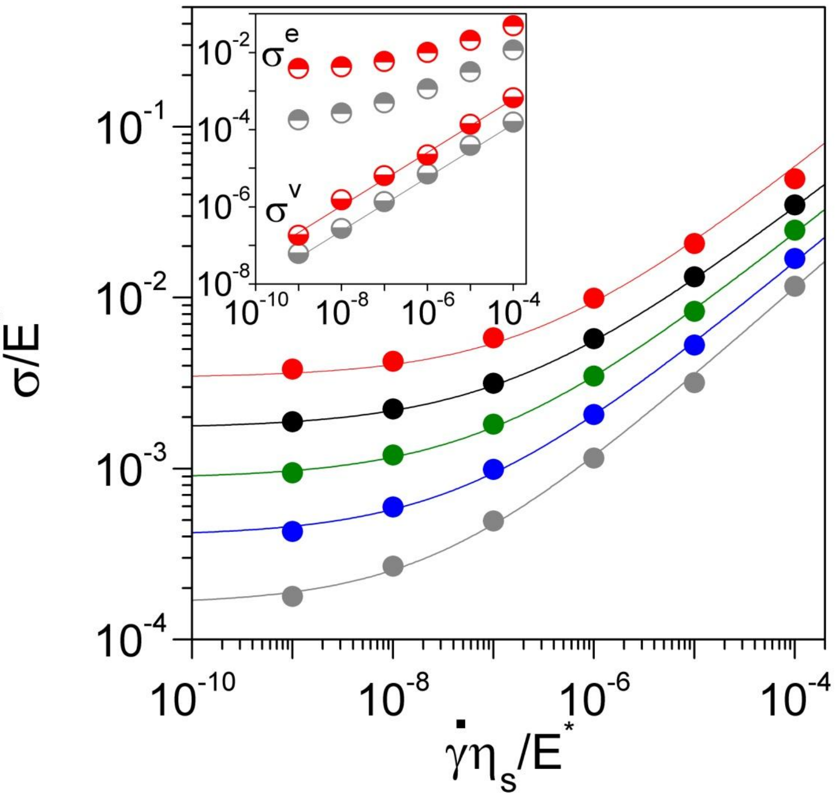

Figure 2.2: Computed shear stress of model soft glasses. Each color refers to a particular volume fraction: $\phi = 0.70$ (grey circle), $\phi = 0.75$ (blue circle), $\phi = 0.80$ (green circle), $\phi = 0.85$ (black circle), $\phi = 0.90$ (red circle). The continuous lines represent the best fits to a Herschel-Bulkley equation; the inset shows the variations of the elastic and viscous components of the stress for $\phi = 0.70$ and $\phi = 0.90$; the full line has a slope 2/3.

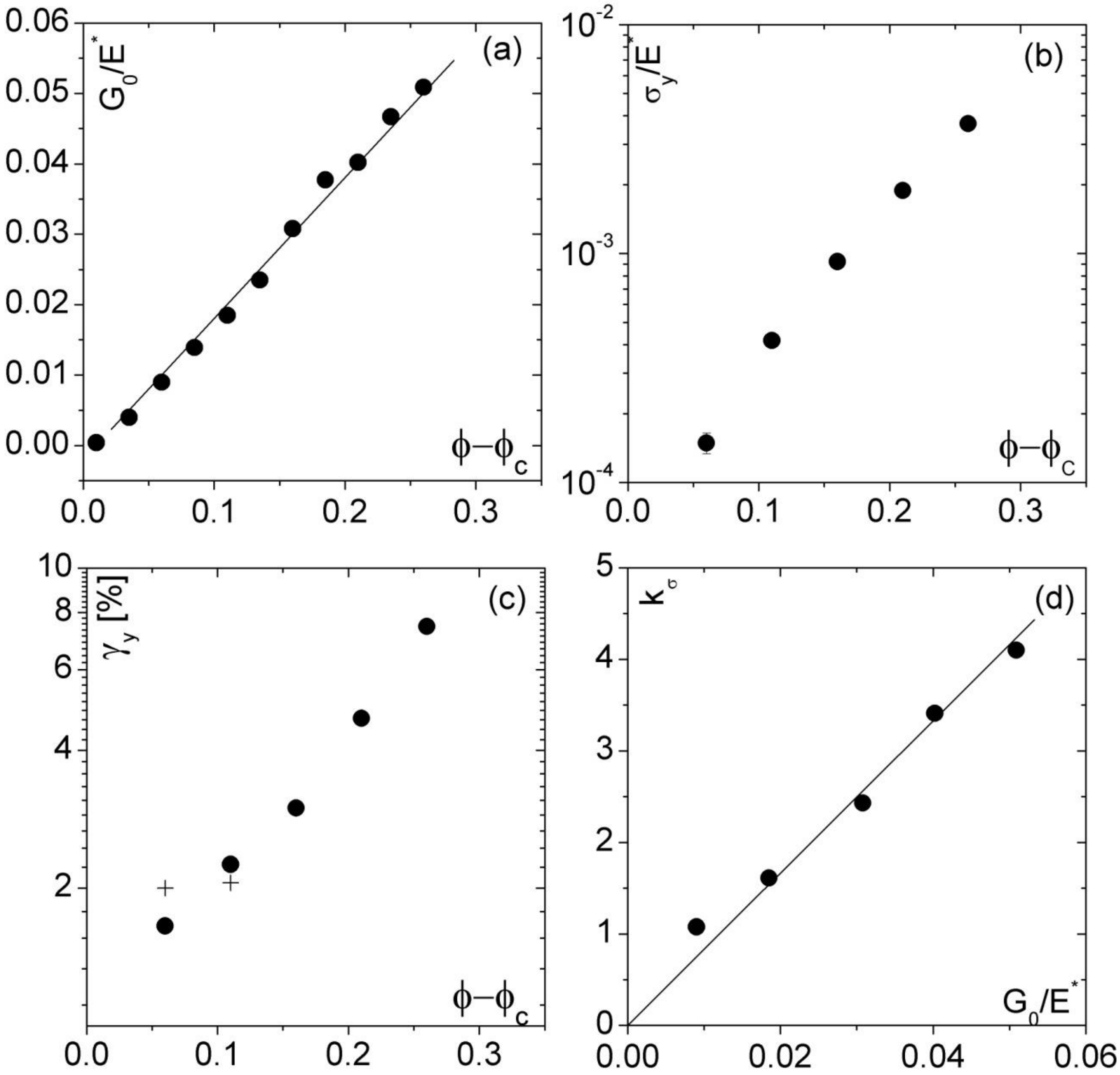

Figure 2.3: Simulated shear modulus, yield stress, yield strain, and Herschel Bulkley parameter. Graphs (a), (b) and (c) show the variations of the low-frequency shear modulus $\left(G_0/E^*\right)$, yield stress $\left(\sigma_y/E^*\right)$, yield strain γ_y versus the reduced volume fraction $\phi-\phi_c$ (ϕ_c = 0.64 is the close-packing volume fraction) respectively. Black dots are the results from simulations; crosses in (c) refer to analytical predictions from the model presented in section 2.5.4. Graph (d) shows the parameter k_σ in the Herschel-Bulkley equation and it varies linearly with the low-frequency shear modulus.

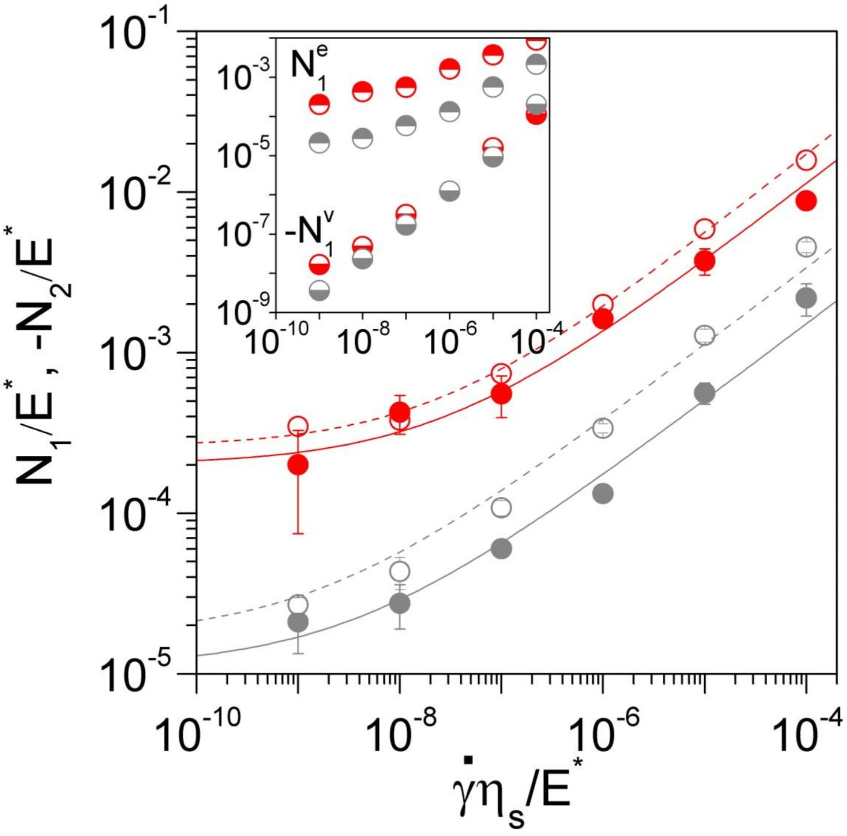

Figure 2.4: Computed first and second normal stress differences of model soft glasses. The first normal stress differences data are denoted by full symbols, the second normal stress difference by open symbols. Only data for $\phi = 0.70$ (grey) and $\phi = 0.90$ (red) are plotted for the sake of clarity; the inset shows the variations of the elastic and viscous components of the first normal stress difference.

2.5 MICROSTRUCTURAL ANALYSIS

2.5.1 Pair correlation function: g(r)

The elastic stress $\boldsymbol{\sigma}^e$ can be calculated from the dynamic pair correlation function $g(\mathbf{r})$ using the pairwise elastic force $f^e(r)$ from

$$\boldsymbol{\sigma}^e = -\frac{\rho^2}{2}\int f^e(r)\mathbf{r}g(\mathbf{r})d\mathbf{r}, \tag{2.8}$$

where ρ is the particle number density. The integration domain includes only radial distances smaller than the particle radius since the elastic force vanishes otherwise. The dynamic pair correlation function characterizes the distortion of the microstructure during shearing and is defined as:

$$g(\mathbf{r}) = \frac{1}{\rho \Delta V_{\mathbf{r}}}\sum_{i=1}^{N}\sum_{j=1,\, j\neq i}^{N}\delta(\mathbf{r}-\mathbf{r}_{ij}), \tag{2.9}$$

where $\Delta V_{\mathbf{r}}$ is the bin volume.

A brief review of the microstructure of the suspension at rest is first discussed [Seth *et al.* (2006)]. Figure 2.5a shows the radial pair distribution function computed at rest at a volume fraction $\phi = 0.8$. The constituent particles are soft, and therefore at concentrations greater than the hard sphere random close packing limit ($\phi = 0.64$), they are pressed against one another and the radial separation at which the pair probability is maximum is less than twice the particle radius. This contrasts with the case of hard spheres where the radial pair distribution function shows a sharp rise at the hard sphere diameter. Figure 2.5b shows the two-dimensional pair distribution function at rest in the *x-y* plane. Since the range of compression between particles is small compared to the particle radius, it is beneficial to represent the microstructure in the r-θ or azimuthal plane, so that the focus can be on the range of separations where particle contacts occur and the angular distortion can be studied more closely. In figure 2.5c we clearly see that the microstructure at rest is radially symmetric without any preferential orientation or angular distortion. As a reference, the particle separation where the pair distribution function is maximum is indicated by a white line. In the following, we will use the azimuthal representation to present the two-dimensional pair distribution functions computed during steady state at different rates of steady shear.

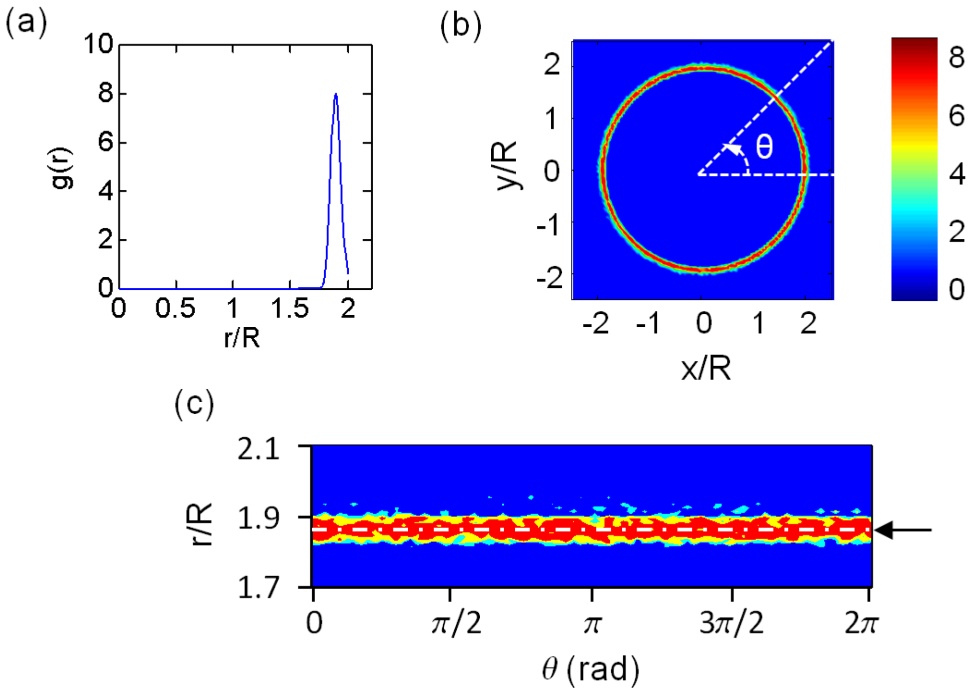

Figure 2.5: Microstructure of soft particle glass at rest; the volume fraction is $\phi = 0.80$. (a) Static radial distribution function. (b) Pair distribution function shown in the *x*-*y* plane. (c) Pair distribution function shown in the azimuthal $r-\theta$ plane with the most probable center-to-center distance indicated by a white dash dotted line and a black arrow.

Figure 2.6 shows azimuthal plots of $g(\mathbf{r})$ in the flow-gradient planes at different shear rates for volume fraction of 0.8. During shear, neighbouring particles tend to accumulate in the upstream compressive quadrant $(\pi/2 \le \theta \le \pi)$, where they are more compressed, and deplete along the extensional axis $(\theta = \pi/4)$, where they are less distorted. The particles also get more compressed with increasing shear rate. The white line represents the average radial separation when the soft particle glass is at rest. See Supplemental Material 2.A for representation in the *x*-*y* plane.

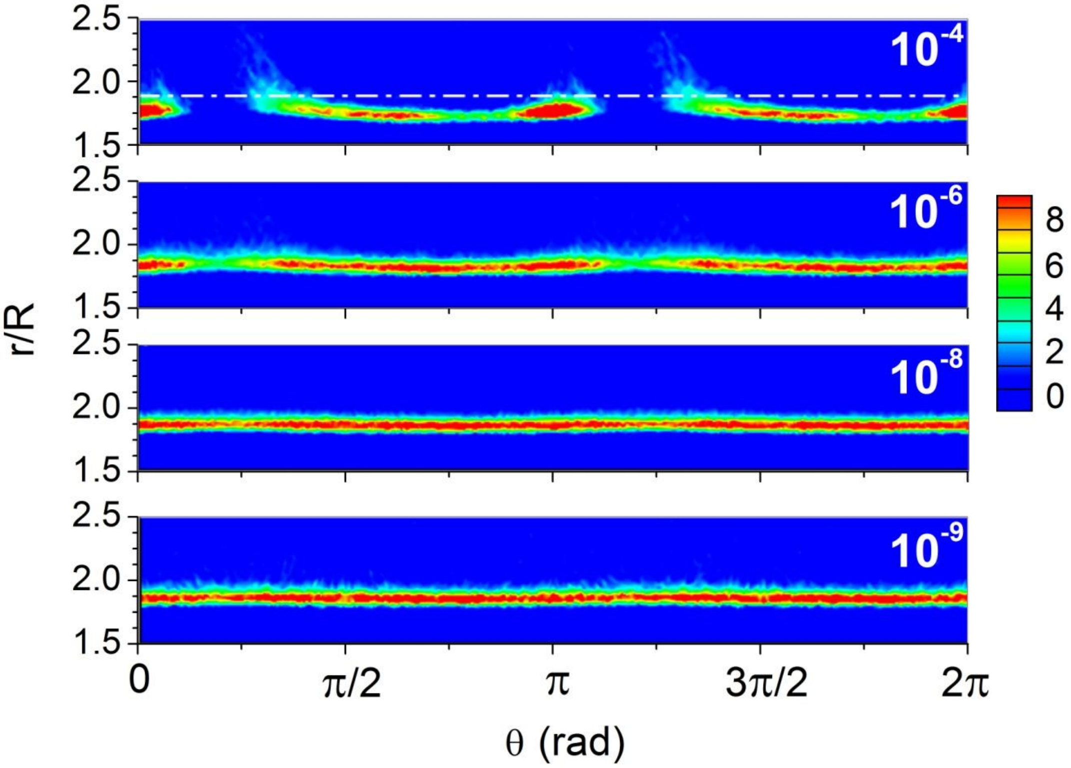

Figure 2.6: Microstructure of sheared soft particle glasses (ϕ = 0.80). Azimuthal plots of the pair distribution function in the flow-gradient plane at different shear rates, which is indicative of the probability of finding a particle centre at position (r,θ) from a test particle centered at (0,0). Red color indicates highest probability of finding particle centres. The dashed line indicates the average centre-to-centre distance between particles at rest.

2.5.2 Analysis of pair distribution using spherical harmonics

To quantify the distortion and asymmetry observed in the dynamic pair distribution function, $g(\mathbf{r})$ is decomposed into an orthogonal series of spherical harmonic functions $Y_{lm}(\theta,\phi)$ [Hanley *et al.* (1987); Morris and Katyal (2002)]:

$$g(\mathbf{r}) = g(r) + \sum_{l=1}^{\infty}\sum_{m=-l}^{l} g_{lm}(r) Y_{lm}(\theta,\phi), \tag{2.10}$$

where r is the pair distance scaled by a mean pair radius, θ is the polar angle in the *x*-*y* plane measured counter clockwise from the positive *x*-axis and ϕ is the azimuthal angle measured from the positive *z*-axis (see Supplemental Material 2.B). The functions $Y_{lm}(\theta,\phi)$ are a set of orthogonal basis functions obtained from solutions of the angular portion of the Laplace equation in spherical coordinates. Every function Y_{lm} (where $l \geq 0$ and $-l \leq m \leq l$), incorporates l and m symmetries in the latitude and longitude direction, respectively. The expressions for $Y_{lm}(\theta,\phi)$ are:

$$\begin{aligned} Y_{0,0} &= \frac{1}{2\sqrt{\pi}} \\ Y_{2,0} &= \frac{1}{4}\sqrt{\frac{5}{\pi}}\left(3\cos^2\phi - 1\right) \\ Y_{2,2} &= \frac{1}{4}\sqrt{\frac{15}{\pi}}\left(\cos 2\theta \sin^2\phi\right) \\ Y_{2,-2} &= \frac{1}{4}\sqrt{\frac{15}{\pi}}\left(\sin 2\theta \sin^2\phi\right) \end{aligned}. \tag{2.11}$$

$g_{lm}(r)$ are weighting functions which can be computed as:

$$g_{lm}(r) = \frac{\int g(\mathbf{r}) Y_{lm}(\theta,\phi) \sin\phi \, d\theta \, d\phi}{\int Y_{lm}(\theta,\phi) Y_{lm}(\theta,\phi) \sin\phi \, d\theta \, d\phi}. \tag{2.12}$$

Since $g(\mathbf{r})$ must be independent of the choice of probe particle *i.e.*, $g(\mathbf{r}) = g(-\mathbf{r})$, and of the shear direction, odd values of l and m can be omitted.

The coefficient $g_{2,-2}(r)$ of the expansion, which measures the asymmetry of the pair distribution between the compression and extension axes, is shown in figure 2.7. The negative minimum at the radial distance r_{m} is due to the accumulation of particles in the compressive region. The larger is the shear rate, the smaller r_{m}, indicating that particles are pushed closer. The depth of the minimum indicates more particles are on average in the compressive region; conversely the height of the maximum indicates fewer particles are on average in the extensional region.

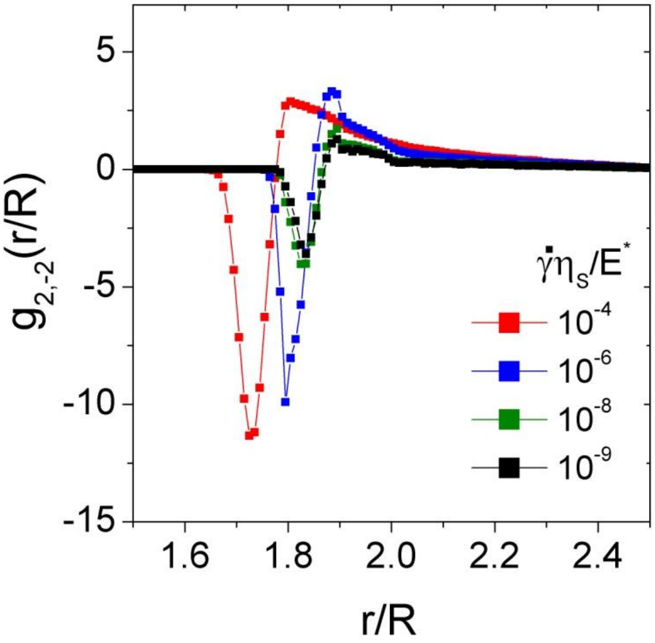

Figure 2.7: Spherical harmonic coefficients $g_{2,-2}(r)$ at different shear rates ($\phi = 0.80$)

2.5.3 Calculation of stress tensor using spherical harmonics

Spherical harmonic dissociation of $g(\mathbf{r})$ into dominant modes is useful because the coefficients are related to the shear and normal stresses. Using the spherical harmonic expansion for $g(\mathbf{r})$ in equation (2.10) in equation (2.8) and by integrating over the angular portions, following expressions for the shear and normal stresses are obtained:

$$\sigma^{e}{}_{yx} = -\rho^2 \sqrt{\frac{\pi}{15}} \int_{r=0}^{2R} r^3 f(r) g_{2,-2}(r) dr \tag{2.13}$$

$$N_1 = \sigma_{xx} - \sigma_{yy} = -2\rho^2 \sqrt{\frac{\pi}{15}} \int_{r=0}^{2R} r^3 f(r) g_{2,2}(r) dr \tag{2.14}$$

$$N_2 = \sigma_{yy} - \sigma_{zz} = \rho^2 \sqrt{\frac{\pi}{5}} \int_{r=0}^{2R} r^3 f(r) \left(g_{2,0}(r) + \frac{g_{2,2}(r)}{\sqrt{3}} \right) dr \tag{2.15}$$

$f(r)$ here is the pairwise elastic repulsive force. The 4th order spherical harmonics also contribute to these stresses but their contributions were insignificant compared to those from the second order spherical harmonic modes. The fourth order harmonics and their connection to the stresses are presented in Supplemental Material 2.B.

2.5.4 Derivation of constitutive equation for shear stress from microstructure

The elastic component of the shear stress σ^e can be computed from $g_{2,-2}(r)$ [Hanley *et al.* (1987)] through equation (2.13). The integral in the expression of σ^e is dominated by the force at the point of maximum accumulation where the particles are highly compressed. Thus, the stress can be accurately estimated by $\sigma \cong f_m \Sigma_m$ where f_m is the magnitude of the elastic force at $r = r_\mathrm{m}$ and Σ_m is the integral of $g_{2,-2}(r)$ over the domain where $g_{2,-2}(r) < 0$: $\Sigma_\mathrm{m} = -\rho^2 \sqrt{\frac{\pi}{15}} \int_{g_{2,-2}(r)<0} r^3 g_{2,-2}(r) dr$. Σ_m represents the surface density of contacts over a particle that significantly contributes to the stress. When the shear rate varies, Σ_{m} is approximately constant (see Supplemental Material 2.C), indicating that the contacts are redistributed but their surface density remains the same. The elastic force f_m represents the force barrier that particles overcome to roll on top of one another. It is derived analytically using simple scaling arguments in Supplemental Material 2.C: $\tilde{f}_m = \tilde{f}_y + k_f \tilde{\dot{\gamma}}^{1/2}$, where $\tilde{f}_{m(y)} = f_{m(y)} / E^* R^2$. The term in the right-hand side, $\tilde{f}_y \propto G_0 / E^*$, represents the elastic force associated with a caged particle at the yield strain. The second term is an additional contribution due to the elastohydrodynamic deformation of the particles under flow; k_f is a dimensionless coefficient that is proportional to the reduced low shear modulus G_0/E^*. To verify this prediction, $\tilde{f}_m$ was computed numerically from r_{m} and the interparticle force law. Figure 2.8 shows the results for the five volume fractions investigated. The curves are well represented by a Herschel-Bulkley expression with a shear thinning exponent $m = 0.50 \pm 0.02$.

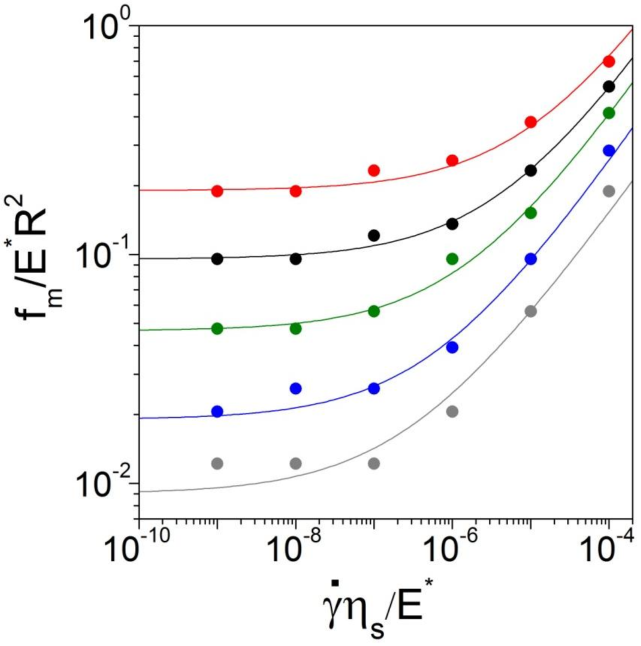

Figure 2.8: Dimensionless force at the radius of maximum accumulation versus applied

shear rate for volume fractions studied in figure 2.3. Each color refers to a particular volume fraction: $\phi = 0.70$ (grey circle), $\phi = 0.75$ (blue circle), $\phi = 0.80$ (green circle), $\phi = 0.85$ (black circle), $\phi = 0.90$ (red circle).

The following constitutive equation is then predicted using $\tilde{f}_m = \tilde{f}_y + k_f \tilde{\gamma}^m$ and $\sigma^e \cong f_m \Sigma_m$:

$$\sigma / \sigma_y = 1 + k \left(\dot{\gamma} \eta_S / \gamma_y^2 E^* \right)^{1/2}, \tag{2.16}$$

where *k* a numerical coefficient and γ_y is the yield strain given by:

$$\gamma_y = \Sigma_{\mathrm{m}} \tilde{f}_y R^2 (G_0 / E^*)^{-1}. \tag{2.17}$$

This result is successfully tested in figure 2.9, which shows that the flow curves calculated for different volume fractions collapse onto a universal flow curve which is close to the prediction. The calculated yield strains also agree with the values determined directly from the simulated flow curves (see figure 2.3). A similar analysis based on coefficients $g_{2,2}(r)$ and $g_{2,0}(r)$ of the expansion (see Supplemental Material 2.D) yields similar relationships for the normal stress differences N_1 and N_2 (see figures 2.10a and 2.10b).

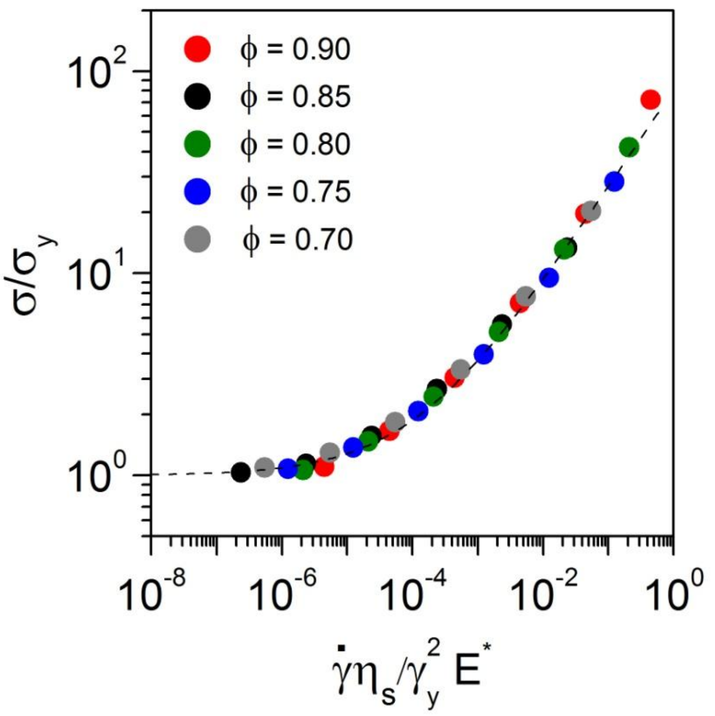

Figure 2.9: Universal constitutive law (line) for shear stress from simulated data (symbols). The dashed line is the best fit to the constitutive equation derived in the text and Supplemental Material 2.C (*k* = 80±3).

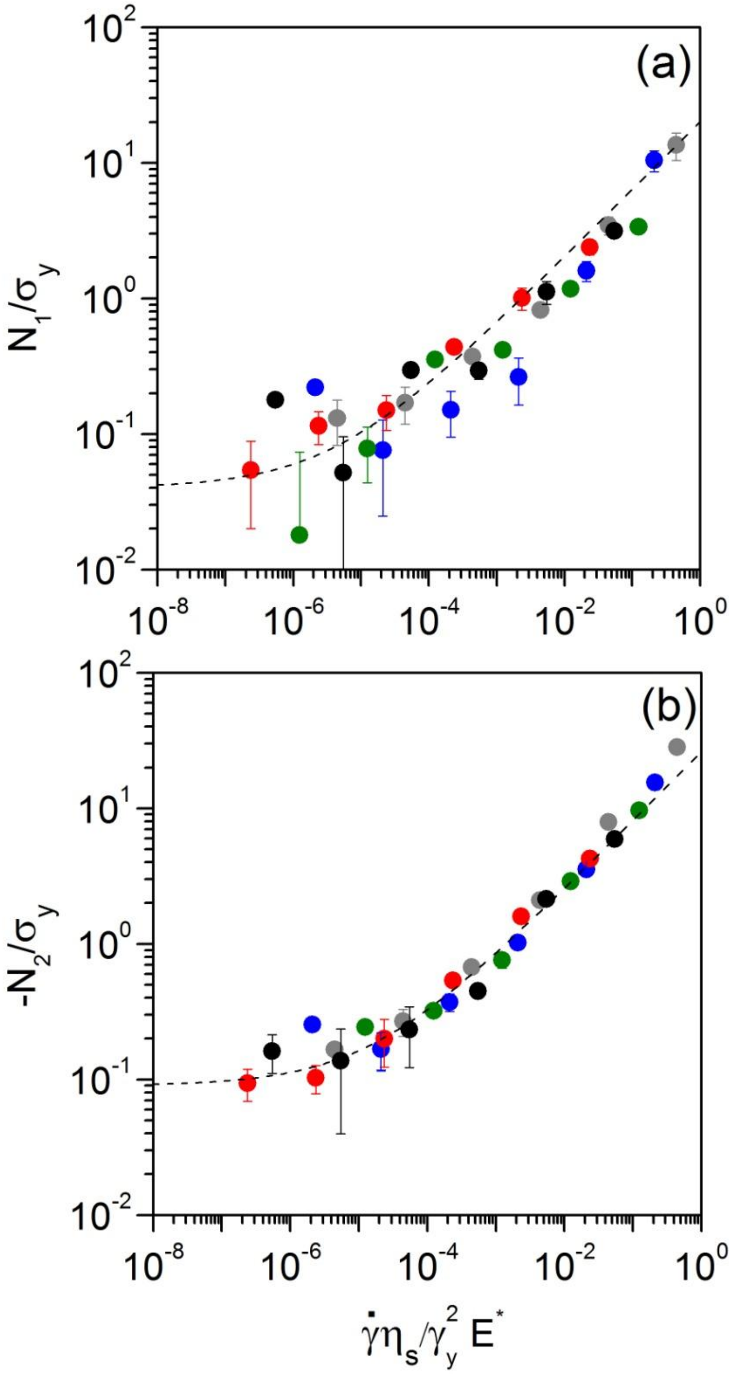

Figure 2.10: Universal constitutive laws (lines) for first (a) and second (b) normal stress differences from simulated data (symbols). The dashed lines are the best fit to the constitutive equation derived in the Supplemental Material 2.D (*k'* = 20±2; *k''* = 26±2).

2.6 COMPARISON TO EXPERIMENTS

The model predictions are tested by comparing them with the rheological properties of concentrated emulsions and suspensions of polyelectrolyte microgels with different volume fractions and solvent viscosities from Dr. Cloitre's lab. The experimental procedure for preparing these suspensions and the rheological measurement is described in Supplemental Material 2.E. Measurements of the shear stress and first normal stress differences produce sets of data resembling those obtained from simulations (see Supplemental Material 2.E). The data for emulsions are rescaled in figures 2.11a and 2.11b using the values of E^* and γ_y determined experimentally. Both the shear stress and the normal stress differences collapse onto universal curves that are in good agreement with the theoretical predictions. For microgels, the contact modulus is unknown and cannot be measured easily. To circumvent this difficulty, E^* is determined in figure 2.11c by adjusting the experimental shear stress variations to the predicted flow curve. Figure 2.11d, shows that the resulting value also collapses the experimental first normal stress differences onto a universal curve that agrees with the prediction from the simulations. As an interesting application, the deduced effective shear modulus of individual microgels, $G_P \approx 20$ kPa, is in qualitative agreement with independent estimates (Supplemental Material 2.E), and with values measured in macroscopic polyelectrolyte gels with similar composition [Meeker *et al.* (2004a); Schosseler *et al.* (1991)].

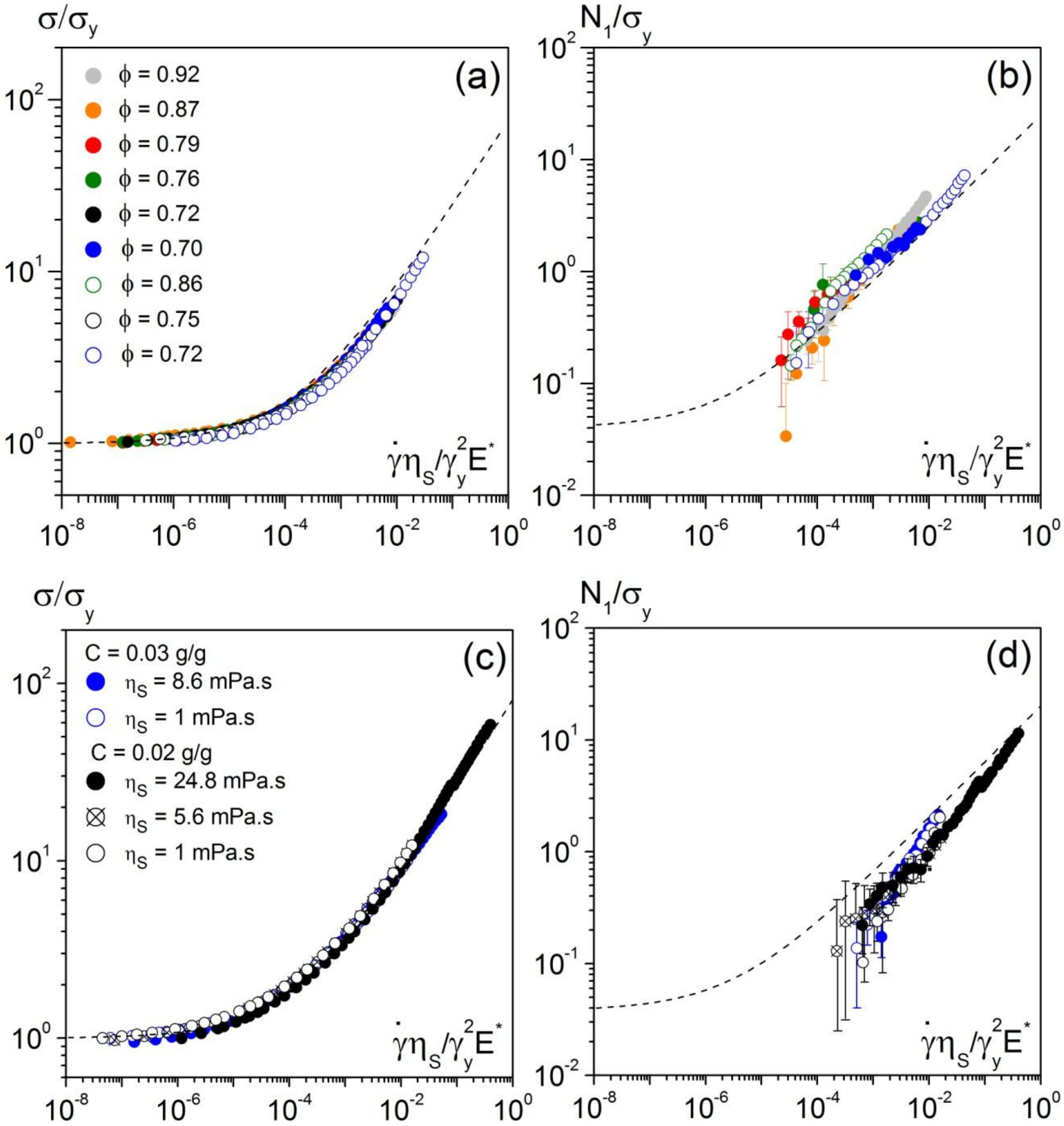

Figure 2.11: Universal scaling of shear stress and first normal stress difference from experimental data. (a) and (b) show data for concentrated emulsions rescaled using σ_y, γ_y and E^* determined independently; solid symbols: oil in water-glycerol emulsions with η_s=7.9 mPa.s; open symbols: oil in water emulsions with η_s = 1 mPa.s. (c) and (d): data for microgel suspensions (E^* = 40 kPa). The dotted lines are the best fits to Herschel-Bulkley variations of the shear stress data and first normal stress differences obtained from the simulations. The raw data are presented in the Supplemental Material figures 2.E.1 and 2.E.2.

2.7 SUMMARY AND CONCLUSIONS

Experiments indicate that soft particle glasses exhibit yield stress and shear thinning behavior. Here a micromechanical model is developed based on elastic repulsion between particles and an elastohydrodynamic (EHD) drag force due to the solvent flow in the thin solvent layer at particle-particle facet. The model is implemented for steady shear flow using a particle based periodic box simulator. The microstructural changes during flow are studied by analyzing the pair distribution function $g(\mathbf{r})$. A detailed microstructural analysis using spherical harmonics is used to derive the constitutive equation for the shear stress and normal stress differences in these soft particle glasses. The particle scale simulation results and the predictions of the model from the microstructural analysis, which have no adjustable parameters, are successfully validated with experiments on concentrated emulsions and polyelectrolyte microgel pastes. The derived constitutive equation connects the microscopic constituent parameters of the soft particle glass like solvent viscosity, particle concentration and particle elasticity to the macroscopic rheological properties of the material like yield stress, shear thinning and normal stress differences.

The constitutive equations established here demonstrate the universality of the flow behaviour of soft glasses as a result of a subtle interplay between elastic interactions and structural rearrangements. This distinguishes our approach from other models of glassy dynamics which do not include contact forces and hydrodynamic contributions [Fuchs and Cates (2002); Sollich *et al.* (1997)]. The importance of EHD lubrication between deformed particles is reflected by the key role played by the characteristic time η_s/E^*, which can be tuned by changing the viscosity of the continuous phase and/or the local elasticity through the particle architecture and composition. The alteration of the pair distribution function under flow together with the elastic contact forces accounts for the generic shear rate dependence of the shear and normal stress differences. At high shear rates, concentrated hard sphere suspensions also exhibit an accumulation and depletion of particle density along the compression and extension axes but the stress is linearly proportional to the shear rate [Brady and Morris (1997); Crassous *et al.* (2008)]. These results indicate that the soft particle glasses considered here form a class of materials singularly distinct from non-Brownian ideal hard sphere suspensions.

The theory and the experimental data presented here are not very sensitive to the exact form of the interacting potential so that the generic properties reported here will be found in many other systems [Erwin *et al.* (2010)]. These results open new strategies to estimate particle properties from macroscopic rheology and conversely provide rational tools for manufacturing and processing soft materials in industrial applications.

SUPPLEMENTAL MATERIAL 2.A: SHEARED MICROSTRUCTURE IN X-Y PLANE

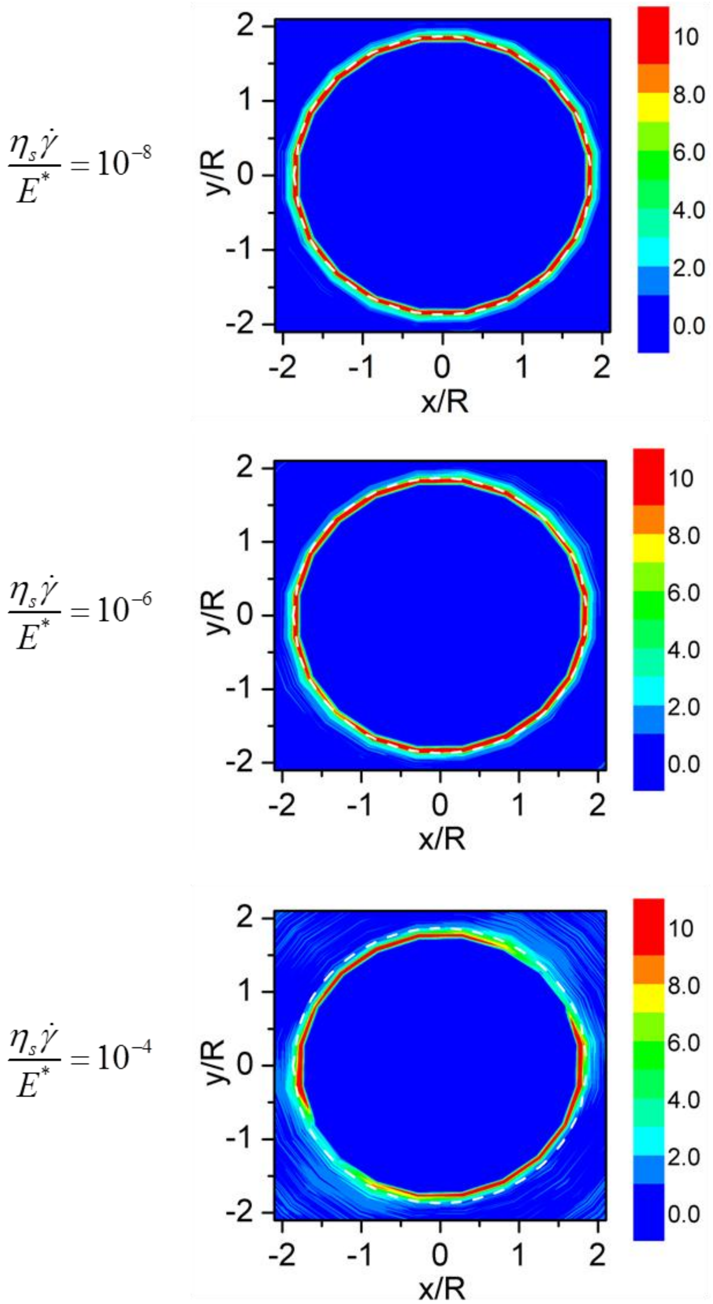

Figure 2.A.1: Pair distribution function $g(\mathbf{r})$ in the *x*-*y* plane during bulk shear flow at $\phi = 0.8$ for comparison. White lines correspond to the most probable radial separation at rest

SUPPLEMENTAL MATERIAL 2.B: SPHERICAL HARMONICS

The polar and azimuthal angles with respect to the flow and gradient directions are presented below in figure 2.B.1.

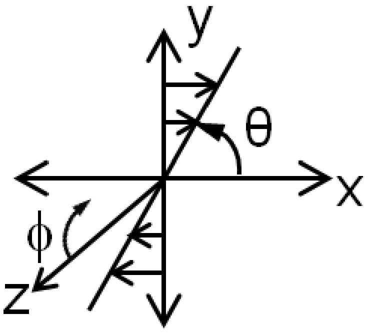

Figure 2.B.1: Co-ordinate system indicating flow direction and the polar and azimuthal angles.

The dynamic pair distribution function, $g(\mathbf{r})$ can be decomposed into an orthogonal series of spherical harmonic functions $Y_{lm}(\theta,\phi)$ [Hanley *et al.* (1987); Morris and Katyal (2002)]:

$$g(\mathbf{r}) = g(r) + \sum_{l=1}^{\infty} \sum_{m=-l}^{l} g_{lm}(r) Y_{lm}(\theta,\phi) \tag{2.B.1}$$

The functions $Y_{lm}(\theta,\phi)$ are a set of orthogonal basis functions obtained from solutions of the angular portion of the Laplace equation in spherical coordinates. Every function Y_{lm} (where $l \geq 0$ and $-l \leq m \leq l$), incorporates l and m symmetries in the latitude and longitude direction, respectively.

The expressions for $Y_{lm}(\theta,\phi)$ are:

$$
\begin{aligned}
Y_{0,0} &= \frac{1}{2\sqrt{\pi}} \\
Y_{2,0} &= \frac{1}{4}\sqrt{\frac{5}{\pi}}\left(3\cos^2\phi - 1\right) \\
Y_{2,2} &= \frac{1}{4}\sqrt{\frac{15}{\pi}}\left(\cos 2\theta \sin^2\phi\right) \\
Y_{2,-2} &= \frac{1}{4}\sqrt{\frac{15}{\pi}}\left(\sin 2\theta \sin^2\phi\right) Y_{4,0} = \frac{3}{16\sqrt{\pi}}\left(35\cos^4\phi - 30\cos^2\phi + 3\right) \\
Y_{4,2} &= \frac{3}{8}\sqrt{\frac{5}{\pi}}\cos 2\theta\left(7\cos^2\phi - 1\right) \\
Y_{4,-2} &= \frac{3}{8}\sqrt{\frac{5}{\pi}}\sin 2\theta\left(7\cos^2\phi - 1\right) \\
Y_{4,4} &= \frac{3}{16}\sqrt{\frac{35}{\pi}}\left(\cos 4\theta \sin^4\phi\right) \\
Y_{4,-4} &= \frac{3}{16}\sqrt{\frac{35}{\pi}}\left(\sin 4\theta \sin^4\phi\right)
\end{aligned}
\tag{2.B.2}
$$

The corresponding spherical harmonic coefficients $g_{lm}(r)$ can be computed using:

$$
g_{lm}(r) = \frac{\int g(\mathbf{r}) Y_{lm}(\theta,\phi)\sin\phi\, d\theta\, d\phi}{\int Y_{lm}(\theta,\phi) Y_{lm}(\theta,\phi)\sin\phi\, d\theta\, d\phi} \tag{2.B.3}
$$

Since $g(\mathbf{r})$ must be independent of the choice of probe particle *i.e.*, $g(\mathbf{r}) = g(-\mathbf{r})$, and of the shear direction, odd values of l and m can be omitted.

The spherical harmonic coefficients can be used to compute the shear and normal stress differences in conjunction with the pairwise elastic repulsion force *f*(*r*) as follows:

$$\sigma^{e}{}_{yx} = -\rho^{2}\left[\sqrt{\frac{\pi}{15}}\int_{r=0}^{2R} r^{3} f(r) g_{2,-2}(r)dr + \sqrt{\frac{\pi}{80}}\int_{r=0}^{2R} r^{3} f(r) g_{4,-2}(r)dr\right] \tag{2.B.4}$$

$$N_{1} = -\rho^{2}\left[\sqrt{\frac{4\pi}{15}}\int_{r=0}^{2R} r^{3} f(r) g_{2,2}(r)dr + \sqrt{\frac{\pi}{20}}\int_{r=0}^{2R} r^{3} f(r) g_{4,2}(r)dr\right] \tag{2.B.5}$$

$$N_{2} = \rho^{2}\left[\sqrt{\frac{\pi}{5}}\int_{r=0}^{2R} r^{3} f(r)\left(g_{2,0}(r) + \frac{g_{2,2}(r)}{\sqrt{3}}\right)dr + \sqrt{\frac{\pi}{80}}\int_{r=0}^{2R} r^{3} f(r) g_{4,2}(r)dr\right] \tag{2.B.6}$$

The 4th order spherical harmonics also contribute to these stresses but in practice their contributions when convoluted with the elastic force *f*(*r*) were insignificant compared to those from the second order spherical harmonic modes.

SUPPLEMENTAL MATERIAL 2.C: DERIVATION OF ELASTIC FORCE AT THE POINT OF MAXIMUM ACCUMULATION

Starting from scaling arguments, it is shown here that the dimensionless elastic force at the radius of maximum accumulation $\tilde{r}_m (= r_m / R)$ follows the expression $\tilde{f}_m = \tilde{f}_y + k_f \tilde{\dot{\gamma}}^{1/2}$ where $k_f \propto G_0 / E^*$. Consider a Taylor series expansion for the dimensionless elastic force about the point of closest contact at the yield strain between a particle and the test particle, $\tilde{r}_y$:

$$\tilde{f}_\mathrm{m} = \tilde{f}_y + \left(\frac{\partial \tilde{f}}{\partial \tilde{r}} \right)_{\tilde{r}_y} \left(\tilde{r}_\mathrm{m} - \tilde{r}_y \right) + \ldots \qquad (2.C.1)$$

The force $\tilde{f}_\mathrm{m}$ is balanced by that exerted by the particle sliding over the test particle due to the osmotic pressure or effectively low frequency shear modulus ($\propto$ G_0/E^*) [Meeker *et al.* (2004a)] and the perpendicular component of the elastohydrodynamic force acting along the line of the centres of the particles, $\tilde{f}_\perp^\mathrm{EHD}$, so that

$$\tilde{f}_y + \left(\frac{\partial \tilde{f}}{\partial \tilde{r}} \right)_{\tilde{r}_y} \left(\tilde{r}_\mathrm{m} - \tilde{r}_y \right) \approx \frac{G_0}{E^*} + \tilde{f}_\perp^\mathrm{EHD} \qquad (2.C.2)$$

The normal component of the elastohydrodynamic force is coupled to the drag force through $\tilde{f}_\perp^\mathrm{EHD} \approx \tilde{f}_\parallel^\mathrm{EHD} (h / R_c)^\alpha$ [Meeker *et al.* (2004a)], h being the overlap distance between the particles. The power of α for h/R_c accounts for the perpendicular component of the elastohydrodynamic force acting along the line of the centres of the particles. For low shear, a particle sliding over the test sphere takes a practically circular path with no perpendicular component of the elastohydrodynamic force. For higher shear rates, the sliding particle takes a straighter path diagonally across the test sphere generating the additional elastohydrodynamic compression force on the test particle. Thus,

$$\tilde{f}_y + \left(\frac{\partial \tilde{f}}{\partial \tilde{r}}\right)_{\tilde{r}_y} \left(\tilde{r}_{\mathrm{m}} - \tilde{r}_y\right) \approx \frac{G_0}{E^*} + (h/R_c)^{1+\alpha}\,\tilde{\dot{\gamma}}^{1/2} \tag{2.C.3}$$

The first terms on the left and the right of equation (2.C.3) balance since $\sigma_y \sim G_0$ implies that the force at yield, $\tilde{f}_y$, is proportional to G_0/E^*. Then,

$$\left(\frac{\partial \tilde{f}}{\partial \tilde{r}}\right)_{\tilde{r}_y} \left(\tilde{r}_{\mathrm{m}} - \tilde{r}_y\right) \approx (h/R_c)^{1+\alpha}\,\tilde{\dot{\gamma}}^{1/2}\,. \tag{2.C.4}$$

Recognizing that $h/R_c \sim \left(G_0/E^*\right)^{2/3}$ [Meeker *et al.* (2004a); Seth *et al.* (2006)], it can be shown that:

$$\left(\frac{\partial \tilde{f}}{\partial \tilde{r}}\right)_{\tilde{r}_y} \left(\tilde{r}_{\mathrm{m}} - \tilde{r}_y\right) \approx \left(\frac{G_0}{E^*}\right)\left(\frac{G_0}{E^*}\right)^{(2\alpha-1)/3} \tilde{\dot{\gamma}}^{1/2} \tag{2.C.5}$$

The exponent α is unknown but is expected to be about unity. Then $\left(G_0/E^*\right)^{(2\alpha-1)/3}$ is a weak function of volume fraction [Meeker *et al.* (2004a); Seth *et al.* (2006)]. Thus, it is demonstrated that $\left(\frac{\partial \tilde{f}}{\partial \tilde{r}}\right)_{\tilde{r}_y} \left(\tilde{r}_{\mathrm{m}} - \tilde{r}_y\right) \approx k_f\,\tilde{\dot{\gamma}}^{1/2}$ with $k_f \propto \left(G_0/E^*\right)$ and this explains the form of equation (2.C.1). Finally, recognizing that $\left(\frac{\partial \tilde{f}}{\partial \tilde{r}}\right)_{\tilde{r}_y} \approx -\left(\frac{G_0}{E^*}\right)$ [Seth *et al.* (2006)], $\left(\tilde{r}_y - \tilde{r}_{\mathrm{m}}\right) \approx \tilde{\dot{\gamma}}^{1/2}$ is also predicted. The results from the simulations plotted in figure 2.C.1 are in agreement with this form.

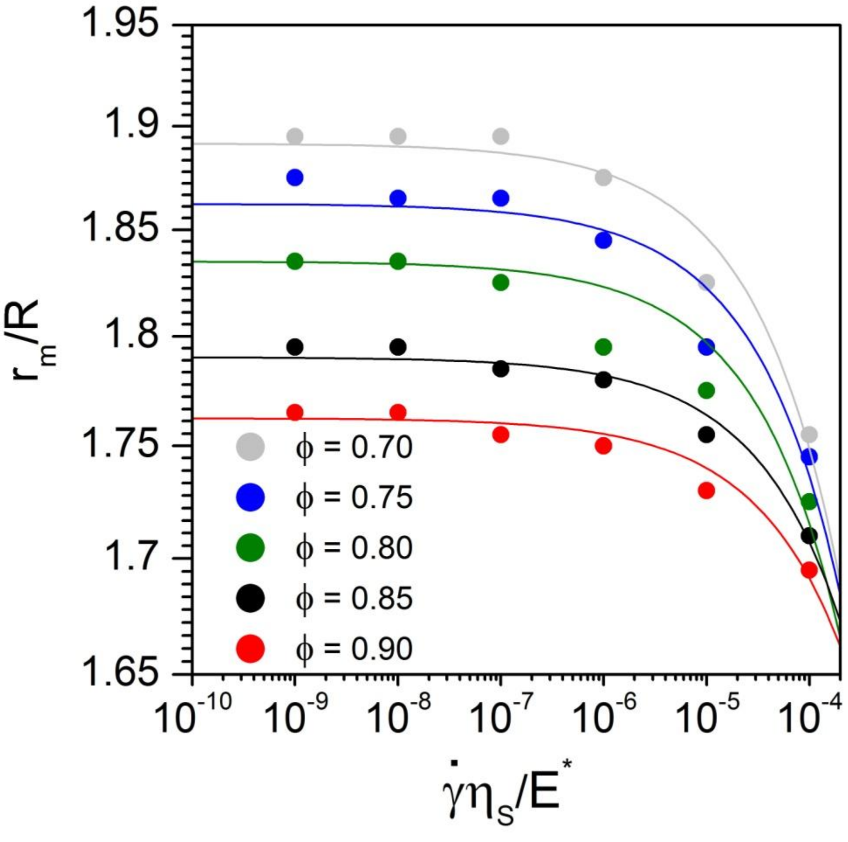

Figure 2.C.1: Variation of radius of maximum accumulation with shear rate. $\tilde{r}_m$ is obtained from the dynamic pair distribution functions for different volume fractions. The solid lines are fits to the equation $\tilde{r}_m = \tilde{r}_y - k_r \tilde{\dot{\gamma}}^m$ where $m = 0.5 \pm 0.02$ and coefficient k_r is constant within the experimental accuracy.

SUPPLEMENTAL MATERIAL 2.D: DERIVATION OF CONSTITUTIVE EQUATIONS FOR NORMAL STRESS DIFFERENCES

Figures 2.D.1a and 2.D.1b below show the variations of the coefficients $g_{2,2}(r)$ and $g_{2,0}(r)$ of the expansion of the pair distribution function into spherical harmonics. These coefficients contribute to the first and second normal stress differences. They have the same characteristic shape as the coefficient $g_{2,-2}(r)$ contributing to the stress expression; the negative minimum at a center-to-center distance r_m is due to the accumulation of particles in the compressive region. The integrals in the expressions of σ_{yx}, N_1 and N_2 are dominated by the contributions from the domain where $g_{2,-2}(r)<0$ (i.e. $0 \le r \le r^*$), where the particles are the most compressed and the elastic forces the largest. Thus, N_1 and N_2 can be expressed as: $N_1 \cong f_m \Sigma'_m$ and $N_2 \cong f_m \Sigma''_m$ where f_m is the magnitude of the compressive elastic force at $r=r_m$, and,

$$\begin{aligned} \Sigma'_m &= -2\rho^2\sqrt{\frac{\pi}{15}}\int_{r=0}^{r_m} r^3 g_{2,2}(r)\,dr \\ \Sigma''_m &= \rho^2\sqrt{\frac{\pi}{5}}\int_{r=0}^{r_m} r^3\left(g_{2,0}(r)+\frac{g_{2,2}(r)}{\sqrt{3}}\right)dr \end{aligned} \qquad (2.D.1)$$

The latter quantities vary very slowly with the shear rate so that they will be considered as constant (see figure 2.D.1c). Using the Herschel-Bulkley form standing for the maximum compression force f_m, we end up with the constitutive equations:

$$\begin{aligned} N_1/\sigma_y &= N_{1,y} + k'\left(\dot{\gamma}\eta_S/\gamma_y^2 E^*\right)^m \\ -N_2/\sigma_y &= N_{2,y} + k''\left(\dot{\gamma}\eta_S/\gamma_y^2 E^*\right)^m \end{aligned} \qquad (2.D.2)$$

where $N_{1,y}$ ($\simeq 0.04$), $N_{2,y}$ ($\simeq$ 0.09), k' ($\simeq$ 20) and k'' ($\simeq$ 26) are numerical coefficients and $m = 1/2$.

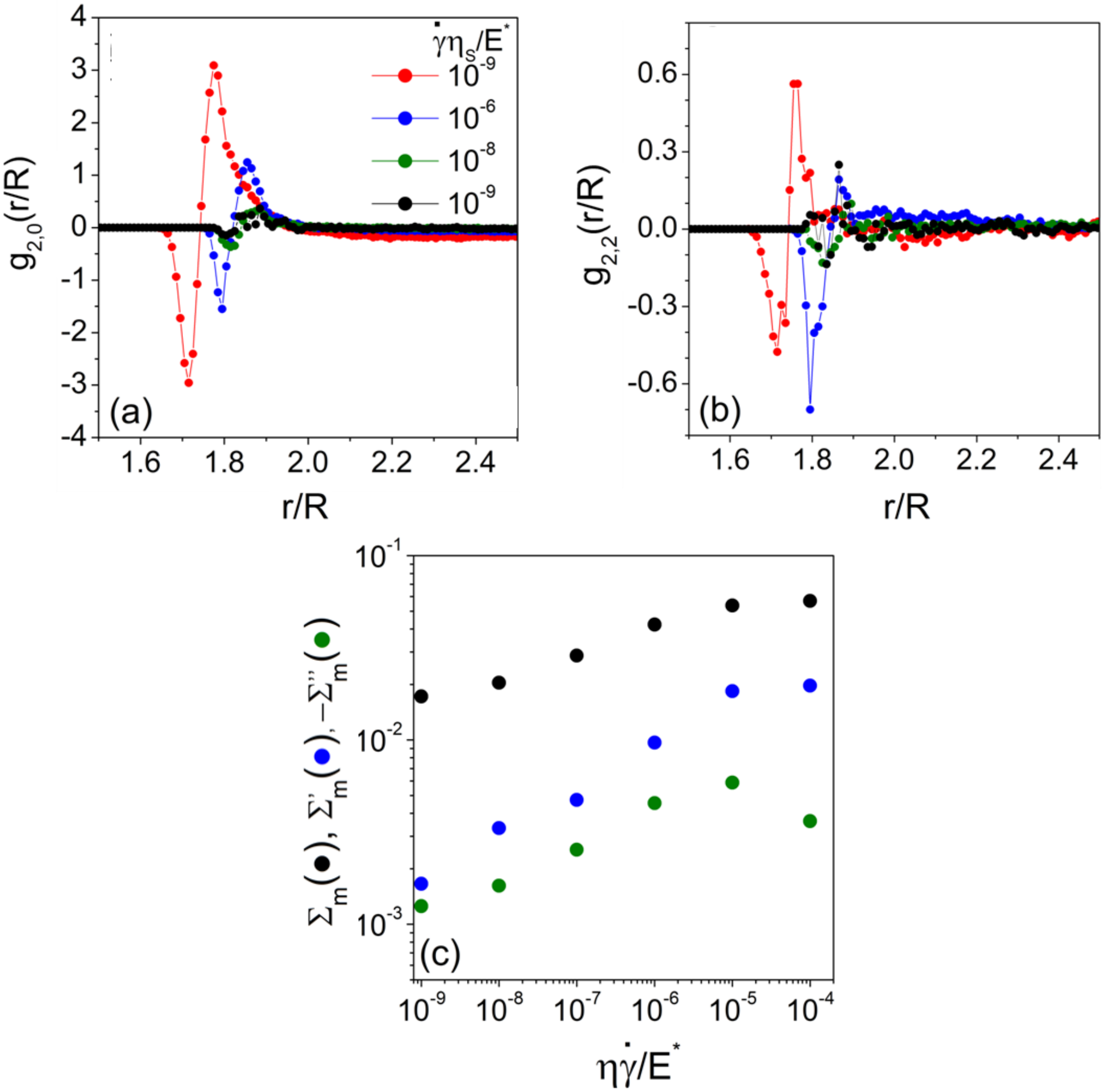

Figure 2.D.1: Variation of the coefficients $g_{2,2}(r)$ (a) and $g_{2,0}(r)$ (b) of the pair distribution function into spherical harmonics and surface densities of contacts (c) that contribute to σ, N_1 and N_2 : $\sum_m, \sum'_m$ and $\sum''_m$ respectively. The volume fraction here is $\phi = 0.8$.

SUPPLEMENTAL MATERIAL 2.E: EXPERIMENTAL DETAILS

This section describes the experimental protocol for preparing the microgels and emulsions used in the comparison section. Their raw unscaled flow curves have also been presented.

2.E.1 Preparation of emulsions

The emulsions are dispersions of silicon oil (viscosity: 0.5 mPa.s) in aqueous solvents stabilized by the non-ionic surfactant Triton X. They were prepared according to the well established protocol previously described [Meeker *et al.* (2004a)]. To ensure purely repulsive interactions, the emulsions were washed up after preparation to eliminate the excess surfactant and avoid depletion interactions between droplets. The droplet size distribution and the structure of the emulsions were determined from confocal microscopy observations. The mean particle radius is $R \approx 1.25 \mu m$ with a polydispersity of about 20%. The structure of the emulsions remains disordered at all volume fractions. The contact elastic modulus E^* was determined from the radius R and the interfacial tension γ_i using the relation [Seth *et al.* (2006)]: $E^* = 9.92\gamma_i/R$. The latter was measured using the pendant drop method. The solvents are water (η_s = 1 mPa.s, $\gamma_i \approx 5$ mJ/m^2, $E^* \approx 40$ kPa) and a water-glycerol mixture (η_s = 7.9 mPa.s, $\gamma_i \approx 4$ mJ/m^2, $E^* \approx 32$ kPa). The volume fraction was set by centrifugation and was measured both by gravimetry and by image processing. With these values of R and E^* and ε = 0.1, the ratio $E^* \varepsilon^{5/2} R^3/kT$ is much larger than 1 ($\approx 10^5$). The flow curves of these emulsions are shown in figure 2.E.1.

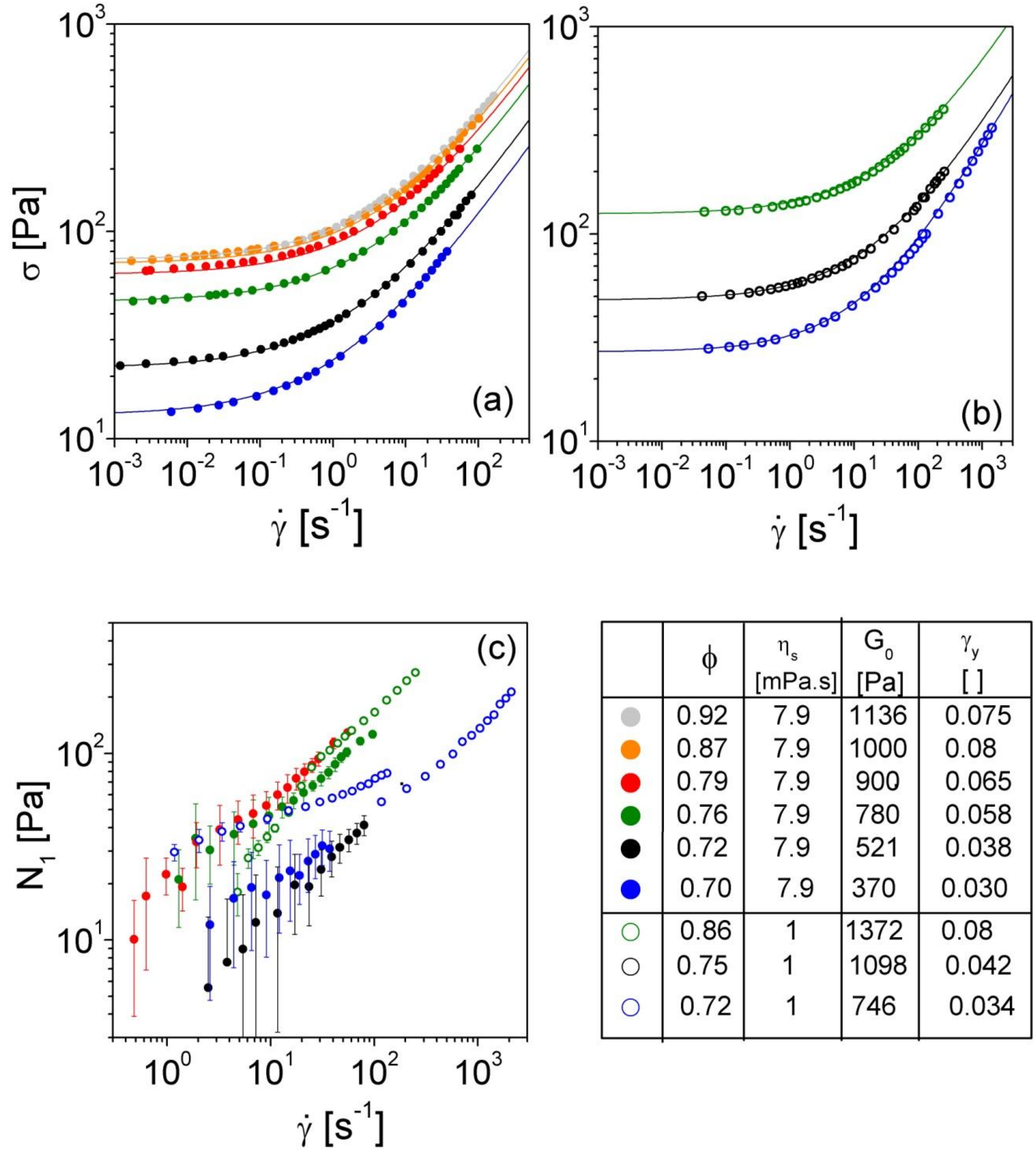

	ϕ	η_s [mPa.s]	G_0 [Pa]	γ_y [ ]
●	0.92	7.9	1136	0.075
●	0.87	7.9	1000	0.08
●	0.79	7.9	900	0.065
●	0.76	7.9	780	0.058
●	0.72	7.9	521	0.038
●	0.70	7.9	370	0.030
○	0.86	1	1372	0.08
○	0.75	1	1098	0.042
○	0.72	1	746	0.034

Figure 2.E.1: Nonlinear rheology data for concentrated emulsions. (a) and (b) show the flow curves of concentrated oil-water/glycerol and oil-water emulsions respectively at different volume fractions. (c) variations of the first normal stress differences. The table gives the volume fraction, the solvent viscosity, the storage modulus and the yield strain of the different emulsions.

2.E.2 Preparation of microgels

Polyelectrolyte microgels consisting of a cross-linked copolymer network of ethyl acrylate and methacrylic acid were used. The microgels were collapsed at low pH and swell when they are ionized by NaOH. At low concentrations, the collapsed and swollen microgels are spherical particles with a hydrodynamic radius $R = 50$ nm and $R = 230$ nm, respectively. They form glasses above close-packing. The particles tend to shrink when the concentration is increased so that the actual volume fraction cannot be determined accurately [Borrega *et al.* (1999)]. The polymer concentration C is used as the control parameter. At swelling equilibrium, the shear modulus of the particle, G_P, and the osmotic pressure of the counterions inside the particles are expected to be equal [Rubinstein *et al.* (1996)], which provides an order of magnitude [Borrega *et al.* (1999)] of $G_P \approx 50$ kPa. With the values of E^* and R for microgels and $\varepsilon = 0.1$, the ratio $E^* \varepsilon^{5/2} R^3 / kT$ is also much larger than 1 ($\approx 10^3$). The flow curves of these microgels are shown in figure 2.E.2.

2.E.3 Rheological measurements

Measurements were made using an Anton-Paar MCR 501 rheometer mounted with a cone and Peltier plate geometry and a solvent trap (diameter: 50mm; angle: 2°; truncation: $48\,\mu\text{m}$; temperature: 20 °C). The shearing surfaces are coated with waterproof sandpaper providing a surface roughness of $20\,\mu\text{m}$ which prevents the occurrence of slip [Meeker *et al.* (2004a)].

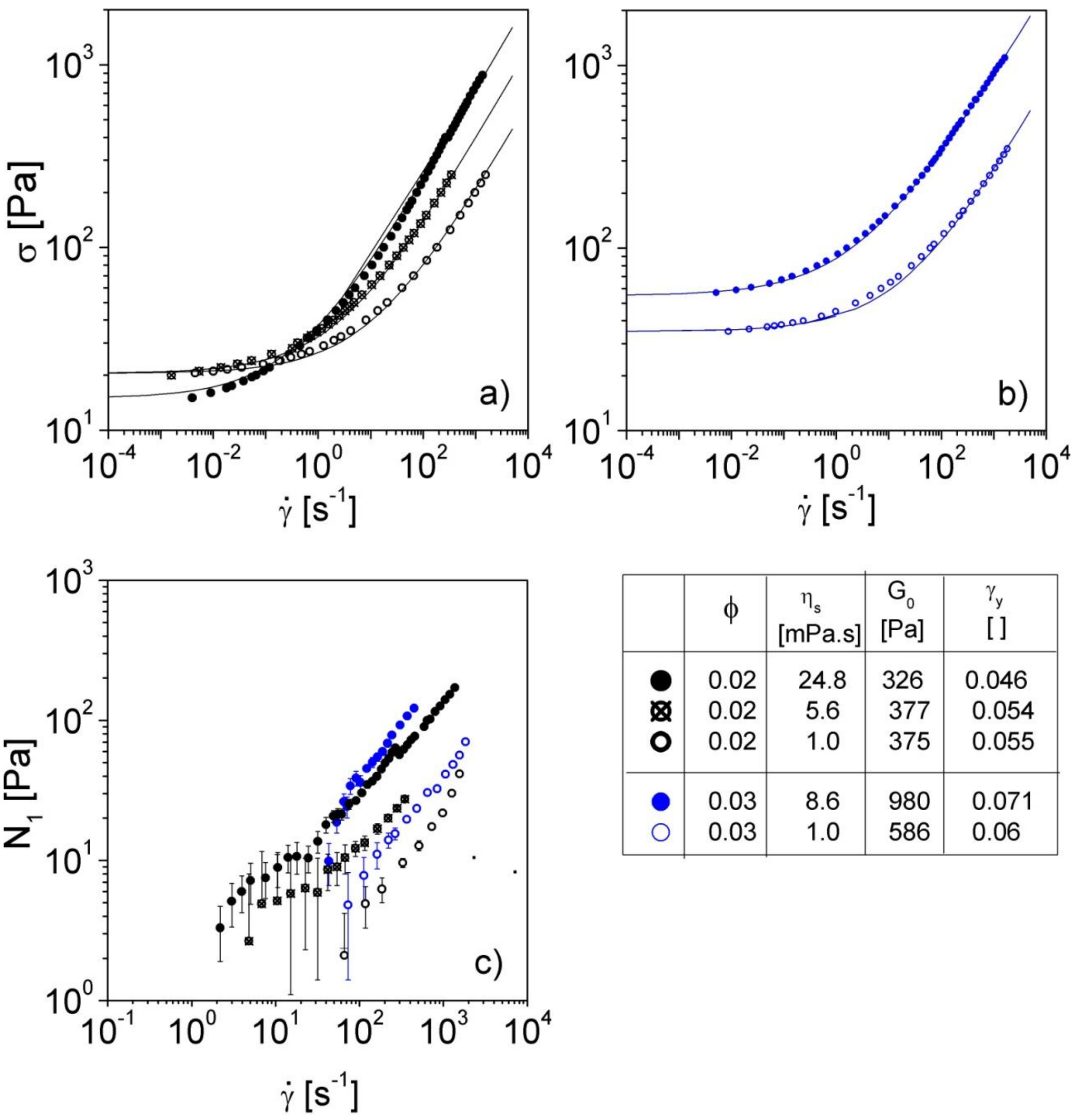

	ϕ	η_s [mPa.s]	G_0 [Pa]	γ_y [ ]
●	0.02	24.8	326	0.046
⊠	0.02	5.6	377	0.054
○	0.02	1.0	375	0.055
●	0.03	8.6	980	0.071
○	0.03	1.0	586	0.06

Figure 2.E.2: Nonlinear rheology data for concentrated microgel suspensions. (a) and (b) show the flow curves of concentrated microgel suspensions at *C*=0.03g/g and *C*=0.03 g/g respectively at different solvent viscosities. (c) shows the variations of the first normal stress difference with shear rate; the symbols are the same as in (a) and (b). The table gives the polymer concentration, the solvent viscosity, the storage modulus and the yield strain of the different suspensions.

SUPPLEMENTAL MATERIAL 2.F: SIMULATION DATA TABLES

Table 2.F.1: Shear and Normal Stress differences

ϕ	$\eta_s\dot{\gamma}/E^*$	$\langle \sigma/E^* \rangle$		$\langle N_1/E^* \rangle$		$\langle N_2/E^* \rangle$	
		Average	**Std. Dev.**	**Average**	**Std. Dev.**	**Average**	**Std. Dev.**
0.7	10^{-4}	0.011644	0.000287	0.002186	0.000495	-0.00455	0.000341
	10^{-5}	0.003181	0.000161	0.000561	8.45E-05	-0.00128	0.000119
	10^{-6}	0.00115	3.79E-05	0.000133	8.01E-06	-0.00034	2.20E-05
	10^{-7}	0.000493	2.12E-05	6.02E-05	2.40E-06	-0.00011	1.19E-05
	10^{-8}	0.000268	9.44E-06	2.75E-05	8.44E-06	-4.34E-05	9.80E-06
	10^{-9}	0.000179	7.45E-06	2.11E-05	7.69E-06	-2.69E-05	2.95E-06
0.75	10^{-4}	0.016919	0.000363	0.004212	0.000739	-0.00625	0.000692
	10^{-5}	0.00529	9.37E-05	0.000645	0.000106	-0.00143	2.41E-05
	10^{-6}	0.002066	4.36E-05	0.000106	4.04E-05	-0.00041	3.10E-05
	10^{-7}	0.00099	2.74E-05	6.10E-05	2.27E-05	-0.00015	1.01E-05
	10^{-8}	0.000595	1.44E-05	3.06E-05	2.06E-05	-6.78E-05	2.17E-05
	10^{-9}	0.000429	1.53E-05	8.93E-05	9.82E-06	-0.0001	7.48E-06
0.8	10^{-4}	0.024851	0.000676	0.00296	0.000306	-0.00843	0.00033
	10^{-5}	0.008313	0.000206	0.001029	5.88E-05	-0.00253	0.000124
	10^{-6}	0.003468	8.37E-05	0.000365	3.37E-05	-0.00066	8.33E-05
	10^{-7}	0.001819	5.57E-05	0.00031	2.18E-05	-0.00028	1.94E-05
	10^{-8}	0.0012	3.07E-05	6.84E-05	3.01E-05	-0.00021	2.03E-05
	10^{-9}	0.000943	2.53E-05	1.57E-05	4.87E-05	-1.19E-05	1.47E-05
0.85	10^{-4}	0.034951	0.000538	0.005407	0.000343	-0.01023	0.000609
	10^{-5}	0.013234	0.000321	0.001925	0.000366	-0.00369	0.000353
	10^{-6}	0.005752	0.000191	0.000506	6.73E-05	-0.00077	5.61E-05
	10^{-7}	0.003155	9.61E-05	0.000509	3.58E-05	-0.0004	0.00019
	10^{-8}	0.00223	9.32E-05	8.95E-05	7.57E-05	-0.00024	0.000169
	10^{-9}	0.001883	5.89E-05	0.000307	2.02E-05	-0.00028	8.85E-05
0.9	10^{-4}	0.049512	0.00109	0.008832	0.001084	-0.01579	0.001743
	10^{-5}	0.020712	0.000515	0.003721	0.000693	-0.00589	0.00045
	10^{-6}	0.009898	0.000241	0.001625	0.000141	-0.00199	0.000173
	10^{-7}	0.005804	0.00016	0.000553	0.00016	-0.00074	0.000285
	10^{-8}	0.004235	0.000172	0.000425	0.000115	-0.00038	9.01E-05
	10^{-9}	0.003824	0.00025	0.000201	0.000126	-0.00035	9.10E-05

Table 2.F.2: Low Frequency Elastic Moduli

ϕ	G_0/E^*
0.7	0.00466
0.75	0.00995
0.8	0.0281
0.85	0.0459
0.9	0.08

Chapter 3: Oscillatory Shear Rheology‡

3.1 INTRODUCTION

Oscillatory shear rheology is widely used to characterize the rheological behavior of materials as diverse as colloidal suspensions, polymer melts and solutions, surfactant mesophases, liquid crystals, and soft glassy materials [Hyun *et al.* (2011)]. A typical dynamic oscillatory test is performed by subjecting the material to a periodic strain or stress of sinusoidal shape at angular frequency ω and measuring its mechanical response as a function of time. The linear viscoelastic regime (LVE) of the material is probed when small amplitude oscillatory strains (SAOS) are applied. The linear viscoelastic properties are characterized by the (elastic) storage modulus G' and (viscous) loss modulus G''. Materials can be probed at a large range of frequencies or time scales, often inaccessible by steady shear experiments, which yield the characteristic relaxation times and moduli. $G'(\omega)$ and $G''(\omega)$ fully describe the material response near equilibrium and provide insights into the relation between microstructure and rheology. Predictions of moduli based on molecular or microscopic theories are now available for a wide range of materials. Unlike steady shear at constant shear rate where the material is always above the yield stress, oscillatory shear is a technique which allows the material to move across the yield stress and can be used to additionally probe the signatures of yielding at different scales.

During large amplitude oscillatory shear (LAOS), the equilibrium structure is distorted far from equilibrium and the response is no longer proportional to the excitation. The analysis used for small strain amplitudes is no longer meaningful and is insufficient to characterize the nonlinear rheology of materials. The complexity and richness of

---

‡ Much of this chapter has appeared in Mohan L., C. Pellet, M. Cloitre and R. Bonnecaze, "Local mobility and microstructure in periodically sheared soft particle glasses and their connection to macroscopic rheology," J Rheol **57**, 1023-1046 (2013).

LAOS tests reside in two main features. First, the amplitude and the frequency can be varied independently. Secondly, LAOS tests are usually non-equilibrium processes in that the material periodically returns to the same state of deformation without necessarily having time to reach steady state during the cycle. This makes LAOS experiments useful for studying highly nonlinear situations where materials are subjected to large deformations for a short period of time, as in fatigue tests.

The analysis of LAOS measurements constitutes a very active area of research [Hyun *et al.* (2011)]. The oscillatory stress responses are often visualized in the form of closed curves in the strain and stress versus shear rate planes, and are generally referred to as elastic and viscous Lissajous-Bowditch plots, respectively, [Dealy and Wissbrun (1990); Philippoff (1966)] or as 3-D space with stress, strain and strain rate coordinates [Cho *et al.* (2005)]. General methods of analyzing non-linearities consist of decomposing the response waveforms into various basis functions, yielding a series expansion with an arbitrary number of terms. Fourier-transform rheology uses trigonometric functions to represent the response into a series of harmonics in the frequency domain [Wilhelm *et al.* (1998); Wilhelm (2002)]. Cho *et al.* (2005) decompose the response into a sum of so-called elastic and viscous contributions. The idea was later generalized by Ewoldt *et al.* (2008) who used a set of orthogonal Chebyshev polynomials. Another method of decomposition uses combinations of characteristic basis functions which are associated with specific physical events [Klein *et al.* (2007)].

Despite these important achievements, the interpretation of LAOS experiments in terms of physical mechanisms remains challenging. The question of how data extracted from LAOS experiments correlate to constitutive models has motivated investigations of various materials such as polymer solutions and melts with various molecular architectures [Hyun and Wilhelm (2009); Pearson and Rochefort (1982); Wagner *et al.*

(2011)], wormlike micelles [Gurnon and Wagner (2012)], and yield stress fluids [Ewoldt *et al.* (2010)]. A conceptually useful framework analyzes the response waveforms as temporal sequences of physical processes that repeat over time [Rogers *et al.* (2011a); Rogers *et al.* (2011b); Rogers (2012); Rogers and Lettinga (2012)]. With this technique it is possible to acquire multiple parameters that would otherwise require several independent rheological tests. In some instances, it has been possible to relate the LAOS response to the structural changes occurring during cycles [Gurnon and Wagner (2012); Lopez-Barron *et al.* (2012); Rogers *et al.* (2012)]. Nonetheless, fundamental descriptions where the non-linear shear response is derived explicitly from microscopic theories are absent. Here, the microstructural changes that occur during LAOS experiments for soft particle glasses are determined from particle scale simulations and used to establish the microscopic events that occur during the strain cycle. These microscopic events are then connected to the macroscopic behavior of soft particle glasses during oscillatory shear.

As discussed earlier, the structure of soft particle glasses which is amorphous, shares common features with hard sphere glasses. Each particle is trapped in a “cage” formed by its neighbors, which restrict and even arrest macroscopic motion. However, where hard sphere colloids only experience excluded volume interactions, soft particles at high volume fractions are compressed against each other by bulk osmotic forces and particles that are in contact interact via soft elastic repulsions. The rheological properties of soft jammed materials are dominated by the existence of the so-called yield stress below which they behave like weak elastic solids whereas they yield and flow like viscous liquids above it.

In the previous chapter it was shown that the steady-shear properties of soft particle glasses result from a subtle interplay between elastic interactions and structural rearrangements between interlocked particles. A micromechanical model was proposed that provides physical insights into yielding and flow mechanisms and lead to quantitative predictions of the shear stress and the normal stress differences without any adjustable parameters [Seth *et al.* (2011)]. Here this approach is extended to soft particle glasses subjected to oscillatory shear flow. The signatures of yielding at different scales are captured and the microstructural changes during an oscillatory shear cycle are determined.

The remainder of the chapter is organized as follows. The simulation technique is described in section 3.2. The simulation results at small and large amplitudes for the dynamics at the particle scale are presented in section 3.3. Section 3.4 contains the microstructure at the mesoscopic scale and section 3.5 contains the macroscopic rheology. The viscoelastic moduli at low strain amplitudes, the strain sweeps and the Bowditch-Lissajous plots are found in good agreement with real experiments on microgels from Dr. Cloitre's lab at ESPCI ParisTech, which validates the technique. A discussion connecting the evolution of the particle mobility and the microstructure to the macroscopic rheology is presented in section 3.6 and 3.7 and it is demonstrated that a large amplitude cycle can be decomposed into a sequence of physical processes that repeat periodically.

3.2 SIMULATION TECHNIQUE

Soft particle glasses are modeled as three dimensional packings of N periodically replicated non-Brownian elastic spheres dispersed in a solvent with viscosity η_s at volume fractions exceeding the random close-packing of hard spheres. The 3D packings are built as described in section 2.3 with a 10% polydispersity. The suspension is subjected in the x-direction to an oscillatory shear strain of amplitude and frequency, γ_0 and ω, respectively: $\gamma = \gamma_0 \sin(\omega t)$. The resulting velocity is in the x-direction with y axis being the gradient direction (see figure 3.1). The dynamics of the suspension is modeled using the micromechanical model described in section 2.2. The governing equation including the elastic and elasto-hydrodynamic interactions at particle-particle contact presented earlier in section 2.2 is given below for easy reference.

$$\frac{\mathrm{d}\tilde{\mathbf{x}}_\alpha}{\mathrm{d}\tilde{t}} = \tilde{\mathbf{u}}_\alpha^\infty + \frac{f_r(\phi)}{6\pi\tilde{R}_\alpha}\left[\frac{4}{3}C\sum_\beta \varepsilon_{\alpha\beta}^{n}\tilde{R}_c^2\mathbf{n}_\perp - \sum_\beta\left(C\tilde{u}_{\alpha\beta,\|}\tilde{R}_c^3\right)^{1/2}\varepsilon_{\alpha\beta}^{(2n+1)/4}\mathbf{n}_\|\right] \tag{3.1}$$

The symbols here have the same meaning as before. $\tilde{\mathbf{u}}_\alpha^\infty = \frac{\dot{\gamma}\eta_s}{E^*} y\mathbf{e}_x$ represents the velocity field due to applied strain, but here the shear rate is time varying due to the oscillatory nature of the shear with $\dot{\gamma} = \gamma_0\omega\cos(\omega t)$ being the instantaneous shear rate and $\mathbf{e}_x$ the unit vector in the x-direction.

These N coupled equations of motion were integrated numerically to determine the evolution of the spatial position and velocity of each particle. Periodic boundary conditions were applied in the x- and z- directions and Lee-Edwards boundary condition was implemented in y- direction. At each step, the positions of particles leaving the box were shifted by a cumulative strain $\gamma = \int_0^t \dot{\gamma} d\tau$. The open source code LAMMPS [Plimpton

(1995)] was used to perform the simulations. Packings of 1,000 and 10,000 particles of volume fraction 0.8 were generated. Configurations with 1 000 particles were used for the large amplitude simulations, γ_0 = 2.0, 1.0, 0.5 and 0.1. Each simulation was run up to 50 cycles and averaged over five different initial configurations. Configurations with 10000 particles were used for the small amplitude simulations, γ_0 = 0.05, 0.01 and 0.003. These simulations were run for up to 20 cycles and averaged over five different initial particle configurations. The cycles for averaging were chosen after reaching steady state. The approach to steady state was defined as the cycle beyond which all other cycles were the same, *i.e.* the stress-strain data for all cycles overlapped on top of each other.

The average stress σ at different points during the cycle was computed from the Kirkwood formula as described in section 2.3 (see equations 2.4-2.6). The viscoelastic moduli were computed by taking the Fourier transform of the stress-strain data computed over a cycle with period T_{cycle}.

$$\begin{aligned} G' &= \frac{2}{\gamma_0 T_{cycle}} \int_0^{T_{cycle}} \sigma \sin(\omega t)\,dt \\ G'' &= \frac{2}{\gamma_0 T_{cycle}} \int_0^{T_{cycle}} \sigma \cos(\omega t)\,dt \end{aligned} \qquad (3.2)$$

The microstructure of suspensions was characterized through the dynamic pair distribution function $g(\mathbf{r})$ which is defined in the previous chapter in section 2.5.1 [Brady and Morris (1997); Morris and Katyal (2002); Seth *et al.* (2011); Sierou and Brady (2002)]. The dynamic pair distribution function $g(\mathbf{r})$ was computed at different points in the cycle. It can be decomposed into a series of orthogonal spherical harmonic functions and $g_{2,-2}(r)$ which is the most relevant harmonic to the shear stress was calculated as described earlier in section 2.5.2.

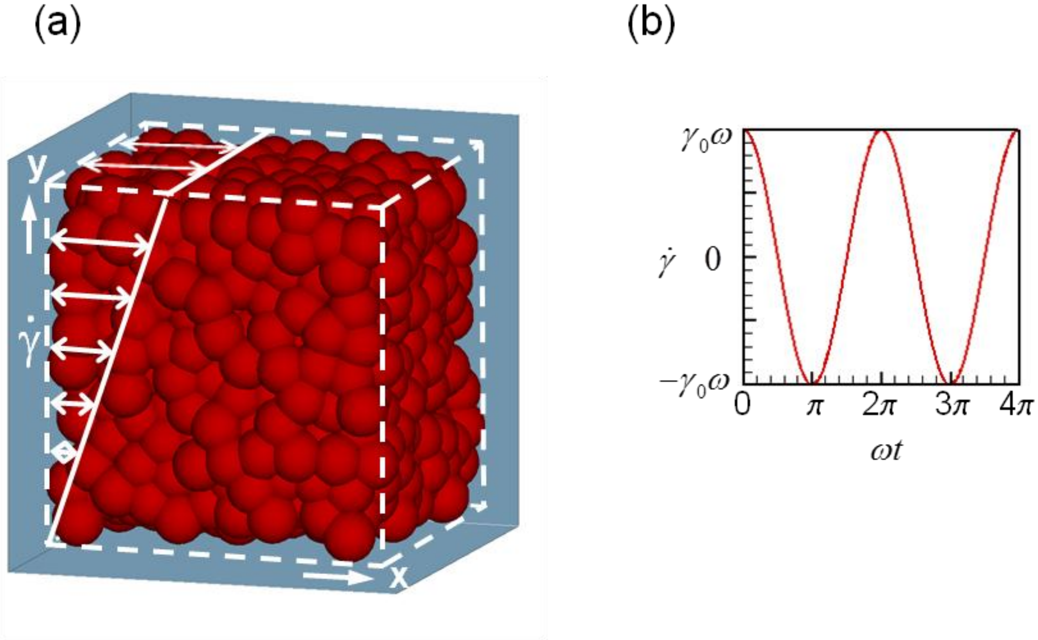

Figure 3.1: (a) Periodic simulation box (b) Imposed oscillatory shear rate.

3.3 PARTICLE SCALE DYNAMICS

In this section, the particle dynamics in 3D jammed packings of soft particles subjected to oscillatory shear flow is presented. The individual particle motions are tracked in the simulations and the mean square displacements of the particles are analyzed.

3.3.1 Particle mean square displacements: Effect of Strain Amplitude

Figure 3.2 represents the variations of the mean square displacements in the *x*-, *y*- and *z*- directions versus the number of oscillations n_{osc} ($=\omega t/2\pi$) for a fixed frequency and various strain amplitudes. In the *x*- direction, the mean square displacement is modulated by oscillations due to the periodic forcing unlike along *y*- and *z*- directions. The top panel shows data computed at low strain amplitudes γ_0 close or smaller than the macroscopic yield strain, γ_y; in the bottom panel γ_0 is much larger than γ_y. At the smallest strain amplitudes investigated $(\gamma_0/\gamma_y \leq 1.5)$, the mean square displacements $\langle \Delta x^2 \rangle$, $\langle \Delta y^2 \rangle$, and $\langle \Delta z^2 \rangle$ slowly increase in time before reaching a plateau value which is much less than a particle diameter. This indicates that the particles explore restricted regions of space around their mean positions. In other words they can be seen as trapped in cages formed by their neighbors. At larger strain amplitudes $(\gamma_0/\gamma_y \geq 3)$, the particles move over distances larger than their diameter, i.e., they escape their local environments and jump to other cages where they experience different neighbors. These rearrangements give rise to large mean square displacements of individual particles even though the macroscopic strain is purely oscillatory.

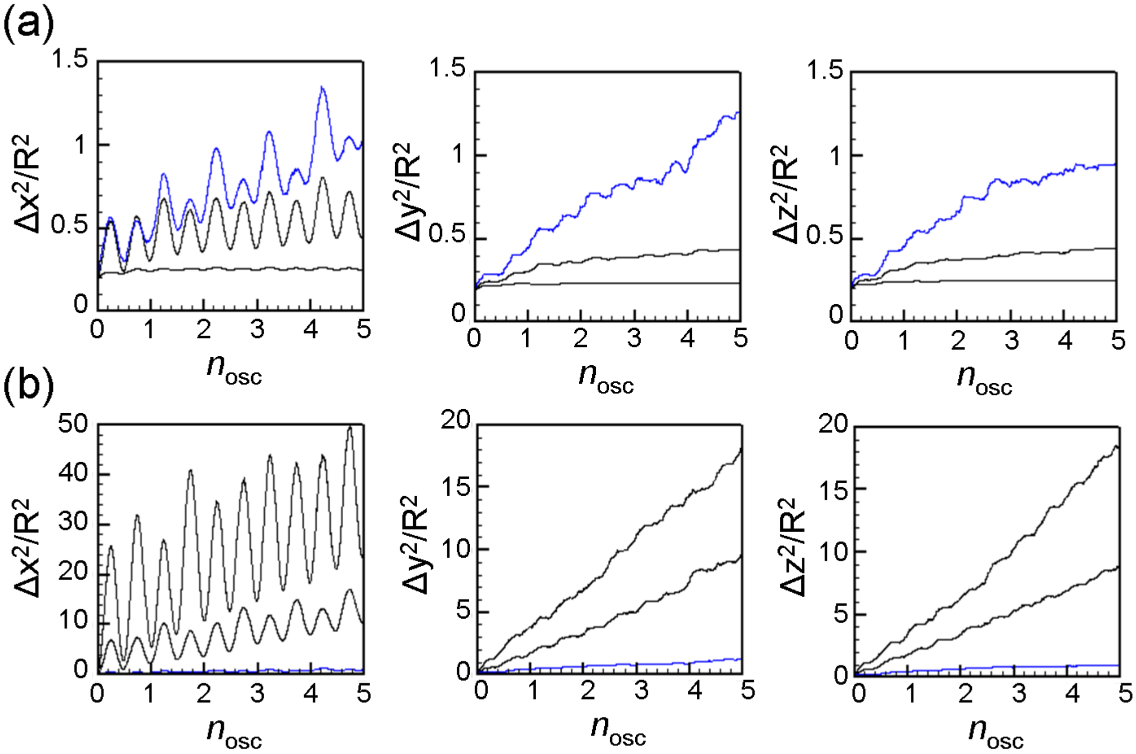

Figure 3.2: Mean square displacements of particles in the *x*-, *y*- and *z*- directions versus number of oscillations for different strain amplitudes: (a) γ_0/γ_y = 3.0, 1.5, 0.3 (top to bottom); (b) γ_0/γ_y = 30, 15, 3.0 (top to bottom). The frequency is $\eta_s\omega/E^* = 2\times10^{-8}$.

3.3.2 Particle mean square displacements: Effect of frequency

Figure 3.3 presents the mean square displacements in the *x*-, *y*- and *z*- directions at small and large strain amplitudes when the frequency is varied. In the top panel, the strain amplitude is smaller than the yield strain $(\gamma_0/\gamma_y = 0.09)$ and the non-dimensional frequency $\eta_s\omega/E^*$ varies between 2×10^{-8} to 10^{-3}. In the low strain amplitude regime, the particles get trapped at all frequencies after a few oscillations. The steady state, where the mean square displacements reach their plateau values, occurs at longer times for lower frequencies. It is interesting to note that the plateau values of $\langle\Delta x^2\rangle$, $\langle\Delta y^2\rangle$, and $\langle\Delta z^2\rangle$ are similar, as already noted in figure 3.2. The bottom panel shows data computed for large strain amplitude $(\gamma_0/\gamma_y = 30)$ and non-dimensional frequencies varying again between 2×10^{-8} to 10^{-6}. The mean square displacements steadily increase at all frequencies showing that the particles are not permanently trapped at these large amplitudes. It is interesting to note that the mean square displacement per cycle remains of the same order even though the time taken for completing one oscillation is orders of magnitude different for the different frequencies.

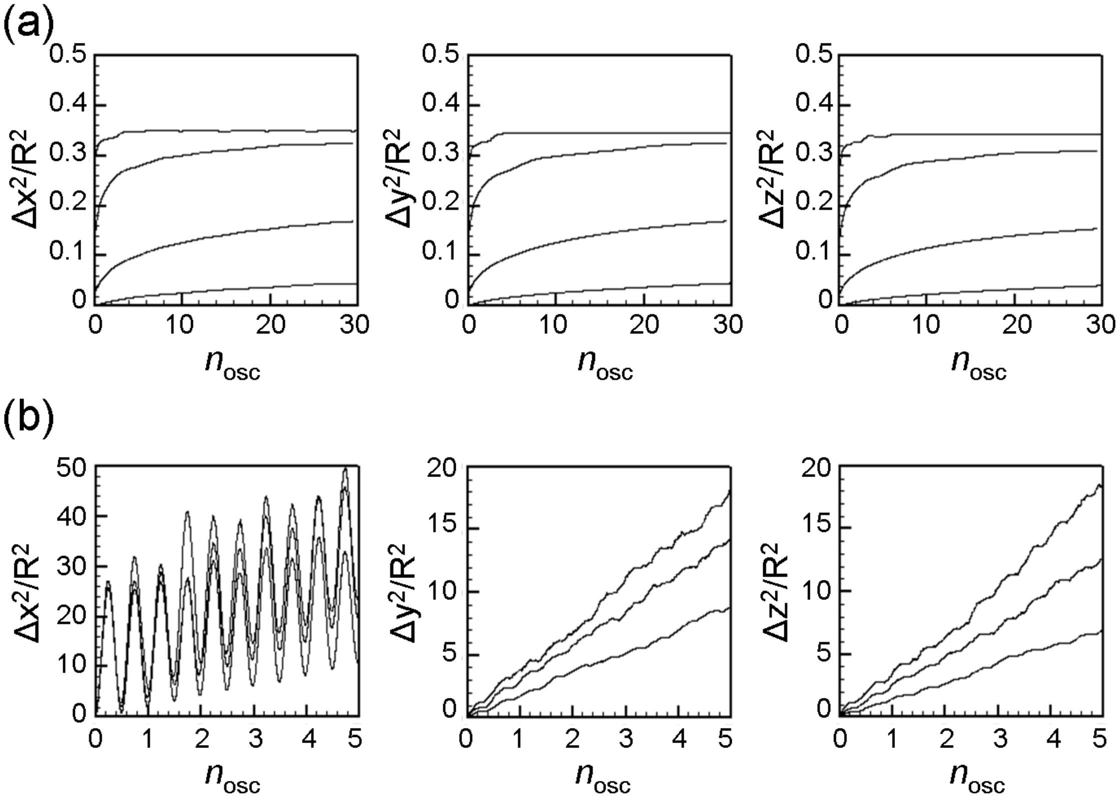

Figure 3.3: Mean square displacements of particles in the *x*-, *y*- and *z*- directions at small and large strain amplitudes versus oscillation number for different frequencies. (a) Small strain amplitude (γ_0/γ_y = 0.09) at frequencies of $\eta_s\omega/E^* = 2\times10^{-8}, 10^{-6}, 10^{-4}, 2\times10^{-3}$ (top to bottom). (b) Large strain amplitude (γ_0/γ_y =30) at frequencies $\eta_s\omega/E^* = 2\times10^{-8}, 10^{-7}, 10^{-6}$ (top to bottom).

3.3.3 Shear induced diffusivity

For strain amplitudes larger than the yield strain, the particle mean square displacements $\left\langle \Delta x^2 \right\rangle$, $\left\langle \Delta y^2 \right\rangle$, and $\left\langle \Delta z^2 \right\rangle$ increases with time. After steady state is reached, the variations are linear with periodic modulations in the oscillatory flow direction (see figure 3.2 and 3.3). This allows us to define effective diffusion coefficients of the particles in the *x*-, *y*- and *z*- directions (the oscillatory shear is in the *x*- direction) by fitting the mean square displacement curves as follows,

$$\begin{aligned} \left\langle \Delta \mathrm{x}^2 \right\rangle &= 2\mathrm{D_x t} \\ \left\langle \Delta \mathrm{y}^2 \right\rangle &= 2\mathrm{D_y t} \\ \left\langle \Delta \mathrm{z}^2 \right\rangle &= 2\mathrm{D_z t} \end{aligned} \tag{3.3}$$

In practice, the mean square displacements were computed over the last four cycles. The variations of the non-dimensional effective diffusion coefficients D_x, D_y, and D_Z normalized by the scaling factor $D_0 = R^2 E^* / \eta_s$ for different strain amplitudes at $\eta_s \omega / E^* = 2\times10^{-8}$ is presented in figure 3.4a. Again, the amplitude of the maximum strain γ_0 is normalized by γ_y. All three diffusion coefficients are equal, except at the largest strain amplitude where the diffusion coefficient in the *x*- direction is slightly larger. This indicates that the shear induced diffusivity associated with particle rearrangements is isotropic under these conditions, even though the shearing motion is applied along the *x*- axis. Only the averaged diffusion coefficient, $D = (D_\mathrm{x} + D_\mathrm{y} + D_\mathrm{Z})/3$ will be considered in the following. The diffusion coefficients increase linearly with strain amplitude beyond $\gamma_0/\gamma_y \sim 1$. This further confirms that the large scale rearrangements responsible for the increase of the shear induced diffusivity start taking over around the yield strain.

The effect of frequency on the particle scale diffusivity at large amplitudes was also determined. The variations of the averaged diffusion coefficient *D* with the dimensionless frequency $\eta_s\omega / E^* = 2\times10^{-8}$ for two values of $\gamma_0/\gamma_y > 1$ are plotted in figure 3.4b. *D* increases linearly with the applied frequency. In figure 3.4c the averaged diffusion coefficients for different strain amplitudes greater than the yield strain and frequencies are plotted against the non-dimensional shear-rate amplitude $\dot{\gamma}_0\eta_s/E^*$ where $\dot{\gamma}_0 = \gamma_0\omega$. The data obtained for different strain amplitudes and frequencies collapse onto a single master curve. They are well described by a linear variation. It is interesting to note the similarities between the non-dimensional variable $\dot{\gamma}_0\eta_s/E^*$ and that involved in the constitutive equation $\sigma/\sigma_y = 1 + k\left(\eta_s\dot{\gamma}/E^*\gamma_y^2\right)^{1/2}$ derived in section 2.5.4. The diffusivities computed from steady shear simulations also agree with those computed from oscillatory shear measurements here (see Supplemental Material 3.B). This suggests that the same underlying mechanisms, i.e. disorder and elastohydrodynamic interactions lay at the heart of the behavior of soft particle glasses at the local and macroscopic scale.

From figure 3.4c one may also conclude that the diffusivity $D \cong 0.1\dot{\gamma}R^2$. Remarkably, this is practically the same scaling for shear induced hydrodynamic diffusion for hard spheres in suspensions with volume fractions greater than 30% [Nott and Brady (1994)], despite the fact the physics driving the behavior (long-ranged hydrodynamic interactions versus near-field elastohydrodynamics) are quite different.

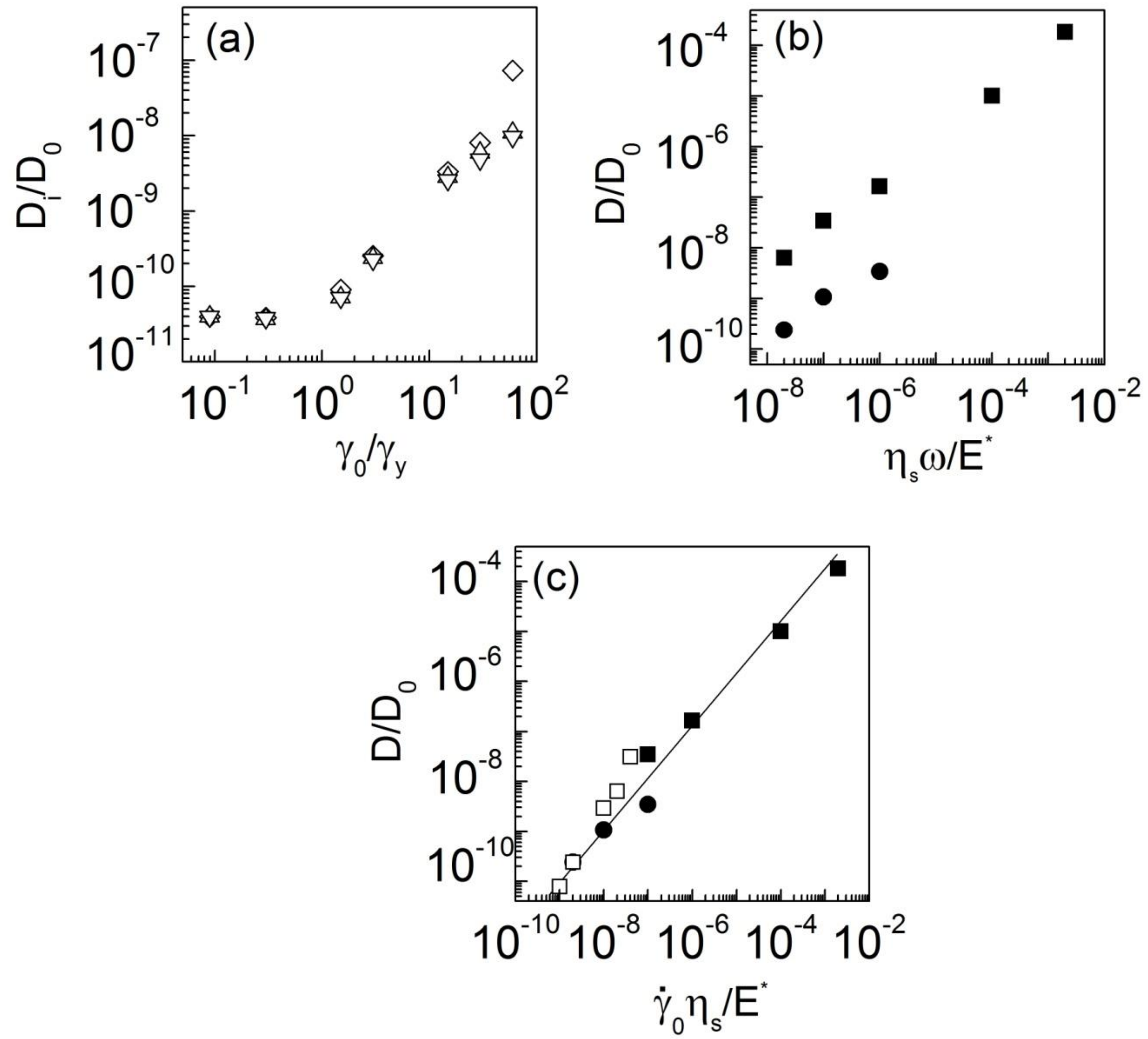

Figure 3.4: Shear-induced diffusion coefficients computed from the mean square displacements of particles. (a) Variations with the strain amplitude of the diffusion coefficients D_i ($i = x, y, z$) computed from $\left\langle \Delta x^2 \right\rangle$ (◇), $\left\langle \Delta y^2 \right\rangle$ (△), and $\left\langle \Delta z^2 \right\rangle$ (▽), at non dimensional frequency $\eta_s \omega / E^* = 2\times10^{-8}$; the data for $\gamma_0/\gamma_y < 1$ have been estimated from the last computed oscillation where the mean square displacements approach their plateau values. (b) Variations with frequency of the non-dimensional averaged diffusion coefficient, $D = (D_x + D_y + D_z)/3$ at $\gamma_0/\gamma_y = 30$ (■) and $\gamma_0/\gamma_y = 3.0$ (●). (c) Variations of the averaged diffusion coefficients D/D_0 for $\gamma_0/\gamma_y > 1$ with the non-dimensional shear-rate amplitude (same symbols as in (a) and (b)).

3.4 MICROSTRUCTURE OF SUSPENSIONS

In this section the pair distribution function $g(\mathbf{r})$ is presented at different points in the cycle for small, medium and large strain amplitude oscillatory shear. For reference, the radially symmetric microstructure at rest and the distorted microstructure at steady shear were presented in section 2.5.1.

3.4.1 Microstructure at small amplitude oscillatory shear

First, the evolution of the microstructure within a cycle when the strain amplitude γ_0 is smaller than the yield strain ($\gamma_0/\gamma_y < 1$) was studied. Figure 3.5a shows the variations of the applied strain γ and of the resulting stress σ. γ and σ are nearly in phase and linearly proportional, which corresponds to the linear viscoelastic regime. The pair correlation function was computed at five particular locations of the cycle, denoted by t_i ($i = 1,5$). t_1 and t_5 are the points where the stress amplitude has positive and negative extrema, respectively; t_3 is where the stress is zero; at t_2 and t_4, the stress takes intermediate values of opposite signs. Note that in this small strain limit where γ and σ are nearly in phase, the strain has also its positive and negative extrema approximately at t_1 and t_5 and is zero in t_3. The five pair distribution functions which are computed are shown in figure 3.5b. At all times, the pair distribution function appears to be essentially uniform. The white line represents the most probable centre-centre separation at rest. The particle separation r/R at which the pair correlation function is maximum is about the same as at rest. In order to better analyze the three-dimensional pair correlation function, the spherical harmonics $g_{2,-2}(r)$ was calculated at t_1, t_3 and t_5, which are plotted in figure

3.5c. At t_3 where the stress is zero, $g_{2,-2}(r)$ vanishes within the statistical fluctuations. At t_1 and t_5 where the stress has its extrema, $g_{2,-2}(r)$ exhibits a small negative minimum at small center-to-center distances r/R and a small positive maximum at large distances during the positive part of the cycle (t_1) and vice versa during the negative part (t_5). This means that there is a small accumulation of particles along the compression axis or in the upstream quadrant and depletion along the extension axis or in the downstream quadrant. In conclusion, a small amplitude oscillatory shear flow induces only very slight distortions of the pair distribution function with respect to the static situation.

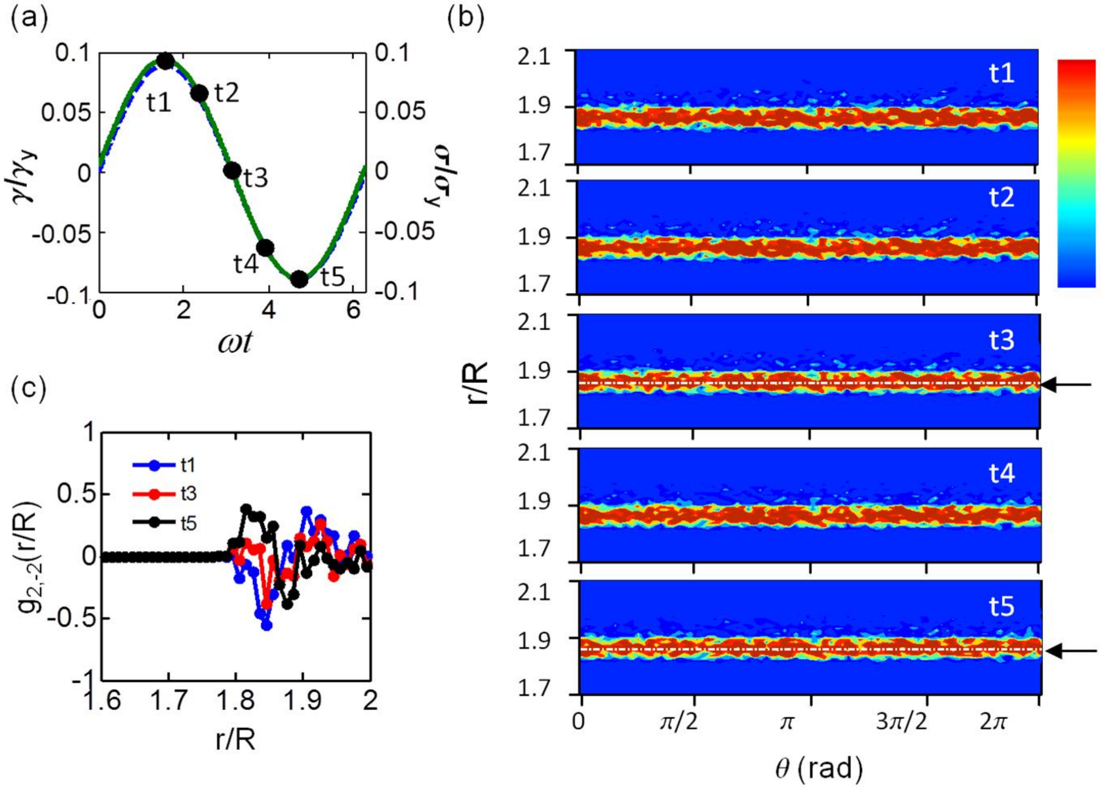

Figure 3.5: Microstructure of soft particle glass ($\phi = 0.80$) subjected to small amplitude oscillations ($\gamma_0/\gamma_y = 0.09$; $\eta_s\omega / E^* = 2\times10^{-8}$). (a) Variations of the strain (- - -) and stress (—) waveforms over one cycle and positions of the five characteristic points where $g(\mathbf{r})$ is presented. (b) Pair distribution functions in the azimuthal r-θ plane; the most probable center-to-center separation at rest is indicated in the maximum and zero stress states by a white dash-dot line and a black arrow. (c) $g_{2,-2}(r)$ spherical harmonics.

3.4.2 Microstructure at medium amplitude oscillatory shear

Figure 3.6 analyzes the change of microstructure when the strain amplitude is slightly larger than the yield strain ($\gamma_0/\gamma_y \sim 1$), the maximum stress being of the order of the yield stress. This situation is referred to as the medium amplitude case. Figure 3.6a shows the variations of the applied strain and resulting stress within a cycle. The stress waveform is no longer sinusoidal indicating that we are outside the linear viscoelastic regime. The two-dimensional pair correlation function was computed at six characteristic intracycle positions: t_1 and t_4 where the stress has its positive and negative extrema, respectively, t_3 and t_6 where it is zero, and t_2 and t_5 where the strain has its positive and negative extrema. The corresponding azimuthal plots are presented in figure 3.6b. The pair distribution functions are no longer radially symmetric and reveal significant distortions of the microstructure. These distortions are the most visible at the positions in the cycle where the stress is the largest (t_1 and t_4, t_2 and t_5). The positions of the maxima of the particle pair distribution functions vary with the angle and the distribution of particles centers along the radial direction is no longer symmetric. In particular, there are particles at smaller separations than found at rest or in the linear viscoelastic regime. This indicates that neighboring particles tend to accumulate in the upstream quadrant ($\pi/2<\theta<\pi$), where they are more compressed, and to deplete along the extensional axis ($0<\theta<\pi/2$), where they are less distorted. It is interesting to note that the angular position of the accumulation and depletion effects in the negative part of the cycle are shifted by $\pi/2$ radians with respect to their positions in the positive part due the reversal of the flow. At t_3 and t_6, where the stress vanishes, the accumulation-depletion effect is significantly reduced, the particle distribution becomes more uniform and resembles that in the static state.

The accumulation-depletion mechanism that has been identified here is also supported by the variations of the spherical harmonics shown in figure 3.6c. $g_{2,-2}(r)$ has a negative peak at low separations ($r/R \cong 1.83$), i.e. large degrees of compression, which corresponds to an accumulation of particles along the compression axis. There is a positive peak of smaller amplitude at large separations ($r/R \cong 1.9$), i.e. low degrees of compression, which corresponds to the depletion of particles around the downstream extension axis of the flow. From the depth of the minimum and the height of the maximum, it is deduced that there are fewer particles in the extensional region. The asymmetry between the peaks associated with upstream accumulation and downstream depletion is more pronounced when the stress is large (t_1 and t_4, t_2 and t_5). On the contrary, at t_3 and t_6, where the stress vanishes, the asymmetry is weak and $g_{2,-2}(r)$ approaches that computed for the low amplitude case. The spherical harmonics $g_{2,-2}(r)$ computed at locations where the stress takes opposite values (t_1 and t_2, t_3 and t_6) are equal but with opposite signs, which again express the fact that the particle distribution simply reverses upon flow reversal.

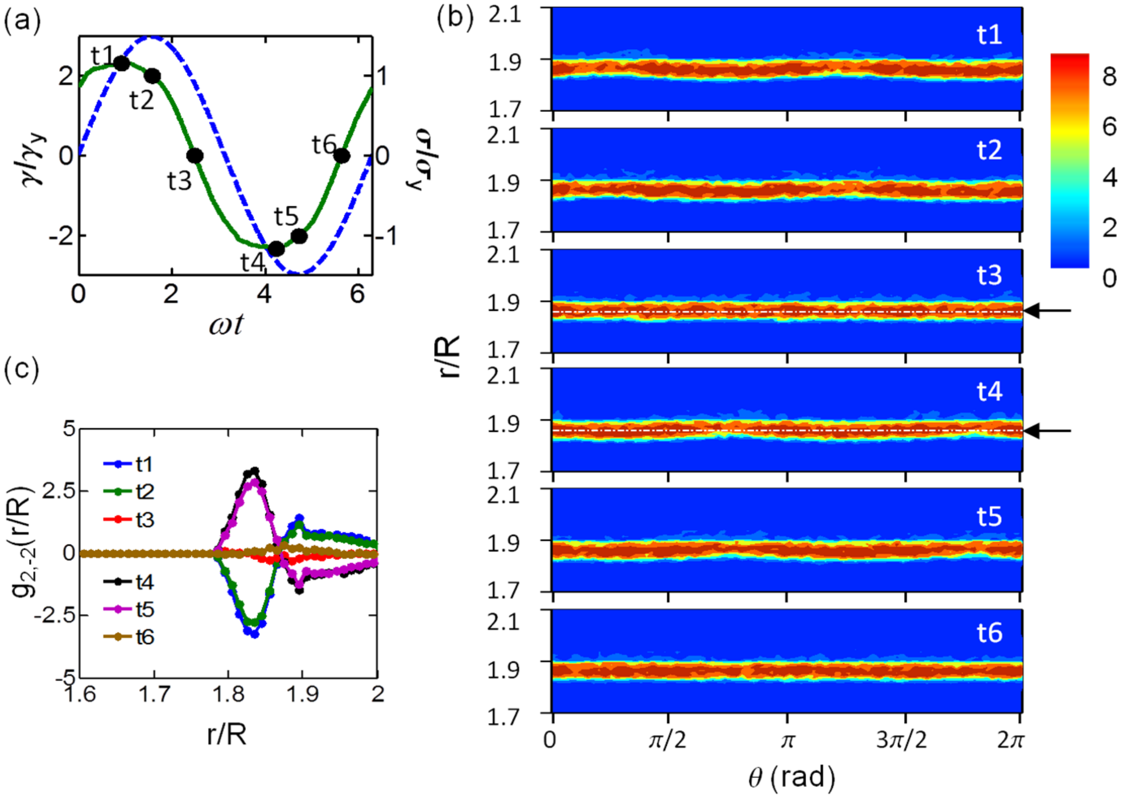

Figure 3.6: Microstructure of soft particle glass (ϕ = 0.80) subjected to medium amplitude oscillations ($\gamma_0/\gamma_y = 3.0$; $\eta_s\omega / E^* = 2\times10^{-8}$). (a) Variations of the strain (- - -) and stress (—) waveforms over one cycle and positions of the six characteristic points where $g(\mathbf{r})$ is presented. (b) Pair distribution functions in the azimuthal r-θ plane; the most probable center-to-center separation at rest indicated in the zero stress states by a white dash-dot line and a black arrow. (c) $g_{2,-2}(r)$ spherical harmonics.

3.4.3 Microstructure at large amplitude oscillatory shear

Figure 3.7 shows the evolution of the microstructure during strain amplitudes that are large relative to the yield strain (γ_0/γ_y >>1); here, the maximum stress exceeds the yield stress. In figure 3.7a the stress waveform is considerably distorted with respect to the strain, indicating that the response is highly non linear. In figure 3.7 b the pair distribution functions are shown for the same characteristic times as in the medium amplitude case. The evolution of the microstructure within the cycles is somewhat similar to that for the medium amplitude case but the amplitudes of the distortions are much larger. At times t_1 and t_4, where the stress reaches its maximum positive and negative values, which largely exceeds the yield stress, important asymmetries are observed in the pair distribution function both along the azimuthal and radial directions. There is a significant accumulation of particles upstream and depletion downstream indicating an important redistribution of particles. At t_2 and t_5, where the strain reaches its positive and negative values, the stress has significantly decreased and the accumulation and depletion regions are much less pronounced. Finally, at t_3 and t_6, where the stress goes to zero, the particle distribution is nearly isotropic, the maximum compression and the average separation between the particles being comparable to that observed at rest or at small strain amplitudes.

The spherical harmonics $g_{2,-2}(r)$ computed at the characteristic times t_i are presented in figure 3.7c. As already discussed for the medium amplitude case, the negative minimum and positive maximum during the positive part of the strain cycle are associated with the accumulation of particles in the compressive quadrant and the depletion in the extension quadrant. The peak heights are the largest at t_1 and t_4, when the stress is the largest. They decrease rapidly at t_2 and t_5, when the stress amplitude drops and finally they nearly vanish at t_3 and t_6, when the stress goes to zero. Again we observe symmetry between upstream and downstream upon flow reversal.

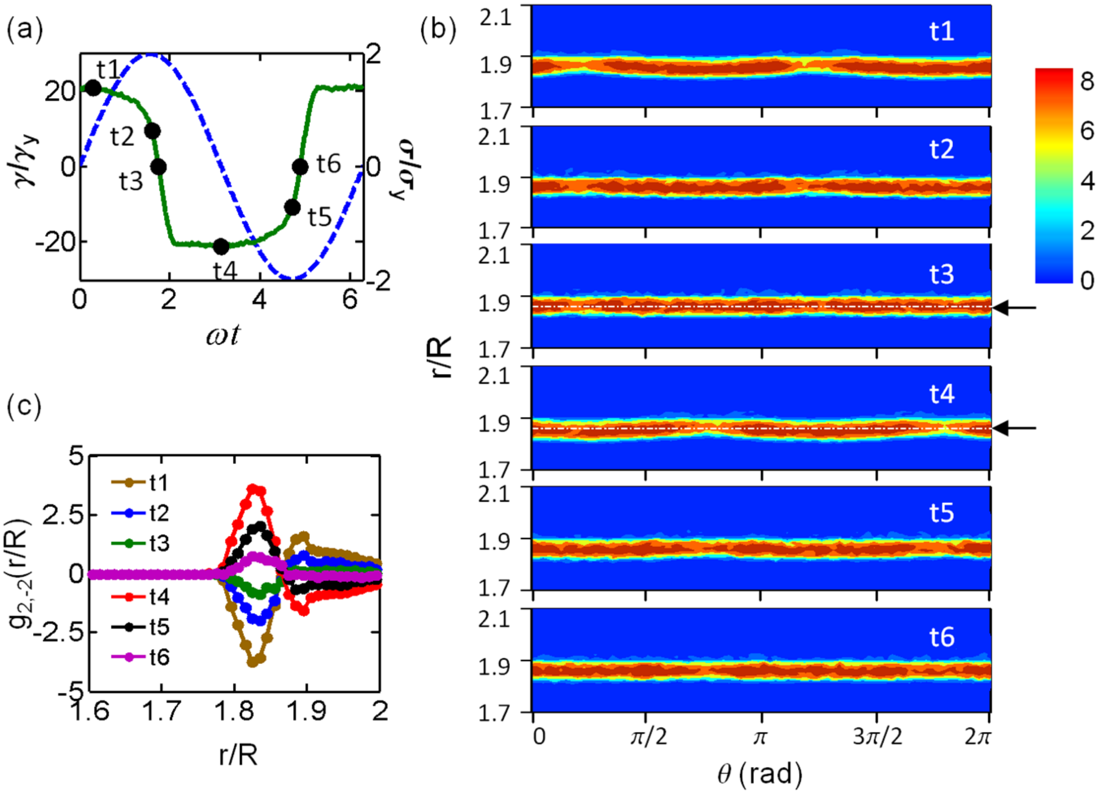

Figure 3.7: Microstructure of soft particle glass ($\phi = 0.80$) subjected to large amplitude oscillations ($\gamma_0/\gamma_y = 30$; $\eta_s\omega / E^* = 2\times10^{-8}$). (a) Variations of the strain (- - -) and stress (—) waveforms over one cycle and positions of the six characteristic points where $g(\mathbf{r})$ is presented. (b) Pair distribution functions in the azimuthal r-θ plane; the most probable center-to-center separation at rest is indicated in the zero stress states by a white dash-dot line and a black arrow; (c) $g_{2,-2}(r)$ spherical harmonics.

3.5 MACROSCOPIC RHEOLOGY

3.5.1 Viscoelastic moduli at low strain amplitude

Oscillatory experiments at low strain amplitudes probe the linear viscoelastic response of the unperturbed microstructure. Systematic simulations were performed in this regime, varying the frequency of oscillations over several decades, and compared to the results with experimental observations from Dr. Cloitre's lab. The materials used and the experimental protocol are described in Supplemental Material 3.A. The variations of the storage and loss moduli with frequency are shown in figure 3.8. At low frequencies, the elasticity and dissipation associated with the deformation of the particles through their contacting facets is probed. The storage modulus exhibits a plateau that is much larger than the loss modulus. The value of the plateau modulus, G_0, is in good agreement with independent calculations based on uniaxial deformation of small amplitude [Seth *et al.* (2006)]. For convenience, all the storage and loss moduli presented are scaled by the plateau modulus G_0. At high frequencies both the storage and loss moduli increase. The power law variation which is often followed by the loss modulus in experiments on compressed emulsions and foams ($G'' \sim \omega^{1/2}$) is shown for reference [Cohen-Addad *et al.* (1998); Liu *et al.* (1996)]. Although more simulations at higher frequencies would be necessary to draw a definite conclusion, the data calculated in the simulations fit reasonably well to this expectation. The storage and loss moduli which were measured for the microgel suspension described in Supplemental Material 3.A, using a conventional rheometer is also plotted in figure 3.8 for comparison. For the sake of comparison, the experimental moduli are normalized to the plateau modulus measured experimentally and the reduced frequency is calculated using the value of the contact modulus which was determined experimentally and the solvent viscosity. The correspondence between the simulation and experimental data validates the ability of the 3D elastohydrodynamic model to reproduce quantitatively the linear viscoelastic behavior of real soft particle glasses.

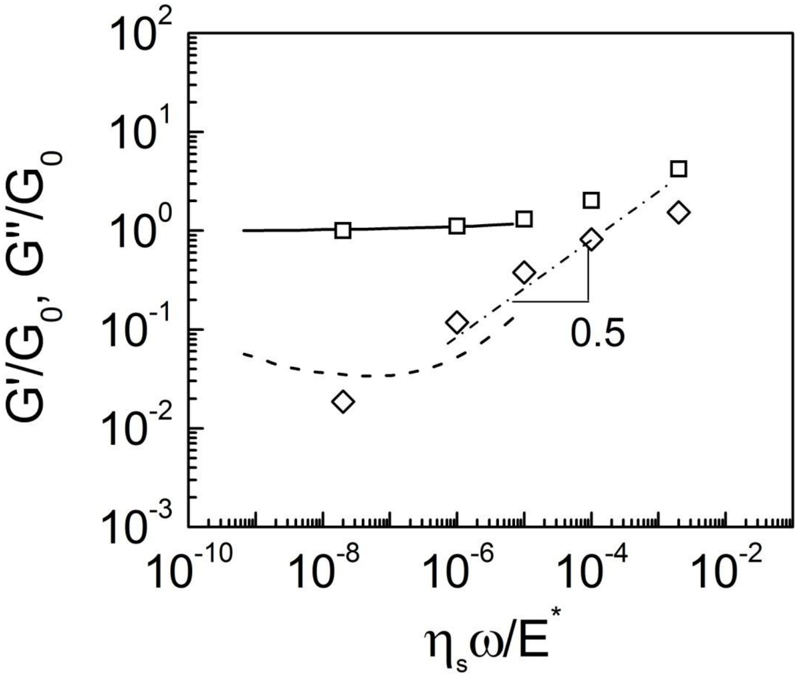

Figure 3.8: Storage modulus G' (□ and —) and loss modulus G'' (◇ and – –) versus reduced frequency from simulations (symbols) and experiments (lines) in the low strain amplitude or linear regime at γ_0/γ_y = 0.09. A reference slope of 0.5 is shown.

3.5.2 Effective viscoelastic moduli during large amplitude oscillation

The effective storage and loss moduli as well as the stress amplitude for any strain of arbitrary amplitude were calculated to construct simulated strain sweep plots. The results are presented in figure 3.9 together with the corresponding experimental data measured for the $\phi = 0.8$ microgel suspension. The moduli are again normalized by the plateau modulus G_0, the stress by the yield stress, and the strain amplitude by the yield strain. Both sets of data agree quantitatively, which further confirms the capacity of the 3D model and the simulations to reproduce non linear responses in oscillatory shear rheology. Figure 3.9 gives evidence for a change of mechanical behavior around $\gamma_0/\gamma_y \cong 1$, where the maximum stress exceeds the yield stress. The small strain amplitude regime where $\gamma_0/\gamma_y < 1$, intermediate strain amplitude regime where $\gamma_0/\gamma_y \approx 1$, and large strain amplitude regime where $\gamma_0/\gamma_y > 1$, can be mapped on the regimes defined in the analysis of the microstructure in section 3.4. In the low strain amplitude regime, where the microstructure is essentially non disturbed by the mechanical excitation, both moduli are constant with $G' > G''$ indicating linear elastic behavior. The intermediate strain amplitude regime, where large scale rearrangements start to occur, is associated with a break in the stress curve, a decrease of the storage modulus and a bump in the loss modulus. At large amplitudes, where particles continuously rearrange and move over long distances, both G' and G'' vary as power laws according to $G' \propto \gamma_0^{-\mu}$ and $G'' \propto \gamma_0^{-\nu}$ with $\mu \cong 1.45$ and $\nu \cong 0.80$ ($\mu/\nu \cong 1.8$). Similar variations are ubiquitous in soft glassy materials [Erwin *et al.* (2010); Hyun *et al.* (2002); Miyazaki *et al.* (2006)]. One major drawback of this analysis, however, is that these effective moduli which are calculated or measured experimentally in the nonlinear regime provide only qualitative information about the actual rheological properties of the materials. In the next section, the analysis is furthered by presenting a full non-linear analysis of the rheological response using Bowditch-Lissajous plots.

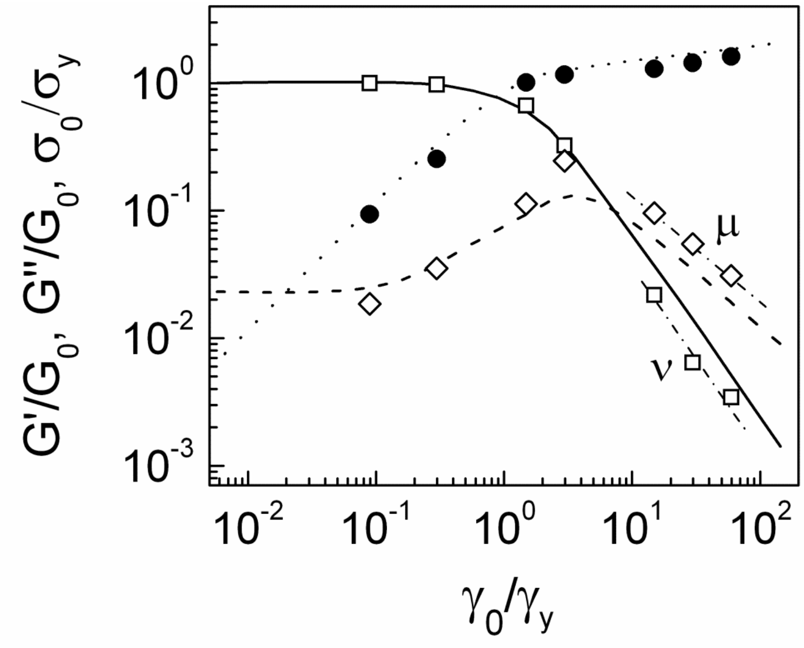

Figure 3.9: Storage modulus G' (□ and —), loss modulus G'' (◇ and ----) and stress amplitude σ_0 (● and ……) as functions of strain amplitude γ_0/γ_y, from simulations (symbols) and experiments (lines) at a frequency of $\eta_s\omega/E^* = 2\times10^{-8}$. Dotted lines represent power law variations with exponents μ and ν respectively, as discussed in the text.

3.5.3 Bowditch-Lissajous plots for arbitrary strain amplitudes

Stress-strain plots or elastic Bowditch-Lissajous (BL) for different strain amplitudes are shown in figure 3.10. Simulation results are presented in figures 3.10a-c. In figure 3.10a, the strain amplitude is smaller than the yield strain (γ_0/γ_y ≅ 0.09). The elastic BL plot is an ellipse, which is the typical response expected for a linear viscoelastic material. The slope of the long axis is the storage modulus while the short axis, which characterizes the openness of the ellipse, depends on the loss modulus. The elongated shape of the ellipse indicates that $G' > G''$, which is in agreement with the previous results shown in figure 3.8. Ellipses with similar features are obtained for different strain amplitudes as long as γ_0/γ_y <1, since we remain in the linear viscoelastic regime. Data at intermediate strain amplitudes is presented in figure 3.10b. The BL curve for γ_0/γ_y =1 is still an ellipse but that for $\gamma_0/\gamma_y = 3.0$ it begins to deform. The distortions are the largest when the strain becomes of the order of the yield strain and the stress comparable to the yield stress. The BL plot is then stretched along the strain axis. Data for large strain amplitudes is presented in figure 3.10c. The BL plots then adopt a parallelogram shape. The lateral sides of the parallelogram correspond to the regime where the stress is smaller than the yield stress. The top and bottom horizontal sides of the BL curves correspond to the portion of the cycles where the stress is larger than the yield stress. It is interesting to note that the point where yielding starts is signaled by a small overshot of the stress, which is reminiscent of the static yield stress. Experimental data for the concentrated microgel suspensions are presented in figures 3.10d-f. They agree reasonably well with the simulated data both in shape and in amplitude. There is a small difference near the yield point around $\sigma = \sigma_y$, which is less apparent for the microgel suspension. Note however that a well-defined static yield stress has been observed star polymer glasses [Rogers *et al.* (2011b)]. The importance of frequency was also investigated both in simulations and experiments and the results are presented in Supplemental Material 3.C. The BL plots essentially keep the same characteristic shapes in the low, intermediate and large amplitude regimes. In the large amplitude regime, the slope of the lateral sides of the BL plots increases with frequency, in accordance with the increase of the linear storage modulus; the absolute value of the stress in the top and bottom section of the BL plots, which corresponds to macroscopic flow, increase.

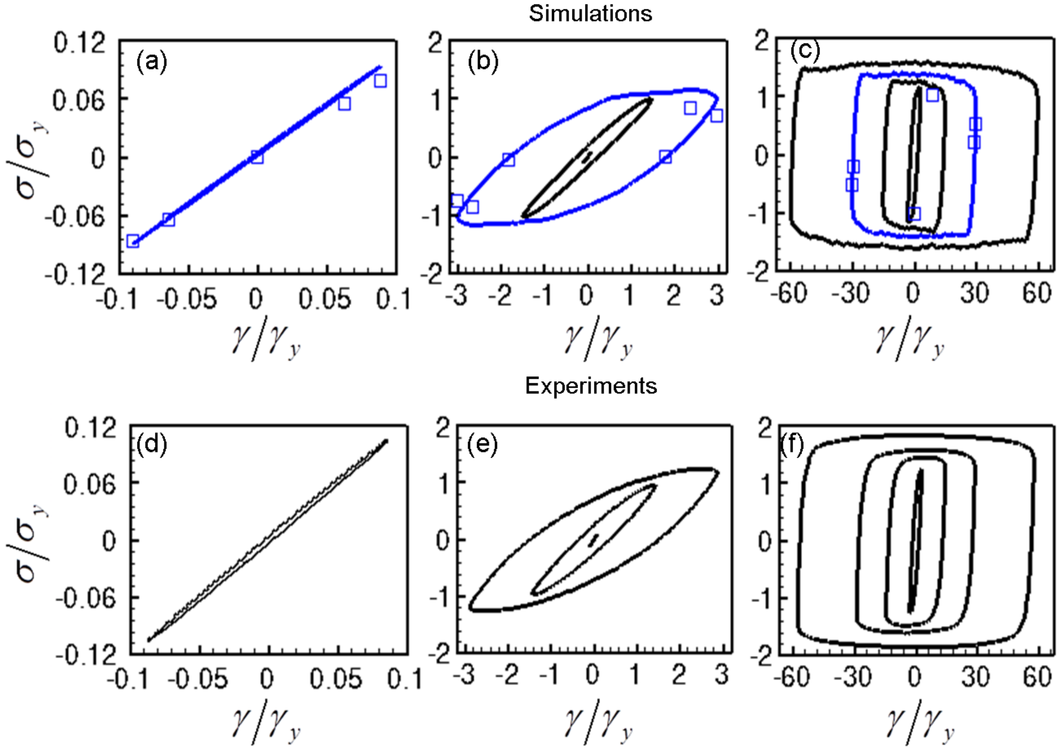

Figure 3.10: Bowditch-Lissajous plots from simulations and experiments at different strain amplitudes. Left to right: linear viscoelastic regime (γ_0/γ_y = 0.09; panels (a) and (d)); medium amplitude regime (inner to outer: γ_0/γ_y = 0.09, 1.5, 3.0; panels (b) and (e)); large amplitude regime (inner to outer: γ_0/γ_y = 3.0, 15, 30, 60; panels (c) and (f)). The symbols in panels (a), (b) and (c) represent the shear stress values which are predicted from the $g_{2,-2}(r)$ spherical harmonics as discussed in the text.

3.6 INTERPRETATION OF PHYSICAL EVENTS WITHIN OSCILLATORY CYCLES

The particle scale simulations and experiments described in the previous section provide a deep understanding of the microstructural changes occurring during the oscillatory shear of soft particle glasses. At small strain amplitudes, the particles remain trapped in the cages formed by their neighbors as they periodically move back and forth to follow the applied strain. Interestingly, the particles execute some in-cage motion of small amplitude around the mean position. The mean square displacement of the particles slowly increases in time and tend to a constant plateau after many cycles. The spherical harmonic $g_{2,-2}(r)$ reveal that there is a small accumulation of particles in the compressed quadrant and a depletion in the extension quadrant, the effect reversing upon flow reversal. Since the particles remain caged, this change of microstructure simply corresponds to a local redistribution of contacts and a mild distortion of the static cages, the overall microstructure being unchanged and reversible after a few oscillations.

At strain amplitudes larger than the yield strain, the particles can escape their position and rearrange over large distances. The cages are continuously advected and renewed by the oscillatory shear flow. The mean-square displacements of the particles in the three x-, y-, and z- directions increase linearly in time, which indicates that the shearing oscillatory motion along the x- direction induces a spatially isotropic shear-induced diffusive motion of the particles. The evolution of the microstructure along a cycle is controlled by the value of the shear stress σ relative to the yield stress σ_y. Along the portions of the cycle where $|\sigma|<\sigma_y$, i.e. where the instantaneous shear rate is small, both the pair correlation function $g(\mathbf{r})$ and the associated harmonic $g_{2,-2}(r)$ exhibit little changes with respect to the low amplitude case or the static situation. This suggests that the particles are locally trapped in their cages so that the material instantaneously responds like an elastic solid. However, contrary to what happens to the low amplitude case, the particles start to yield and rearrange once the yield stress is exceeded. The evolution of the microstructure is then characterized by an accumulation-depletion mechanism where particles accumulate in the compressive directions of the flow, where they are more compressed, and deplete in the extension directions where they are less compressed. To slide on top of one another and rearrange, particles have to overcome the barrier force at the point of maximum accumulation, where the particles are highly compressed. This mechanism is quite similar to that previously described and discussed in chapter 2 for steady shear flows. This analogies indicates that the portions of the cycles where $|\sigma| > \sigma_y$, i.e. where the instantaneous shear rate is large, correspond to macroscopic shear flow.

In conclusion, it is demonstrated that soft jammed suspensions sheared periodically at large amplitudes undergo a sequence of well-defined physical events: elastic caging in the low stress portions of the cycle, cage breaking near the yield stress, and flow rearrangements in the portions of the cycle where the stress exceeds the yield stress. This approach was recently proposed from the perspective of rheology by Rogers *et al.* (2011b). Here it is shows that this framework is also relevant with respect to the evolution of the microstructure. To finish, it is interesting to discuss the respective significance of the strain and stress amplitudes. The ratio of the strain amplitude to the yield strain, γ_0/γ_y, discriminates the low and medium/large amplitude regimes. For γ_0/γ_y <1, particle diffusivity is very low, the microstructure is similar to that at rest, and the mechanical response is in the linear regime. For γ_0/γ_y >1, particles diffuse through the suspension, the microstructure is distorted with respect to quiescent states, and the mechanical response is the non linear regime. It is worth noting that a single quantity, γ_0/γ_y, thus suffices to characterize the onset of yielding at the particle scale (local mobility), mesoscopic scale (microstructure), and macroscopic scale (rheology). Now when $\gamma_0/\gamma_y > 1$, the instantaneous value of the stress relative to the yield stress characterizes the state of the material, i.e. caged ($\sigma/\sigma_y < 1$), yielding ($\sigma/\sigma_y \sim 1$) or flowing ($\sigma/\sigma_y > 1$), along the cycle.

3.7 CONNECTING THE MICROSTRUCTURE TO MACROSCOPIC OSCILLATORY SHEAR RHEOLOGY

The elastic component of the shear stress can be computed from the $g_{2,-2}(r)$ spherical harmonic of the pair correlation function as described in section 2.5.3. The results are plotted in figure 3.10, where we observe the data fall onto the BL plots obtained numerically. This result is interesting since it shows that the total stress is dominated by the elastic contribution coming from the microstructure and the elastic repulsive potential, the viscous contribution being negligible. A similar conclusion was drawn previously for steady shear flows.

An alternative technique is now proposed based on the previous result that the material behavior along cycles can be decomposed in a sequence of processes, namely caging, yielding and flow. Starting from the regions of the LAOS cycle where the strain amplitude is near its extrema or the shear rate is zero, from section 3.6 above, it is known that the particles are instantaneously trapped in cages, the cages being only mildly distorted from their static configuration, so that the suspensions essentially respond elastically. Following Rogers *et al.* (2011b), we define the cage modulus as the local slope of the Bowditch-Lissajous plots at σ = 0:

$$G_c = \left.\frac{d\sigma}{d\gamma}\right|_{\sigma=0} \tag{3.4}$$

The results are plotted in figure 3.11 both for the simulations and the experiments. Again, good agreement is observed between the two sets of data. The other interesting result is that the cage modulus for increasing strain amplitudes remains constant and comparable to the storage modulus at low strain amplitudes. For comparison, the effective storage modulus *G* calculated over one cycle decreases when $\gamma_0/\gamma_y > 1$. The data in figure 3.11 are obtained for a frequency of $\eta_s\omega/E^* = 2\,\mathrm{x}10^{-8}$. Similar results are obtained at higher frequencies, the cage modulus being the low strain amplitude storage modulus for that frequency. This means that the lateral segments of the BL plots are the signatures of the cage elasticity and they can be used to determine the magnitude of the linear storage modulus in LAOS experiments.

Next, the portions of the cycles associated with post-yielding behavior ($\sigma > \sigma_y$) are analyzed. From section 3.6 above, it is known that the material flows in a way similar to that in steady shear flows. Thus the relationship between the shear rate and the stress can be used as an indicator of the flow curve. The data obtained for LAOS simulations and experiments at different strain amplitudes and frequencies altogether with the macroscopic flow curves computed and measured independently for steady shear flows (from Chapter 2) are plotted in figure 3.12. The data obtained from LAOS rheology are in good agreement with the steady shear flow curve as shown in figure 3.12. Thus, in the large stress region of the cycle the flow mechanism is similar to that in steady shear where the material exhibits a shear thinning viscoelastic behavior. The unifying effect of the shear rate amplitude on the particle scale diffusivities exemplified in figure 3.4 must lie at the root of this collapse of LAOS cycles onto to the flow curve. Figure 3.12 also shows that the experimental and simulation data are in good agreement which supports the validity of the micromechanical model.

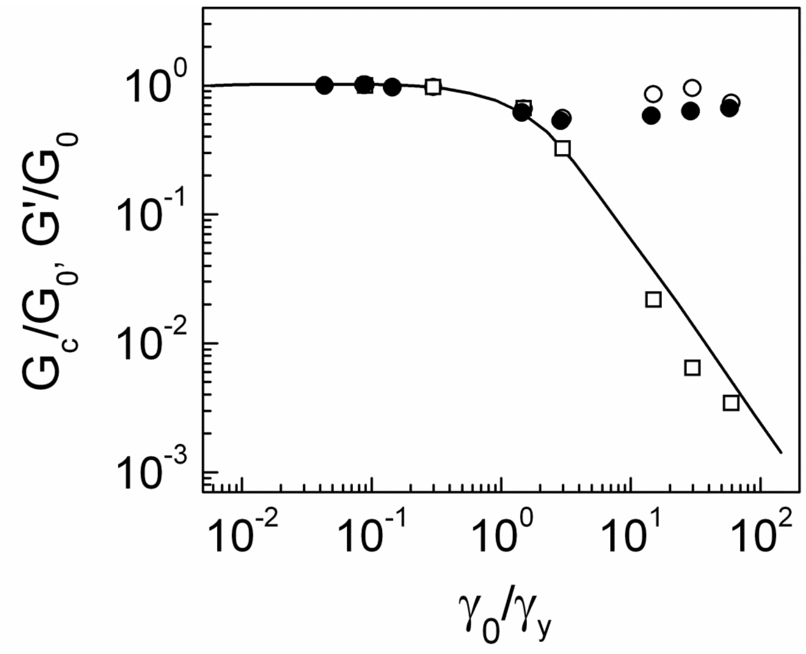

Figure 3.11: Cage modulus versus strain amplitude at $\eta_s\omega/E^* = 2\,\mathrm{x}10^{-8}$ from simulations (○) and experiments (●). For comparison the values of the low frequency storage modulus at low strain amplitude are also plotted (□: simulations; —: experiments).

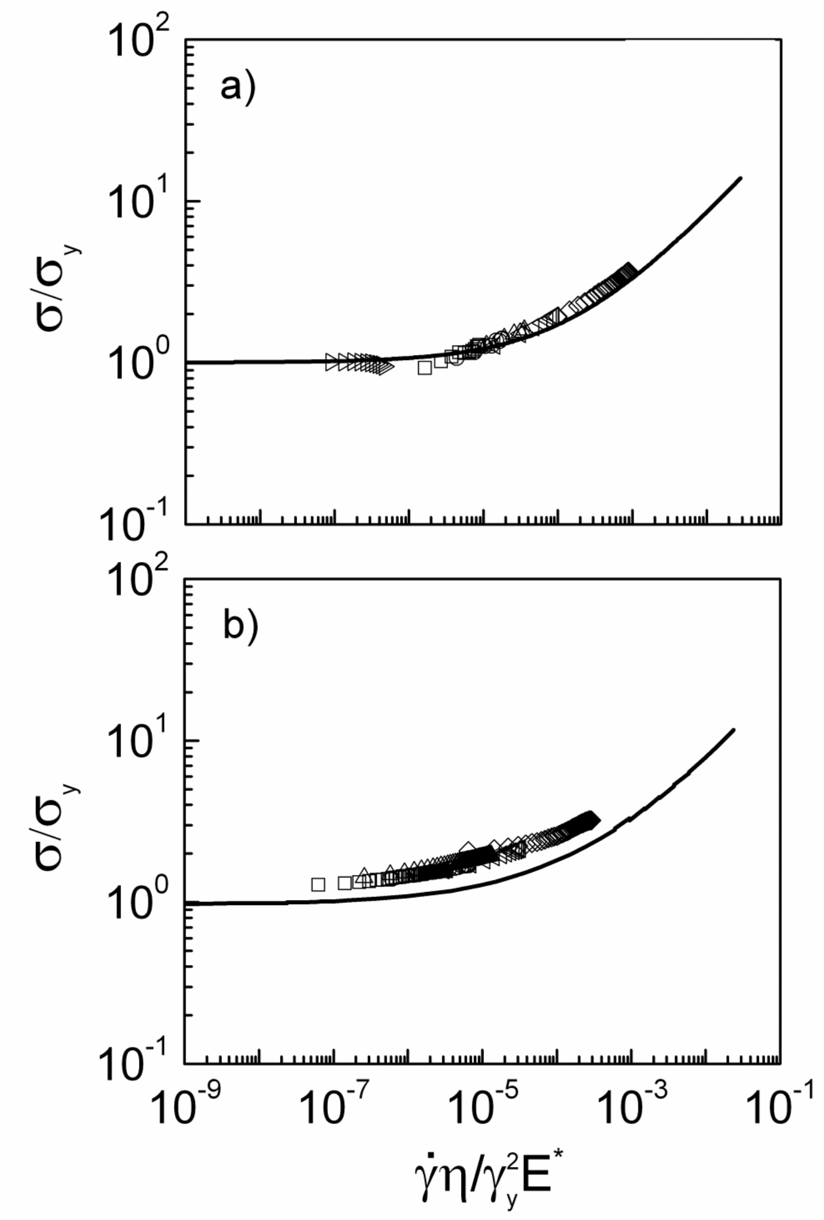

Figure 3.12: Flowing portions of the BL plots for different strain amplitudes and frequencies (symbols) collapsed and superimposed to the flow curve from steady shear (symbols). For the sake of comparison between experiments and simulations, the data are represented in the set of reduced coordinates exemplified in the constitutive equation derived in chapter 2 (equation 2.16).

3.8 SUMMARY AND CONCLUSIONS

Particle scale simulations at small, intermediate and large strain amplitudes are built using the micromechanical model proposed in the previous chapter to determine the microstructure, particle scale mobility and macroscopic rheology of soft particle glasses. The macroscopic properties computed from simulations quantitatively agree with experimental measurements on well-characterized microgel suspensions, which validate the model. At the mesoscopic scale, the evolution of the particle pair distribution during a cycle reveal the physical mechanisms responsible for yielding and flow and also leads to quantitative prediction of shear stress. At the local scale, the particles remain trapped inside their surrounding cage below the yield strain and yielding is associated with the onset of large scale rearrangements and shear-induced diffusion. This multiscale analysis thus highlights the distinct microscopic events that make these glasses exhibit a combination of solid like and liquid like behavior and also accounts for the generic linear and non-linear behavior of many materials made of soft particles [Ewoldt *et al.* (2010); Hyun *et al.* (2011)]. The study also elucidates the signature of yielding in the micro (cage breaking), meso (asymmetry in $g(\mathbf{r})$) and macro scales (appearance of non-linear stress-strain behavior).

The results concerning the local dynamics of particles echo a former investigation of yielding in concentrated emulsions [Hebraud *et al.* (1997)]. Using diffusive wave spectroscopy to measure the motion of droplets in concentrated emulsions subjected to oscillatory shear, they found that the particles reversibly retrace their trajectories at low strain amplitudes but undergo irreversible rearrangements above the yield strain. In these simulations, the plateauing of the mean square displacements at low strain amplitudes indeed indicate that particles don’t undergo large scale rearrangements, while the linear increase at large scale amplitudes shows that irreversible rearrangements take place.

Hebraud *et al*. were also able to detect that a finite fraction droplets systematically exhibit chaotic motion while the rest of the sample follows reversible trajectories over many periods. This surprising feature would deserve more attention in the simulations presented here, which will help to understand further the physical mechanisms associated with yielding.

The findings concerning the particle scale dynamics, also exhibit interesting analogies with the behavior of non-Brownian hard sphere suspensions in a viscous fluid, which are subjected to oscillatory shear motion [Corte *et al.* (2008); Pine *et al.* (2005)]. The physical origin of interparticle interactions is *a priori* significantly different in both systems: in non-Brownian suspensions, particles interact through long-range hydrodynamic interactions; in dense suspensions of soft particles, particles experience short-range elastohydrodynamic forces at particle contacts. It was found that irreversibility in non-Brownian viscous suspensions occurs above a well-defined critical strain amplitude above which particles diffuse over long distances and below which they organize after a few cycles into a configurations that remain undisturbed. This critical strain in non-Brownian hydrodynamic suspensions thus plays the role of the yield strain in the dense suspensions considered here. This analogy suggests some common underlying physics originating from the existence of many contact interactions, independently of the detailed nature of interparticle forces. In addition, the threshold between the reversible and irreversible states in hydrodynamic suspensions was recently described as a phase transition. It would be interesting to analyze and push forward this concept in dense suspensions of soft particles, where it may provide a new description of yielding as the onset of irreversibility and unpredictability. The micromechanical model and the simulations presented here can give access to crucial dynamical quantities like the fraction of active particles at any time, the equilibration time, and spatial correlations between particles and help to analyse our conjecture in more detail. Preliminary results show that the fraction of active particles, *i.e.,* those that move irreversibly, is indeed zero at small strain amplitudes and goes to unity beyond the yield strain.

At the mesoscopic level the statistical properties of the particle distribution provide unambiguous signatures of the onset of yielding. At very low strain amplitudes, the mesoscopic structure adjusts itself to the periodic shearing motion through localized relaxation of contacts, expressing that the deformation of soft particle suspensions is essentially non affine [Lacasse *et al.* (1996)]. At larger strain amplitudes, the occurrence of rearrangements is associated with a periodic modification of the pair distribution function, where particles accumulate upstream where they are more compressed and deplete downstream where they are less compressed. At high shear rates, concentrated hard sphere suspensions also exhibit an accumulation and depletion of particle density along the compression and extension axes, but the stress is linearly proportional to the shear rate and not quadratic as described here [Brady and Morris (1997); Crassous *et al.* (2008)]. These results indicate that the soft elastohydrodynamic interactions are central to the rheology of deformable particles. The accumulation-depletion mechanism is dominant along the portions of the oscillatory cycles where the stress exceeds the yield stress but negligible elsewhere. In particular the pair distribution function when the stress is zero resembles that at rest, indicating that particles are instantaneously trapped in cages. This shows that the behaviour of the material along one oscillation can be analyzed in terms of a sequence of microstructural events that repeat periodically.

At the macroscopic level the interpretation in terms of a succession of physical processes provide a way of mapping the information obtained from LAOS onto the results of several independent rheological tests like linear viscoelasticity measurements, strain sweep tests and steady shear flow both for simulations and experiments.

SUPPLEMENTAL MATERIAL 3.A: EXPERIMENTAL DETAILS

3.A.1 Microgel description and sample preparation

The suspensions used in the experimental study in Dr. Cloitre's lab were prepared from polyelectrolyte microgels in water. The microgels were synthesized by standard emulsion polymerization at low pH (≅ 2) using the two monomers ethyl acrylate (64 wt.%) and methacrylic acid (35 wt.%), and dicyclopentenyloxyethyl methacrylate (1 wt.%) as a crosslinker. In order to remove unreacted monomers, surfactants and other impurities present in the final emulsion, the polymer latexes obtained from the synthesis were cleaned by ultrafiltration. The solid content of the stock suspension was determined by thermogravimetry and samples were subsequently prepared by dilution with ultrapure water ($\eta_s = 9.8\times10^{-4}$ Pa.s). At low pH, the microgels are insoluble in water, and hence they are essentially hard particles. When sodium hydroxide (1M) is added to the microgel suspensions, the acidic units become ionized and the osmotic pressure of the counter ions provokes the swelling of the microgels. In a previous study they have shown that most of the counter-ions are trapped in the polymer network, so that the net charge carried by the particle is extremely low and electrostatic interactions are negligible [Cloitre *et al.* (2003a)]. In dilute suspensions, the swollen particles have a spherical shape with a hydrodynamic radius R (≅ 295 nm). Above $C_m = 1.5 \times 10^{-2}$ g/g, the suspensions exhibit solid-like properties with a yield stress. The concentration can be increased much further because microgels are able to deform and deswell osmotically. The concentration of the suspension investigated in the following is $C = 2\times10^{-2}$ g/g.

3.A.2 Rheological Measurements

Rheological measurements were carried out using an Anton Paar MCR 501 rheometer mounted with a cone and Peltier plate geometry with a diameter of 50 mm, a

2° angle, and a truncation of 48 μm. The shearing surfaces were sandblasted to provide a surface roughness of 2-4 μm, which prevented the occurrence of slip. A solvent trap was placed around the sample to minimize water evaporation, the interior atmosphere of the trap being saturated using a few droplets of distilled water. All measurements were made at 20.0 +- 0.1°C. Prior to any measurement, the suspensions were presheared at a shear rate 500 s^{-1} for about 30 s in order to erase their mechanical history. Then they were kept at rest for a waiting time of about 4 hours, which is sufficiently long to make aging effects negligible.

Several types of rheological tests were performed by them. Steady shear experiments, where the stress σ was measured as a function of the applied shear rate $\dot{\gamma}$, were performed by applying constant shear rates varying from 10^3 to 10^{-4} s^{-1} and recording the stress until steady state was reached. Oscillatory frequency sweeps were used to measure the storage modulus G' and loss modulus G'' as function of the angular frequency ω ($10^{-2} < \omega < 10^2$ rad/s) at small strain amplitudes in the linear viscoelastic regime ($\gamma_0 = 6 \times 10^{-3}$). The storage and loss moduli show the characteristic variations exhibited by many soft materials, *i.e.*, a nearly constant plateau in $G'(\omega)$ and a much lower $G''(\omega)$ with a small minimum around a frequency ω_m. The elastic modulus of the suspension G_0 was defined as the value of $G'(\omega)$ at ω_m. Large amplitude oscillatory shear measurements were performed in strain-controlled mode using the expert mode package provided by the Anton Paar rheometer software. The strain and stress signals were recorded at a sampling rate of 256 data points per oscillation cycle. The strain amplitude was varied from 3×10^{-3} to 10 and the frequency was in the range between 0.3 rad/s and 15 rad/s.

3.A.3 Material Properties

In order to compare simulations and experimental results, the material properties of their suspensions had to be characterized. The storage modulus G_0 was determined from oscillatory frequency sweep tests as explained in the previous section. The yield stress σ_y was obtained from the variations of the stress in strain amplitude sweep tests at low frequencies. The yield strain γ_y was obtained from the relation $\sigma_y = G_0\ \gamma_y$. An important parameter involved in the micromechanical model presented above is the particle contact modulus E^*, which is unknown a priori and cannot be easily measured for submicron particles. To circumvent this difficulty, the following method proposed in Chapter 2, section 2.6 is used. Steady shear experiments were performed to measure the flow curve $\sigma(\dot{\gamma})$ of the suspension. It reaches a constant value at low shear rates, which corresponds to the yield stress measured in oscillatory tests. To determine E^*, the experimental flow curve was fitted to the theoretical expression predicted in section 2.5.4: $\sigma/\sigma_y = 1 + \mathrm{k}\left(\dot{\gamma}\eta_s/\gamma_y^2 \mathrm{E}^*\right)^{1/2}$, where k ≅ 80 is a numerical coefficient deduced from simulations. Since $\sigma_{y,}$ $\gamma_{y,}$ and η are known independently, E^* is the only free parameter. The experimental and fitted flow curves are shown in figure 3.A.1 and the resulting value of E^* is reported in Table 3.A.1. In the inset of figure 3.A.1, by comparing the experimental value of G_0/E^* to the theoretical variations of G_0/E^* with volume fraction [Seth *et al.* (2006)], they estimate the effective volume fraction ϕ, which is of the order of 0.80. This justifies that the simulations reported in the flowing were performed at $\phi = 0.80$. The values of the elastic modulus, yield strain and yield stresses measured experimentally and obtained from simulations are summarized in Table 3.A.1.

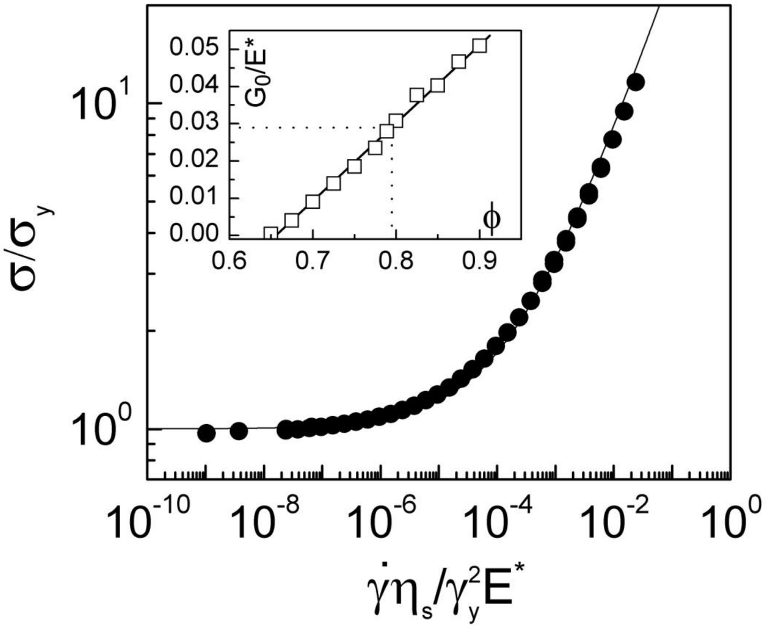

Figure 3.A.1: Theoretical flow curve (——) given by $\sigma/\sigma_y = 1 + k\left(\dot{\gamma}\eta_s/\gamma_y^2E^*\right)^{1/2}$ and experimental flow curve (●) in the same set of coordinates for the microgel suspension at c = 2 wt% with E^* = 18 kPa (σ_y = 35 Pa, γ_y = 0.067, G_0 = 510 Pa, and $\eta_s = 9.8\times10^{-4}$ mPa.s). The inset shows the variations of G_0/E^* versus ϕ computed from simulations from which the effective volume fraction of the experimental suspension is determined.

Table 3.A.1: Material properties of the experimental and simulated suspensions.

	E*	γ_y	σ_y/E^*	G_0/E^*
c = 2 wt. %	18 ± 1 kPa	0.067	1.94×10^{-3}	0.028
$\phi = 0.80$		0.03355	9.43×10^{-4}	0.0281

The storage modulus and yield stress of the experimental microgel suspensions are G_0 = 510 Pa and σ_y =35 Pa.

SUPPLEMENTAL MATERIAL 3.B: COMPARISON OF DIFFUSIVITIES FROM STEADY AND OSCILLATORY SHEAR

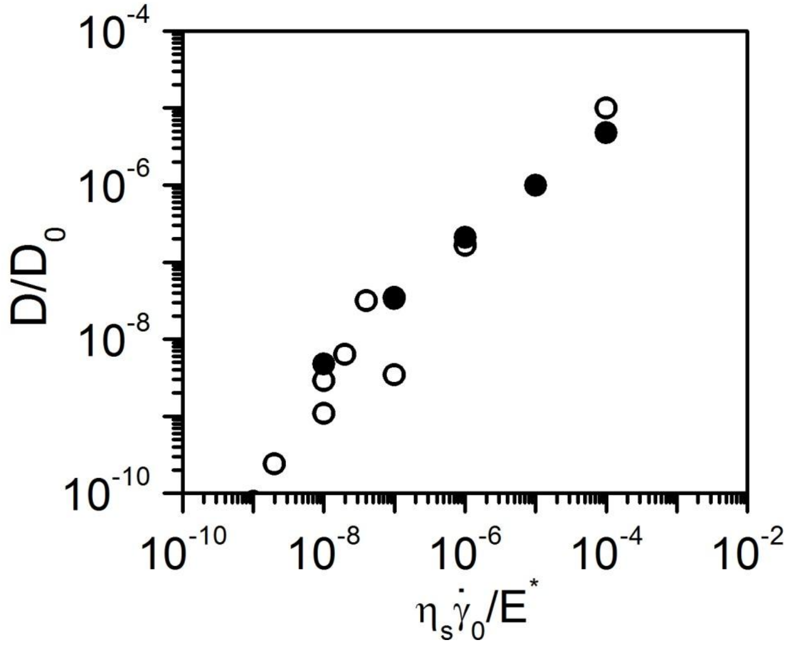

Figure 3.B.1: Comparison of diffusivity data from steady (●) and oscillatory shear (○) simulation data. Note that the average D was computed for steady shear from the *y*- and *z*- direction diffusivities only.

SUPPLEMENTAL MATERIAL 3.C: BOWDITCH-LISSAJOUS PLOTS – EFFECT OF FREQUENCY

3.C.1 Frequency effect at small strain amplitudes

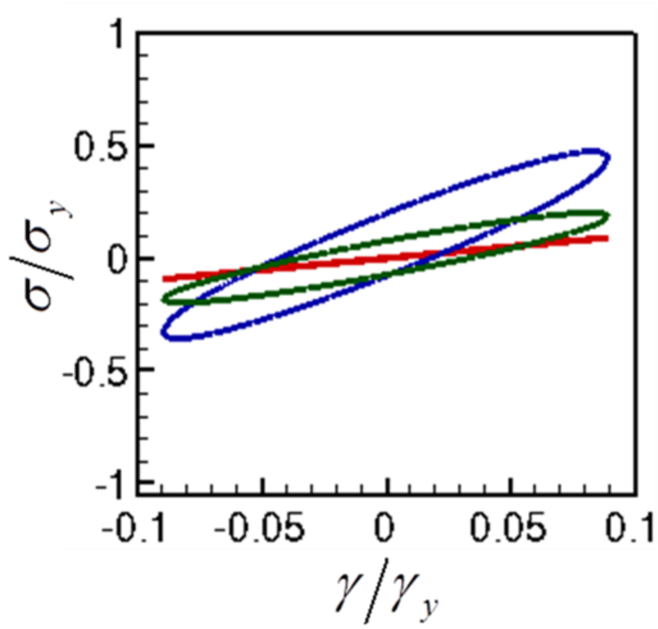

Figure 3.C.1: Effect of frequency in the linear regime from simulations at γ_0/γ_y =0.09. $\eta_s\omega/E^* = 2\,\text{x}10^{-8}$ (red), 10^{-4} (green), $2\,\text{x}10^{-3}$ (blue) .

3.C.2 Frequency effect at large strain amplitudes

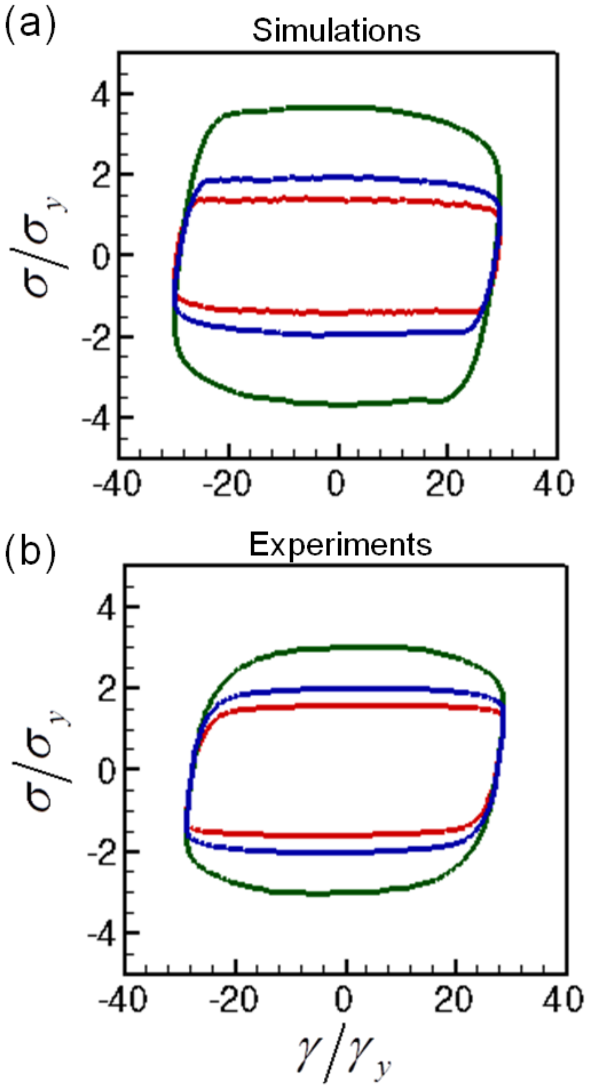

Figure 3.C.2: Effect of frequency in the flow regime at γ_0/γ_y=30. From inside to outside: $\eta_s\omega/E^* = 2\,\text{x}10^{-8}, 10^{-7}, 10^{-6}$.

Supplemental Material 3.D: Simulation Data Tables

Table 3.D.1: Particle scale diffusivity for different strain amplitudes at $\eta_s \omega / E^* = 2\,\mathrm{x}10^{-8}$

γ_0/γ_y	D_x/D_0	D_y/D_0	D_z/D_0	D/D_0
59.6	7.32E-08	1.10E-08	9.66E-09	3.13E-08
29.8	8.09E-09	5.93E-09	4.87E-09	6.30E-09
14.9	3.31E-09	2.83E-09	2.58E-09	2.91E-09
2.98	2.57E-10	2.39E-10	2.28E-10	2.41E-10
1.49	9.16E-11	7.17E-11	7.05E-11	7.79E-11
0.298	3.87E-11	3.68E-11	3.83E-11	3.80E-11
0.0894	3.94E-11	3.99E-11	4.00E-11	3.98E-11

Table 3.D.2: Particle scale diffusivity for different frequencies

γ_0/γ_y	$\eta_s\omega/E^*$	D/D_0
29.80626	2.00E-08	6.30E-09
29.80626	1.00E-07	3.45E-08
29.80626	1.00E-06	1.64E-07
29.80626	1.00E-04	9.99E-06
29.80626	0.002	1.84E-04
2.98	2.00E-08	2.41E-10
2.98	1.00E-07	1.08E-09
2.98	1.00E-06	3.45E-09

Table 3.D.3: Viscoelastic moduli at γ_0/γ_y = 0.09 - Frequency sweep

$\eta_s\omega/E^*$	G'/G_0	G''/G_0
2.00E-08	1	0.01861
1.00E-06	1.11385	0.11833
1.00E-05	1.3103	0.37771
1.00E-04	2.02622	0.81774
0.002	4.22174	1.53754

Table 3.D.4: Viscoelastic moduli, cage modulus and maximum stress at $\eta_s\omega/E^* = 2\text{x}10^{-8}$ - Strain sweep

γ_0/γ_y	G'/G_0	G''/G_0	σ_0/σ_y
59.61293	0.00344	0.03089	1.61843
29.80646	0.00642	0.05462	1.43707
14.90323	0.02183	0.09571	1.2918
2.98065	0.32454	0.24622	1.1624
1.49032	0.66756	0.11288	1.01037
0.29806	0.97107	0.03536	0.25438
0.08942	1	0.01861	0.09353

Chapter 4: Stress Relaxation on Flow Cessation

4.1 INTRODUCTION

Many materials with countless applications in science and industry are processed in the liquid state where they can be easily manipulated and shaped and are subsequently quenched to solid state. Solidification can be achieved through a temperature drop in thermoplastic polymers and metals, interruption of flow when shaping ceramic pastes and latex coatings, or chemical reactions in the case of gels or thermosets. As they solidify, such materials generally do not relax to their structural and mechanical equilibrium instantaneously and some of the stress created during the initial flow remains trapped for long periods of time, giving rise to a net internal or residual stress. The presence of internal stresses has been observed in materials as diverse as polymers films [Damman *et al.* (2007)], bulk polymers [Freidin and Sholokhova (1966)], metallic glasses [Zhang *et al.* (2006)], supercooled liquids [Abraham and Harrowell (2012)], hard sphere glasses [Ballauff *et al.* (2013)], laponite suspensions [Negi and Osuji (2010)], colloidal gels [Negi and Osuji (2009)], vesicle suspensions [Ramos and Cipelletti (2001)] and cytoskeletal networks [Lieleg *et al.* (2011)].

The control of internal stresses has stimulated significant research in the field of inorganic and metallic glasses as a way to design unique materials with improved mechanical properties [Green *et al.* (1999); Zhang *et al.* (2006)]. In disordered soft materials, local stress relaxations have been invoked to explain the unusual dynamics observed during aging [Lieleg *et al.* (2011); Negi and Osuji (2009); Negi and Osuji (2010); Ramos and Cipelletti (2001)] or the spontaneous motion that sometimes occurs without forced flow [Chung *et al.* (2006); Cipelletti *et al.* (2000); Cloitre *et al.* (2000); Ramos and Cipelletti (2001); Ramos and Cipelletti (2005); Wang *et al.* (2006)]. Little is known about the physical origin of these internal stresses and the relation between their amplitude and the preparation conditions. Part of the difficulty comes from the fact that the microstructural origin of the frozen-in internal stresses and its relaxation is quite elusive; most attempts to correlate the macroscopic internal stress to microscopic mechanisms in colloidal glasses having been relatively unsuccessful in the past [Cianci *et al.* (2006)]. A recent investigation has identified the volume fraction and the shear rate during the initial flow as the key parameters that control internal stress in hard sphere glasses [Ballauff *et al.* (2013)]. Nonetheless, important questions concerning the generality of this description and the connection between internal stress and particle scale mechanisms remain open.

Soft particle glasses are highly concentrated suspensions of soft and deformable particles which exhibit solid-like properties at low stresses and begin to flow at high stresses. The constituent particles interact through elastic contacts, which make these materials different from hard sphere glasses. Their use as rheological additives in many applications including processing of food, cosmetics, drilling muds, paints and solid inks require the materials to be quenched to a solid state by flow cessation during processing during which they are known to develop internal stresses. The rheological properties may be different depending on the quenching conditions that determine the internal stresses. Here, particle scale simulations and well defined rheological experiments on microgel glasses where the constituent properties are systematically varied are combined to understand the stress relaxation behavior on flow cessation in soft particle glasses. Rheological experiments are performed to investigate the fate of the shear stresses inside the glass after flow cessation. The existence of trapped internal stresses was observed and their long time fate was investigated. The microstructural changes and mechanisms associated with internal stress accumulation and relaxation were determined through particle scale simulations.

The rest of this chapter is organized as follows. The materials used in the experiments and the experimental methodology are presented in section 4.2. The simulation technique used in the particle scale simulations is presented in section 4.3. The trapped internal stresses observed on flow cessation for concentrated microgel samples with systematically varied constituent properties and particle scale simulations is presented in section 4.4. The microstructural changes during the quick initial relaxation and the microscopic mechanisms associated with the internal stress accumulation is determined from particle scale simulations and is presented in section 4.5. The two regimes of relaxation, a rapid initial relaxation leading to the trapped internal stress and another slow long term relaxation are discussed in section 4.6 and 4.7, respectively.

4.2 EXPERIMENTAL MATERIALS AND METHODS

4.2.1 Microgel Description and Sample Preparation

The microgels were synthesized by standard emulsion polymerization at low pH using the two monomers ethyl acrylate (EA) and methacrylic acid (MAA), and dicyclopentenyloxyethyl methacrylate as a crosslinker. The concentration of crosslinker (C_{clink}) determines the crosslink density of particles. Stock suspensions synthesized with 1 and 2% crosslinker were used to obtain microgel particles with two different particle contact moduli (E^*). The stock suspension with 1% crosslinker contained the monomers EA and MAA in the ratio 65/35 and that with 2% crosslinker in the ratio 64.5/34.5. In order to remove unreacted monomers, surfactants and other impurities present in the final emulsion, the polymer latexes obtained from the synthesis were cleaned by ultrafiltration. The solid content of the stock suspension was determined by thermogravimetry and samples were subsequently prepared by dilution with ultrapure water. The microgels were swollen with water or water-glycerol mixtures. The viscosity of the suspending medium η_s was varied systematically by varying the ratio of water and glycerol in the water glycerol mixtures. The volume fraction ϕ of the suspension was varied by varying the concentration of polymer (C) in the sample. The flow curves, frequency sweeps (at 0.5% strain amplitude) and strain sweeps (at 1 rad/s) are presented in figures 4.1 and 4.2. The flow curves are fitted to the Herschel Bulkley form: $\sigma = \sigma_y + k\dot{\gamma}^n$. The properties of the samples used in this study are presented in table 4.1. E^* and ϕ of the samples were determined using a procedure previously described in Chapter 2 and 3.

Table 4.1: Sample properties

C (%)	**ϕ**	**C_{clink} (%)**	**E^* (kPa)**	**Solvent (ratio)**	**η_s (mPa.s)**	**σ_y (Pa)**	**k**	**n**	**G_0 (Pa)**
2	0.82	1	18	water	1	44.98	12.92	0.44	651
2.6	0.94	1	18	water	1	89.31	17.51	0.47	1037
2	0.81	1	18	water-glycerol (53/47)	5	43.24	20.06	0.49	621
2	0.8	1	18	water-glycerol (36/64)	14	38.88	27.13	0.51	541
2	0.77	1	18	water-glycerol (23/77)	40	27.70	38.07	0.52	389
3	0.73	2	42	water	1	39.21	9.53	0.43	656
3.8	0.84	2	42	water	1	109.78	19.33	0.43	1649
4	0.88	2	42	water	1	124.15	25.24	0.40	1965

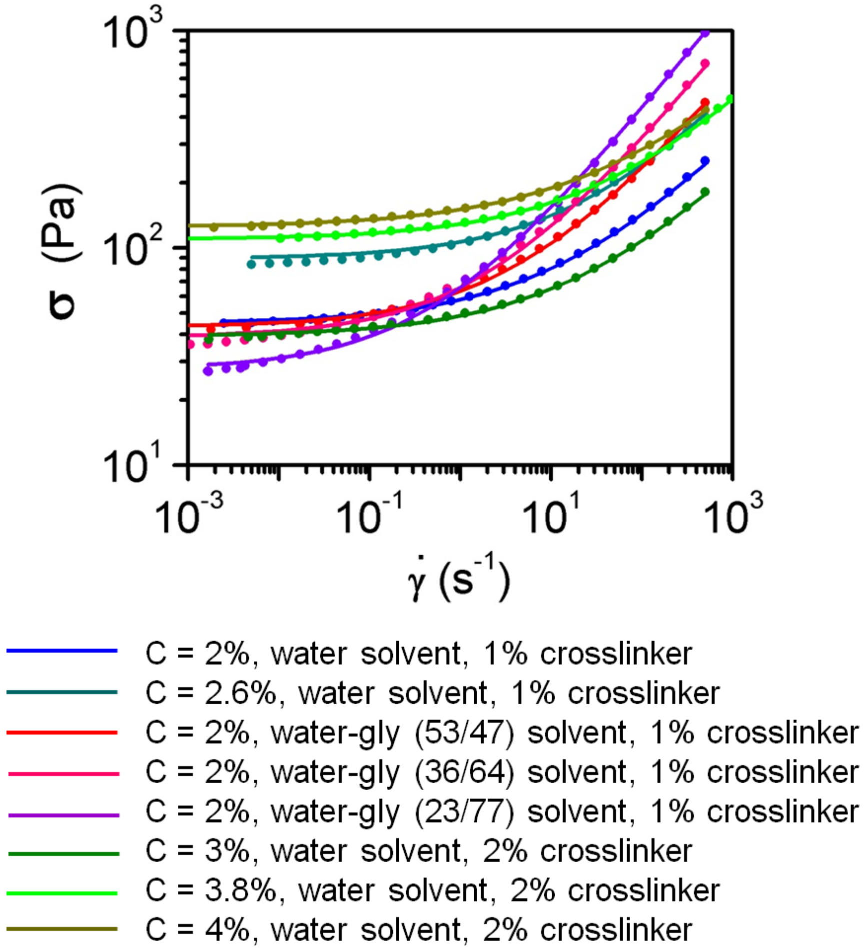

Figure 4.1: Flow curves (symbols) and Hershel-Bulkley fits (lines) of different samples used.

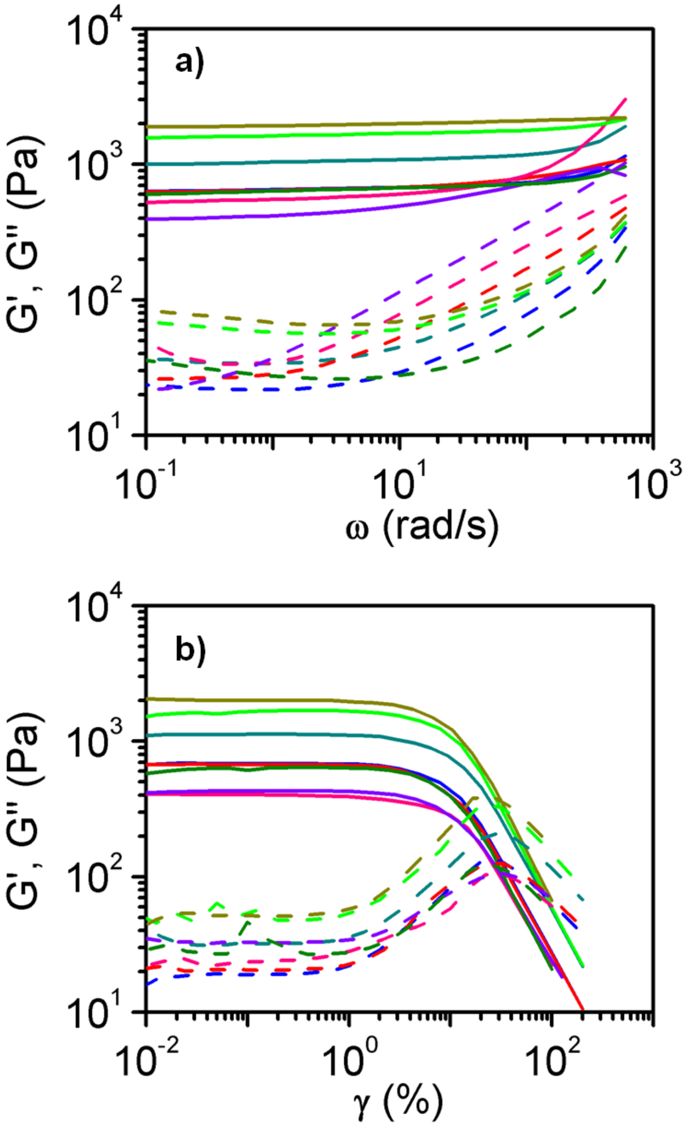

Figure 4.2: Viscoelastic moduli G' (solid lines) and G'' (dashed lines) of samples used. a) Frequency sweep at 0.5% strain amplitude. b) Strain sweep at 1 rad/s frequency. Colors correspond to the same definition as in figure 4.1.

4.2.2 Rheological Measurements

Rheological measurements were carried out using an Anton Paar MCR 501 rheometer mounted with a cone and Peltier plate geometry with a diameter of 50 mm, a 2° angle, and a truncation of 48 μm. The shearing surfaces were sandblasted to provide a surface roughness of 2-4 μm, which prevented the occurrence of slip. In the experimental conditions used here, microgel suspensions flow homogeneously without any kind of strain localization including slip, shear-banding or fracture [Seth *et al.* (2012)]. A solvent trap was placed around the sample to minimize water evaporation, the interior atmosphere of the trap being saturated using a few droplets of distilled water. The gap was sealed with silicone oil one minute after flow cessation for the long term relaxation experiments (10^5 s) to further reduce evaporation losses. All measurements were made at 20.0 +- 0.1°C. The yield stress σ_y of each sample is first determined using different well established protocols – creep measurements, oscillatory strain sweeps, and steady shear experiments – all determinations agreeing within the experimental accuracy. Relaxation experiments are performed by preshearing the sample at a constant stress greater than the yield stress for 30 s, setting the shear rate to zero at the end of preshear, and recording the shear stress.

4.3 SIMULATION TECHNIQUE

Three dimensional packings of 10,000 periodically replicated non-Brownian elastic spheres (contact modulus: E^*) at a volume fraction of 0.8 in a solvent of viscosity η_s was built as described in section 2.3 with a 10% polydispersity. The particles are subjected to pairwise interactions of two types: repulsive elastic forces described by generalized Hertzian potentials and solvent mediated elastohydrodynamic forces as described in the micromechanical model in section 2.2. The governing equation is given below for easy reference.

$$\frac{\mathrm{d}\tilde{\mathbf{x}}_\alpha}{\mathrm{d}\tilde{t}} = \tilde{\mathbf{u}}_\alpha^\infty + \frac{f_r(\phi)}{6\pi\tilde{R}_\alpha}\left[\frac{4}{3}C\sum_\beta \varepsilon_{\alpha\beta}^n \tilde{R}_c^2 \mathbf{n}_\perp - \sum_\beta \left(C\tilde{u}_{\alpha\beta,||}\tilde{R}_c^3\right)^{1/2} \varepsilon_{\alpha\beta}^{(2n+1)/4} \mathbf{n}_{||}\right] \tag{4.1}$$

The symbols here have the same meaning as before. The suspension was first subjected to a steady shear in the *x*-direction during the preshear step for five shear strain units to ensure that steady state was reached. $\tilde{\mathbf{u}}_\alpha^\infty = \left(\dot{\gamma}\eta_s / E^*\right) y\mathbf{e}_\mathrm{x}$ represents the velocity field due to applied preshear. The packings were then allowed to relax at zero shear rates where $\tilde{\mathbf{u}}_\alpha^\infty = 0$. Periodic boundary conditions were applied in the *x*- and *z*- directions and Lee-Edwards boundary condition was implemented in *y*- direction. During the relaxation step the Lee-Edwards boundary condition in the *y*- direction also reduces to a simple periodic boundary condition. These coupled equations of motion were integrated numerically to determine the evolution of the spatial position and velocity of each particle. The open source code LAMMPS [Plimpton (1995)] was used to perform the simulations as before. The results were averaged over five different initial configurations.

The microstructure of suspensions was characterized through the dynamic pair distribution function $g(\mathbf{r})$. The angular distortion of the microstructure was quantified by expanding the pair distribution function using spherical harmonics: $g(\mathbf{r}) = g(r) + \sum_{l=1}^{\infty}\sum_{m=-l}^{l} g_{lm}(r) Y_{lm}(\theta,\phi)$. $g_{2,-2}(r)$ is the coefficient of the harmonic $Y_{2,-2}(\theta,\phi) = \frac{1}{4}\sqrt{\frac{15}{\pi}}\left(\sin 2\theta \sin^2\phi\right)$ and represents the angular asymmetry due to accumulation-depletion of particles between the compression and extension axes during flow.

4.4 TRAPPED INTERNAL STRESSES ON FLOW CESSATION

4.4.1 Experimental results

Figure 4.3 shows typical variations of the stress on flow cessation in concentrated microgel samples made with different constituent properties. In all cases the stress is constant during preshear and drops rapidly but does not vanish on flow cessation, indicating that stresses remain trapped in the material. The stress relaxation thus occurs in two steps, a rapid initial decay after which there are trapped internal stresses which then decay slowly with time. It is important to note that the internal stress is larger for smaller preshear stress as previously found in other materials [Ballauff *et al.* (2013); Negi and Osuji (2010)]. The ability of the material to relax its stresses decreases when the preshear stress is close to the yield stress. For a given preshear stress the internal stress that gets trapped on flow cessation depends on the constituent properties of the sample as illustrated in figure 4.4a. The internal stress sensitively depends on volume fraction and particle modulus for a given preshear stress; increasing the particle elasticity and/or volume fraction results in a significantly larger internal stress on flow cessation, while changing the viscosity has little effect. Also note that the steady state shear stress for a given shear rate will depend on all the above parameters. The internal stress is determined from these data by linear extrapolation of the stress measured over a short time interval (< 50 s) to the instant of flow cessation. The experiment was then conducted with samples made of varying polymer concentration, solvent viscosity and particle crosslinking to characterize the internal stresses trapped on flow cessation. The internal stress in different samples is plotted as a function of preshear stress in figure 4.4b.

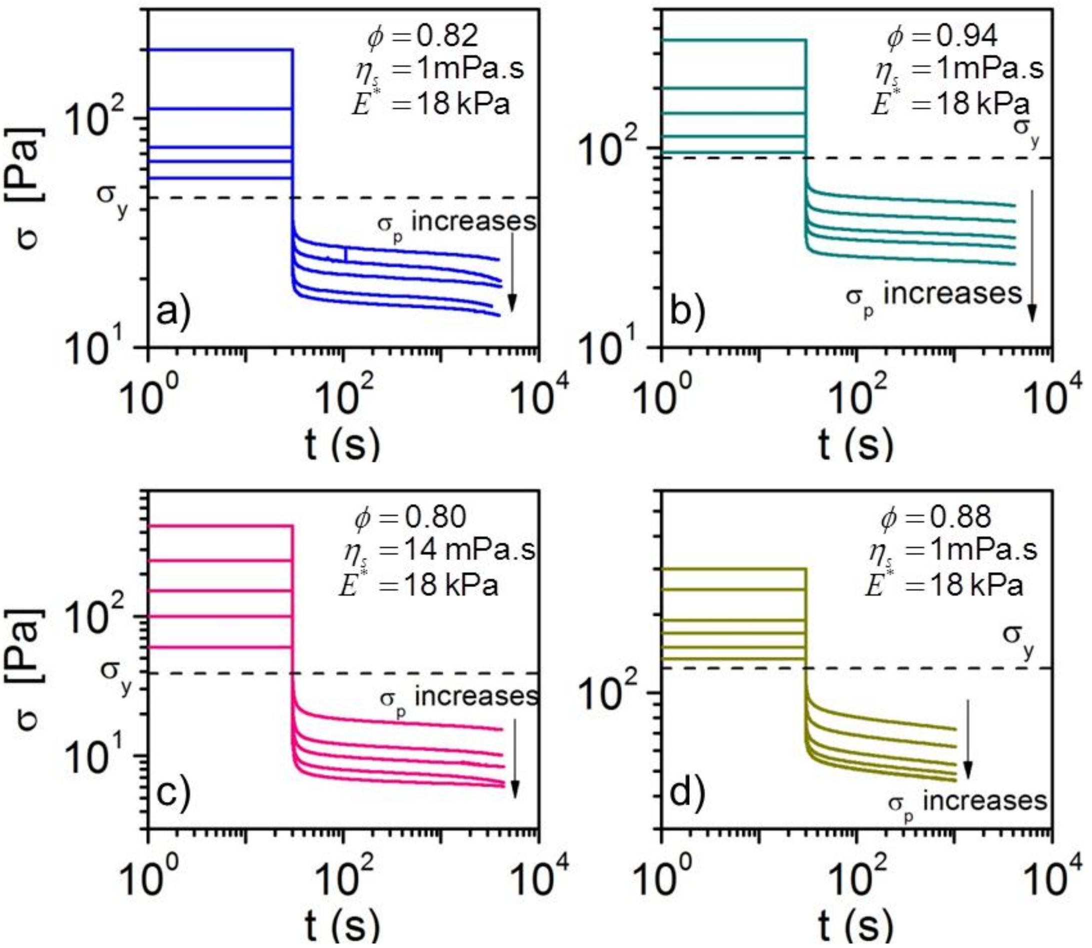

Figure 4.3: Stress relaxation on flow cessation in concentrated microgels with different constituent properties.

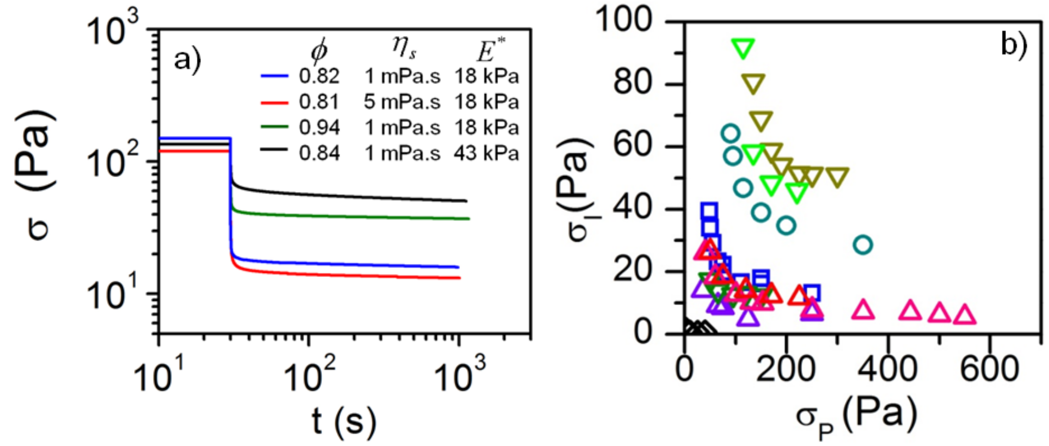

Figure 4.4: Variation of trapped internal stresses on flow cessation with the microgel constituent properties in experiments. Data, varying the concentration: C = 1.3% (◇), 2 wt% (□), 2.6 wt% (○) with η_s =1 mPa.s and E* = 18 kPa; the solvent viscosity η_s = 5 (△), 14 (△) and 40 mPa.s (△) with C = 2 wt% and E* = 18 kPa; the particle softness: E* = 42 kPa with C = 3 (▽), 3.8 (▽) and 4 (▽) wt% and η_s = 1 mPa.s.

4.4.2 Simulation results and comparison with experiments

In order to elucidate the microstructural origin of the internal stress, numerical simulations were performed based on the three-dimensional micromechanical particle scale model described before. Figure 4.5a shows results of simulations for five preshearing conditions. Stress is scaled by the particle contact modulus E^* and time by the microscopic time $\tau_0 = \eta_s / E^*$. For the parameters relevant to the experiments ($\eta_s \approx 10^{-3}$ Pa.s; $E^* \approx 10^4$ Pa), τ_0 is of the order of 10^{-7} s. The simulations capture the initial preshear, the rapid short time relaxation of the stress and the beginnings of the long time relaxation. In the following the internal stress is taken to be the value of the stress at the last instant computed and is presented in figure 4.5b as a function of the preshear stress. The computational time required to simulate out to the longest times accessible in experiments is prohibitive. Nevertheless the simulations successfully capture the important trends already described for experiments: upon flow cessation, the stress drops and the closer is the preshear stress to the yield stress, the lesser the stress relaxes. A direct comparison of simulations and experiments is presented in figure 4.6.

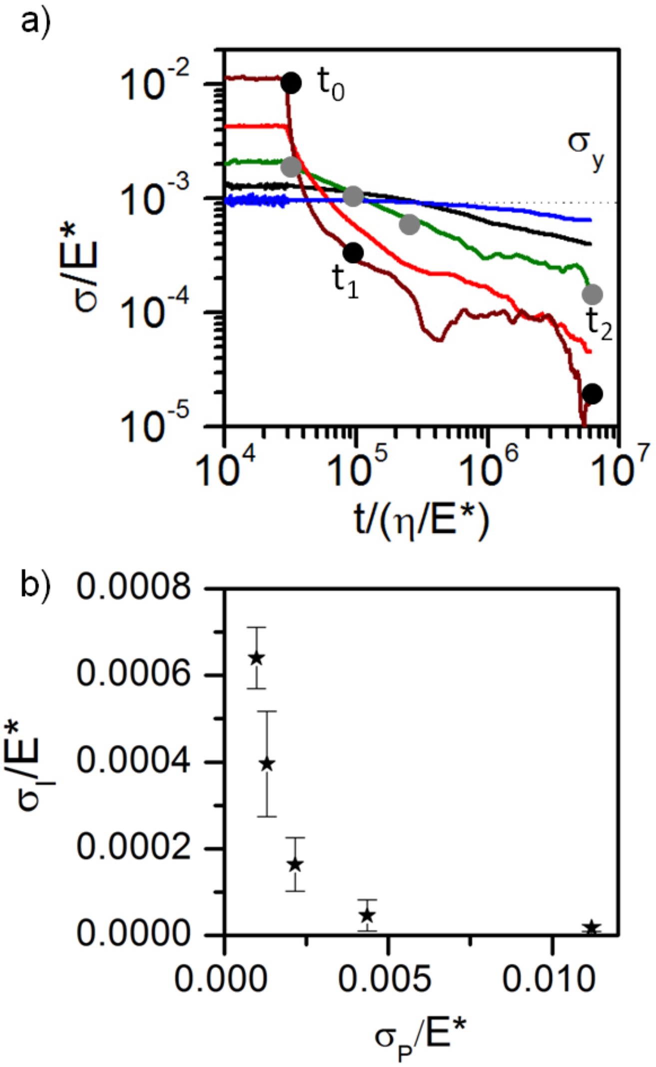

Figure 4.5: Stress relaxation on flow cessation (a) and variation of trapped internal stresses in simulations of soft particle glasses of volume fraction 0.8. The instant of flow cessation in (a) has been shifted for better comparison with different preshear conditions

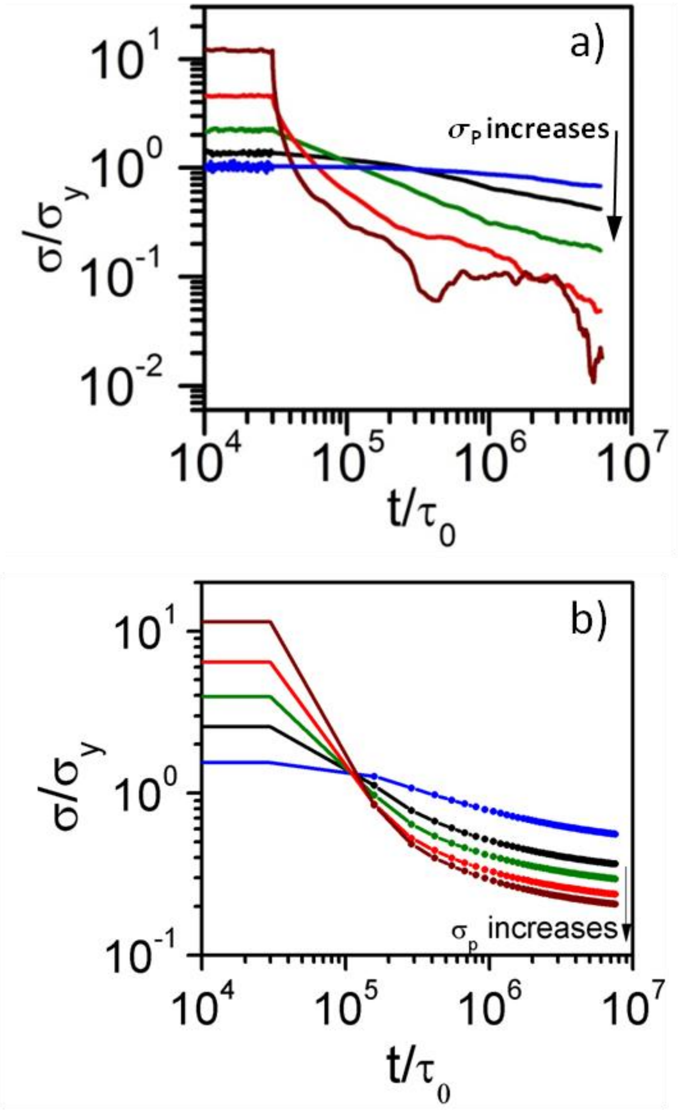

Figure 4.6: Comparison of stress relaxation on flow cessation in simulations (a) and experiments (b) for a volume fraction of 0.8. The experiments correspond to the sample presented in figure 4.3c. The data points collected from experiments after flow cessation is represented by dots. The instant of flow cessation is shifted in (a) and (b) for better comparison

4.4.3 Generalized scaling for the trapped internal stresses

A universal scaling for the internal stress σ_I with the preshear stress σ_P in soft particle glasses with results from experiments on different samples is presented in figure 4.7. The internal stress here is scaled by the yield stress σ_y. The simulation results are shown using filled stars (★) and they agree reasonably well with the experimental data. The flow curve for soft particle glasses follows the constitutive equation $\sigma/\sigma_y = 1 + K\left(\eta_s\dot{\gamma}/E^*\gamma_y^2\right)^{1/2}$ [Seth *et al.* (2011)], where γ_y is the yield strain and E^* is the particle contact modulus. From the flow curve, $\left(\sigma - \sigma_y\right)/\sigma_y = K\left(\eta_s\dot{\gamma}/E^*\gamma_y^2\right)^{1/2}$ is the stress accumulated in the material due to an imposed shear rate $\dot{\gamma}$. The trapped internal stress in soft glasses with different constituent properties collapses to a single universal curve when the mechanical history is represented by the elastic stress accumulated in the material due to the flow. A comparison of this scaled data to the raw data in figure 4.4b further supports the efficiency of the scaling but the microscopic origins of the two step relaxation, internal stresses and their scaling remained an open question. The microstructural changes during stress relaxation on flow cessation were probed using the particle scale simulations to further answer these questions.

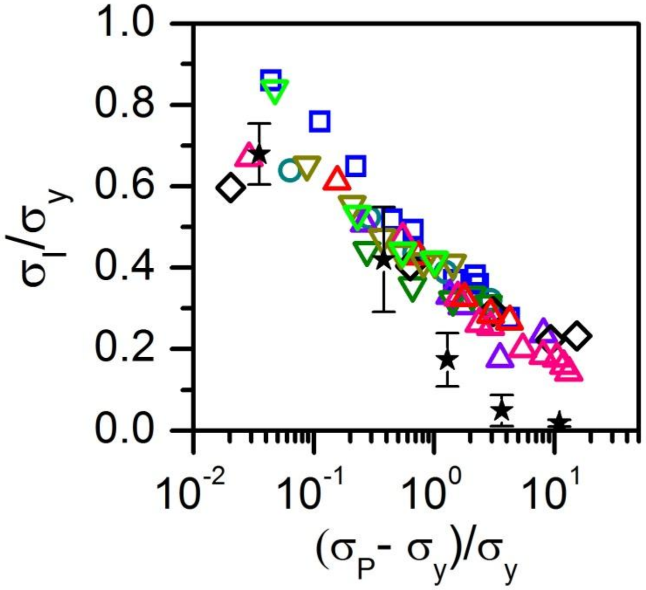

Figure 4.7: Universal scaling for the effect of preshear stress σ_P on the internal stress σ_I on flow cessation with the yield stress σ_y. The open symbols represent experimental data with microgels of different constituent properties. Data, varying the concentration: C = 1.3% (◇), 2 wt% (□), 2.6 wt% (○) with η_s =1 mPa.s and E^* = 18 kPa; the solvent viscosity η_s = 5 (△), 14 (△) and 40 mPa.s (△) with C = 2 wt% and E^* = 18 kPa; the particle softness: E^* = 42 kPa with C = 3 (▽), 3.8 (▽) and 4 (▽) wt% and η_s = 1 mPa.s. Simulation data (★).

4.5 MICROSTRUCTURAL CHANGES ON FLOW CESSATION

4.5.1 Microscopic mechanism of relaxation on flow cessation

Figure 4.8a shows the time variation of the particle mean square displacements after preshear ($t > t_0$). There are three important observations to note here. Firstly, the mean square displacements are quadratic in time, identifying ballistic motion as the particle scale mechanism associated with the initial stress relaxation that takes place on flow cessation. The characteristic velocity of ballistic motion, i.e. the intercepts of the curves with the vertical axis, is the largest for the largest preshear, where stress relaxation is the fastest and internal stress the smallest. Experimentally, ballistic motion has been observed in the relaxation of depletion gels [Chung *et al.* (2006)] and multilamellar vesicle assemblies [Ramos and Cipelletti (2005)]. Secondly, after the initial ballistic motion all the curves tend to a nearly constant plateau, the value of which is less than one particle radius for all preshearing stresses, indicating that the particles are instantaneously trapped in cages and that rearrangements associated with stress relaxation are local contact rearrangements. These two observations indicate that there are two distinct microscopic mechanisms at work which gives rise to the two step macroscopic stress relaxation on flow cessation: an initial rapid relaxation driven by ballistic particle motion and a slow decay at long times due to slow local particle facet rearrangements. Thirdly the mean squared displacements are isotropic in *x*-, *y*- and *z*- directions as shown by figures 4.8c-d. This might be due to isotropic nature of shear induced diffusivities identified earlier during the study of oscillatory shear rheology of these soft particle glasses in chapter 3.

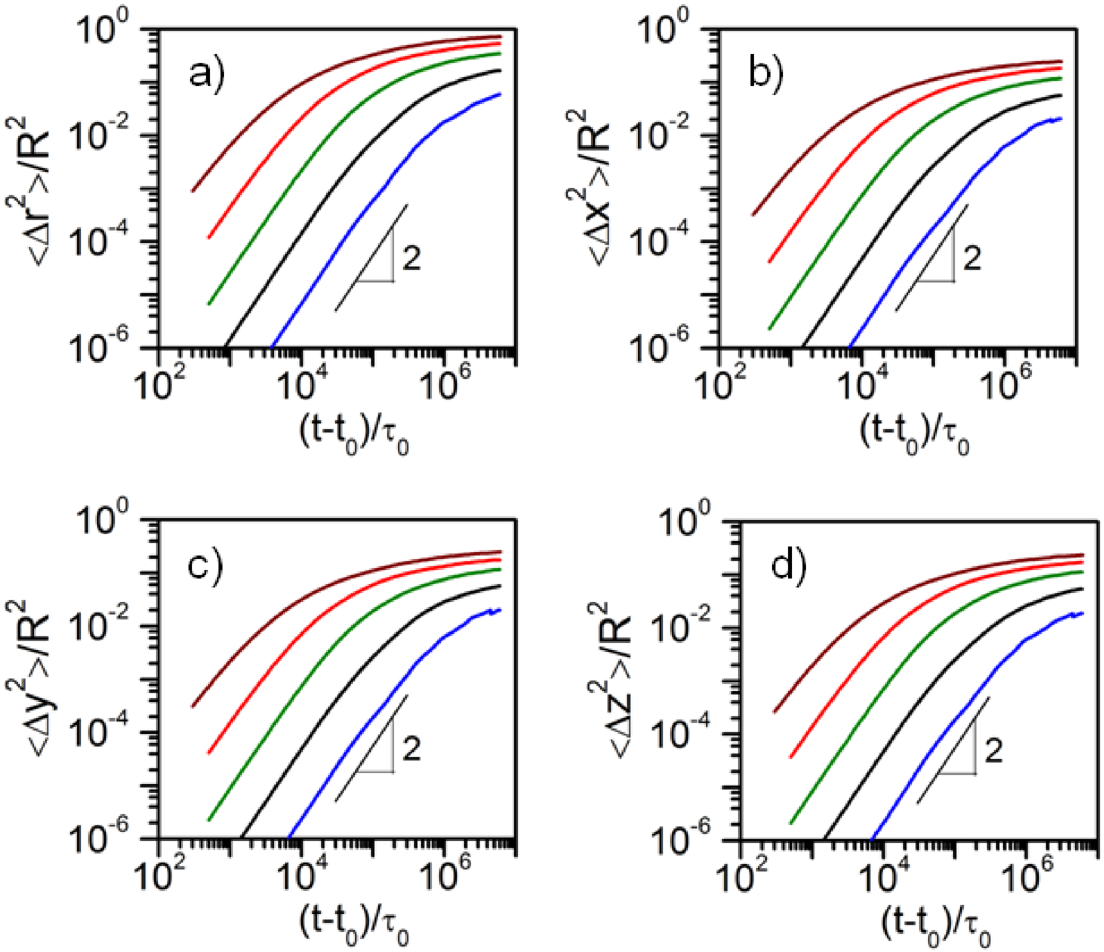

Figure 4.8: Mean squared displacement of particles in *r*- (a), *x*- (b), *y*- (c), and *z*- (c) directions for different preshear rates (from top to bottom: $\eta_s\dot{\gamma}/E^* = 10^{-4}$, 10^{-5}, 10^{-6}, 10^{-7}, 10^{-8}).

4.5.2 Evolution of microstructure with time

Figure 4.9a and b show the evolution of the pair distribution functions computed in the flow-velocity gradient plane at three different times: during preshear (t_0), at an intermediate time during relaxation (t_1), and at the beginning of the internal stress plateau (t_2), for two different preshear flow conditions. t_0, t_1 and t_2 are indicated in figure 4.5. The pair distribution functions are presented in polar coordinates (r,θ) where θ is measured from the positive flow direction. The mean particle center-to-center separation in a packing which was fully equilibrated using the conjugate gradient method is shown with a white line. During preshear (t = t_0), we observe a clear angular distortion of the microstructure revealing accumulation of neighboring particles in the compressive upstream quadrant $(\pi/2<\theta<\pi)$, and depletion in the extensional quadrant $(0<\theta<\pi/2)$. Most particles are more compressed than at equilibrium. The asymmetry of the pair distribution function and the increased compression of particles persist at intermediate times (t = t_1), albeit quite reduced. At the end of the simulation (t = t_2), the mean center-to-center distance has relaxed to its equilibrated value but some degree of angular asymmetry seems to persist. These two processes constitute the microstructural signature of stress relaxation following flow cessation and are discussed in detail below to quantitatively describe the spatial rearrangements associated with stress relaxation.

The angular distortion of the microstructure can be quantified by expanding the pair distribution function using spherical harmonics: $g(\mathbf{r})=g(r)+\sum_{l=1}^{\infty}\sum_{m=-l}^{l}g_{lm}(r)Y_{lm}(\theta,\phi)$. $g_{2,-2}(r)$ is the coefficient of the harmonic $Y_{2,-2}(\theta,\phi)=\frac{1}{4}\sqrt{\frac{15}{\pi}}\left(\sin 2\theta\sin^2\phi\right)$ and represents the angular asymmetry due to accumulation-depletion of particles between the compression and extension axes during flow [Mohan *et al.* (2013); Seth *et al.* (2011)]. The evolution of $g_{2,-2}(r)$ on flow cessation is shown in figure 4.9 c and d. The depth of the minimum of $g_{2,-2}(r)$ indicates that more particles are on average in the compressive region. This minima depth decreases with time during the relaxation process indicating that the asymmetry of the pair distribution function is decreasing. The position of the minima (r_{min}) shifts towards that of the static case compression and its depth decreases during the relaxation process. Thus, the stress relaxation occurs through a redistribution of particle-particle contacts towards a more symmetric unsheared distribution. The case shown in figure 4.9c is for the maximum preshear stress investigated where most of the preshear stress relaxes and microscopically the $g_{2,-2}(r)$ is almost flat. On the other hand in 4.9d where the preshear stress is smaller, there is more asymmetry remaining at the end of the simulation.

The radial distortion of the microstructure is quantified by the radial distribution of particle-particle contacts. The number of elastic contacts and the radial distribution of contacts equilibrate to the static case scenario during the rapid initial relaxation on flow cessation as shown in figure 4.10. The histograms in figure 4.10 represent the radial distribution of particle contacts at different times shown in figure 4.5 and the black dashed line represents the static case distribution.

This suggests that the remaining angular asymmetry in the pair distribution function is the microscopic origin of the internal stress trapped on flow cessation in these soft particle glasses.

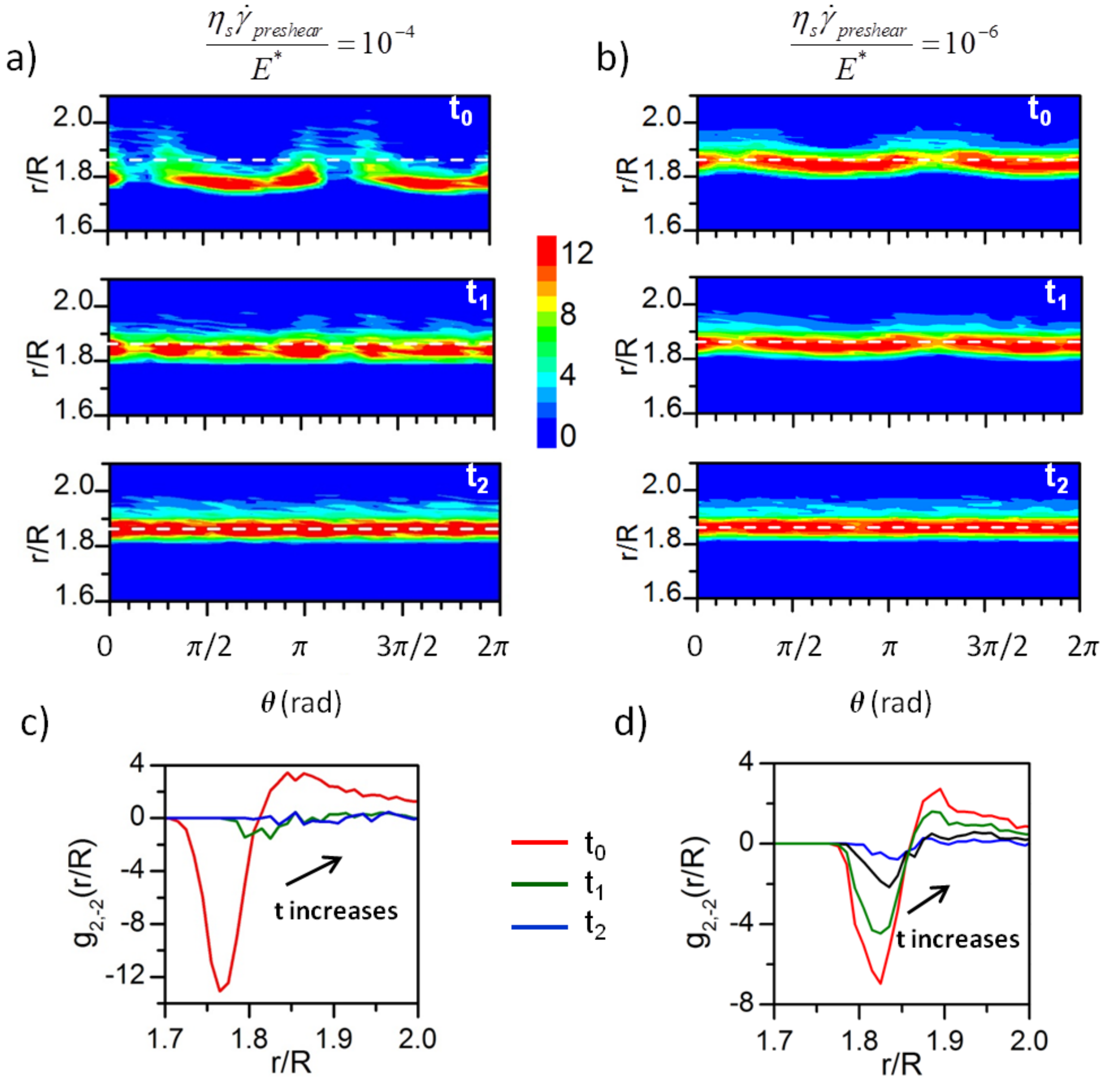

Figure 4.9: Evolution of the pair correlation function $g(\mathbf{r})$ (a and b) and the spherical harmonic $g_{2,-2}(r)$ (c and d) with time during relaxation for two different preshear flow conditions.

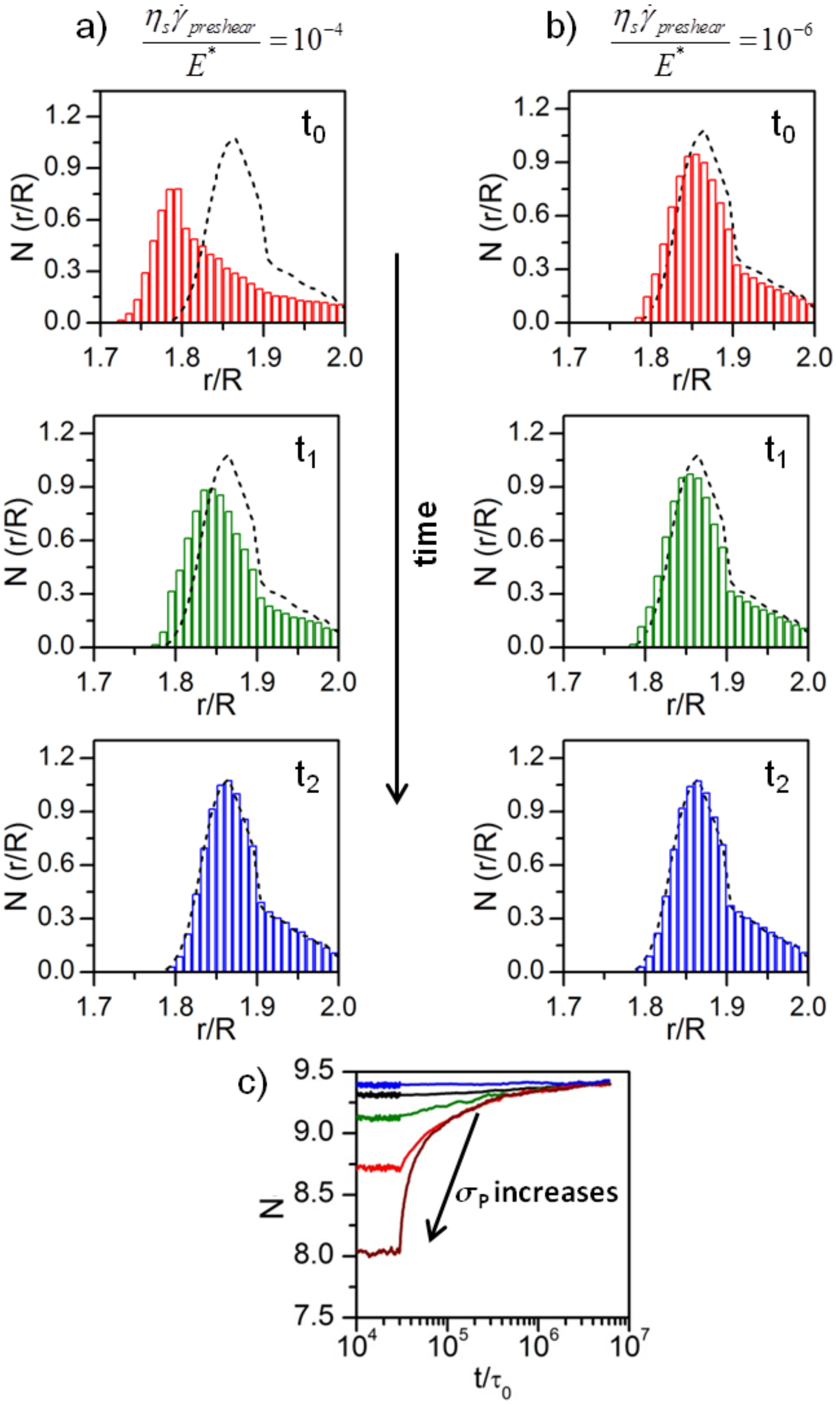

Figure 4.10: Time evolution of radial distribution of contacts (a and b) and number of contacts per particle (c). The black dashed lines in (a) and (b) correspond to the static case distribution of particle contacts

4.5.3 Microscopic origin of internal stresses

The radial and angular distribution of particle-particle contacts during preshear (t_0) and at the beginning of the internal stress plateau after the rapid initial stress relaxation (t_2) for different preshear rates (or stresses) is presented in figure 4.11. Figures 4.11a and 4.11b show the spherical harmonic coefficients $g_{2,-2}(r)$ which represent the angular asymmetry computed for different preshear rates during preshear ($t < t_0$) and at the beginning of the stress plateau ($t = t_2$). The asymmetry in the pair distribution function due to the accumulation-depletion mechanism appears clearly at $t < t_0$ and persists at $t = t_2$. A deeper minimum of $g_{2,-2}(r)$ indicates that more particles have accumulated along the axis of compression of the preshear flow, yielding a higher stress. Interestingly, the variations of the depth of minima inverts from figure 4.11a to figure 4.11b. In figure 4.11a, the largest preshear rate and stress is associated with the largest asymmetry, i.e. the largest shear stress, resulting in figure 4.11b with the smallest asymmetry, i.e. the smallest internal stress. Also, note that the position of minima in figure 4.11b does not depend on the preshear stress. Figures 4.11c and 4.11d show the radial distribution of contacts computed for different preshear rates during preshear ($t < t_0$) and at the beginning of the stress plateau ($t = t_2$). During shear flow, the particles are more compressed and the mean particle-particle separation is the smallest for the largest preshear rate but this radial distortion relaxes quickly on flow cessation and the distribution returns to that of the static case for all preshear flow conditions. This clearly demonstrates that the distortion of the angular distribution of particle contacts does not relax completely on flow cessation and is the microscopic origin of internal stresses. In Chapter 3 on oscillatory shear rheology of these soft particle glasses it was shown that the appearance of significant distortions (asymmetry) of the microstructure and the $g_{2,-2}(r)$

arise only beyond the yield stress of the material due to flow induced rearrangements and this explains the scaling of the internal stresses with the flow induced stresses $(\sigma_P - \sigma_y)$.

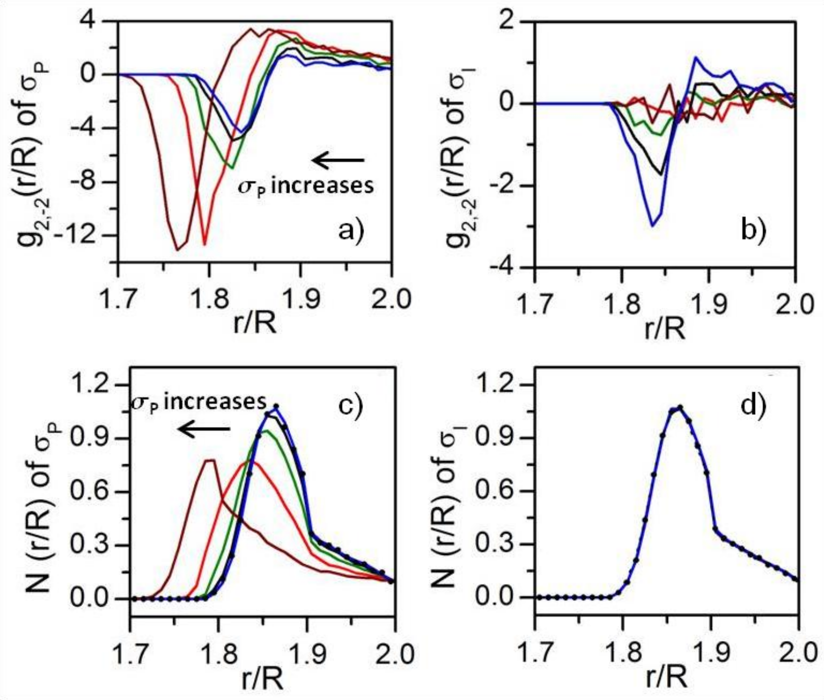

Figure 4.11: Spherical harmonic coefficient $g_{2,-2}(r)$: (a) during preshear at different rates (from left to right: $\eta_s\dot{\gamma}/E^*=10^{-4}$, 10^{-5}, 10^{-6}, 10^{-7}, 10^{-8}); (b) at the final time of relaxation in simulations (same rates, from top to bottom). Radial distribution of contacts per particle: during preshear (same rates, from left to right) (c) and at the final time of relaxation from simulations (d). The black dots in (c) and (d) correspond to the static case distribution of particle contacts.

4.6 NATURE OF SHORT TIME RELAXATION ON FLOW CESSATION

4.6.1 Macroscopic short time stress relaxation

The soft particle glass accumulates stress during the preshear flow and on flow cessation (at t_0) this stress decays through a rapid initial relaxation after which there remain trapped internal stresses which relax slowly with time. It was shown earlier that the internal stresses are larger for smaller preshear stresses thus the rate of short time stress relaxation on flow cessation depends on the flow conditions during preshear and this can be clearly seen in Figure 4.12 (a and b). The larger the preshear rate (or stress) the faster the material relaxes immediately on flow cessation and the stress relaxation curves cross over at very short times. The first data point in experiments is collected at 0.1s which is larger than the time at which the crossover occurs and thus cannot be observed in experiments. In figure 4.12c (and d) the stress relaxation is presented by scaling the stress by the preshear flow stress and the systematic trend with the preshear flow conditions where the material which undergoes a larger preshear rate relaxes faster is clearly observed.

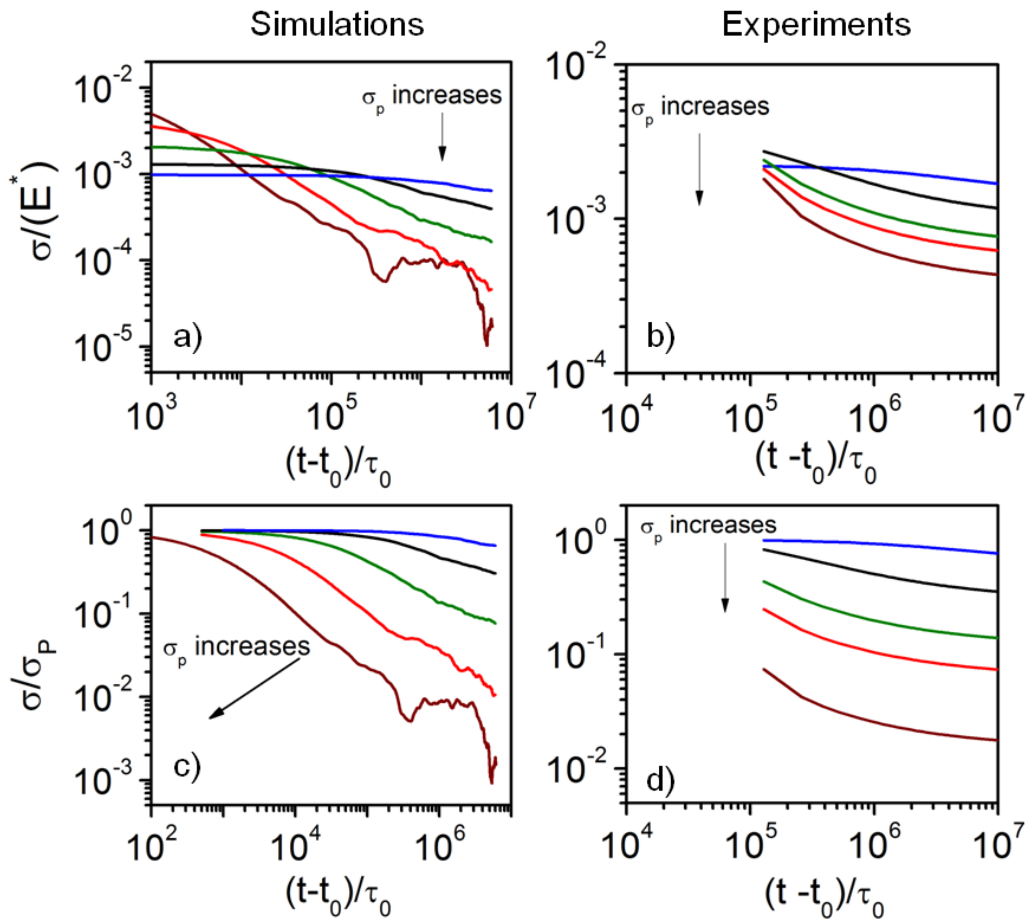

Figure 4.12: The rapid relaxation immediately upon flow cessation from simulations and experiments. The experiments correspond to the sample with C=2% water-glycerol (36/64) solvent and 1% crosslinker.

4.6.2 Mapping the evolution of microstructure to the macroscopic stress relaxation

The evolution of the asymmetric or angular distortion of the pair distribution function as the material relaxes is further quantified by studying the variation of the depth of the minima of $g_{2,-2}(r)$ with time. Figure 4.13a shows the evolution of the minima with time for different shear rates. The distortion relaxes but does not vanish as discussed before and here it can be clearly seen that the evolution of the asymmetry in microstructure also slows down and reaches a non-zero plateau after the rapid initial relaxation. The trends in the evolution of microstructure in figures 4.13a resemble that of the macroscopic stress relaxation in figures 4.12a. And this relaxation is mapped on to the macroscopic stress relaxation from figure 4.12c and is shown in figure 4.13c which shows good qualitative and quantitative agreement. The stress relaxation and variation of the minima of $\mathrm{g}_{2,-2}(r)$ for the largest preshear flow condition considered do not overlap at short times. The minima is shifted to large compressions during large preshear rates and since the stress depends on both the elastic force at the minima of $g_{2,-2}(r)$ and the depth of the minima, there is some deviation at short times when the minima is heavily shifted.

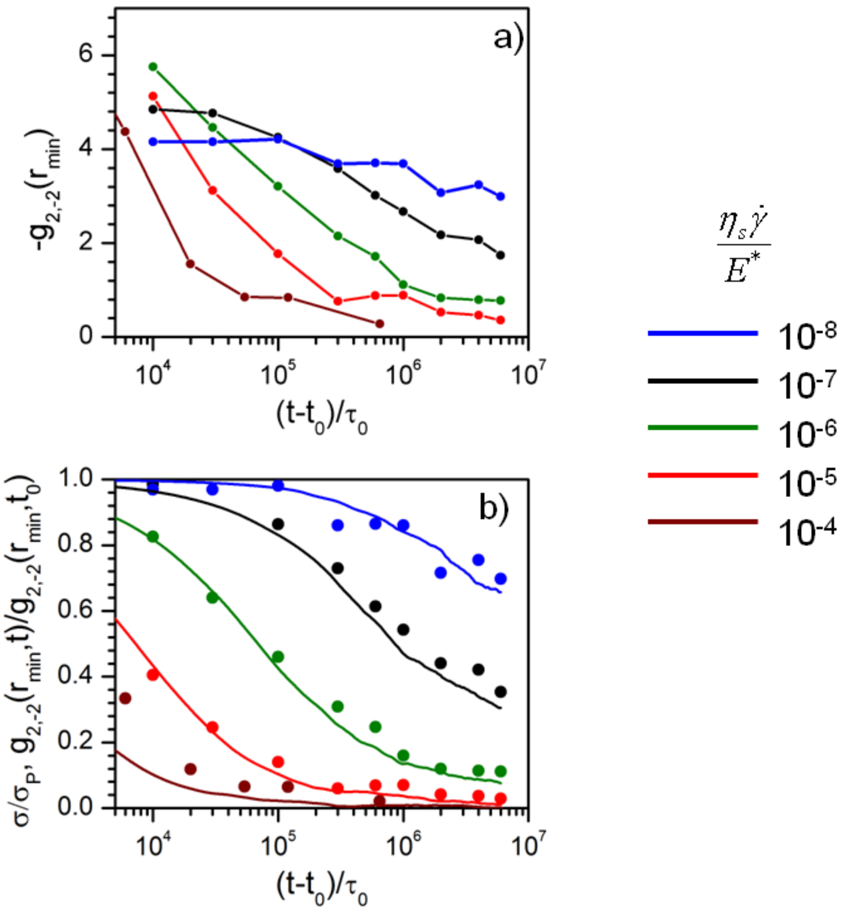

Figure 4.13: (a) Evolution of the depth of minima of $g_{2,-2}(r)$ with time (symbols and lines). (b) Initial relaxation path of the angular asymmetry in the soft particle glass (symbols) with time on flow cessation for different preshear flow conditions and its mapping to the macroscopic stress relaxation (lines).

4.6.3 Generalized short time relaxation path on flow cessation

Figure 4.14a shows the rapid initial relaxation on flow cessation for samples with different constituent properties and similar flow conditions, namely similar $(\sigma_P - \sigma_y)/\sigma_y$ which was determined to be the important parameter characterizing the preshear flow in the previous section. Though the trapped internal stress is the same for different samples due to their similar $(\sigma_P - \sigma_y)/\sigma_y$, the rate at which the material reaches the internal stress plateau is different for different samples. The intrinsic timescale that comes from the simulations is $\tau_0 = \eta_s / E^*$ and figure 4.14b shows the efficiency of this in scaling the relaxation path of samples with different constituents on flow cessation when the preshear flow conditions are the same.

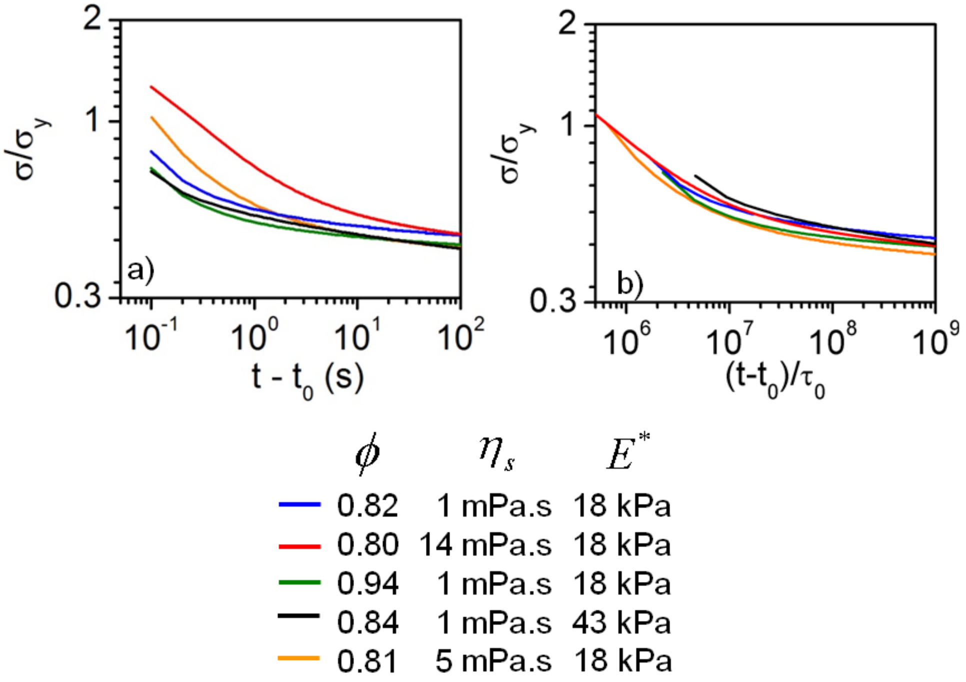

Figure 4.14: Unscaled (a) and scaled (b) relaxation path from the preshear stress to the internal stress on flow cessation for samples with different constituent properties but similar preshear flow condition- $(\sigma_P - \sigma_y)/\sigma_y$.

The relaxation path during the rapid initial relaxation on flow cessation is a function of the preshear flow conditions for a given sample as shown in section 4.4. Scaling the time with the preshear rate and the stress with the preshear stress is known to collapse the relaxation paths for different flow conditions [Ballauff *et al.* (2013)] as shown in figure 4.15 a and b. But the relaxation path is not universal and soft particle glasses with different constituent properties exhibit different short time relaxation paths as shown in figure 4.15c.

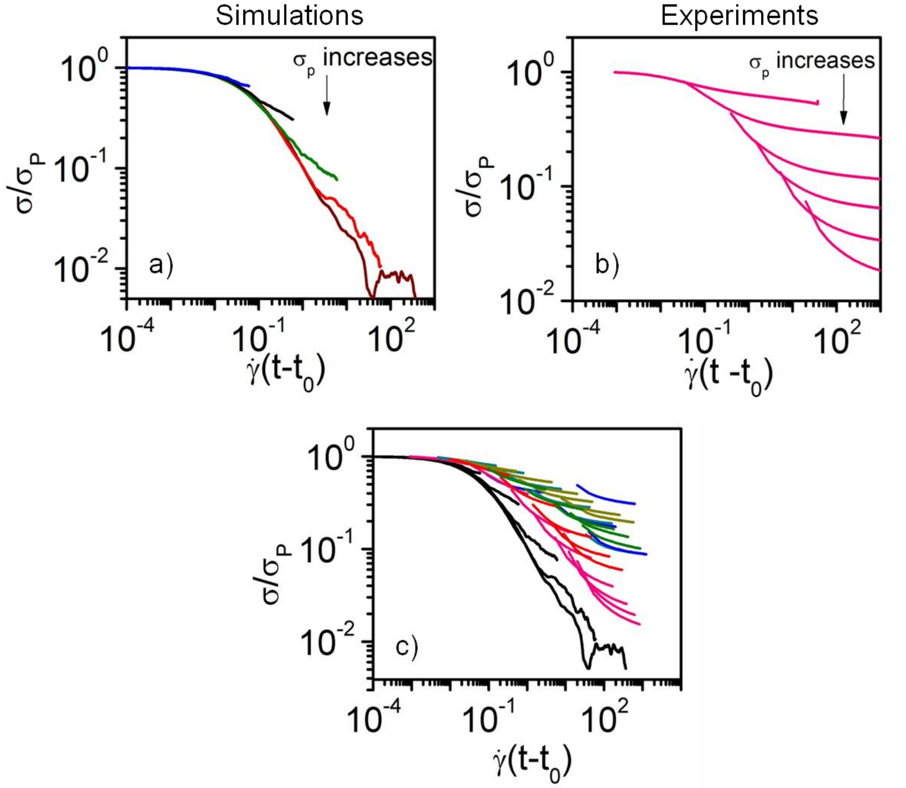

Figure 4.15: Scaled short term relaxation from simulations (a) and experiments (b). The experiments in b) are C=2% η_s=14 mPa.s and 1% crosslinker. (c) The dispersion in the relaxation path of microgel samples with different constituent properties. The color scheme is same as that used in figure 4.1. The black lines correspond to simulation data.

Figure 4.15 shows that even though the relaxation path for different preshear flow condition collapses, the relaxation path of the smaller preshear flow conditions break off the path very quickly and get trapped with an internal stress that relaxes slowly and thus does not follow the entire generalized relaxation path. Thus to generalize the short term relaxation path a new measure of relaxation is defined as $(\sigma-\sigma_I)/(\sigma_P-\sigma_I)$. Figures 4.16 a and b show the relaxation as a function of time scaled by the intrinsic time scale τ_0 and again the relaxation is faster when the preshear is larger.

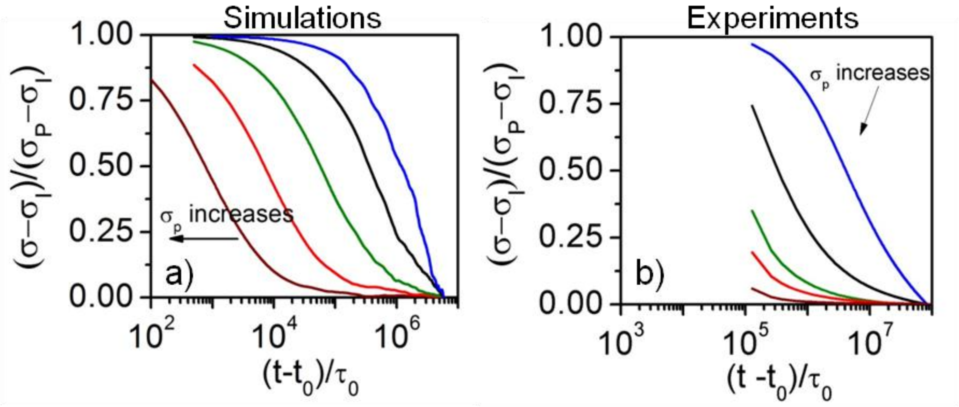

Figure 4.16: Relaxation path from the preshear stress to the internal stress from simulations (a) and experiments (b). The experiments in b) are C=2% η_s=14 mPa.s and 1% crosslinker.

A microscopic time scale was further identified from the microstructural information from simulations to capture the preshear flow effect. It was shown in section 4.5.1 that the microscopic mechanism of the short time relaxation is through ballistic motion of the constituent particles. The mean squared displacement of the particles followed $\langle \Delta r^2 \rangle / R^2 \sim V^2 (t/\tau_0)^p$ where p = 1.89 ± 0.9. The non-dimensional velocity V was larger for larger shear rates. Figure 4.17c shows the variation of this velocity and $V \sim (\eta_s \dot{\gamma} / E^*)^{0.71}$ when fit with a power law. So the dimensional ballistic velocity $V_b = V \dfrac{R}{\tau_0}$. Thus $V_b \sim \dfrac{R}{\tau_0} \left(\dfrac{\eta_s \dot{\gamma}}{E^*} \right)^{0.71}$. A short term relaxation time scale can be defined based on this ballistic velocity as $R/V_b \sim \tau_0 \left(\dfrac{\eta_s \dot{\gamma}}{E^*} \right)^{-0.71}$. This does not include the volume fraction effect and thus a short term relaxation scale $\tau_s \sim \tau_0 \left(\dfrac{\eta_s \dot{\gamma}}{G_0^*} \right)^{-0.71}$ is suggested.

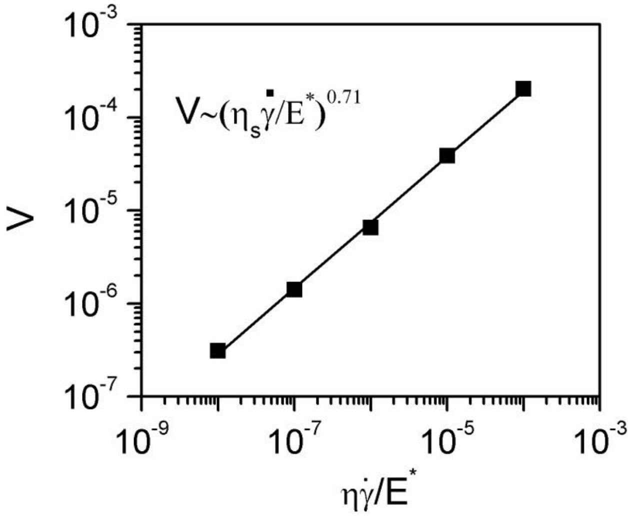

Figure 4.17: Variation of the non-dimensional ballistic velocity of the particles during the rapid initial relaxation. The symbols correspond to the raw data and the solid line represents the fit: $V \sim (\eta_s \dot{\gamma} / E^*)^{0.71}$.

Figure 4.18 a and b show the relaxation path scaled by τ_s and curves with different flow histories collapse. This scaled relaxation path for samples with different constituent properties and the simulations is presented in figure 4.18c. The curves for different constituent properties collapse and this presents a universal short time relaxation path on flow cessation for soft particle glasses of varying properties with varying preshear flow conditions. The relaxation path from simulations are slightly faster and this can be because the simulations just capture the beginning of the internal stress plateau and the term $\left(\sigma-\sigma_I\right)/\left(\sigma_P-\sigma_I\right)$is sensitive to the actual value of the internal stress.

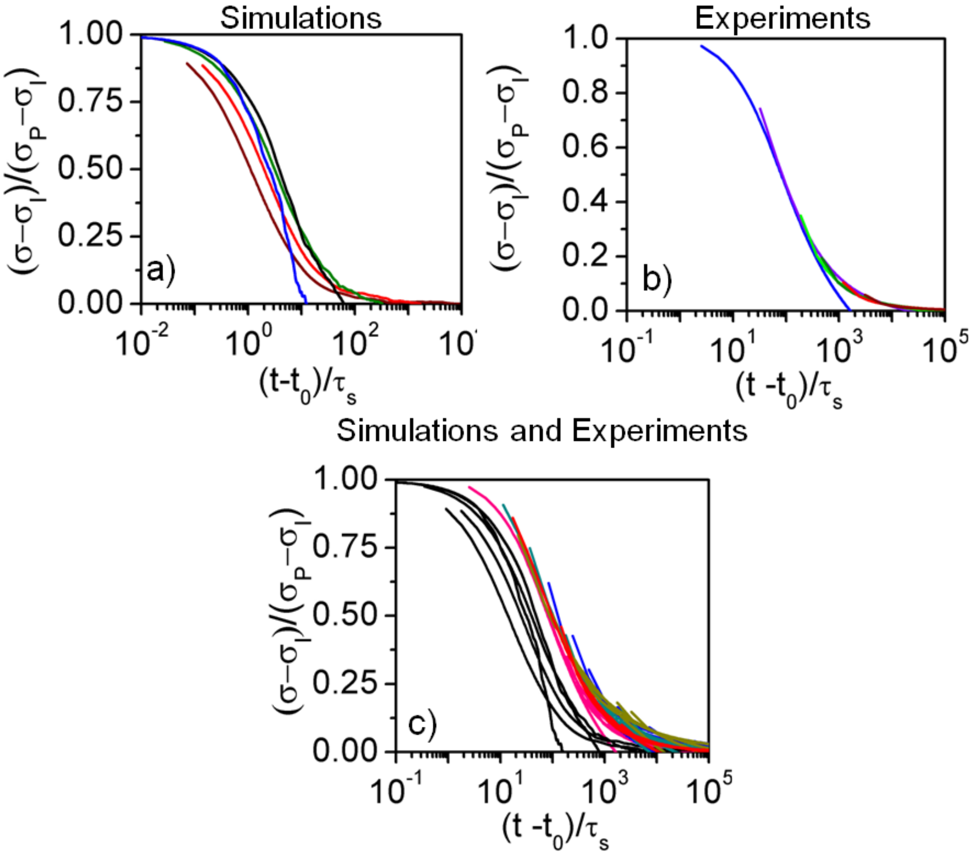

Figure 4.18: Scaled relaxation path from simulations (a) and experiments (b) using a ballistic time scale identified from microscopic dynamics. (c) Universal relaxation path for different preshear flow conditions, constituent properties and volume fractions. The experiments in (b) correspond to C =2% η_s=14 mPa.s and 1% crosslinker. The color scheme in (c) is the same as that used in figure 4.1. The black lines correspond to simulation data

4.7 NATURE OF RELAXATION AT LONG TIMES AFTER FLOW CESSATION

Long term relaxation experiments were performed for times up to 100,000s after flow cessation to investigate the fate of the internal stresses at long times. Figure 4.19a shows the long time stress relaxation behavior after flow cessation and the trapped internal stresses continue to relax very slowly for long times. The effect of preshear flow on the relaxation at long times is shown in figure 4.19b. It was shown in figure 4.13 that the asymmetry in microstructure also begins to freeze after the initial rapid decay and hence the long time relaxation is a slow equilibration of this residual asymmetry in the microstructure and this regime must depend only on the asymmetry at the beginning of this slow relaxation and not the preshear flow. Figure 4.19c presents the stresses scaled by the internal stress on flow cessation and this further shows that the nature of the long term relaxation is independent of the preshear flow conditions. The effect of the constituent properties of the soft particle glass on the long term relaxation was also investigated by performing the long term relaxation experiments with samples of varied constituent properties but no observable scaling was observed as shown in figure 4.20.

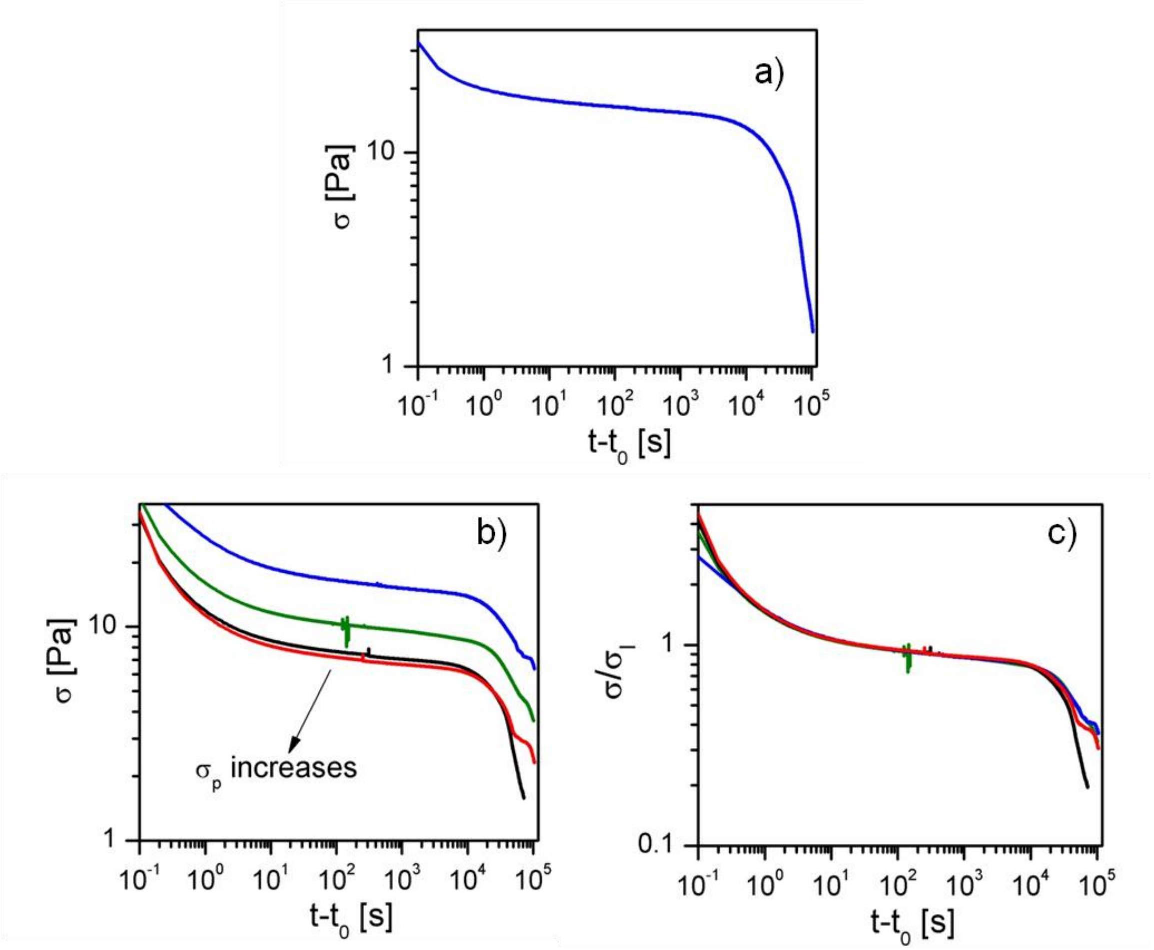

Figure 4.19: (a) Long term relaxation of trapped internal stresses in a soft particle glass with 2% polymer, water solvent and 1% crosslinker presheared at 148 Pa. (b) and (c) Effect of preshear flow on the long term relaxation demonstrated using a soft particle glass with 2% polymer, water-glycerol (36/64) solvent and 1% crosslinker presheared at 62Pa (blue), 148 Pa (green), 250 Pa (black) and 350 Pa (red).

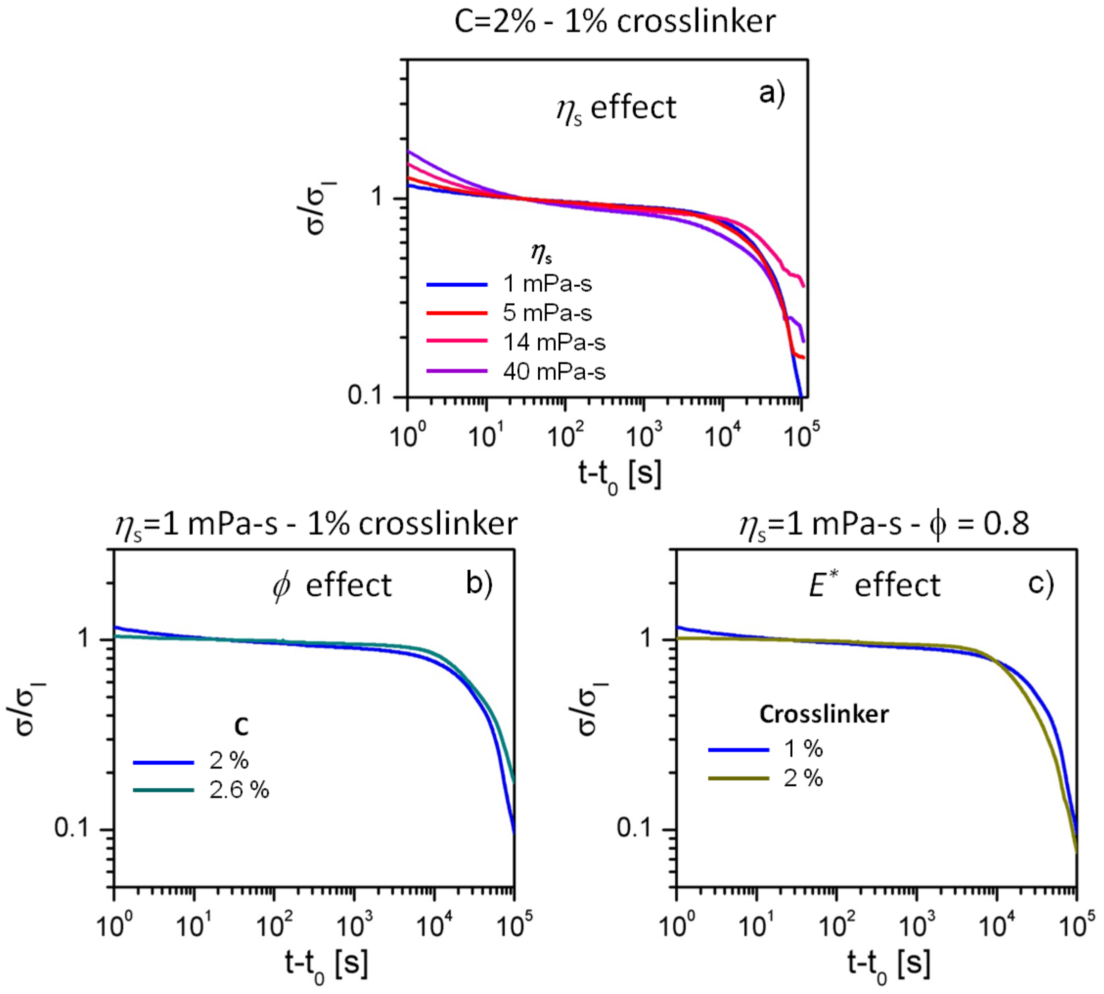

Figure 4.20: Investigation of the effect of constituent properties of soft particle glasses on long term relaxation behavior.

4.8 SUMMARY AND CONCLUSIONS

Experiments were performed using concentrated microgel samples with systematically varied constituent properties to determine their stress relaxation behavior on flow cessation. Unlike viscous liquids the stress in these materials does not vanish on flow cessation and instead there is a quick initial relaxation after which the material gets trapped with an internal stress which relaxes slowly and this internal stress is smaller for larger preshear stresses. Long term relaxation experiments were performed to determine the fate of these trapped internal stresses. The internal stresses continue to relax slowly and in this regime the preshear flow conditions do not affect the rate of stress relaxation.

Particle scale simulations using a soft particle glass packed to a volume fraction of 0.8 were built to further elucidate the microscopic origin of these internal stresses. During preshear, the macroscopic flow distorts the microstructure: more particles are in the compressive region of the flow, where they are more compressed than at equilibrium, and fewer particles are in the extensional region, where these are less compressed. On flow cessation the elastic stress drives the material back to equilibrium according to two different processes. The center-to-center distance and the average number of contacts relax quickly through ballistic motion to their equilibrium values. This process is fast because only central forces at particle-particle contacts are important in order to change particle compression. However, some asymmetry in the angular distribution of particles persists because the particles cannot move over large distances. This metastable asymmetry in the pair distribution function is the origin of the internal stress and is characterized by the spherical harmonic $g_{2,-2}(r)$. The larger the elastic stress is during the preshear flow, i.e. the driving force, the more easily the isotropy of the pair distribution function is restored and the smaller is the internal stress ($0 < \sigma_I < \sigma_y$). The subsequent relaxation of the internal stress is extremely slow because any change of the local topology between two contacting particles requires collective rearrangements over long distances.

The internal stress follows a universal scaling with the elastic stress created in the material which itself depends on the preshear stress. This scaling allows us to predict the internal stress for various processing conditions. At the microscopic level two parameters are important: the solvent viscosity and the particle elasticity which can be tuned by the nature and the architecture of the particles. While the microgels are soft and non-Brownian ($E^{*}R^{3}/kT \approx 10^{5}$), it will be interesting to use the same framework to investigate ultrasoft particles like star polymers where thermal effects come into play and potentially provide new relaxation mechanisms [Erwin *et al.* (2011)]. The connection between internal stress and slow relaxation and aging phenomena in soft particle glasses is another intriguing question for which preliminary investigations are presented in Supplemental Material 4.A.

SUPPLEMENTAL MATERIAL 4.A: CONSEQUENCES OF INTERNAL STRESSES IN AGING EXPERIMENTS

Concentrated microgels are soft particle glasses which exhibit physical aging which is the evolution of material properties with time. This section describes the consequence of the presence of internal stresses on aging. All experiments in this section were performed with a microgel sample of *C*=2%, solvent viscosity of 1 mPa.s and the constituent particles have an elastic modulus E^* of 18,000 Pa. The preshear step in all the experiments was performed by shearing the sample at the rate of 200s^{-1} for 30s.

4.A.1 Variation of viscoelastic moduli with time

The viscoelastic moduli of concentrated microgels evolve with time. Microgel samples were presheared and then allowed to evolve with time and the viscoelastic moduli were computed at a frequency of 1 rad/s to follow their evolution. Figure 4.A.1 shows this evolution. The elastic modulus of the material increases and the loss modulus decreases with time.

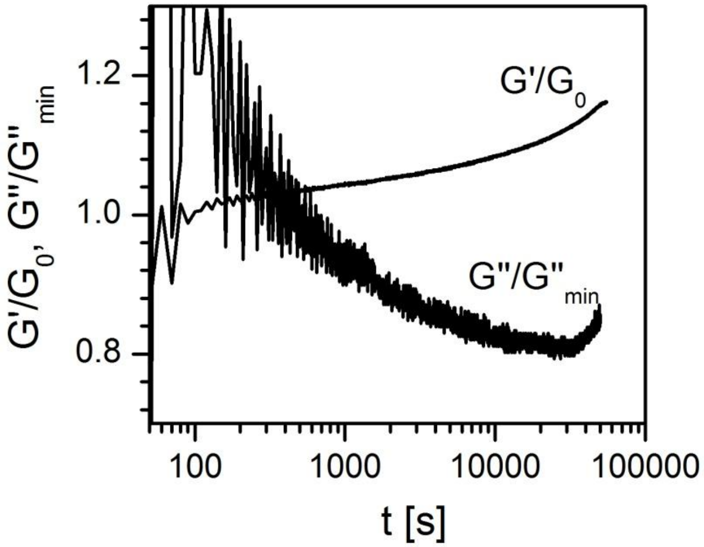

Figure 4.A.1: Evolution of viscoelastic moduli with time

4.A.2 Difference between aging at zero stress and zero shear rate

The aging behavior of such soft particle glasses is monitored by first preshearing the material to remove the internal stresses during preparation and loading and to bring the material to a reproducible state and then allowing the material to rest for a waiting time t_w and then applying a probe stress smaller than the yield stress to study the material behavior [Cloitre *et al.* (2000)]. Aging experiments were performed by "resting" the material at zero stress and zero shear-rate to determine if the internal stresses had any effect on the aging behavior. Figure 4.A.2 shows that the internal stresses do affect the material behavior as the probe stress is much smaller than the yield stress and does not erase the internal stress.

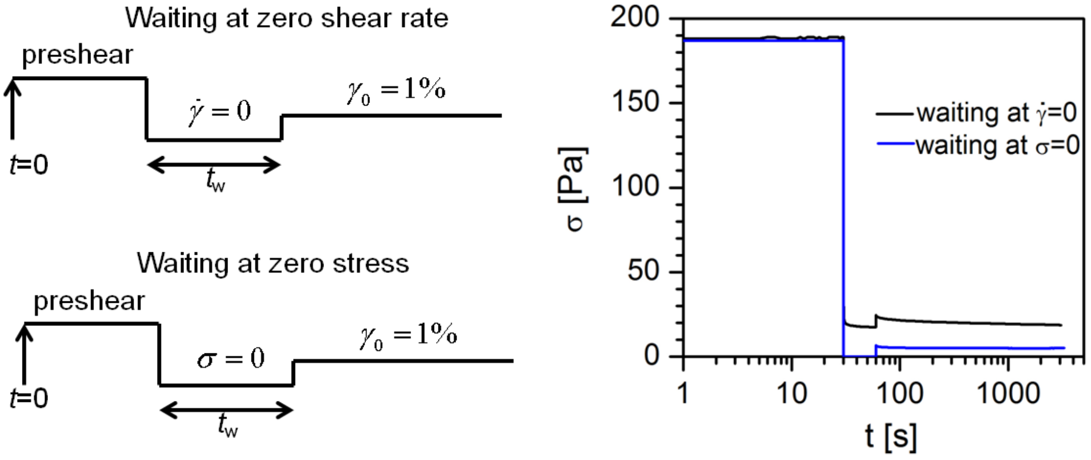

Figure 4.A.2: Waiting at zero stress and zero shear rate during aging experiments

An experiment consisting of preshearing, relaxing the sample at zero stress for a time t_w and then setting the shear rate to zero was performed to understand the effect of relaxing the material at zero stress on the trapped internal stress in the material. Interestingly the internal stress builds up when the shear rate is set to zero as shown in figure 4.A.3 revealing that relaxing the material at zero stress does not completely equilibrate the material.

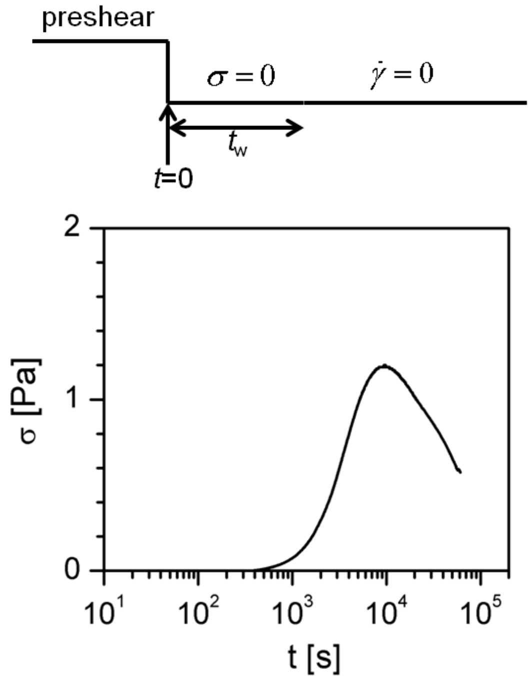

Figure 4.A.3: Effect of zero stress relaxation on the internal stresses trapped in the material

4.A.3 Effect of internal stresses in aging

Now that it has been demonstrated that performing the waiting step in the aging experiments at zero shear rate and zero stress are different due to the presence of the internal stresses, aging experiments were performed using both protocols at different waiting times and the results are presented in figure 4.A.4. Figure 4.A.4a shows the evolution of stress after the preshear step when the shear rate is set to zero. Now the elastic modulus of the material presented in section 4.2.1 is 651 Pa and thus the stress created due to the 1% constant strain should be $\sim 6.51\mathrm{Pa}$ or slightly higher due to aging during waiting time $t_{w,}$ but this disturbance is much smaller than the yield stress and does not erase the internal stress and hence the stress response we note is a combination of the internal stress and the effect of the 1% strain. In figure 4.A.4b the stress evolution is presented with the origin as the instant the probe strain is applied, here we can clearly see that the material with a longer waiting time exhibits a higher stress jump due to the increased modulus. Even though the material is loaded with a constant 1% strain the material continues to relax its stresses and evolves with time. In figure 4.A.4c the stress evolution for the zero stress waiting case is presented. The stress jump at the instant of probe strain application exhibits similar trends with the waiting time. The most remarkable distinction here is that the material continues to relax with time under loading at short times but at long times it tends to reach a stress plateau. It was shown in Figure 4.A.3 that when the shear rate is set to zero after waiting at zero stress, the internal stresses build up initially but they relax at long times. This suggests that the internal stresses trapped in these materials is at the root of their aging characteristics and the evolution of the asymmetry of the microstructure which give rise to these internal stresses might be the microscopic driver of the physical aging process.

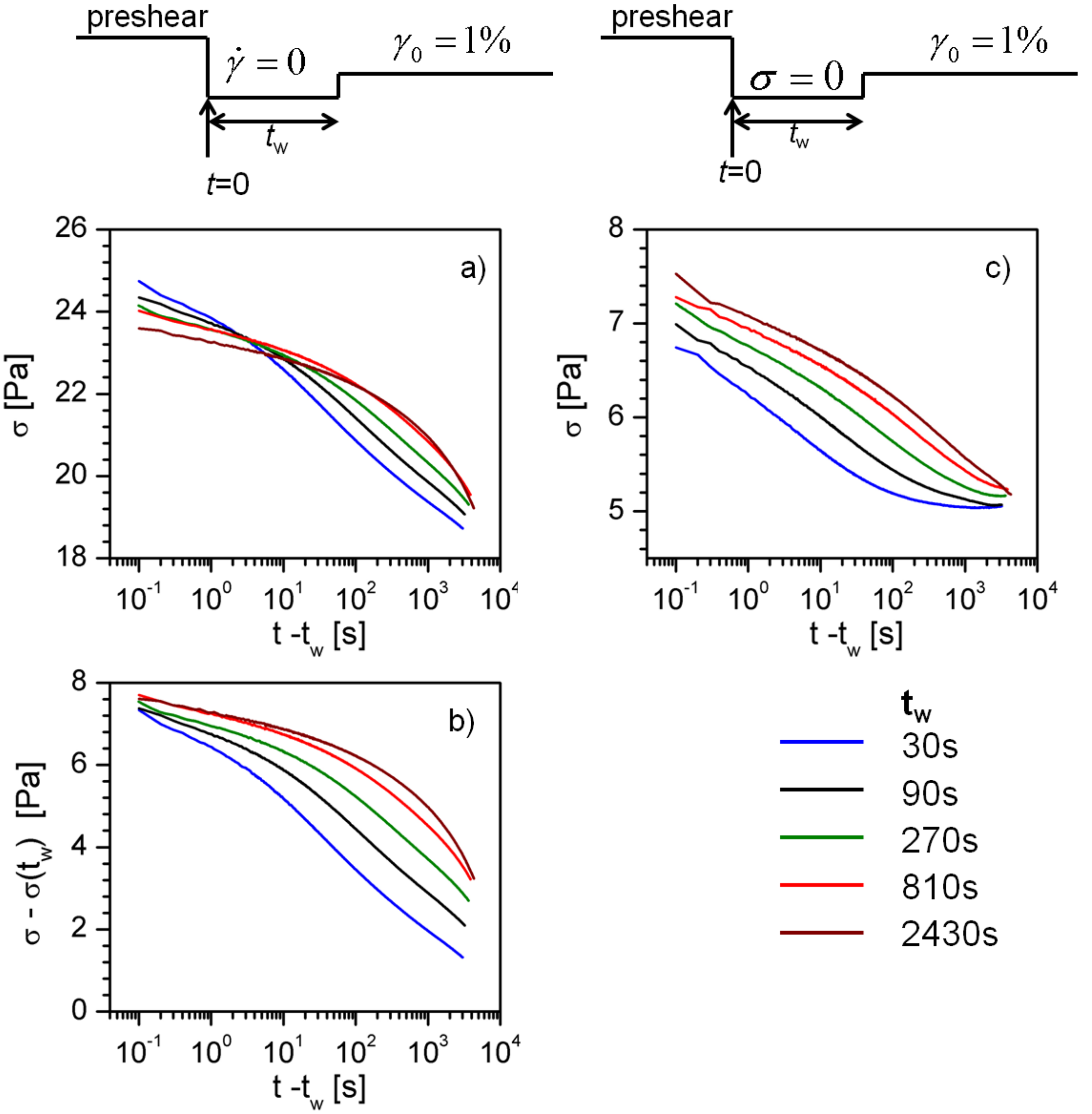

Figure 4.A.4: Effect of internal stresses on aging of soft particle glasses. (a) The evolution of stress after application of probe strain with 0 and end of waiting time as origin using a zero shear rate waiting protocol. (b) The evolution stress after application of probe strain using a zero stress waiting protocol

4.A.4 Time-waiting time rescaling

A time waiting time rescaling is characteristic of aging phenomenon in many glassy materials [Cloitre *et al.* (2000); Struik (1978)]. A similar scaling is presented here for the two different aging protocols used. The curves collapse for both cases but interestingly the relaxation path is different for the two cases. The presence of internal stresses and associated microstructural distortions drive the material to continue to relax at long times but in the zero stress waiting case the material reaches a constant plateau. The internal stresses and the stresses due to the probe strain are of similar order of magnitudes and hence it would be interesting to apply a probe strain in the opposite direction to the internal stress (-1%) to investigate further the interaction of the internal stresses with the probe strain.

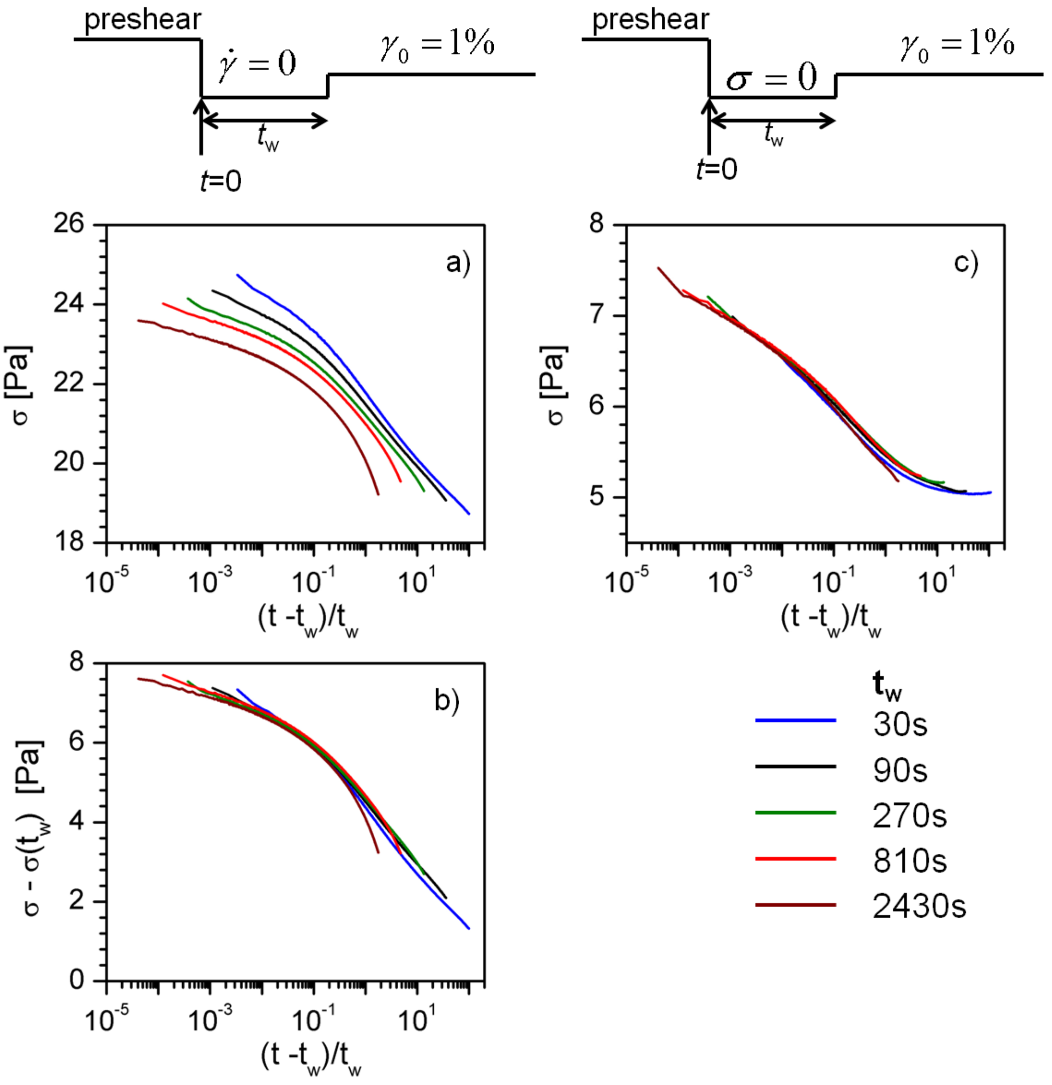

Figure 4.A.5: Time-waiting time rescaling for the stress evolution on application of a probe strain for zero shear rate waiting time (a,b) and zero stress waiting time (c).

SUPPLEMENTAL MATERIAL 4.B: SIMULATION DATA TABLES

Table 4.B.1: Variation of internal stresses with preshear stresses in microgels

Sample	**σ_P (Pa)**	**σ_I (Pa)**
C = 2 wt. %, 1% crosslinker, water solvent	55	29.2
	65	23.3
	75	19.9
	110	16.6
	150	16.2
	250	13.2
C = 2.6 wt. %, 1% crosslinker, water solvent	90	64.2
	95	57.0
	115	46.7
	150	38.9
	200	34.7
	350	28.6
C = 2 wt. %, 1% crosslinker, water-glycerol solvent (53/47)	50	26.4
	75	18.5
	120	14.1
	170	12.3
	225	11.6
C = 2 wt. %, 1% crosslinker, water-glycerol solvent (36/64)	40	26.008
	60	18.363
	100	12.712
	131	10.221
	153	9.9099
	250	7.7944
	350	7.14442
	443	6.8836
	500	6.1788
	550	5.5094

Table 4.B.1 (Continued)

Sample	σ_P **(Pa)**	σ_I **(Pa)**
C = 2 wt. %, 1% crosslinker, water-glycerol solvent (23/77)	35	14.083
	65	9.1763
	75	8.488
	125	4.8806
	250	6.5822
C = 3 wt. %, 2% crosslinker, water solvent	50	17.348
	65	13.939
	95	12.595
	120	13.045
	150	12.206
C = 3.8 wt. %, 2% crosslinker, water solvent	115	92.294
	135	58.279
	170	48.402
	220	45.974
C = 4 wt. %, 2% crosslinker, water solvent	135	80.984
	150	68.97
	170	58.856
	190	54.081
	225	51.416
	250	51.213
	300	51.059

Table 4.B.2: Variation of internal stresses with preshear stresses in simulations

Volume fraction	$\boldsymbol{\eta_s\dot{\gamma}/E^*}$	$\boldsymbol{\langle \sigma_I/E^* \rangle}$
0.8	10^{-4}	1.72E-05
	10^{-5}	4.61E-05
	10^{-6}	1.64E-04
	10^{-7}	3.96E-04
	10^{-8}	6.40E-04

Chapter 5: Active Microrheology

5.1 INTRODUCTION

Soft particle glasses form a diverse family of materials including microgels [Borrega *et al.* (1999)], compressed emulsions [Lacasse *et al.* (1996)], block copolymer micelles [Buitenhuis and Forster (1997)], star polymers [Likos (2006)], and foams [Princen and Kiss (1989)]. The ability of these soft glasses to exhibit both solid like and liquid like properties has made them useful as rheological additives for coatings, ceramic pastes, textured food and cosmetic products. The structure and dynamics of biological materials such as tissues [Angelini *et al.* (2011)] and intracellular cytoplasm [Trepat *et al.* (2007)] also resemble those of soft particle glasses. Rheological characterization and control of soft particle glasses is crucial for efficient industrial use as well as furthering our understanding of the physics behind such soft jammed systems.

Bulk rheological measurement techniques like shear and extensional rheometry have been extensively used to characterize such complex fluids [Macosko (1994)]. Microrheology is a relatively newer technique in which particle scale motion of a probe particle inside the material is tracked in response to an applied stimulus to determine the local viscoelastic properties of the material. It is widely used to characterize hard and soft suspensions including polymers, laponite clays, colloids and biomaterials [Cicuta and Donald (2007); Squires and Mason (2010); Waigh (2005); Wilson and Poon (2011); Wirtz (2009)] as it offers many advantages over bulk measurements. The small size of the probe allows investigation of the local microstructure and viscoelasticity of the material and this can be particularly useful in understanding the variations of properties across the sample in composite and heterogeneous materials [Chen *et al.* (2003); Gardel *et al.* (2003); Hasnain and Donald (2006); Schmidt *et al.* (1996)]. Microrheology requires small sample volumes of micro-liters compared to milliliters in conventional rheometry, and thus it can be used for scarce materials like biological samples [Gardel *et al.* (2003); Lau *et al.* (2003); Yamada *et al.* (2000); Ziemann *et al.* (1994)]. Microrheology measurements also provide the advantage of in-*vivo* characterization of living cells without disrupting them [Lau *et al.* (2003); Weihs *et al.* (2006); Zaner and Valberg (1989)]. The internal nature of the method also removes the surface effects encountered in conventional rheometers like wall slip. Accurate rheological characterization at high frequencies and shear rates is often not possible using conventional rheometers due to the inertia of the equipment but is feasible with microrheology due to low or negligible inertia of the probe [Schnurr *et al.* (1997)].

There are two broad classes of microrheological techniques, passive and active methods. In passive methods the motion of the probe particle in response to its Brownian motion or thermal forcing is tracked [Chen *et al.* (2003); Mason *et al.* (2000)]. In active methods the probe is forced through the material by external sources like optical tweezers [Helfer *et al.* (2000); Jop *et al.* (2009); Meyer *et al.* (2006); Valentine *et al.* (1996); Velegol and Lanni (2001); Wilking and Mason (2008)] or magnetic fields [Bausch *et al.* (1999); Habdas *et al.* (2004); Rich *et al.* (2011); Schmidt *et al.* (1996); Zaner and Valberg (1989); Ziemann *et al.* (1994)] and its motion in response is tracked. On comparing the Brownian energy density and the elastic energy needed to deform the surrounding material with an elastic modulus G_{local} to a length dL, $kT/R^3 \approx G_{local} dL^2/R^2$ [Breuer (2005)], the imaging technique needs to detect a minimum $dL \approx (kT/G_{local}R)^{0.5}$. At room temperature with 10nm image resolution and a micron sized probe, this method sets an upper limit for G_{local} of around 40 Pa.

Soft particle glasses are highly jammed materials in which each constituent particle is surrounded by a cage of other particles and they form flat facets at contact [Seth *et al.* (2011)]. The elasticity of these glasses stems from the interactions at these facets due to the jamming and is athermal in nature. Their elastic shear moduli can range from 100’s to 1000’s of Pascals [Cloitre *et al.* (2003b); Mason *et al.* (1995); Seth *et al.* (2006)]. Thus, active microrheological methods involving external forcing of probe particle are necessary to characterize these soft particle glasses. Glassy yield stress fluids like laponite suspensions have been investigated using active magnetic probes [Rich *et al.* (2011)].

The probe forcing in active microrheology can be of constant velocity or constant force nature or sometimes even mixed modes are possible [Carpen and Brady (2005); Squires and Brady (2005)]. Theory and simulations are being developed to understand the different modes of operation and to relate the local viscoelastic information obtained from microrheology to the bulk measurements for a variety of suspensions. Detailed theory and simulations have been developed for pulling a probe particle through hard sphere suspensions using different modes [Carpen and Brady (2005); Khair and Brady (2006); Khair and Brady (2008); Squires and Brady (2005); Zia and Brady (2013)]. Molecular dynamics simulations and lattice field models [Jack *et al.* (2008)] of a probe particle dragged through a suspension of particles interacting through screened Coulombic interactions [Reichhardt and Reichhardt (2008)], binary L-J mixtures [Williams and Evans (2006)], nematic [Foffano *et al.* (2012)] and Yukawa fluids [Winter *et al.* (2012)] have been developed recently. Mode-coupling theoretical models have also been developed to study the active micro-rheology of Brownian systems [Gazuz *et al.* (2009); Gnann *et al.* (2011)].

Here particle-scale simulations of active microrheology where a tagged soft particle is pulled through a suspension of soft jammed particles is developed. In the constant velocity case the probe particle always undergoes a consistent directed motion because of the nature of the forcing and thus it cannot be used to investigate the microscopic origins of yielding behavior observed in these soft particle glasses [Wilson *et al.* (2009)]. So a constant external force is applied to the tagged probe particle to drag it through the jammed soft particle suspension, and its response is tracked. The microstructural changes around the probe particle are also determined. Finally, the results from microrheology are connected to the properties obtained from macrorheology.

The rest of the chapter is organized as follows. The simulation technique is described in section 5.2. The simulation results for the tagged particle motion at different forces and suspension concentrations are presented in section 5.3 and the microstructural changes associated with the motion of the tagged particle are presented in section 5.4. The local viscoelastic properties are correlated to the bulk macroscopic properties determined earlier in section 5.5.

5.2 SIMULATION TECHNIQUE

Soft particle glasses are modeled as three dimensional packings of N periodically replicated non-Brownian elastic spheres dispersed in a solvent with viscosity η_s at volume fractions exceeding the random close-packing of hard spheres. The 3D packings are built as described in section 2.3 with a 10% polydispersity and a mean radius R. To study the dynamics of the suspension during active microrheology, a random particle λ is chosen and tagged as the probe particle and it is pulled at a constant external force F in the x-direction as shown in figure 5.1.

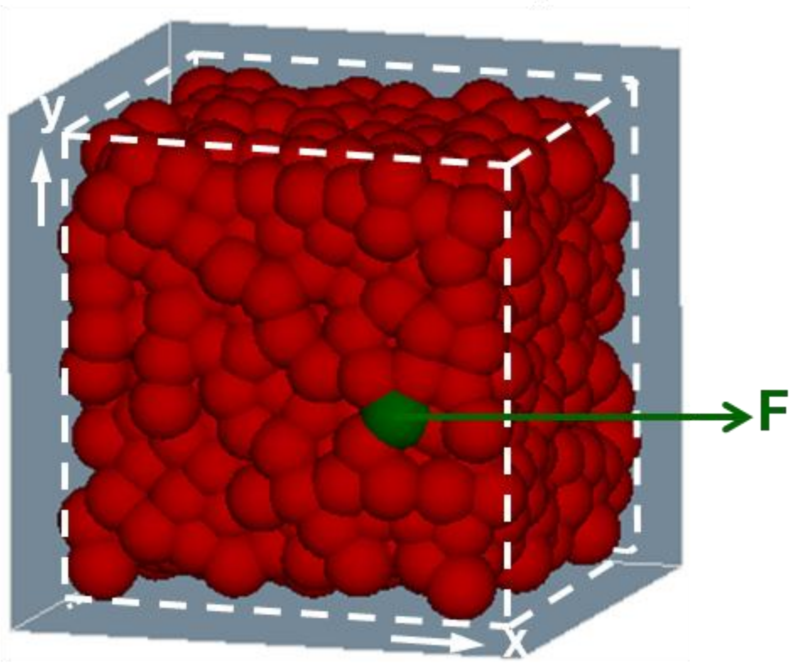

Figure 5.1: Simulation box with a jammed soft particle glass. A tagged particle is pulled with a constant force *F* in the positive *x*-direction

The dynamics of the suspension is modeled using the micromechanical framework described in section 2.2. The elastic repulsion between two particles α and β is modeled with a modified Hertz potential and when the probe particle is pulled through the suspension there is a sheared, thin film of solvent at the facets between the particles which move relative to each other which creates an elastohydrodynamic (EHD) drag force. The form of the elastic repulsion and elastohydrodynamic drag has been described in section 2.2. The particles also experience an effective drag force due to relative motion with the solvent. The tagged particle alone faces an additional force *F* in the *x*-direction due to the external pull. Neglecting particle and fluid inertia, the sum of all forces on each particle is zero. The resulting equation of motion can be made dimensionless by scaling lengths, time and velocity by *R*, η_s / E^* and RE^* / η_s, respectively. It has the form:

$$\frac{d\tilde{\boldsymbol{x}}_\alpha}{d\tilde{t}} = \frac{f_r(\varphi)}{6\pi\tilde{R}_\alpha}\left[\frac{4}{3}C\sum_\beta \varepsilon_{\alpha\beta}^{n}\tilde{R}_c^2\boldsymbol{n}_\perp - \sum_\beta\left(C\tilde{u}_{\alpha\beta,\|}\tilde{R}_c^3\right)^{1/2}\varepsilon_{\alpha\beta}^{(2n+1)/4}\boldsymbol{n}_\| + \left(F\delta_{\alpha\lambda}/E^*R^2\right)\boldsymbol{e}_x\right] \quad (5.1)$$

where $\tilde{\boldsymbol{x}}_\alpha$ is the non-dimensional particle position; $f_r(\phi)$ is a coefficient that accounts for the hindered mobility of particles due to the high concentration and is set equal to 0.01 for these simulations; $\tilde{R}_\alpha$ is the radius of particle α non-dimensionalized by the mean radius *R*; $\varepsilon_{\alpha\beta} = (R_\alpha + R_\beta - r_{\alpha\beta})/R$ is the relative deformation between particles α and β where $r_{\alpha\beta}$ is their center-to-center distance; $\boldsymbol{n}_\perp$ and $\boldsymbol{n}_\|$ are directions perpendicular and parallel to the flat facet at particle-particle contact respectively. $u_{\alpha\beta,\|}$ is their relative velocity parallel to the flat facet at contact; $\delta_{\alpha\lambda}$ is the Kronecker delta function which enforces that the external force is applied only to the tagged probe particle λ. $\mathbf{e}_x$ is the unit vector in the *x*-direction.

These *N* coupled equations of motion were integrated to determine the evolution of the spatial position and velocity of each particle. Periodic boundary conditions were applied. The open source code LAMMPS [Plimpton (1995)] was used to perform the simulations. Packings of 1,000 particles were generated for five different volume fractions 0.7, 0.75, 0.8, 0.85 and 0.9. Each simulation was averaged over five different probe pulls and for long times after steady state was reached. Simulations using 10,000 particles were also performed to confirm the absence of box size effect. The microstructure presented in section 5.4 for volume fraction 0.8 was calculated by averaging over 50 different probe pulls and long times after steady state for a better average.

5.3 TAGGED PROBE PARTICLE MOTION

5.3.1 Position and velocity of tagged probe particle

The position and velocity of the tagged particle was tracked as it was pulled through the suspension with a constant external force *F*. Figure 5.2 shows the velocities, of the tagged particle in *x*-, *y*- and *z*- directions in a suspension of volume fraction 0.8 at small (figure 5.2a) and large forces (figure 5.2b). These are highly jammed suspensions and each particle is surrounded by a cage of other particles with flat facets at particle-particle contact. When the applied force is small, the tagged particle velocities in *x*-, *y*- and *z*- directions oscillate around zero and are of similar small magnitude even at long times. On the other hand at large forces, the velocity in the direction of pull (U_x) is always in the positive *x*- direction or the direction of pull and is of much larger magnitude than U_y and U_z. The probe is pulled with a constant force and not constant velocity and so it can move in lateral directions as well as the direction of pull when it encounters particles in front of it.

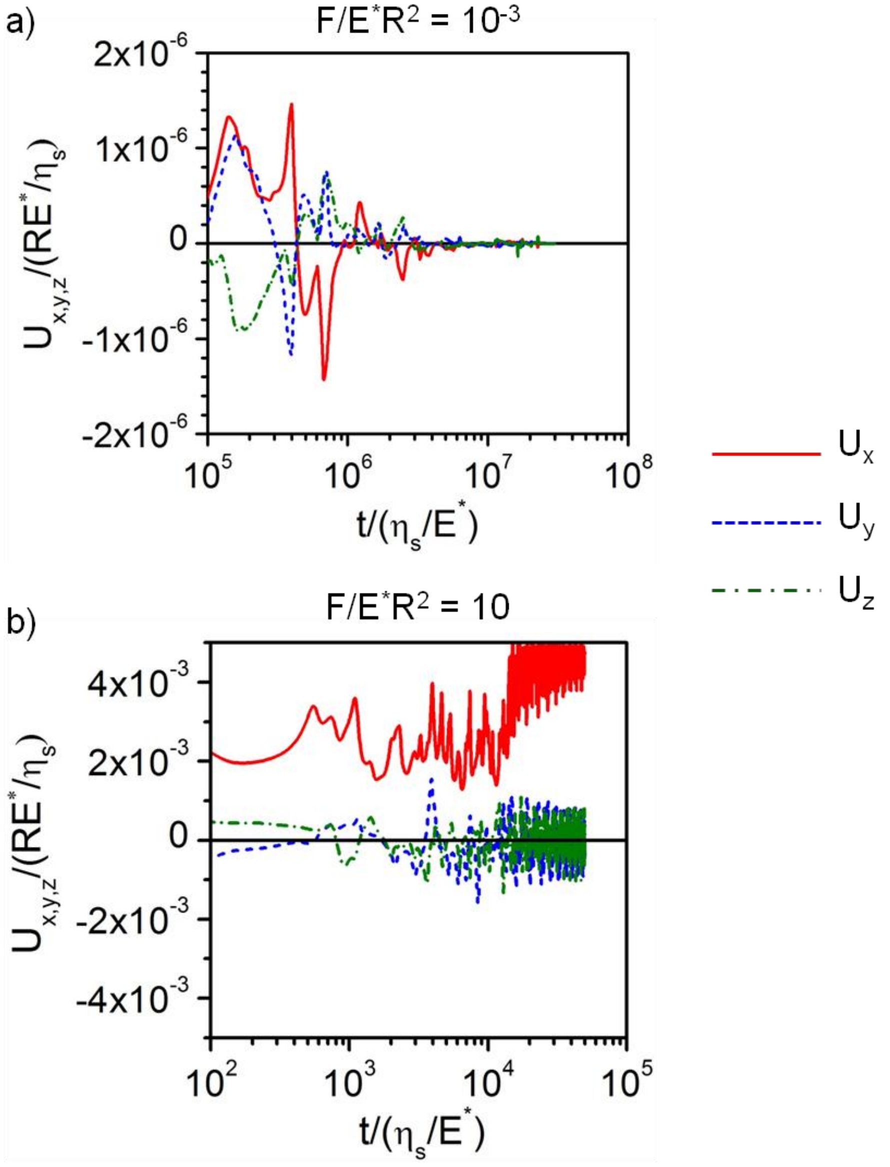

Figure 5.2: Instantaneous velocity U of the tagged particle in x- (red solid lines), y- (blue dashed lines) and z- (green dash dotted lines) direction being pulled through the jammed suspension at small: F=0.001 E^*R^2 (a) and large: F=10 E^*R^2 (b) force; x- is the direction of pull.

The displacement of the tagged probe particle was tracked in *x*-, *y*- and *z*-directions. Figure 5.3 shows the displacements of the tagged particle in a suspension of volume fraction 0.8 at small (figure 5.3a) and large forces (figure 5.3b). Figure 5.3a shows that when the applied external force is small, the tagged particle displacements are less than a particle radius. When the applied force is large the tagged probe particle translates several particle radii in the *x*- direction. Displacement in the *x*- direction is larger than that in the *y*- and *z*- directions due to the dominance of the external pulling force in the same direction.

These results show that there exists a threshold force beyond which the tagged probe particle will escape its cage. When the cage elasticity is stronger than the applied force, the tagged particle just “rattles” inside its cage. When the external force is large enough, the tagged particle overcomes the cage elasticity and moves with a constant average velocity. Thus, the presence of a threshold force and yielding phenomenon at the particle scale is identified.

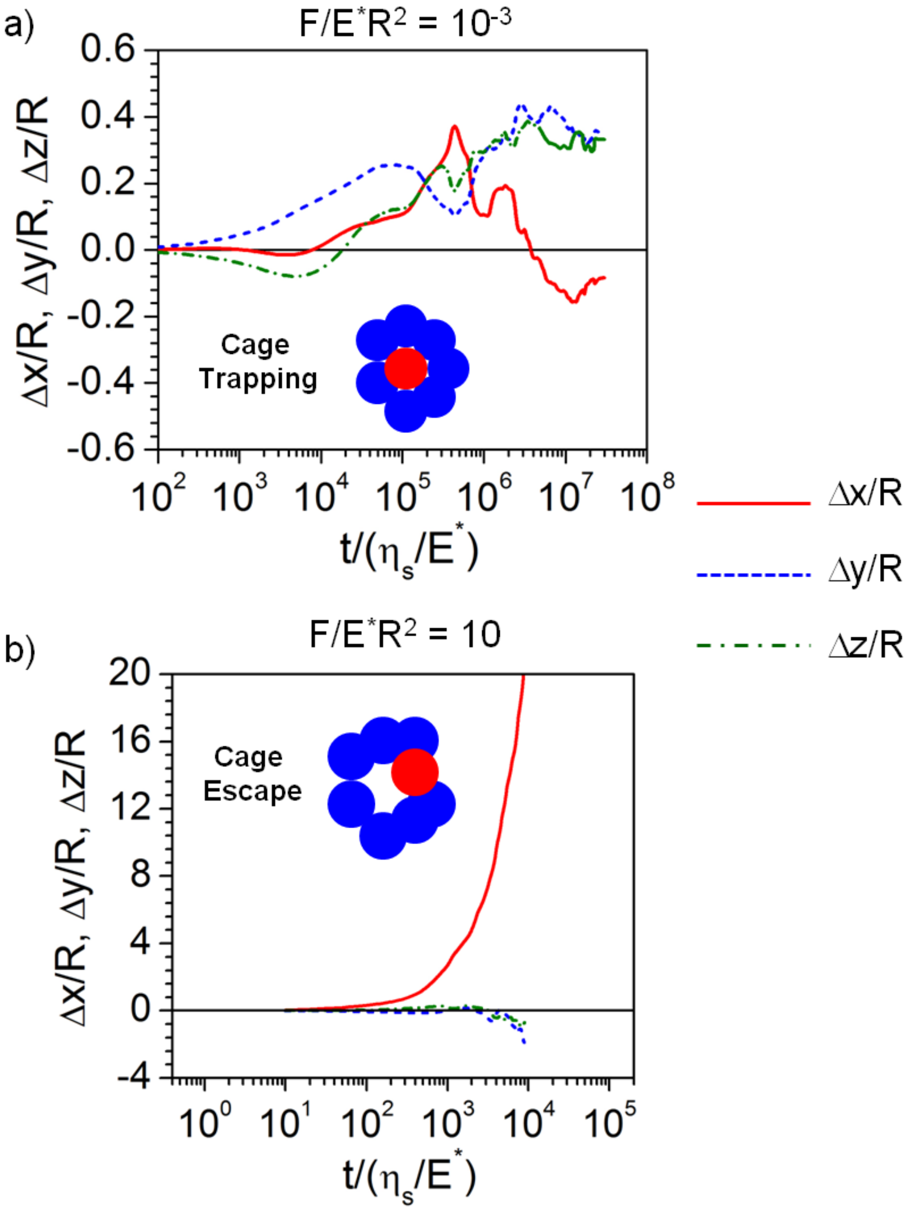

Figure 5.3: Displacement of the tagged particle in *x*- (red solid lines), *y*- (blue dashed lines) and *z*- (green dash dotted lines) directions being pulled through the jammed suspension at small: F=0.001 $E^{*}R^{2}$ (a) and large: F=10 $E^{*}R^{2}$ (b) force. *x*- is the direction of pull.

5.3.2 Force-velocity relationship of tagged probe particle in pull direction

The average velocity of the tagged particle in the direction of pull $\langle U_x \rangle$ is computed for different forces of pulling F. The instantaneous velocities of the tagged particle are time averaged after reaching steady state and then the time average is again averaged over different simulation runs in which different particles were tagged and pulled to get $\langle U_x \rangle$. Figure 5.4 shows the variation of $\langle U_x \rangle$ of the tagged particle for different forces and different volume fractions. For forces less than the threshold force, the magnitude of the average pull velocity is smaller than the standard deviation which spans zero velocity and so the velocity is set to zero.

This threshold force is greater for larger volume fractions as the cage elasticity is higher. Reference slopes of 1 and 2 are also shown in the figure for clarity. Above the threshold force the slope is 2 suggesting that $F \propto \langle U_x \rangle^{0.5}$. It is noteworthy that the elastohydrodynamic (EHD) force at particle-particle contact has the same scaling and this suggests that the EHD forces dominate this regime and the external force acts to counter it when the tagged particle is pulled through the suspension. The EHD forces depend on the particle-particle compression and so for the same external force the tagged particle exhibits a smaller average velocity at larger volume fractions due to the increased resistance. At very large forces a Stokes-like drag scaling: $F \propto \langle U_x \rangle$ is observed and this suggests that this regime is dominated by the external force. The absence of the effect of volume fraction in this large force regime further confirms the domination of the external force in this regime.

Based on the presence of the threshold force and the identification of the EHD and Stokes-like drag dominated regimes the following model is proposed for the force-velocity relationship of the tagged particle in the *x*- direction:

$$\frac{F}{E^*R^2} = \frac{F_y}{E^*R^2} + k_1\left(\frac{U_x}{RE^*/\eta_s}\right)^{0.5} + k_2\left(\frac{U_x}{RE^*/\eta_s}\right) \tag{5.2}$$

where F_y is the threshold force beyond which a particle escapes its cage. The solid lines in figure 5.4 correspond to the numerical fits of this model and the agreement with the simulation data shows that this model captures the physics of the tagged particle motion.

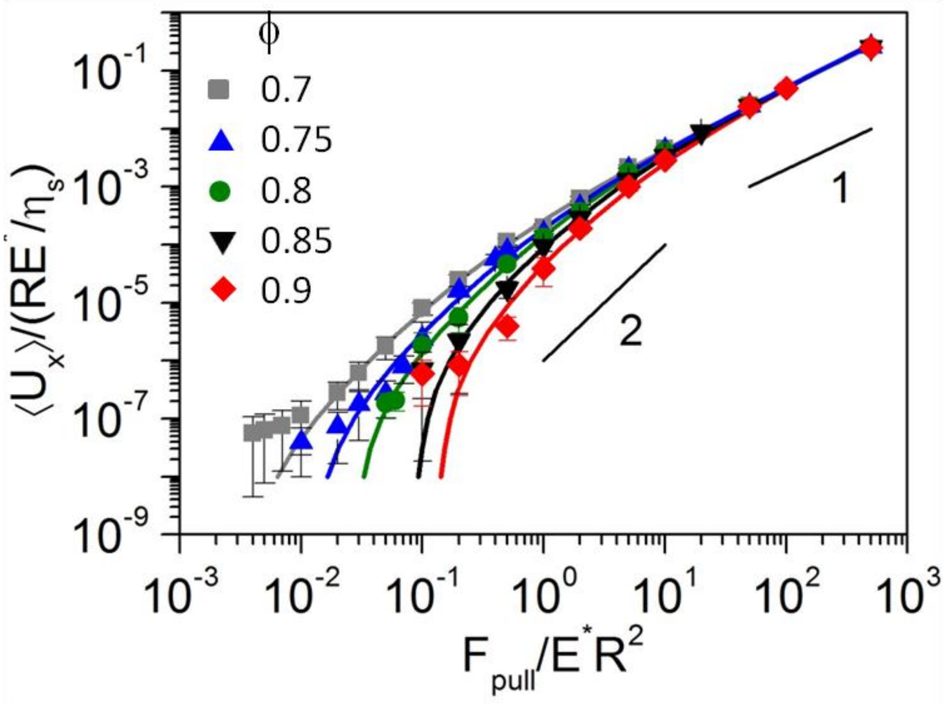

Figure 5.4: The velocity of the tagged particle in the direction of pull (*x*-) at different force of pull for different volume fractions. Slopes of 1 and 2 are indicated for reference. The lines are fits to the model in equation (5.2) based on the observed threshold force and slopes.

The next step is to connect the coefficients of the model in equation (5.2) to the material properties. The threshold force is a measure of the microscopic cage strength and oscillatory shear experiments and simulations (see Chapter 3) on soft jammed suspensions suggest that the elasticity of the cage $G_{cage} \sim G_0$ where G_0 is the low frequency elastic modulus which depends on volume fraction [Mohan *et al.* (2013); Rogers *et al.* (2011b); van der Vaart *et al.* (2013)] The threshold force from equation (5.2) is presented as a function of the low frequency elastic modulus in figure 5.5a and indeed $F_y \approx 1.62 G_0 R^2$.

The coefficient k_1 in the model is associated with the EHD force. The coefficient of the EHD force at particle-particle contact is $\left(CE^*\right)^{1/2} \varepsilon_{\alpha\beta}^{(2n+1)/4}$. This coefficient involves $E^{*1/2}$ which is a measure of elasticity of the particle itself and does not depend on the concentration of the suspension. On the other hand $(G_0/E^*)^{0.5}$ represents the elasticity of the jammed suspension. Figure 5.5b presents the variation of k_1 with $(G_0/E^*)^{0.5}$ and shows that $k_1 \propto \left(G_0/E^*\right)^{0.5}$ which is further confirmed by figure 5.5c In which the dotted line corresponds to a value of 387 which is the slope of k_1 versus $(G_0/E^*)^{0.5}$ in figure 5.5b. This suggests that $k_1 \approx 387\left(G_0/E^*\right)^{0.5}$.

The coefficient k_2 in the model is associated with the hindered stokes drag as described earlier. The hindered stokes drag force $F_{stokes} \sim \frac{6\pi\eta_s R}{f_r(\phi)} U_{particle}$. On non-dimensionalization, $\frac{F_{stokes}}{E^* R^2} \sim \frac{6\pi}{f_r(\phi)}\left(\frac{U_{particle}}{RE^*/\eta_s}\right)$. Figure 5.5d presents the coefficient k_2 for different volume fractions and the dotted line corresponds to the coefficient of $\frac{6\pi}{f_r(\phi)}$ from the definition of the hindered stokes drag. This suggests that $k_2 \approx 6\pi/f_r(\phi)$.

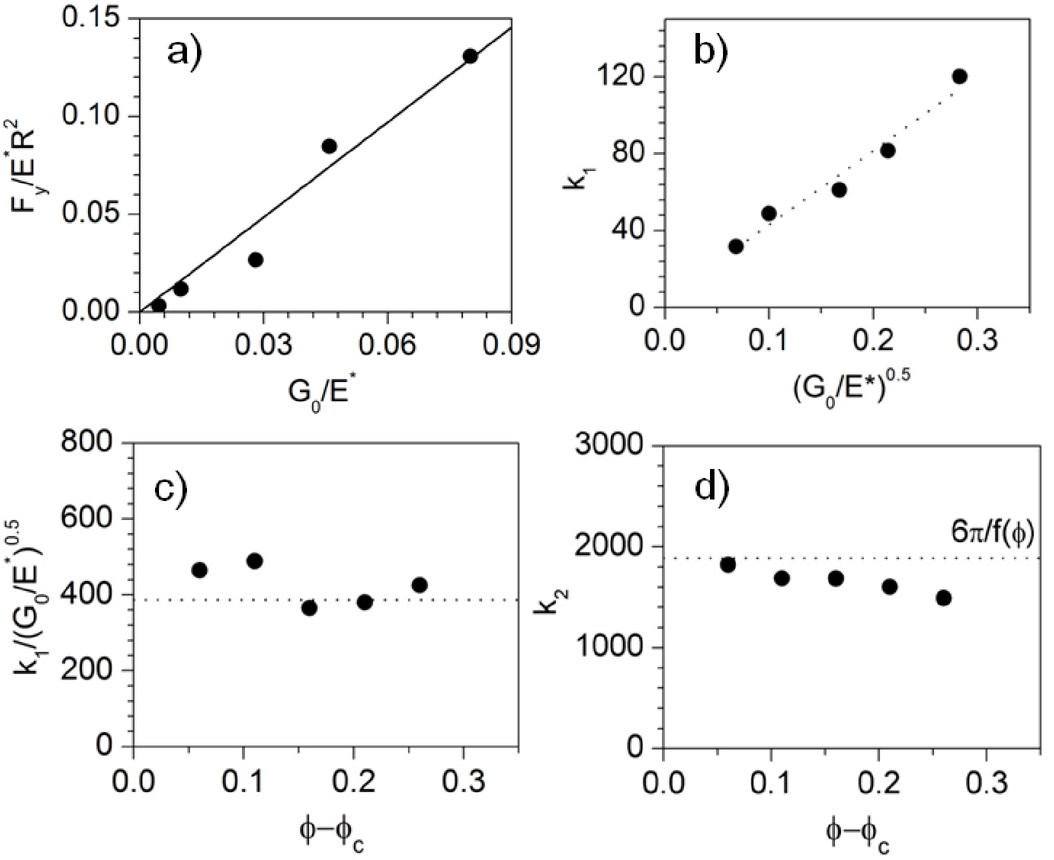

Figure 5.5: Variation of the parameters of the model in equation (5.2). (a) The threshold force vs low frequency elastic modulus from bulk rheology. The line corresponds to a linear fit: $F_y \approx 1.62 G_0 R^2$. (b) Variation of k_1 in the model with $(G_0/E^*)^{0.5}$ and the dotted line corresponds to a linear fit of slope 387. (c) Efficiency of $k_1/(G_0/E^*)^{0.5}$ scaling for different volume fractions and the dotted line corresponds the slope from (b) (d) Variation of k_2 with volume fraction and the dotted line corresponds to the coefficient of the hindered stokes drag.

Now, with $F_y \approx 1.62 G_0 R^2$, $k_1 \approx 387\left(G_0/E^*\right)^{0.5}$ and $k_2 \approx 6\pi/f_r(\phi)$ in the model in equation (5.2) we find that,

$$\frac{F}{G_0 R^2} \approx 1.62 + 387\left(\frac{U_x}{\left(RG_0/\eta_s\right)}\right)^{0.5} + \left(\frac{6\pi}{f_r(\phi)}\right)\left(\frac{U_x}{\left(RG_0/\eta_s\right)}\right) \tag{5.3}$$

Figure 5.6 presents the simulation data for different volume fractions in these new scaled co-ordinates and the master curve in equation (5.3) is presented as a dashed line.

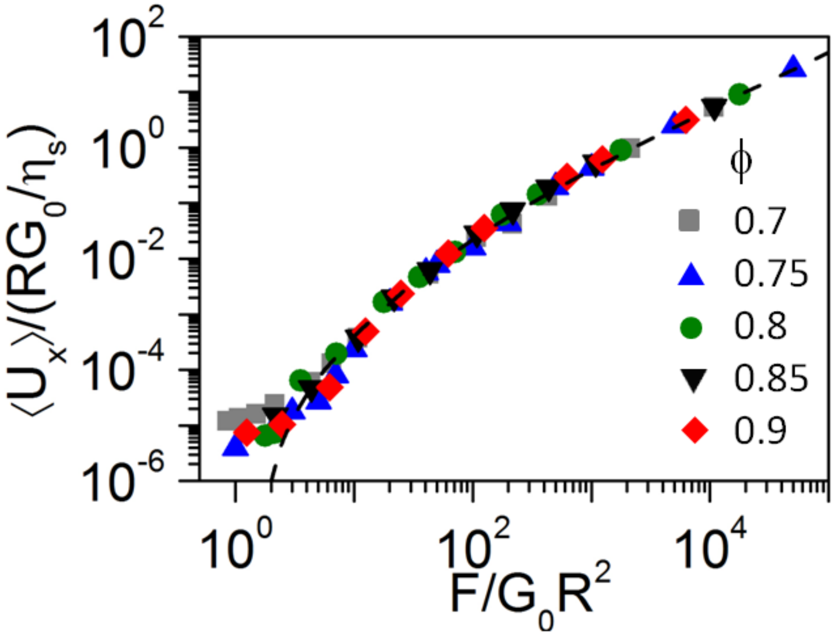

Figure 5.6: Scaled force-velocity master curve. The symbols correspond to simulation data and the dashed line represents the master curve: $\frac{F}{G_0 R^2} = 1.62 + 387\left(\frac{U_x \eta_s}{RG_0}\right)^{1/2} + \frac{6\pi}{f(\phi)}\left(\frac{U_x \eta_s}{RG_0}\right)$.

5.3.3 Force-velocity relationship of tagged probe particle in perpendicular directions

The tagged particle is pulled with a constant force and not constant velocity so it has room to drift laterally to accommodate better the other particles on its way. The signed values of the tagged particle velocities in the *y*- (U_y) and *z*- (U_z) directions oscillate around zero as shown in figure 5.3 and so the average of the absolute values of these velocities will be a better measure of the effect of the external force on the tagged particle motion in perpendicular directions. So in figures 5.7a and 5.7b the ratio of the average velocity of the tagged particle in *x*- and *y*-, and, *x*- and *z*- directions respectively are presented. Firstly, all the volume fraction data collapse considerably suggesting that $\left(RG_0/\eta_s\right)$ might be the relevant scaling for velocities in the *y*- and *z*- directions as well. Secondly, at forces below the threshold force $|U_x| \sim |U_y| \sim |U_z|$ confirming that below the threshold force, the test particle is trapped and is rattling inside the cage. At forces greater than the threshold force the external force exceeds the cage elasticity and the particle moves out of the cage and this transition can be clearly seen in figure 5.7.

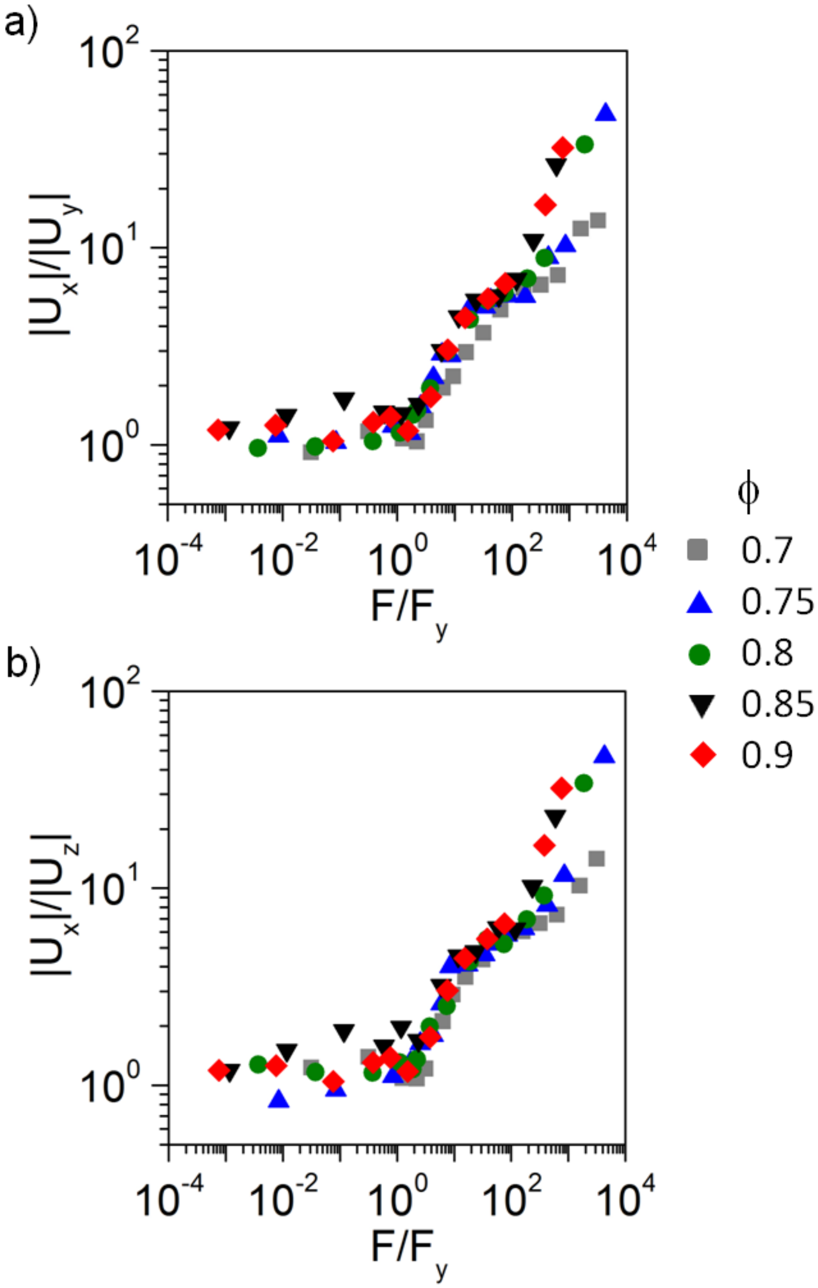

Figure 5.7: The ratio of average magnitudes of velocity of the tagged particle parallel (*x*-) and perpendicular (*y*- a) and *z*- b)) to the direction of pull at different force of pull for different volume fractions.

5.4 MICROSTRUCTURAL CHANGES AROUND TAGGED PROBE PARTICLE

The microstructure at rest is radially symmetric and the most probable radial separation of the jammed constituent particles is less than twice the particle radius [Mohan and Bonnecaze (2012); Mohan *et al.* (2013); Seth *et al.* (2006)]. Figures 5.8 shows the pair distribution around the tagged probe particle pulled in a suspension of $\phi = 0.8$ at different forces in the *x-y* plane (parallel to direction of pull) and *y-z* plane (perpendicular to direction of pull), *x-* being the direction of pull. The white lines represent the radial separation at which the pair probability is maximum (r_m) for the static case. At forces below the threshold force the pair distribution is symmetric and the radial separation at which the pair probability is maximum is the same as the static case value. At forces above the threshold force (where EHD interactions are dominant) there is an accumulation of particles in front of the tagged particles as it tries to push through the particles in front of it and there is a depletion of particles behind the tagged particle as it moves away [Carpen and Brady (2005); Meyer *et al.* (2006); Squires and Brady (2005); Sriram *et al.* (2010)]. The particles in front of the tagged particle are more compressed than the static case. It is noteworthy that this distortion is qualitatively different from the accumulation depletion in compression-extension axes observed in bulk shear flow (see figure 2.A.1). At very large forces the external force is dominant and the particles in front are very highly compressed and pushed away due to the elastic repulsion. Thus neighboring particles accumulate in the plane perpendicular to the pull direction and the paste seems locally fluidized in the direction of motion of the particle which might be the microstructural origin of the linear force-velocity relationship at these large forces. The $g(\mathbf{r})$ including next nearest neighbors is presented in Supplemental Material 5.A. Simulations with 10,000 particle boxes were also performed for volume fraction 0.8 and the force-velocity relationship collapsed on to the data from the other 1,000 particle boxes indicating that this is not a box size effect (Supplemental Material 5.B).

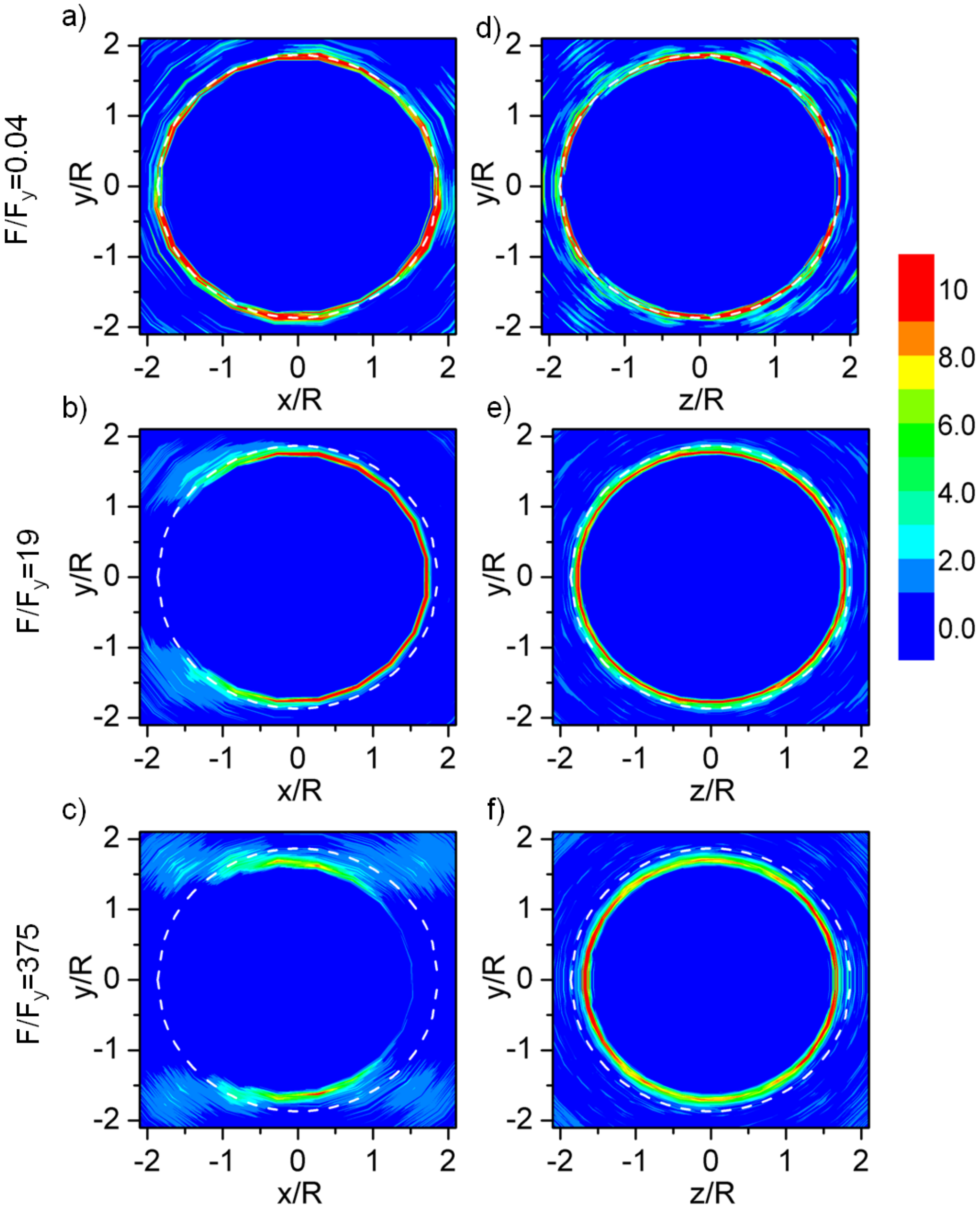

Figure 5.8: Pair distribution function $g(\mathbf{r})$ in the (a-c) x-y plane and (d-f) y-z plane, x-being the direction of pull when the tagged particle is pulled at different forces for $\phi = 0.8$. White lines correspond to the most probable radial separation at rest.

The radially averaged pair distribution function is presented in figure 5.9a. As the external force exceeds the threshold force, the radius of maximum pair density (r_m) between the tagged probe particle and its nearest neighbors decreases and at very large forces (as it goes into the linear stokes regime) r_m becomes constant as the elastic repulsion of the particles do not allow further compression. The number of contacts (N_c) of the tagged probe particle decreases as the probe particle begins to move at forces exceeding the threshold force and becomes constant at very large forces as shown in figure 5.9b. This constancy in r_m and N_c suggests that at very large forces, the microstructural distortion around the probe particle reaches a limit and doesn't change anymore. The variation of the peak of accumulation of particles and the number of contacts from microrheology show good agreement with the results from bulk simulation results of chapter 2 as shown in figure 5.9c and d.

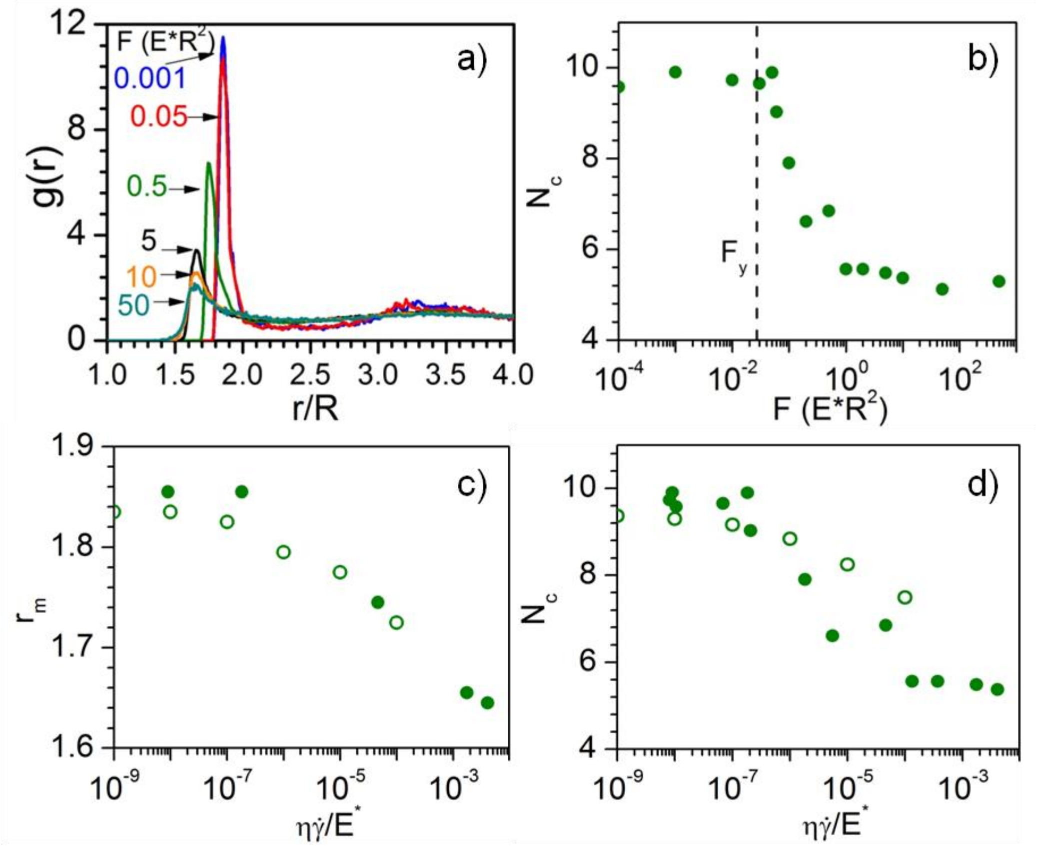

Figure 5.9: Evolution of radially averaged g(r) (a) and number of contacts N_c (b) when the tagged particle is pulled at different forces in a suspension of volume fraction 0.8. Comparison of radius of maximum accumulation (c) and number of contacts (d) from micro- (closed symbols) and macro- rheology (open symbols).

The tagged particle disturbs its neighbors as it is pulled through the suspension. The speed map of its neighbors is presented in figure 5.10a-c. If the external force is smaller than the threshold force the tagged particle is trapped inside its cage and thus it does not move the particles around it. As the external force exceeds the threshold force the particle breaks free of its cage and pushes the particles in front of it and pulls the particles behind it. At very large forces this pushing and pulling intensifies. The average speed of neighbors as a function of distance from the tagged particle is presented in figure 5.10d. As expected, the disturbance is larger in magnitude for larger forces and it is noteworthy that this disturbance extends to the tagged particle’s next nearest neighbors as well. The average speed of neighbors non-dimensionalized by the speed of tagged particle is presented in figure 5.10e. At forces below the threshold force the tagged particle is rattling inside the cage and is as trapped as the other particles in the jammed suspension so the ratio of its average speed to that of its neighbors is close to 1. At forces exceeding the threshold force the tagged particle moves but the disturbance caused by it is much smaller than its own speed.

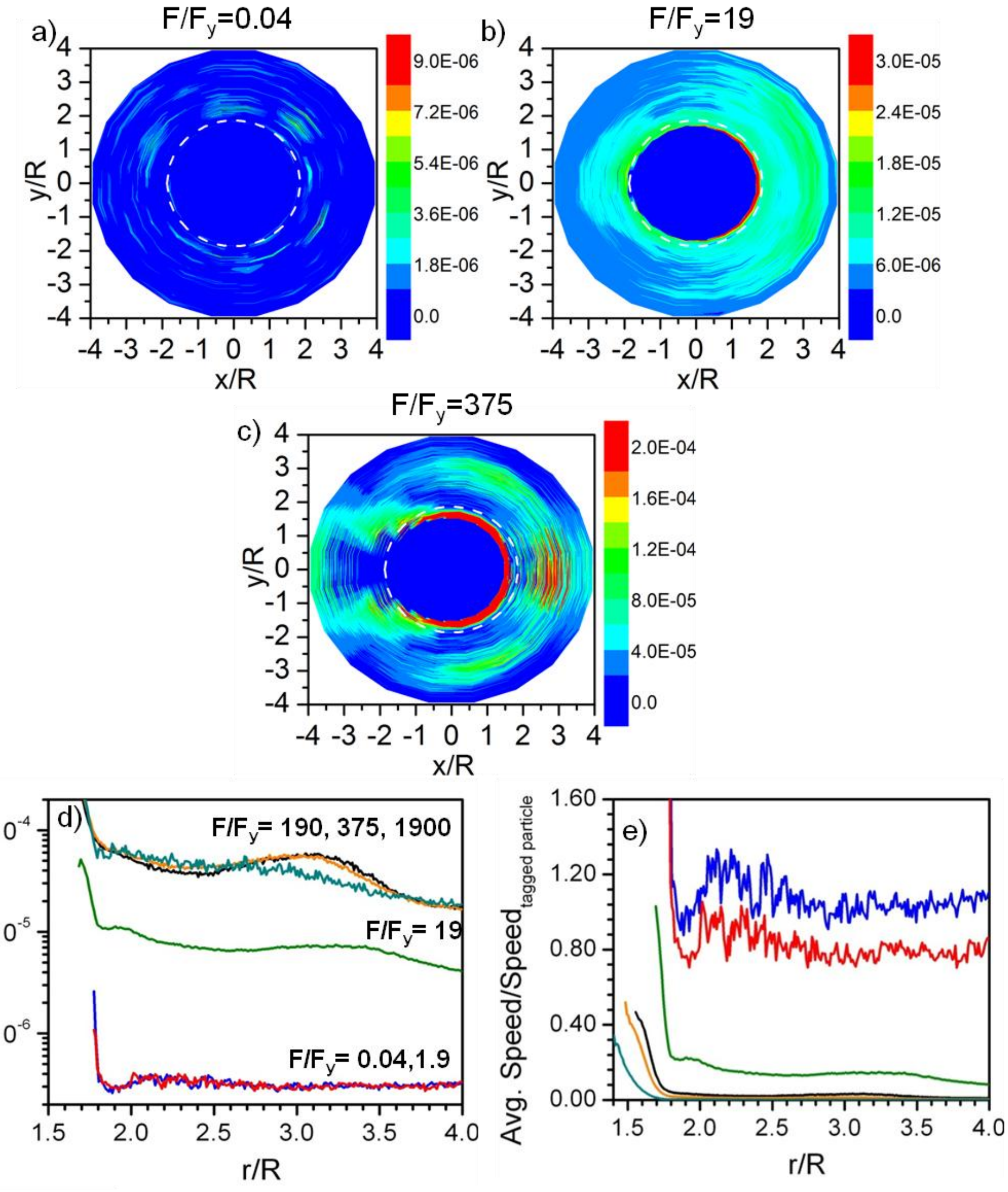

Figure 5.10: (a-c) Map of distribution of speeds around tagged particle when pulled at different forces in a suspension of volume fraction 0.8. The color mapping uses represents the speed and is in units of RE^*/η_s. (d) The average speed of neighbors at volume fraction 0.8. (e) The average speed of neighbors non-dimensionalized by the average speed of the tagged particle itself (colors correspond to scheme in figure 5.9a).

5.5 CORRELATION OF MICRORHEOLOGY TO THE BULKRHEOLOGY

In Chapter 2 the simulations on rheology of bulk steady shear flow and the microstructural analysis showed that the microstructural distortion gave rise to the yield stress and shear thinning. A comparison of the microstructural distortion in micro and macro rheology show that they are qualitatively different and hence it is crucial to connect the properties obtained from microrheology to those from macrorheology in order to use active microrheology as a standalone technique.

Figure 5.11a shows the variation of the threshold force with volume fraction and the variation of the yield stress with volume fraction from Chapter 2. Figure 5.11b shows the direct correlation between the threshold force and the yield stress which further confirms that the yield stress from bulk measurements and the threshold force from microrheology measurements are equivalent information. The motion of a sphere in a Bingham plastic has been numerically investigated by Beris *et al.* (1985) and the critical yield number ($Y = 2\pi R^2 \sigma_y / F$) above which there is no flow was found to be 0.143 which implies that $\sigma_y = 0.143 F_y / 2\pi R^2 = 0.023 F_y / R^2$ and it noteworthy that the slope in the figure 5.11b is 0.027 which is close to this.

Experiments by Atapattu *et al.* (1995) on Carbopol which are microgel based Herschel Bulkley fluids with shear thinning exponent (*p*) close to 0.5 suggest $\sigma_y = 0.183 F_y / 2\pi R^2 = 0.029 F_y / R^2$ and they say that this difference of co-efficient from Beris *et al.* (1985) might be due to the shear thinning nature which is not present in Bingham plastics. Recent magnetic tweezer microrheology experiments of Rich *et al.* (2011) on laponite suspensions which are even more shear thinning than the microgels (*p*=0.95 from bulk measurements) indicate that using $\sigma_y = 0.023 F_y / R^2$ under-predicts the yield stress by 40-50% on comparison to bulk measurements. This suggests that $\sigma_y = 0.038 F_y / R^2$ might be more fitting in their case. The soft particle glasses investigated here exhibit a shear thinning exponent of 0.5 [Seth *et al.* (2011)] and it is noteworthy that the coefficient of 0.027 from our simulation agrees more closely with the experiments of [Atapattu *et al.* (1995)]. Thus the variation in this coefficient seems to be systematic and increasing with increase in the shear thinning exponent. This is not entirely surprising because in a material with a larger shear thinning exponent, the decreased particle resistance is smaller once the probe particle begins to move and hence a smaller external force is sufficient to drag the probe particle. Though small, this effect needs to be kept in mind when extracting a yield stress from microrheological measurements.

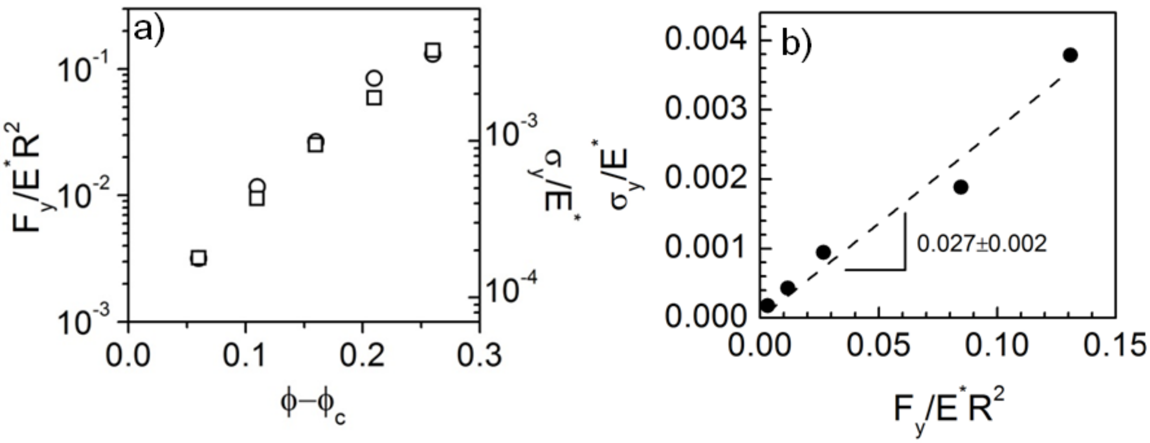

Figure 5.11: (a) The threshold force from microrheology (circles) and yield stress from bulk rheology (squares) as a function of volume fraction. (b) Direct correlation between yield stress from bulk rheology and the threshold force from microrheology.

Once the threshold force is exceeded an effective viscosity of the suspension is computed from the microrheology measurements using a modified Stokes drag law:

$$\left(\frac{\eta_{eff}}{\eta_s}\right)_{micro} = \frac{F/\left(E^* R^2\right)}{6\pi\left\langle U_x/\left(RE^*/\eta_s\right)\right\rangle} \tag{5.4}$$

The local shear rate corresponding to the effective viscosity is chosen as $\dot{\gamma}_{local} = \langle U_x \rangle / R$ and in non-dimensional terms $\eta_s \dot{\gamma}_{local} / E^* = \langle U_x \rangle / \left(RE^*/\eta_s\right)$. The effective viscosity from bulk steady shear simulations of [Seth *et al.* (2011)] is $\eta_{eff,bulk} = \sigma/\dot{\gamma}$. Figure 5.12a shows the effective micro and macro viscosity (from Chapter 2) vs the local and bulk shear rate respectively. The microviscosity captures the shear thinning nature and the exponent of 0.5 which is observed in bulk rheological simulations and experiments of soft particle glasses. Only the lowest (ϕ=0.7) and largest (ϕ=0.9) volume fractions investigated are shown in the main figure for clarity. All other volume fractions follow the same trend and fall in between these two concentrations. The local shear rate for microrheology is fixed by the average velocity of the tagged particle and so for a one on one comparison the macroviscosity is extracted for the same shear rates using the constitutive equation derived in Chapter 2. The direct comparison is shown in figure 5.12b as a parity plot. There seems to be good quantitative agreement between the micro- and macroviscosity. These connections enable microrheology as a viable technique for estimating the yield stress and shear thinning behavior of soft glasses.

Another interesting observation from the microviscosity in figure 5.12a is that it becomes independent of concentration and shear rate at very large pulling forces. This is the regime when the external force dominates and hindered Stokes drag describes the velocity $\frac{F}{E^* R^2} \approx k_2 \frac{U_x}{\left(RE^*/\eta_s\right)}$ where $k_2 \approx 6\pi / f_r(\phi)$ is independent of the local shear rate or concentration (see figure 5.5). In the previous section it was shown that the microstructural distortion does not change with an increase in force at large forces and this implies that the resistance from the other particles does not change with increase in force and this could be at the root of the constant microviscosity in this regime. These high shear rates are not accessible experimentally in bulk rheological measurements (> 10^4 s^{-1}).

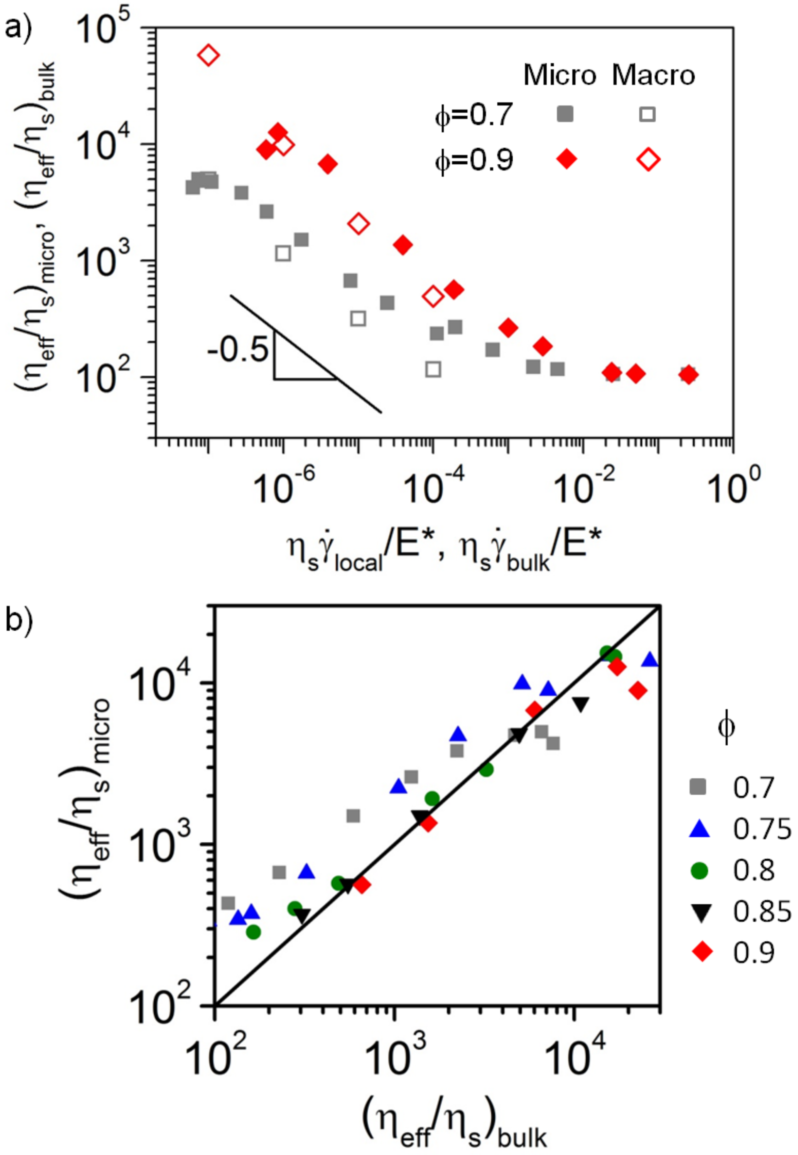

Figure 5.12: (a) The effective viscosity from microrheology (filled symbols) and bulk rheology (open symbols). (b) Direct comparison of effective viscosity from microrheology and bulk rheology for different volume fractions and shear rates

5.6 SUMMARY AND CONCLUSIONS

Particle scale simulations were developed to model the active microrheology of soft particle glasses by pulling a random tagged soft particle with a constant external force and tracking its response. A threshold force is identified below which the tagged probe particle remains trapped in its cage and the microstructure around the particle is symmetric and similar to the static case. Beyond the threshold force the tagged probe particle escapes its cage and exhibits a net positive velocity in the direction of pull. Similar signatures of yielding behavior from microrheology experiments have been observed for concentrated hard sphere suspensions [Habdas *et al.* (2004)] and laponite suspensions [Rich *et al.* (2011)]. In this regime, the neighboring particles accumulate in front of and deplete behind the tagged particle. The force-velocity relationship shows an exponent of 0.5 post yielding where the particle motion is dominated by EHD interactions and our findings include a force-dominated regime independent of concentration at very large forces which are currently not inaccessible with steady shear experiments. In this large force regime the glass is locally fluidized where particles deplete in the pull direction. A similar force dominated linear regime independent of temperature has been observed in microrheology of temperature dependent glassy systems [Winter and Horbach (2013)]. A generalized scaling for the force and velocity data has been identified to obtain a concentration independent master curve for the active micro-rheology of these soft particle glasses.

The microstructural distortion from micro and macro rheology are qualitatively different and thus connecting the information obtained from microrheology to the bulk rheological properties of the material is crucial in interpreting microrheological data [Khan and Sood (2010); Squires and Brady (2005); Wilson *et al.* (2009)]. The findings demonstrate that the threshold force obtained from microrheology is equivalent information to the yield stress obtained from bulk rheological measurements. The shear thinning behavior can be extracted from the effective microviscosity and the values agree well with bulk rheological measurements.

The threshold force here corresponds to $O(G_0R^2)$ and soft particle glasses like microgels and compressed emulsions can have an elastic modulus of 100's or 1000's of Pa. For a material with an elastic modulus of 500 Pa and 200nm radius, the threshold force required would be ≈ 10pN. To reach the shear rates relevant to commercial use the external force required would be $O(100G_0R^2)$ which would be ≈ 1nN. Accessible forces using optical tweezers are limited to the pN range but forces in the range 10pN-10nN are accessible through magnetic tweezers and thus active magnetic methods would be best suited for soft particle glasses [Breuer (2005)]. The effect of the softness of the probe might be a factor in these microrheological measurements, simulations of hard probe particles pulled through soft suspensions will allow determination of the probe particle softness effect. On the experiments side, it might be interesting to synthesize core-shell particles with a magnetic core and a soft shell to maintain the soft contact interactions in these glasses.

The size of the probe particle can also play a role in the measurements made [Meyer *et al.* (2006); Squires and Brady (2005)]. In soft particle glasses the number of contacts of the probe particle can change with the size of the probe and further investigations in this direction are required to determine the effect precisely. Other interesting future directions include using oscillatory pulling forces [Ziemann *et al.* (1994)] to determine if the oscillatory rheology of these glasses could be predicted using microrheology and the use of force pulses [Bausch *et al.* (1999); Ziemann *et al.* (1994)] to investigate the stress relaxation in these materials.

Supplemental Material 5.A: Long Range Microstructure Around Tagged Probe Particle

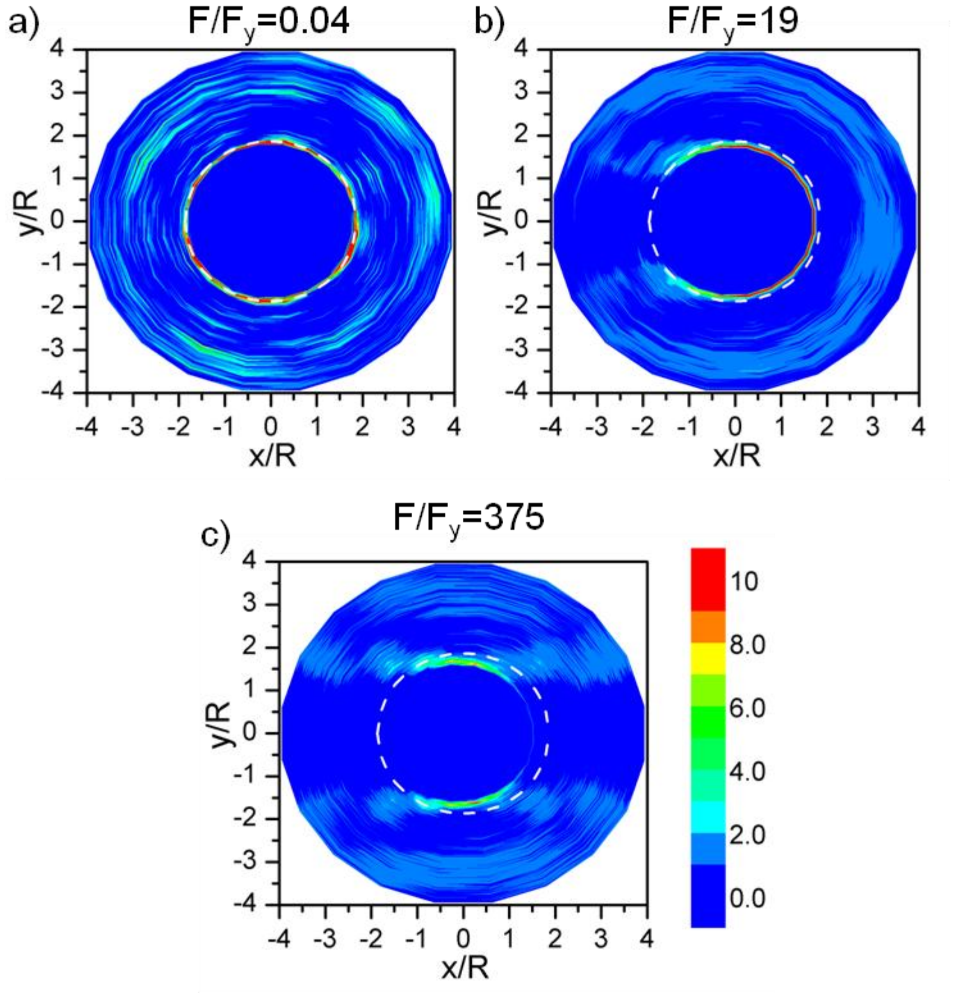

Figure 5.A.1: Long range pair distribution function $g(\mathbf{r})$ in the x-y plane when the tagged particle is pulled at different forces for $\phi = 0.8$. x- is the direction of pull. White lines correspond to the most probable radial separation at rest.

SUPPLEMENTAL MATERIAL 5.B: INVESTIGATION OF BOX SIZE EFFECT

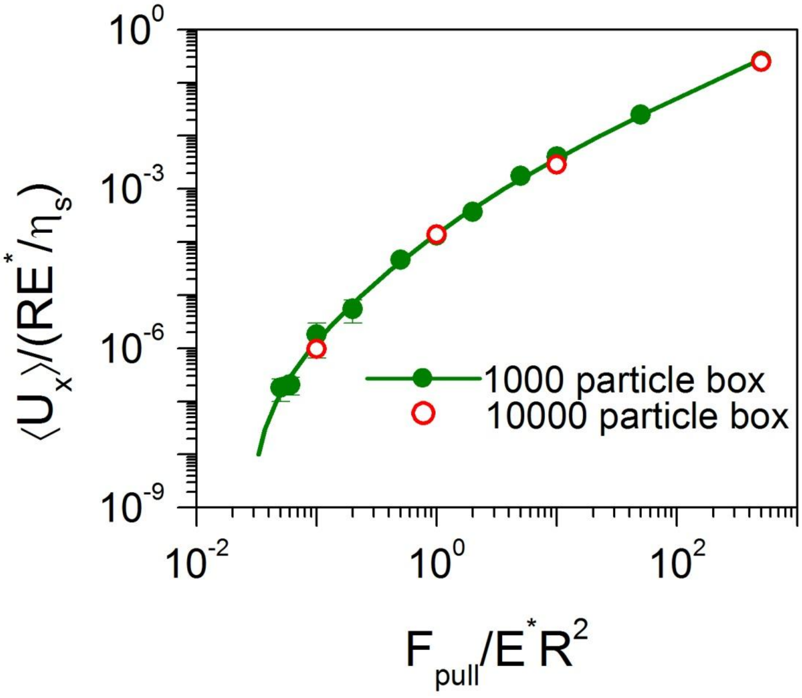

Figure 5.B.1: The velocity of the tagged probe particle at different forces of pull in a suspension of volume fraction 0.8 using a 1000 and 10,000 particle box.

SUPPLEMENTAL MATERIAL 5.C: SIMULATION DATA TABLES

Table 5.C.1 Force-velocity data for probe in volume fraction 0.7

$F/E^* R^2$	$\left\langle U_x / \left(RE^*/\eta_s\right)\right\rangle$	$\mathrm{stdev}\left(U_x/\left(RE^*/\eta_s\right)\right)$
1.00E-04	3.43E-09	1.71E-08
1.00E-03	7.02E-09	3.05E-08
0.004	5.57E-08	5.13E-08
0.005	6.28E-08	5.51E-08
0.007	7.46E-08	6.22E-08
0.01	1.12E-07	8.83E-08
0.02	2.80E-07	1.39E-07
0.03	6.09E-07	3.16E-07
0.05	1.77E-06	7.36E-07
0.1	7.94E-06	1.87E-06
0.2	2.46E-05	5.69E-06
0.5	1.13E-04	1.46E-05
1	1.98E-04	2.95E-05
2	6.26E-04	5.52E-05
5	0.00218	1.38E-04
10	0.00456	2.83E-04
50	0.02509	0.00136

Table 5.C.2 Force-velocity data for probe in volume fraction 0.75

$F/E^* R^2$	$\left\langle U_x/\left(RE^*/\eta_s\right)\right\rangle$	$\mathrm{stdev}\left(U_x/\left(RE^*/\eta_s\right)\right)$
1.00E-04	1.37E-08	2.18E-08
1.00E-03	1.19E-08	4.62E-08
0.01	3.91E-08	2.93E-08
0.02	7.21E-08	5.55E-08
0.03	1.78E-07	1.37E-07
0.05	2.69E-07	1.68E-07
0.07	7.92E-07	3.94E-07
0.1	2.38E-06	2.16E-06
0.2	1.60E-05	2.93E-06
0.4	5.67E-05	1.11E-05
0.5	7.76E-05	1.22E-05
1	1.59E-04	8.67E-06
2	4.43E-04	3.03E-05
10	0.00428	3.37E-04
5	0.00196	1.59E-04
50	0.02493	0.00141
500	0.25898	0.01414

Table 5.C.3 Force-velocity data for probe in volume fraction 0.8

$\mathbf{F/E^{*}R^{2}}$	$\left\langle \mathbf{U_x/\left(RE^{*}/\eta_s\right)} \right\rangle$	$\mathbf{stdev\left(U_x/\left(RE^{*}/\eta_s\right)\right)}$
1.00E-04	1.06E-08	3.50E-08
1.00E-03	9.03E-09	4.93E-08
0.01	8.10E-09	3.57E-08
0.03	6.82E-08	8.16E-08
0.05	1.83E-07	8.28E-08
0.06	2.07E-07	7.52E-08
0.1	1.82E-06	1.17E-06
0.2	5.53E-06	2.54E-06
0.5	4.63E-05	4.64E-06
1	1.33E-04	1.10E-05
2	3.70E-04	3.22E-05
5	0.00174	1.55E-04
10	0.00404	3.23E-04
50	0.02485	0.0014
500	0.25233	0.01369

Table 5.C.4 Force-velocity data for probe in volume fraction 0.85

$F/E^{*}R^{2}$	$\left\langle U_x/\left(RE^{*}/\eta_s\right)\right\rangle$	$\mathrm{stdev}\left(U_x/\left(RE^{*}/\eta_s\right)\right)$
1.00E-04	-1.15E-08	1.01E-08
1.00E-03	2.26E-09	8.67E-08
0.01	-3.03E-09	6.66E-08
0.05	1.22E-07	1.48E-07
0.1	7.00E-07	6.82E-07
0.2	2.18E-06	1.91E-06
0.5	1.75E-05	5.60E-06
1	9.32E-05	1.70E-05
2	2.86E-04	3.26E-05
5	0.00131	1.55E-04
10	0.0034	3.80E-04
20	0.00882	6.16E-04
50	0.02456	0.00141
500	0.25224	0.01369

Table 5.C.5 Force-velocity data for probe in volume fraction 0.9

$\mathbf{F/E^{*}R^{2}}$	$\left\langle \mathbf{U_x} / \left(\mathbf{RE^{*}} / \boldsymbol{\eta}_\mathbf{s}\right)\right\rangle$	$\mathbf{stdev}\left(\mathbf{U_x} / \left(\mathbf{RE^{*}} / \boldsymbol{\eta}_\mathbf{s}\right)\right)$
1.00E-04	-3.67E-09	9.58E-09
1.00E-03	-2.06E-08	3.42E-08
0.01	1.19E-08	1.82E-08
0.05	1.49E-08	2.91E-08
0.1	5.90E-07	4.26E-07
0.2	8.42E-07	5.89E-07
0.5	3.92E-06	1.69E-06
1	3.91E-05	2.01E-05
2	1.88E-04	1.06E-05
5	9.96E-04	1.63E-04
10	0.00289	1.61E-04
50	0.02401	0.00138
100	0.04973	0.00271
500	0.25209	0.01369

Table 5.C.6 Threshold force, k_1, k_2 for different volume fractions

ϕ	$F_y / E^* R^2$	k_1	k_2
0.7	0.00317	31.71443	1823.354
0.75	0.01172	48.80386	1688.481
0.8	0.02668	61.24167	1685.74
0.85	0.08467	81.51242	1602.093
0.9	0.13085	120.2535	1490.746

Note: These are coefficients for fits with the model in equation (5.2) using the data in tables 5.C.1 to 5.C.5 where the average was atleast 1.25 times the standard deviation

Chapter 6: Pairwise Theory for Quiescent Glasses§

6.1 INTRODUCTION

The microstructure of soft particle glasses can be directly connected to the macroscopic rheology of these materials as shown in chapter 2 for steady shear flow and chapter 3 for oscillatory shear flow. The microstructure and its changes with flow also give additional insight on the flow mechanisms at work. Thus, understanding the microstructure of soft particle glasses and developing a method of predicting it would be very useful to determine the macroscopic properties and the microscopic mechanisms at work. The microstructure is embodied by the pair distribution function $g(\mathbf{r})$ which is a local map of the density of pairs of particles. For quiescent glasses the microstructure is radially symmetric and is described by the radial pair distribution function $g(r)$. The dispersed particle sizes in these jammed systems range from a few nanometers [Likos (2006)] to hundreds of micrometers [Fridrikh *et al.* (1996)]. The elasticity of the particles is derived from surface tension, osmotic or entropic/steric forces, depending on their composition [Bonnecaze and Cloitre (2010)]. Despite the different particle sizes and sources of elasticity, these concentrated suspensions of soft particles share many common properties [Bonnecaze and Cloitre (2010); Seth *et al.* (2011)], so a unifying microscopic theory would prove useful in determining the constituent properties and non-dimensional groups that are relevant to understanding the microstructure and rheology of these soft particle glasses.

In these soft jammed suspensions it is the elastic repulsion forces that are dominant and not the thermal forces thus they are referred to as athermal. In the quiescent state when there is no flow and the particle distribution function becomes time

---

§ Much of this chapter has appeared in Mohan L. and R. T. Bonnecaze, "Short-ranged pair distribution function for concentrated suspensions of soft particles," Soft Matter **8**, 4216-4222 (2012) independent, the elastic interactions among the particles at contact determines their microstructure and rheology. Given the microstructure embodied by the pair distribution function, the bulk elastic properties of these concentrated suspensions can be determined, e.g., the high frequency modulus via the Zwanzig-Mountain relationship [Zwanzig and Mountain (1965)]. Since the interaction potentials between soft particles often vanish beyond contact, only the short-ranged pair distribution function (at radial separations less than a particle diameter) is needed to compute their bulk properties.

The athermal nature, ultrasoft interactions and high packing fractions make theoretical determination of the microstructure of these concentrated suspensions of soft particles a challenge. Theories to predict the pairwise distribution function of systems of hard spheres have been developed extensively [Hansen and McDonald (2006); McQuarrie (2000)]. In the case of soft particles, several closure relationships have been coupled with the Ornstein-Zernike relation [Carbajal-Tinoco (2008); Jacquin and Berthier (2010); Lang *et al.* (2000); Louis *et al.* (2000)] to obtain the pairwise distribution function. Hard sphere perturbation theories have been developed for the same, where equivalent diameters with respect to hard sphere systems are chosen based on matching the free energies [Andersen *et al.* (1971); Ben-Amotz and Stell (2004); Jacquin *et al.* (2011); Lado (1984); Mansoori and Canfield (1969); Mon (2002)], Boltzmann factors [Chandler *et al.* (1983)], liquid structure factors [Verlet and Weis (1972)] or second virial coefficients [Hoye and Reiner (2006)] of the system. However, these methods are only applicable at volume fractions below random close packing, where a hard sphere reference states exists. Further, the temperature factor or thermal energy that plays a major role in these theories is not significant in the case of the soft particle suspensions examined here, where the elastic interactions due to the large compressions are dominant, again making it difficult or impossible to apply these theories in practice for highly concentrated, athermal suspensions of soft particles.

Here a microscopic theory is developed to predict the radial pair distribution function $g(r)$ that describes the amorphous structure of these amorphous, jammed systems. The constituent particles are impenetrable and form flat facets at contact and the behavior at these facets determine the properties of these materials. Elastic properties of the soft particle glasses, such as the osmotic pressure and high frequency modulus can be determined from the pairwise radial distribution function [McQuarrie (2000); Zwanzig and Mountain (1965)]. Further, since interaction potentials between soft particles vanish beyond contact, only the distribution function resolved over a short range is needed. The remainder of the chapter is organized as follows. The pairwise theory to predict $g(r)$ is described in section 6.2. A perturbation expansion based analytical approximation is also presented in the same section. Particle scale simulations performed to validate the theory and the insights gained from them are discussed in section 6.3. Theoretical predictions of the short ranged pair distribution function are presented in section 6.4 and the elastic properties that can be calculated from it are presented in section 6.5. The theory is validated by comparison with data from computer simulations and experiments.

6.2 PAIRWISE THEORY - DESCRIPTION

6.2.1 Theoretical approach

A mean-field approach is used where the n-body system is replaced by a two-body problem with an effective mean force. Consider a reference particle located at the origin surrounded by a suspension of compressed soft particles as shown in figure 6.1.

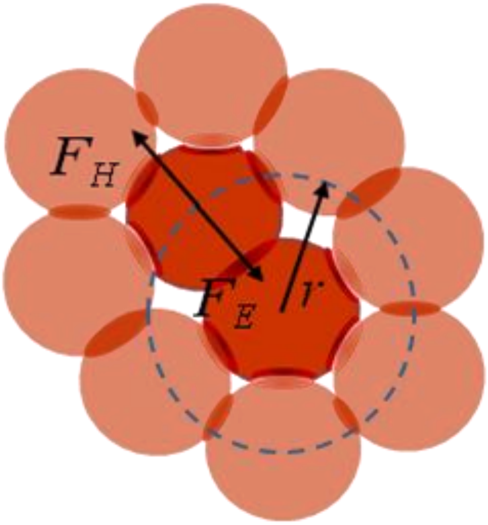

Figure 6.1: Schematic of forces acting on a test particle located a distance r from the reference particle. The forces acting on a particle (dark red) a distance r from the reference particle (dark red at origin) are the pairwise contact force $\boldsymbol{F}_{\mathrm{H}}$ and the effective many body force of the concentrated suspension surrounding the particle $\boldsymbol{F}_{\mathrm{E}}$.

The transport or conservation of mass equation for the pair distribution function $g(r)$ is given by [Batchelor (1977)]:

$$\nabla\cdot\left[g(r)\mathbf{V}(r)\right]=0, \tag{6.1}$$

where $\mathbf{V}(r)$ is the velocity of the test particle, located at r, relative to the reference particle due to elastic forces of all the other particles. This is imagined to be the result of two contributions: the pairwise elastic interaction with the reference particle and the effect of all the other particles surrounding it. Thus, $\mathbf{V}(r)=\mathbf{M}\cdot\left[\mathbf{F}_H+\mathbf{F}_E\right]$ where $\mathbf{M}$ is the mobility of the particles. The pairwise elastic repulsion between the test particle and the reference particle is given by:

$$\mathbf{F}_H(r)=-\frac{du(r)}{dr}\mathbf{e}_r \tag{6.2}$$

where $u(r)$ is the interaction potential between particles and $\mathbf{e}_r$ is the radial unit vector. $\mathbf{F}_E$ is the effective mean elastic force of the bulk suspension acting on the test particle which captures the interaction due to all the other particles. This many body force is postulated as the sum of the pairwise elastic force $\mathbf{F}_H(r_m)$, where r_m is the radius of maximum pairwise density (separation between particles where $\frac{dg(r)}{dr}=0$), and a force analogous to the fluctuating Brownian force in thermal systems [Batchelor (1976)], so that,

$$\mathbf{F}_E(r)=-\mathbf{F}_H(r_m)-\langle U\rangle\nabla\ln g(r), \tag{6.3}$$

where the thermal energy *kT* is replaced by the average elastic energy <*U*>. This average elastic energy depends on the pairwise interaction potential and increases with increasing volume fraction ϕ.

At the stationary state (no flow) the pair distribution function of the suspension is radially symmetric, and thus equation (6.1) becomes,

$$\frac{d}{dr}\left[r^2 g(r)\left(F_H(r)-F_H(r_m)-\langle U\rangle\frac{d\ln g(r)}{dr}\right)\right]=0, \tag{6.4}$$

where $F_H(r)=-\frac{du(r)}{dr}$. Note that the mobility drops out and thus its value is not needed for the remaining analysis. Because the potential vanishes beyond contact, equation (6.4) is only valid for radial positions less than the particle diameter and so only describes the short-ranged pair distribution function. However, only the short-ranged value is needed to compute the bulk properties of the suspension. From the integration of equation (6.4) and the fact that $g(r)$ is finite and continuous, it is found that,

$$g(r)=a(\phi)\exp\left[-\frac{1}{\langle U\rangle}\left[u(r)+F_H(r_m)\left(r-r_m\right)\right]\right]. \tag{6.5}$$

What remains is the determination of the three constants, $\langle U\rangle$, a and r_m, all of which depend on volume fraction. They are determined by the following conditions. First, the average energy $\langle U\rangle$ is proposed to be the energy per contact per particle and is determined self-consistently using the relationship,

$$\langle U\rangle = \frac{\int_0^{2R} 4\pi n r^2 u(r) g(r) dr}{2\int_0^{2R} 4\pi n r^2 g(r) dr}. \qquad (6.6)$$

The factor of two in the denominator is included because each contact is shared between two particles. Second, the number of contacts per particle, N, is also constrained,

$$N = \int_0^{2R} 4\pi n r^2 g(r) dr . \qquad (6.7)$$

It has been found that $N = N_c + K_N\left(\phi - \phi_c\right)^{\nu}$, where $N_c = 6$ is the number of contacts at random close packing, $K_N = 7.7 \pm 0.5$ and $\nu = 0.5 \pm 0.03$ [O'Hern *et al.* (2002); O'Hern *et al.* (2003)]. The constraint on the number of contacts is useful in determining the coefficient $a(\phi)$ in equation (6.5). Finally, the non-dimensional overlap distance $2 - r_m / R$ has been observed to follow the scaling $K_r\left(N - N_c\right)^2$ [van Hecke (2010); Wyart *et al.* (2005)] . A preliminary estimate for K_r can be obtained by the following mass conservation argument. Consider a random close packing of spheres (ϕ_c=0.64) with radius R_{rcp} in a fixed volume V. The random close packing volume fraction $\phi_c = \frac{4/3\pi R_{rcp}^3}{V}$. Imagine the particle radius being increased to R such that the final volume fraction is unity. The final radius $R = \left(\frac{V}{4/3\pi}\right)^{1/3} = R_{rcp}\phi_c^{-1/3}$. Assuming that the spheres were just touching each other at random close packing, the overlap distance $2 - r_m / R$ at the final volume fraction due to the compression is thus given by $\frac{2}{R}\left(R - R_{rcp}\right) = 2\left(1 - \phi_c^{1/3}\right)$. Comparing this to the scaling for the overlap distance and the relationship between number of contacts and volume fraction already available, we find that $K_r \cong 0.013$. Thus using the scaling for r_m in equation (6.5), and self consistently determining $\langle U \rangle$ using equation (6.6), and $a(\phi)$ using equation (6.7), we can determine the short-range pair distribution function for any given volume fraction and interaction potential. In the next section the constants $\langle U \rangle$ and $a(\phi)$ are evaluated by numerical integration.

6.2.2 Analytical approximation using perturbation expansion

The theory requires numerical solution through iterative calculations, and it is insightful to develop an approximate analytical expression of $g(r)$ as follows. For r close to r_m, $u(r)$ can be written as the Taylor-series expansion:

$$u(r) = u(r_m) + u'(r_m)(r - r_m) + \frac{u''(r_m)}{2}(r - r_m)^2 + O\left((r - r_m)^3\right). \tag{6.8}$$

Using this approximation up to the quadratic term in equation (6.5) we find the pair distribution to have the Gaussian form [Seth *et al.* (2006)]:

$$\begin{aligned} g(r) &= a(\phi)\exp\left[-\frac{1}{\langle U \rangle}\left[u(r_m) + \frac{u''(r_m)}{2}(r - r_m)^2\right]\right], \\ &= g_0(\phi)\exp\left[-\frac{u''(r_m)}{2\langle U \rangle}(r - r_m)^2\right]. \end{aligned} \tag{6.9}$$

where,

$$g_0(\phi) = a(\phi)\exp\left[-\frac{u(r_m)}{\langle U \rangle}\right]. \tag{6.10}$$

The constant $a(\phi)$ and thus $g_0(\phi)$ are determined by the constraint on the number of contacts in equation (6.7). Using the form of $g(r)$ in equation (6.9), $a(\phi)$ is determined to be given by,

$$a(\phi) = \frac{N}{4\pi n I} \exp\left[\frac{u(r_m)}{\langle U \rangle}\right] \tag{6.11}$$

where,

$$\begin{aligned} I = {} & \frac{\delta^2}{2} \exp\left(-\frac{\left(4 + r_m{}^2\right)}{\delta^2}\right)\left[\exp\left(\frac{4}{\delta^2}\right) r_m - \exp\left(\frac{4 r_m}{\delta^2}\right)\left(2 + r_m\right)\right] \\ & + \frac{\sqrt{\pi}\delta^3}{4}\left(1 + \frac{2 r_m{}^2}{\delta^2}\right)\left[\operatorname{erf}\left(\frac{r_m}{\delta}\right) - \operatorname{erf}\left(\frac{\left(r_m - 2\right)}{\delta}\right)\right] \end{aligned} \tag{6.12}$$

and the width of the peak of $g(r)$ is given by,

$$\delta = \sqrt{\frac{2\langle U \rangle}{u''(r_m)}} \, . \tag{6.13}$$

The peak value $g_0(\phi)$ can be determined from $a(\phi)$ using equation (6.10).

In general the pairwise interaction potential depends in the overlap, say $u(r) \sim \left(2 - r\right)^{\lambda}$, where λ is some positive exponent. The average elastic energy $\langle U \rangle \sim u(r_m) \sim (2 - r_m)^{\lambda}$. And $u''(r_m)$ is the second derivative of the interaction potential and scales as $(2 - r_m)^{\lambda - 2}$. This makes $\delta \sim (2 - r_m)$. The overlap $\left(2 - r_m\right) \sim \left(N - N_c\right)^2 \sim \left(\phi - \phi_c\right)$ as indicated previously. Thus, the width of the peak scales as $\delta \sim (\phi - \phi_c)$.

6.3 PARTICLE SCALE SIMULATIONS

Particle scale simulations were performed to validate the predictions from the pairwise theory for three different interparticle potentials. Monodisperse 3D packings were built using the technique described in section 2.3. Different interaction potentials were used to build these packings. The three pairwise interaction potentials are listed in Table 6.1 for Hertzian contacts for linearly elastic spheres, the potential for a compressed emulsions and the potential for spheres composed of a non-linear elastic Mooney-Rivlin material. The pairwise elastic repulsion force for these interaction potentials is presented in figure 6.2. These configurations were used to compute the pair distribution functions (*g*(*r*)), osmotic pressure (π) and the high frequency shear moduli (G_∞) using the methodology described in [Seth *et al.* (2006)].

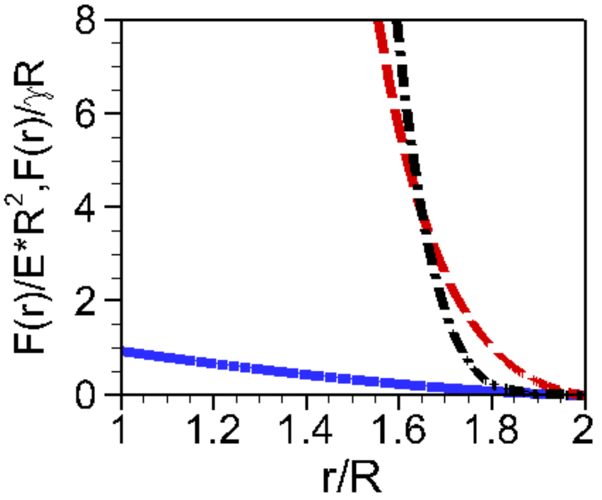

Figure 6.2: Elastic Repulsion forces for hertz potential (solid lines), compressed emulsion potential (dashed) and Mooney-Rivlin material potential (dash-dot)

Table 6.1: Pairwise interaction potential used in simulations.

Interaction Potential	**u(*r*)**	**Parameters**
Hertz Potential [Johnson (1985)]	$\frac{8}{15\sqrt{2}}E^{*}R^{3}\left(2-\frac{r}{R}\right)^{2.5}$	E^{*}-particle contact modulus R - particle radius
Compressed emulsions [Lacasse *et al.* (1996)]	$2\gamma R^{2}C\left(\left(\frac{2R}{r}\right)^{3}-1\right)^{\alpha}$	γ - interfacial tension $C=0.36 \quad \alpha=2.32$
Mooney-Rivlin material[**] [Liu *et al.* (1998)]	$\frac{4}{3\sqrt{2}}\frac{C'}{n+1}E^{*}R^{3}\left(2-\frac{r}{R}\right)^{n+1}$	$C'=1, n=1.5$ for $r/R>1.9$ $C'=31.62, n=3$ for $1.8<r/R<1.9$ $C'=790.57, n=5$ for $r/R<1.8$

The simulations confirm that $N=N_c+K_N\left(\phi-\phi_c\right)^{1/2}$ where $N_c=6$, $\phi_c=0.64$ and $2-r_m/R=K_r\left(N-N_c\right)^{2}$. The constants K_N and K_r were found to depend slightly on the nature of the interacting potential. They were found to be very close to the values in literature and our preliminary estimate cited earlier. Figure 6.3 shows the effect of volume fraction and interaction potential on the number of contacts. Figure 6.3a shows that the number of contacts goes to N_c at random close packing limit and figure 6.3b shows the scaling with volume fraction. Figure 6.4 shows the effect of volume fraction and interaction potential on the overlap at r_m. Figure 6.4a shows that the particle-particle overlap vanishes at random close packing limit and figure 6.4b shows the scaling with number of contacts. The effect of the interaction potential is more evident at higher volume fractions as the particles are more compressed and the interaction energy is more important. Note that the overlap based on the radial separation of maximum pair density is proportional to the overlap based on the average radial separation of pairs of particles (see figure 6.5).

[**] The potential here is $4/\sqrt{2}$ times greater than that used in the dynamic simulations in previous chapters

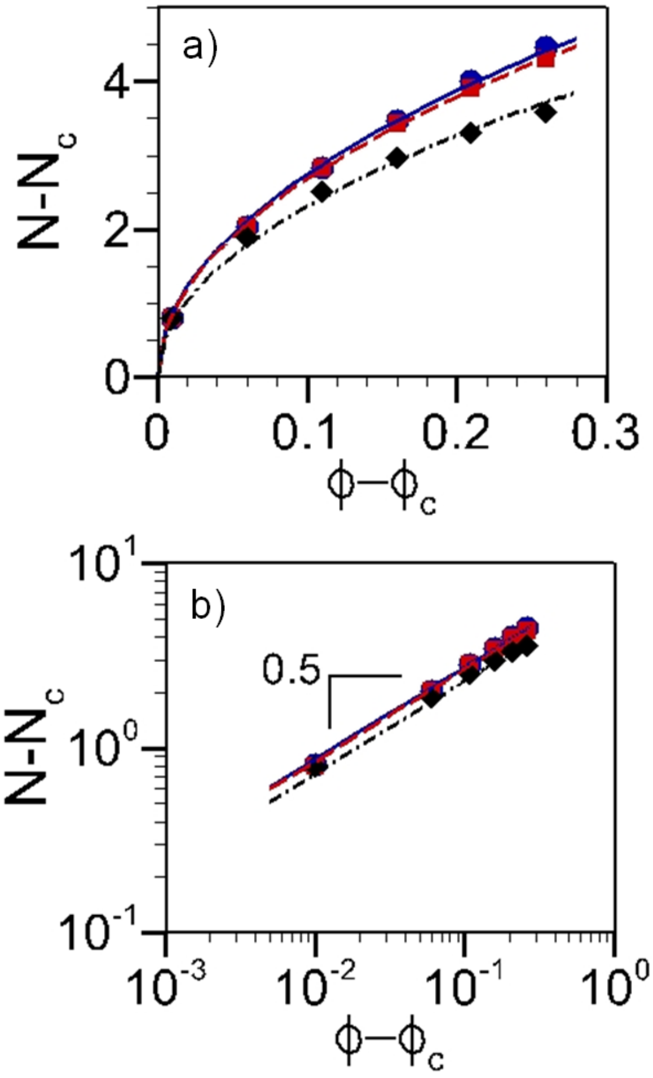

Figure 6.3: Simulation results (symbols) and corresponding models for $N - N_c$. Lines: fits with scaling laws using constants K_N =8.67, 8.49, 7.31 for Hertz (circles), compressed emulsions (squares) and Mooney Rivlin Materials (diamonds), respectively.

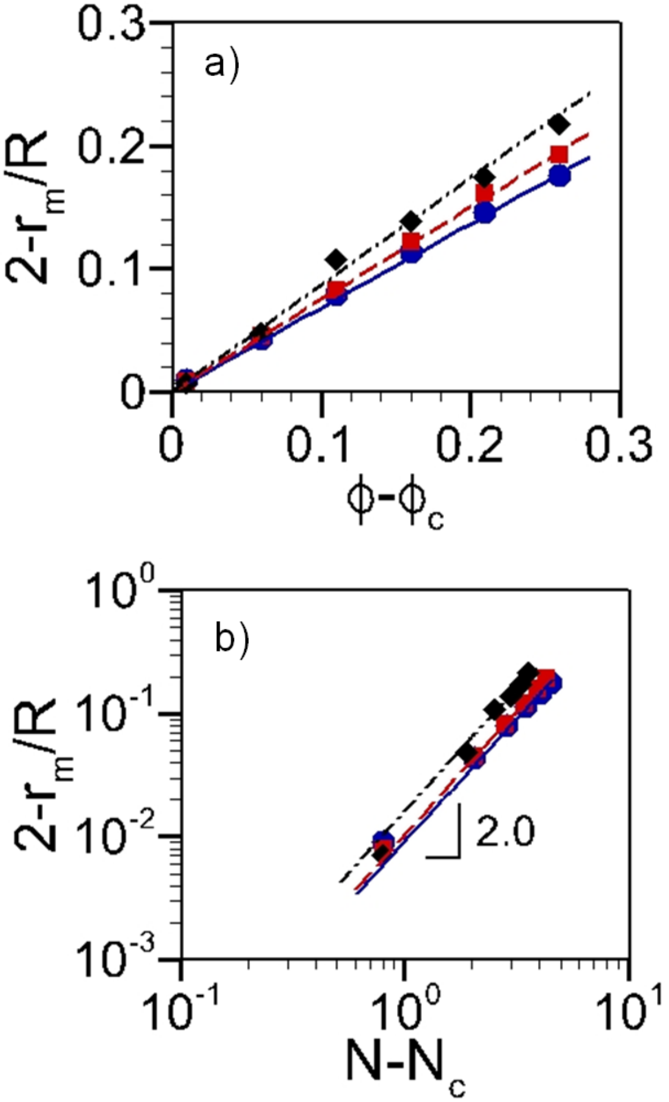

Figure 6.4: Simulation results (symbols) and corresponding models for $2-r_m/R$. Lines: fits with scaling laws using constants K_r=0.0091, 0.0105, 0.016 for Hertz (circles), compressed emulsions (squares) and Mooney Rivlin Materials (diamonds), respectively.

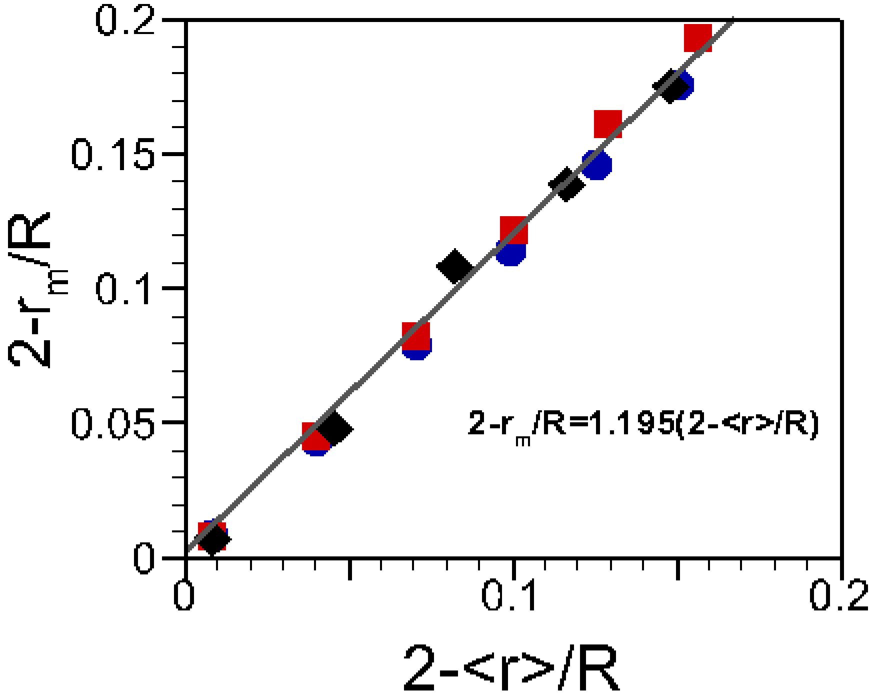

Figure 6.5: Simulation data for comparison of the overlap distance based on the radius of maximum pair density to that based on the average pair separation for Hertz (circles), compressed emulsions (squares) and Mooney Rivlin Materials (diamonds), respectively.

6.4 THEORETICAL PREDICTIONS OF RADIAL PAIR DISTRIBUTION FUNCTION

6.4.1 Average elastic energy

The constants $\langle U \rangle$ and $a(\phi)$ are evaluated by numerical integration to evaluate the radial pair distribution function $g(r)$ in equation (6.5). The self consistently determined values of average energies $\langle U \rangle$ from theory match very closely the values from simulations. The agreement between theoretical predictions and simulation values are shown in figure 6.6a. The average elastic energy vanishes as we move towards the random close packing limit as shown in figure 6.6b, a necessary condition for the pair distribution function to become singular at $\phi_c = 0.64$.

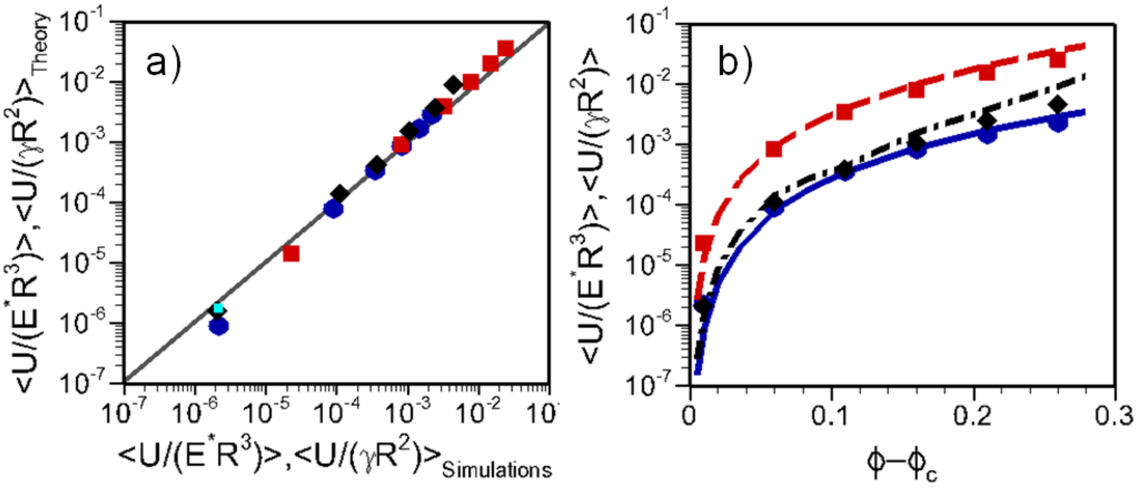

Figure 6.6: (a) Comparison of theoretical predictions (lines) of average elastic energy with simulation results (symbols). (b) Variation of average energy with volume fraction for Hertz (circles), compressed emulsions (squares) and Mooney-Rivlin Materials (diamonds).

6.4.2 Radial pair distribution function *g*(*r*)

Figure 6.7 shows the theoretical predictions of the radial distribution functions computed using equation (6.5) with the three constraints discussed and their comparison to simulation results. Calculations were done with three different pairwise interaction potentials for linear elastic Hertzian spheres, compressed emulsions, and non-linear elastic Mooney-Rivlin spheres as given in Table 6.1. Appropriate values of K_N and K_r were used for each interaction potential. Unlike concentrated hard sphere suspensions, the centers between soft particles can be less than two radii apart. The results have been shown for volume fractions 0.675, 0.7, 0.75, 0.8, 0.85 and 0.9 in the insets and for volume fractions of 0.7, 0.8 and 0.9 in the main figures. Indeed the peak sharpens and narrows as the volume fraction approaches that for hard spheres at random close packing. This transition is shown most clearly, for example, in figure 6.7d for the Hertz potential. For the Hertz potential and compressed emulsions, the peak of $g(r)$ decreases while the spread increases with increase in volume fraction. For a given volume fraction, the spread of the curve is lower for stiffer potentials. In the case of the Mooney Rivlin material at $\phi = 0.9$, compressions > 20% become more likely and the interaction at these compressions becomes stiffer which leads to a narrower $g(r)$ curve with a larger peak. The theoretical predictions closely match the results from simulations and thus validate the theory.

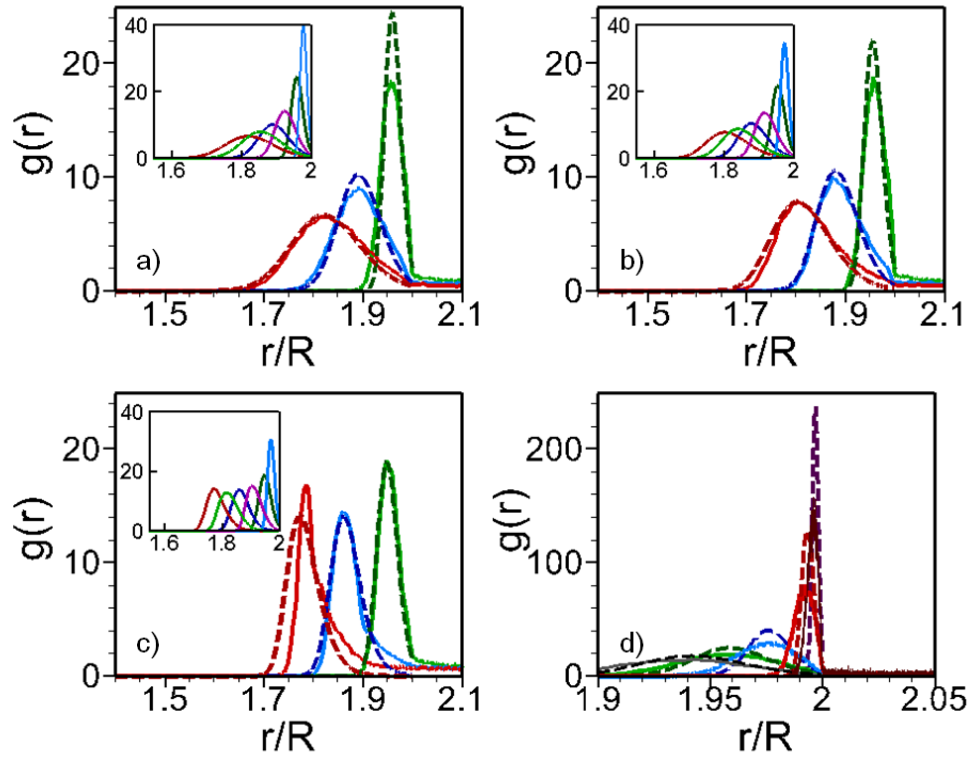

Figure 6.7: Comparison of theoretical predictions from equation (6.5) (dashed lines) of g(r) with computer simulations (solid lines) for (a) Hertz Potential, (b) Compressed emulsions and (c) Mooney-Rivlin Material. Right to left in (a), (b) and (c): volume fraction =0.7, 0.8 and 0.9. Insets: Theoretical predictions for volume fractions 0.675, 0.7, 0.75, 0.8, 0.85 and 0.9 (right to left). (d) Hertz potential – volume fractions 0.645, 0.65, 0.675, 0.7, 0.725 (right to left)

6.4.3 Perturbation expansion based analytical approximation

The analytical expressions for $a(\phi)$, $g_0(\phi)$ and $\delta(\phi)$ determined using the perturbation expansion [equations (6.9)-(6.13)] are plotted as a function of $\phi-\phi_c$ in figure 6.8 and are compared with the numerically evaluated values using equation (6.5). As expected, $a(\phi)$ and $g_0(\phi)$ diverge while the width $\delta(\phi)$ vanishes as $\phi \to \phi_c$, the hard sphere random close packing limit. The scaling for this behavior in the region $\phi-\phi_c = 10^{-3}$ to 10^{-1} are given by:

$$a(\phi) \sim (\phi-\phi_c)^{-0.906\pm0.0144} \tag{6.14}$$

$$g_0(\phi) \sim (\phi-\phi_c)^{-0.933\pm0.0073} \tag{6.15}$$

$$\delta(\phi) \sim (\phi-\phi_c)^{0.986\pm0.0098} \tag{6.16}$$

These scalings are close to those derived by [Jacquin *et al.* (2011)] where it was predicted that the peak of $g(r)$, $g_0(\phi) \sim (\phi-\phi_c)^{-1}$ and that the width of the peak, $\delta(\phi) \sim (\phi-\phi_c)$. Thus, the theory here predicts closely, the behavior of suspensions near the jamming transition as well as for more compressed suspensions.

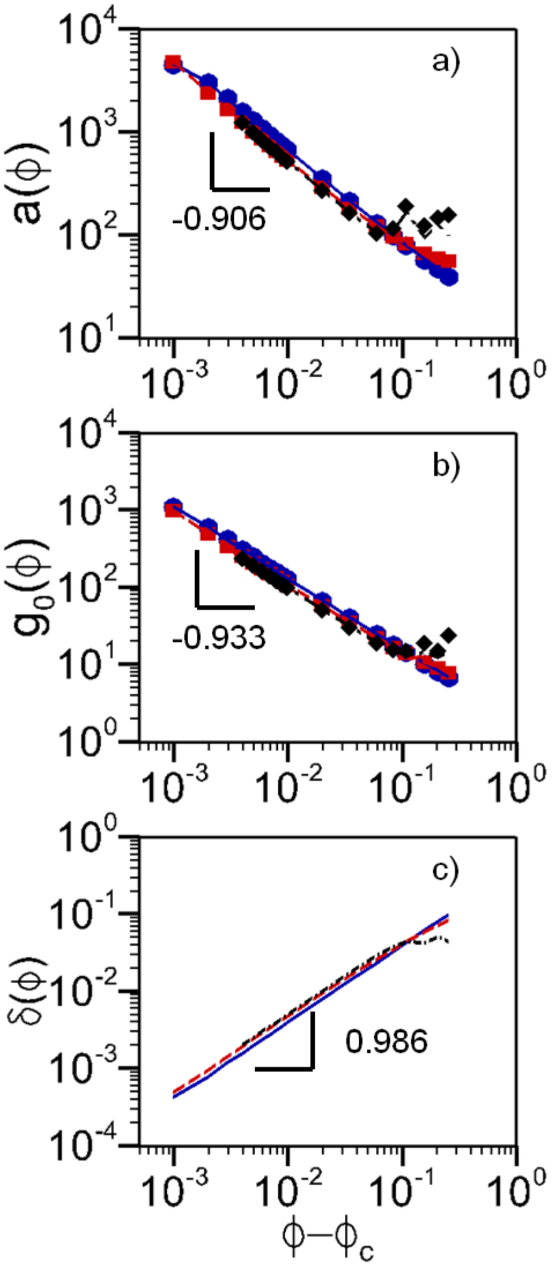

Figure 6.8: Computational (symbol) and analytic (lines) predictions of $a(\phi)$ and peak $g_0(\phi)$ and width $\delta(\phi)$ of $g(r)$ for different volume fractions. (circles/solid lines-Hertz potential, square/dashed lines-compressed emulsion potential, diamonds/dashed-dotted lines-Mooney-Rivlin potential).

From equation (6.9), $\frac{g(r)}{g_0(\phi)} = \exp\left[-\left(\frac{r-r_m}{\delta}\right)^2\right]$ is a universal curve for concentrated soft particle suspensions. Figure 6.9 shows the theoretical curve (black line) and the scaled simulation data. The simulation data has been scaled with the peak, r_m and width from the simulation results. The agreement is good, especially close to r_m since the Gaussian form has been derived using a quadratic expansion of the potential about r_m.

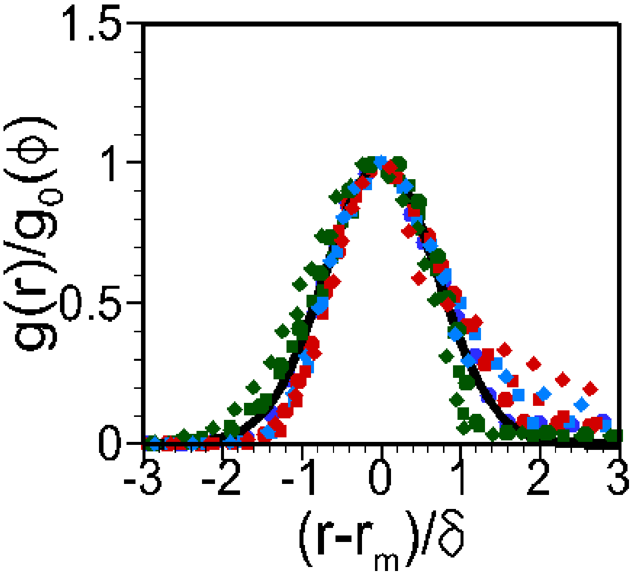

Figure 6.9: Theoretical universal curve (black solid line) and scaled simulation data (symbols). Hertz (circles), compressed emulsions (squares) and Mooney-Rivlin Materials (diamonds). Volume fractions: 0.65 (green), 0.8 (blue) and 0.9(red).

6.5 THEORETICAL PREDICTIONS OF ELASTIC PROPERTIES

Elastic properties of these materials can be predicted using the short ranged pair distribution function $g(r)$. The osmotic pressure π of the suspensions may be determined according to [McQuarrie (2000)]:

$$\pi = -\frac{4\pi n^2}{6} \int_0^{2R} r^3 g(r) \frac{du(r)}{dr} dr . \tag{6.17}$$

The high frequency elastic modulus G_∞ can be computed with the Zwanzig-Mountain formula [Zwanzig and Mountain (1965)]:

$$G_\infty = \frac{2\pi}{15} n^2 \int_0^{2R} g(r) \frac{d}{dr}\left[r^4 \frac{du(r)}{dr} \right] dr. \tag{6.18}$$

Figure 6.10 shows the theoretical predictions of these properties for different interaction potentials as well as predictions from simulations and experimental osmotic pressures for compressed emulsions [Mason *et al.* (1997)] and foams [Princen and Kiss (1987)]. The osmotic pressure and elastic moduli for the Hertzian and compressed emulsion potentials appear to approach a plateau value at the higher concentrations. However, for the Mooney-Rivlin material, the bulk materials stiffen with increasing volume fraction and no such plateau is observed. There is good agreement among the theoretical, computational and experimental values.

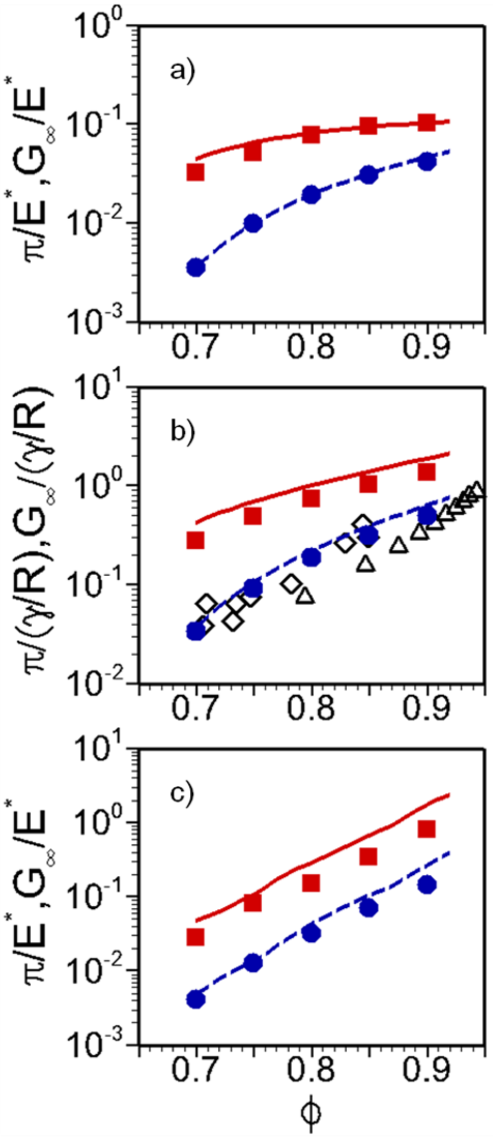

Figure 6.10: Comparison of theoretical predictions (lines) of elastic properties for a) hertz potential, b) compressed emulsion potential and c) Mooney-Rivlin material potential with computer simulations (circles-osmotic pressure and squares-high frequency modulus) and experiments on osmotic pressure of compressed emulsions (diamond) [Mason *et al.* (1997)] and foams (triangle) [Princen and Kiss (1987)]. Upper lines: high frequency elastic modulus and lower lines: osmotic pressure.

6.6 SUMMARY AND CONCLUSIONS

A theory and methodology has been developed to predict the short ranged radial distribution function for athermal, highly concentrated, amorphous suspensions of soft particles based on the transport equation for the distribution function and a component of its flux from a proposed mean elastic force. An analytical approximation for the radial distribution function has also been developed based on perturbation expansion of the elastic energy around radius of maximum pair density r_m. The theory accurately predicts the distribution function for a variety of soft particles compared to computational simulations. The predicted distribution functions can further be used to accurately predict the osmotic pressure and high frequency modulus. The elastic properties and the radial distribution function $g(r)$ do not change significantly for polydispersities upto 20% [Seth *et al.* (2006)]. Thus the theory can be used even for mildly polydisperse systems with the average particle radius. Although the main focus of theory is to predict the microstructure and elastic properties at concentrations much larger than random close packing for hard spheres, the predicted radial distribution function becomes singular with the expected scalings as the volume fraction approaches random close packing. This theory provides a new tool for predicting the microstructure for these concentrated soft particle materials.

SUPPLEMENTAL MATERIAL 6.A: SIMULATION DATA TABLES

Table 6.A.1: Hertz Potential

ϕ	N	r_m/R	$\langle \mathrm{U}\rangle/\mathrm{E}^*\mathrm{R}^2$	π/E^*	$\mathrm{G}_\infty/\mathrm{E}^*$
0.65	6.805	1.992	2.18E-06	0.00026	0.0139
0.7	8.043	1.9565	9.14E-05	0.0036	0.0328
0.75	8.838	1.921	3.60E-04	0.01005	0.0514
0.8	9.469	1.886	8.28E-04	0.01953	0.078
0.85	10.013	1.854	1.47E-03	0.0306	0.0965
0.9	10.472	1.824	2.28E-03	0.0418	0.1024

Table 6.A.2: Compressed Emulsions

ϕ	N	r_m/R	$\langle \mathrm{U}\rangle/\gamma\mathrm{R}^2$	$\pi/(\gamma/R)$	$\mathrm{G}_\infty/(\gamma/R)$
0.65	6.804	1.992	2.33E-05	3.16E-03	0.1183
0.7	8.037	1.955	8.41E-04	3.37E-02	0.2768
0.75	8.828	1.918	3.35E-03	9.36E-02	0.4859
0.8	9.429	1.878	8.03E-03	0.1878	0.7400
0.85	9.915	1.839	1.53E-02	0.3212	1.0294
0.9	10.301	1.807	2.53E-02	0.4991	1.3733

Table 6.A.3: Mooney-Rivlin material

ϕ	N	r_m/R	$\langle \mathbf{U} \rangle / \mathbf{E}^* \mathbf{R}^2$	$\pi / \mathbf{E}^*$	$\mathbf{G}_\infty / \mathbf{E}^*$
0.65	6.804	1.993	2.14E-06	3.03E-04	1.23E-02
0.7	7.8948	1.952	1.14E-04	4.24E-03	2.86E-02
0.75	8.5222	1.892	3.85E-04	1.27E-02	8.29E-02
0.8	8.9718	1.861	1.09E-03	3.28E-02	1.53E-01
0.85	9.3124	1.825	2.50E-03	7.13E-02	3.45E-01
0.9	9.5954	1.782	4.60E-03	1.47E-01	8.15E-01

SUPPLEMENTAL MATERIAL 6.B: THEORY DATA TABLES

Table 6.B.1: Hertz Potential

ϕ	$a(\phi)$ (equation 5)	$\langle U\rangle / E^* R^2$	π / E^*	G_∞ / E^*
0.7	130.418	7.72E-05	3.66E-03	4.38E-02
0.75	77.4092	0.000346	9.89E-03	6.47E-02
0.8	56.8626	0.000872	1.92E-02	8.04E-02
0.85	45.9658	0.00169	3.13E-02	9.29E-02
0.9	39.2681	0.00285	4.63E-02	1.02E-01

Table 6.B.2: Compressed Emulsions

ϕ	$a(\phi)$ (equation 5)	$\langle U\rangle / \gamma R^2$	$\pi / (\gamma / R)$	$G_\infty / (\gamma / R)$
0.7	120.2923	0.00091	3.69E-02	4.26E-01
0.75	81.0637	0.0039	1.057E-01	6.85E-01
0.8	66.3913	0.0099	2.18E-01	9.97E-01
0.85	58.9524	0.0198	3.87E-01	1.385
0.9	54.6925	0.0350	6.32E-01	1.872

Table 6.B.3: Mooney-Rivlin Material

ϕ	$a(\phi)$ (equation 5)	$\langle \mathbf{U} \rangle / \mathbf{E}^* \mathbf{R}^2$	$\pi / \mathbf{E}^*$	$\mathbf{G}_\infty / \mathbf{E}^*$
0.7	103.49	0.000138	4.765E-03	4.74E-02
0.75	190.65	0.000422	1.32E-02	1.05E-01
0.8	92.78	0.00150	4.206E-02	2.836E-01
0.85	131.65	0.00363	1.032E-01	6.591E-01
0.9	93.70	0.00883	2.658E-01	1.701

Chapter 7: Pairwise Theory for Sheared Glasses

7.1 INTRODUCTION

The successful prediction of microstructure and elastic properties for jammed suspensions by the pairwise theory presented in the previous chapter established the wide applicability of this framework. The distortion of this static microstructure by flow causes elastic stresses which are at the root of the yield stress and shear thinning behavior of these soft particle glasses. Thus, developing a microscopic theory for sheared glasses would be useful for increased understanding and to have a faster design tool than simulations to formulate soft particle glasses.

Suspensions of hard particles in shear have been studied theoretically at length and pairwise theories have been developed to explain the microstructural changes and their relation to macroscopic properties [Batchelor (1977); Brady and Morris (1997)]. Mode coupling theory (MCT) [Fuchs and Cates (2002); Fuchs and Ballauff (2005); Hebraud and Lequeux (1998)] and soft glassy rheology (SGR) models [Sollich *et al.* (1997); Sollich (1998)] are theoretical frameworks which explain the flow curves of near hard sphere glasses close to the glass transition. These theories predict the yielding and shear thinning of glassy suspensions but they contain many adjustable parameters which are not directly related to the constituent properties which can be tuned to formulate these suspensions. Also, they do not specifically consider the soft elastic contact repulsions which are at the root of the viscoelastic properties of the highly jammed soft particle glasses. Thus a simple theoretical tool to rapidly describe these materials is in need.

Here the pairwise theory presented in Chapter 6 is extended to include flow effects and is tested to predict the microstructure and rheology of soft particle glasses under shear. An external velocity field is added to the quiescent model and the resulting transport equation is derived for sheared glasses. Appropriate parameters including elastic energy and particle mobility, and, boundary conditions for the governing equation are chosen based on the relevant microscopic properties and the resulting equation is solved using a commercial PDE solver-COMSOL to determine the pair distribution function. Finally, the shear stresses are calculated from the pair distribution function. The remainder of the chapter is organized as follows. The pairwise theory to predict the microstructure under shear is presented in section 7.2 and the theoretical predictions using a particle scale mobility computed from microrheology simulations in chapter 5 is presented in section 7.3. The theoretical predictions show good qualitative agreement with particle simulations but quantitatively they predict higher elastic stresses. The cause for this higher prediction is identified as the particle scale mobility and the theoretical predictions using a larger particle scale mobility is presented in section 7.4.

7.2 PAIRWISE THEORY - DESCRIPTION

7.2.1 Theoretical Approach

The mean-field approach presented in chapter 6 for quiescent glasses is extended to sheared glasses. The many-body system is replaced by a two-body problem with an effective mean force. A reference particle located at the origin is surrounded by a suspension of compressed soft particles under simple shear flow of shear rate $\dot{\gamma}$ as shown in figure 7.1. All particles are considered to be of radius R.

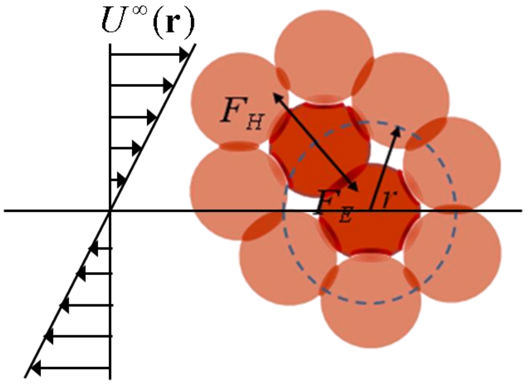

Figure 7.1: Schematic of forces acting on a test particle located a distance *r* from the reference particle under a simple shear flow $U^\infty(\mathbf{r})$. The forces acting on a particle (dark red) a distance *r* from the reference particle (dark red at origin) are the pairwise contact force $\boldsymbol{F}_\mathrm{H}$ and the effective many body force $\boldsymbol{F}_\mathrm{E}$.

The transport or conservation equation for the three dimensional pair distribution function $g(\mathbf{r})$ is given by:

$$\nabla \cdot \left[g(\mathbf{r})\mathbf{V}(\mathbf{r}) \right] = 0 \tag{7.1}$$

where $\mathbf{V}(\mathbf{r})$ is the velocity of the test particle, located at $\mathbf{r}$, relative to the reference particle located at the origin. This velocity is due to elastic forces of all the other particles and the external flow field which in this case is simple shear flow represented by $U^\infty(\mathbf{r}) = \dot{\gamma} y \hat{\mathbf{e}}_x$. The effect of the elastic forces is the result of two contributions as in the static case: the pairwise elastic interaction with the reference particle and the effect of all the other particles surrounding it. Thus, $\mathbf{V}(\mathbf{r}) = U^\infty(\mathbf{r}) + M \cdot \left[\mathbf{F}_H(r) + \mathbf{F}_E(\mathbf{r}) \right]$ where M is the mobility of the particle. The pairwise elastic repulsion between the test particle and the reference particle is given by: $\mathbf{F}_H(r) = -\dfrac{du(r)}{dr}\mathbf{e}_r$ where $u(r)$ is the pairwise interaction potential. This force can be written as a perturbation expansion around $\mathbf{F}_H(r_m)$, where r_m is the radius of maximum pairwise density at rest (separation between particles where $\frac{dg(r)}{dr} = 0$ at equilibrium):

$$\boldsymbol{F}_H(r) = \boldsymbol{F}_H(r_m) + \boldsymbol{F}'_H(r_m)(r - r_m) + \frac{\boldsymbol{F}''_H(r_m)}{2}(r - r_m)^2 + O\left((r - r_m)^3\right). \tag{7.2}$$

$\boldsymbol{F}_{\mathrm{E}}(\mathbf{r})$ is the many body force as before but now it depends on the three dimensional pair distribution function $g(\mathbf{r})$: $\mathbf{F}_E(r) = -\mathbf{F}_H(r_m) - \langle U \rangle \nabla \ln g(\mathbf{r})$; $\langle U \rangle$ is the average elastic energy.

The governing equation thus takes the form:

$$\nabla \cdot \left[g(\mathbf{r}) \left[U^{\infty}(\mathbf{r}) + M \cdot \left(\boldsymbol{F}_H(r) - \boldsymbol{F}_H(r_m) - \langle U \rangle \nabla \ln g(\mathbf{r}) \right) \right] \right] = 0 . \tag{7.3}$$

7.2.2 Numerical Implementation

For a given interaction potential and steady shear flow r_m, $\langle U \rangle$ and M are required to determine the governing equation above. r_m is a function of volume fraction and can be determined using the scaling presented in Chapter 6 and $\langle U \rangle$ is the elastic energy per particle per contact as in the static case and is self consistently determined using the following integrals over the entire domain:

$$\langle U \rangle = \frac{\int_{domain} n u(r) g(\mathbf{r}) dV}{2 \int_{domain} n g(\mathbf{r}) dV} \tag{7.4}$$

where n represents the number density of particles and is a function of volume fraction ϕ. M is initially chosen as the particle scale mobility computed from the microrheology simulation results in Chapter 5 where a tagged particle is pulled at a constant force through the jammed soft particle glass. Using equation (5.3) from Chapter 5,

$$M = \frac{U_x}{F} = \frac{1}{1.62\left(\frac{G_0 R^2}{\dot{\gamma} y}\right) + 387\left(\frac{G_0 \eta_s R^3}{\dot{\gamma} y}\right)^{0.5} + \left(\frac{6\pi\eta_s R}{f_r(\phi)}\right)} \tag{7.5}$$

where F is the force of external pull, U_x is the velocity in pull direction in response, G_0 is the low frequency elastic modulus, η_s is the solvent viscosity and $f_r(\phi)$=0.01 as in the particle scale simulations. This mobility is again a function of velocity and the appropriate velocity is chosen as the external steady shear flow $U^{\infty}(\mathbf{r}) = \dot{\gamma} y \hat{\mathbf{e}}_x$ and thus M is a function of the y- co-ordinate.

The computational domain around the reference particle where the test particle could be in contact with the reference particle is a sphere of radius 2R around the centre of the reference particle. All the flow induced asymmetries are assumed to occur in the layer of contact between particles and the pair distribution function is chosen to be a constant over the surface r=2R. This constant is chosen such the number of particles in contact with the reference particle is the same as the number of contacts per particle in the static case:

$$N = \int_{domain} n g(\mathbf{r}) dV \; . \tag{7.6}$$

The shear stress σ is computed from the pair distribution function as:

$$\langle \sigma \rangle = -\frac{n^2}{2} \int_{domain} \left(\frac{xy}{r}\right) \boldsymbol{F}_H(r) g(\mathbf{r}) dV \tag{7.7}$$

The computational domain used in the PDE-solver COMSOL is presented in figure 7.2 and is 1/4th of the entire domain due to prevailing symmetries. Symmetry boundary conditions are used on the other surfaces as shown in figure 7.2.

The elastic energy $\langle U \rangle$ is initially chosen based on the elastic energy at equilibrium presented in Chapter 6: $\langle U \rangle = 2\langle U \rangle_{eq}$ and equation (7.3) is solved using the boundary conditions mentioned. This solution is then iterated using the new elastic energy obtained using equation (7.4) until convergence is achieved. Other starting elastic energies were also tested to produce similar results (see Supplemental Material 7.A).

The computational domain was meshed with 95000 elements and was tested for convergence using 160,000 elements (see Supplemental Material 7.A).

The compressed emulsion potential $u(r) = 2\gamma R^2 C\left(\left(\frac{2R}{r}\right)^3 - 1\right)^\alpha$, where γ is the interfacial tension, $C = 0.36$ and $\alpha = 2.32$ is used for testing the theoretical predictions. Out of the three interaction potentials used for testing the pairwise theory for soft glasses in Chapter 6 this was chosen as it closely represented the interaction in compressed emulsions which is a soft particle glass with particle contact modulus $E^* = 9.92\gamma/R$ for comparison with particle scale simulations in Chapter 2 and this interaction potential and all higher derivatives are continuous across the domain which simplifies the use of the perturbation expansion for the elastic force in equation (7.2).

Linear and quadratic terms were used in the theoretical predictions presented in sections below and the convergence was tested using cubic terms (see Supplemental Material 7.A).

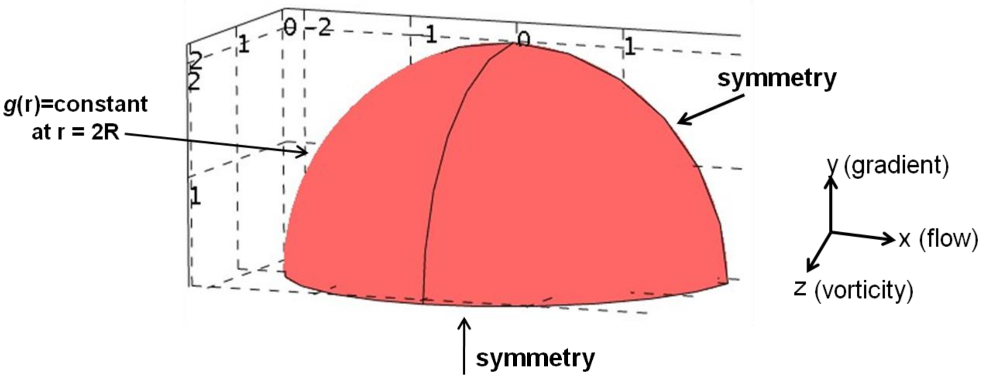

Figure 7.2: Computational domain (distance in units of *R*) and boundary conditions used to solve the governing equation (7.3) in the PDE-solver COMSOL

7.3 THEORETICAL PREDICTIONS USING MOBILITY FROM MICRORHEOLOGY

7.3.1 Prediction of microstructure

Figure 7.3 presents the microstructure for three different shear rates for a volume fraction of 0.8. There is an accumulation of particles in the compressive quadrant and depletion of particles in the extensive quadrants. But the distortion is much higher for low shear rates as compared to the particle scale simulations in Chapter 2.

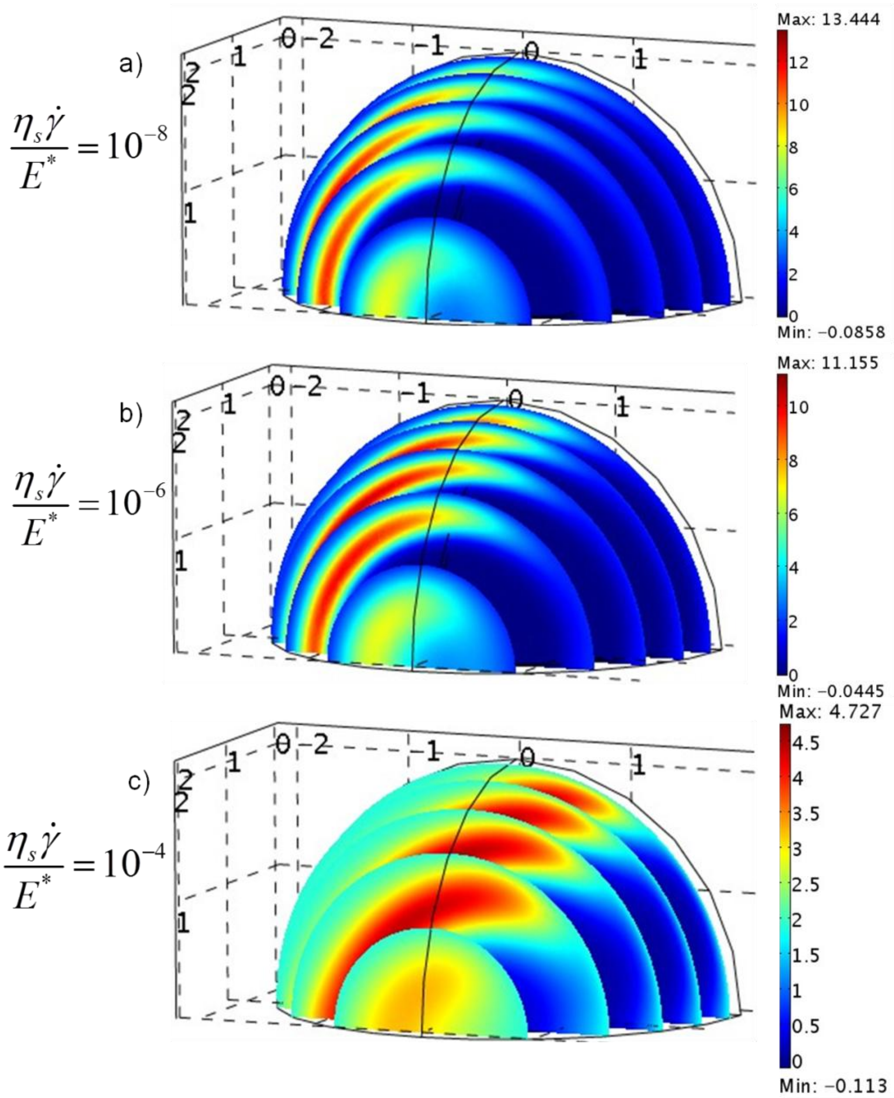

Figure 7.3: Theoretical prediction of pair distribution function $g(\mathbf{r})$ for sheared glasses of volume fraction 0.8 using particle mobility from microrheology

7.3.2 Prediction of flow curve and comparison to simulations

Figure 7.4 presents the steady shear stress computed from the microstructure presented above for a volume fraction of 0.8. The theory qualitatively predicts the presence of a yield stress and shear thinning at high shear but quantitatively the theory over predicts the stress as compared to the particle scale simulations from Chapter 2 which were in good quantitative agreement with experiments. Now, the mobility from microrheology was computed through simulations where a single tagged particle was pulled through a jammed suspension whereas in steady shear flow all the particles are moving and each particle pushes the others around and this would give rise to a collective increase in mobility which could be the cause of the stress over prediction. The governing equations were solved again with a higher mobility to check this hypothesis.

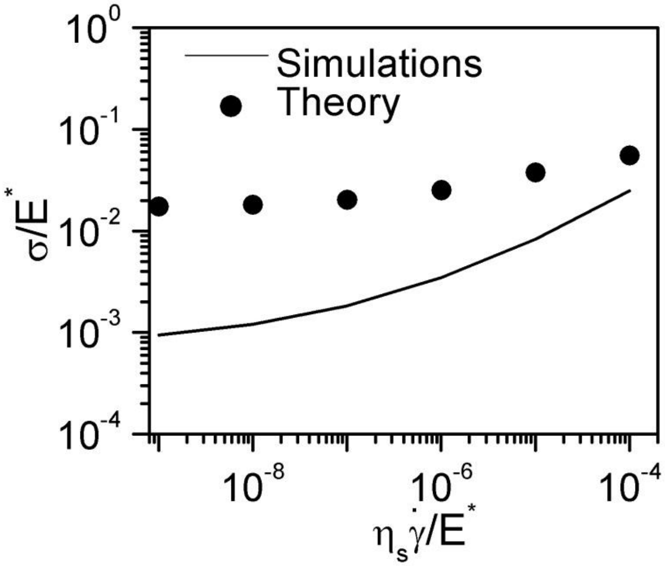

Figure 7.4: Theoretical prediction of flow curve using mobility from microrheology (circles) and comparison to particle scale simulations from chapter 2 (line)

7.4 THEORETICAL PREDICTIONS USING A HIGHER MOBILITY

7.4.1 Prediction of microstructure

Figure 7.5 presents the microstructure for three different shear rates for a volume fraction of 0.8 computed using a higher mobility (15 times) than that obtained from microrheology simulations in chapter 5. The extent of accumulation of particles in the compressive quadrant and depletion of particles in the extensive quadrants has reduced from the previous case. A direct comparison made between the theoretical predictions of the pair distribution function and the particle scale simulation results from Chapter 2 in figure 7.6 shows reasonable agreement. The numerical convergence of these results was checked by using more iterations, higher number of elements in the model, adding higher order terms in the definition of elastic force and starting the iteration with a different elastic energy and is presented in Supplemental Material 7.A. The relevant solver parameters and grid sizing is presented in Supplemental Material 7.B.

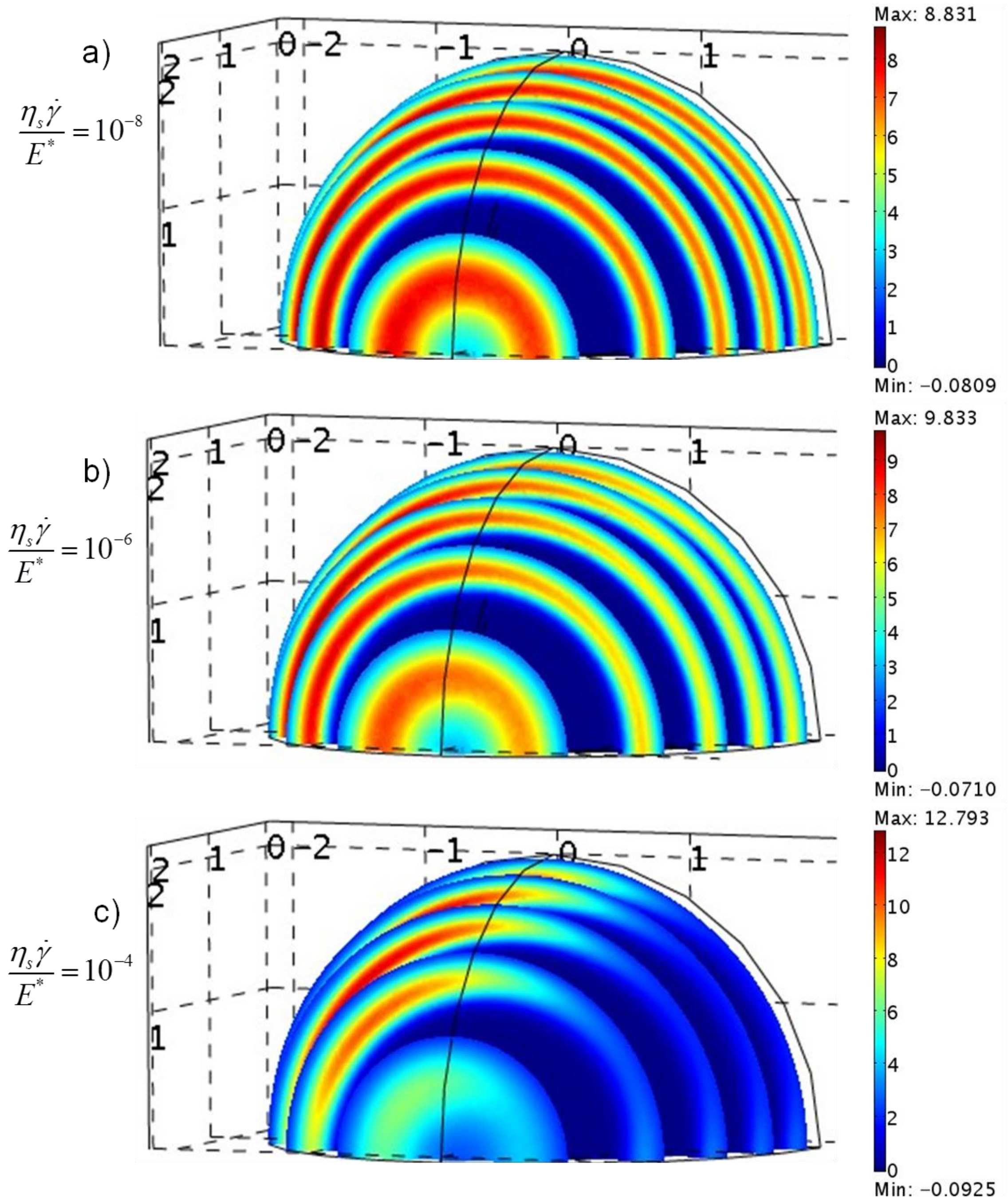

Figure 7.5: Theoretical prediction of pair distribution function $g(\mathbf{r})$ for sheared glasses of volume fraction 0.8 using a higher mobility than that from microrheology

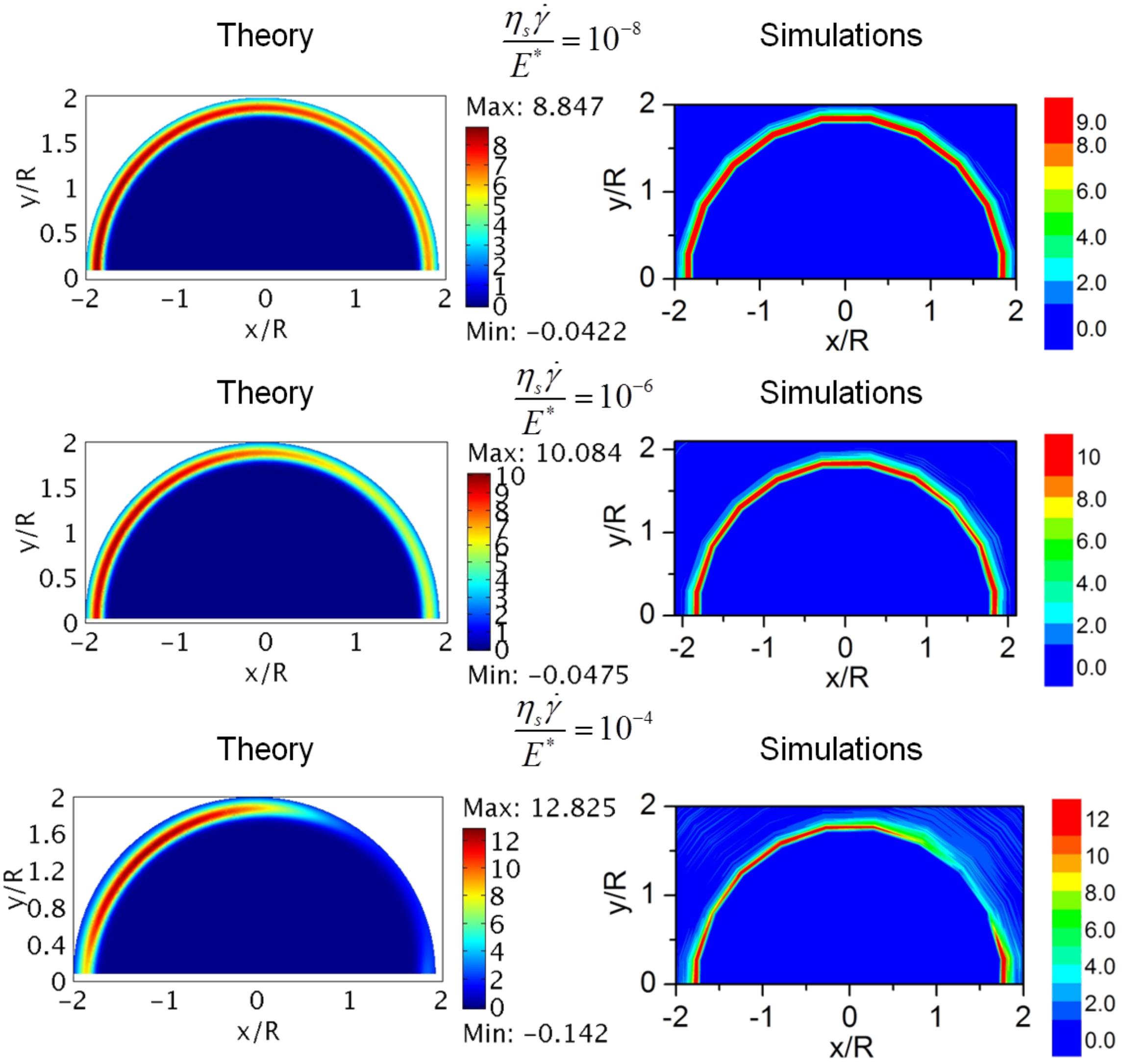

Figure 7.6: Comparison of predictions of pair distribution function $g(\mathbf{r})$ for sheared glasses of volume fraction 0.8 in the flow gradient plane at different shear rates from theory (left) and simulations (right).

7.4.2 Effect of using higher mobility on prediction of flow curve

Figure 7.7 presents the steady shear stress computed from the microstructure presented above for a volume fraction of 0.8. The theory now using a higher mobility quantitatively predicts the yield stress and shear thinning at high shear and shows good agreement with simulation results from Chapter 2. This study establishes that the pairwise theory can be successfully extended to sheared soft particle glasses to quantitatively predict their rheology if appropriate particle scale mobility is used taking into account the collective neighbor effects under flow.

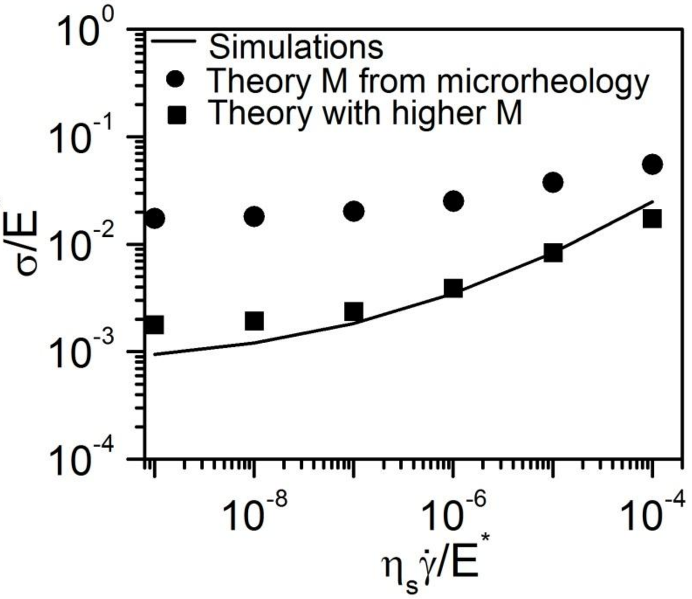

Figure 7.7: Theoretical prediction of flow curve using higher mobility than from microrheology (squares) and comparison to particle scale simulations from chapter 2 (line)

7.4.3 Prediction of flow curves and comparison to simulations

Figure 7.8a shows theoretical predictions of flow curves for different volume fractions and comparison to simulations from Chapter 2. Figure 7.8b and c show the variation of the converged average elastic energy and the boundary condition at $r=2R$.

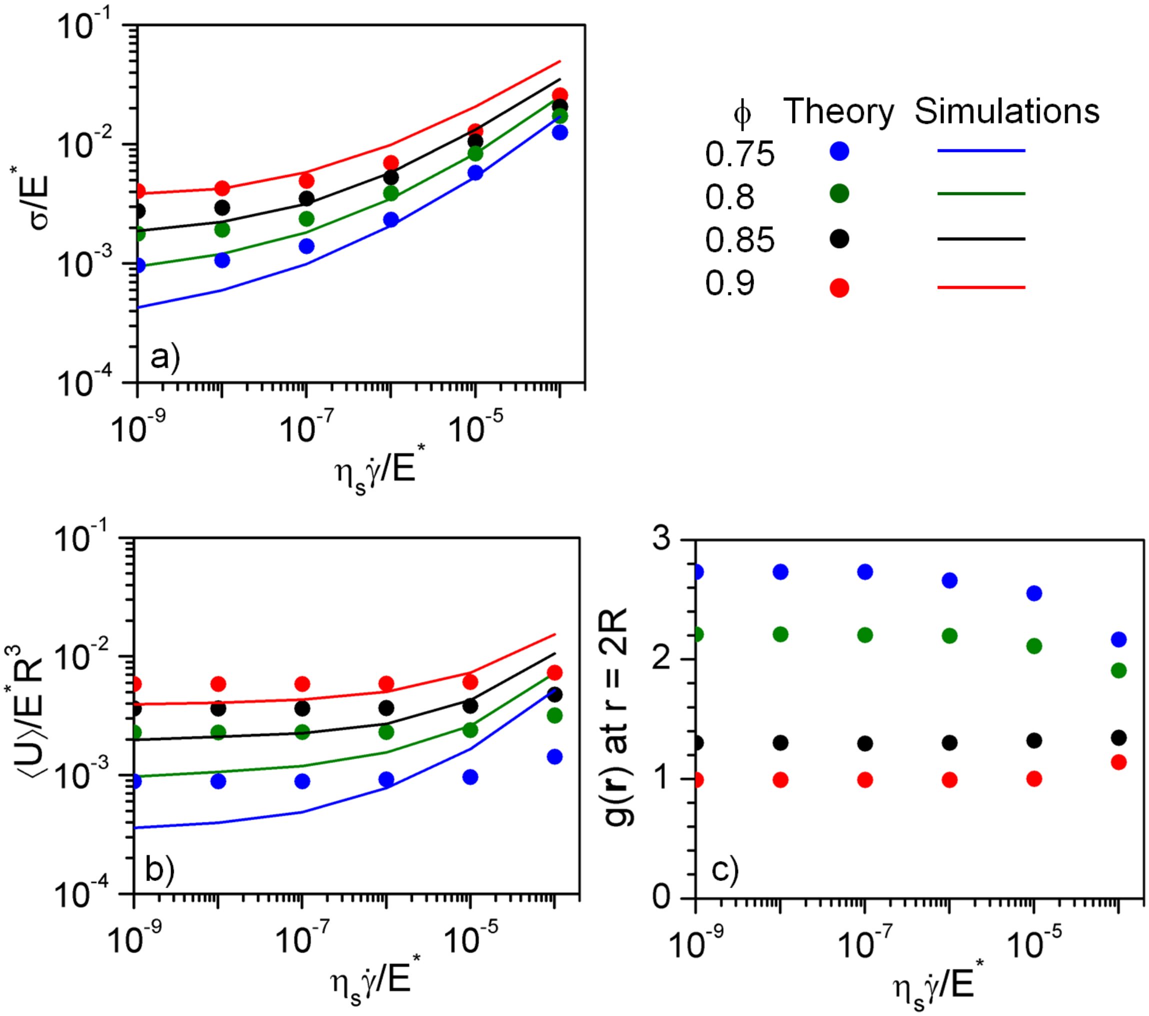

Figure 7.8: Theoretical prediction of flow curve (a) and average elastic energy (b) using higher mobility than that from microrheology (circles) and comparison to particle scale simulations from chapter 2 (lines). (c) Boundary condition at *r* = 2*R*.

7.5 SUMMARY AND CONCLUSIONS

The pairwise theory presented previously to predict the short ranged pair distribution function for quiescent soft particle glasses was extended to steadily sheared glasses. A transport equation for the distribution function with components of its flux from a proposed mean elastic force and convective flow was developed. Appropriate boundary conditions were also determined based on maintaining the number of contacts per particle and self consistently determining the average elastic energy. Since the governing equation included flow, a particle scale mobility term came into the picture when solving the governing equation. A microscopic mobility computed from the microrheology simulations in Chapter 5 was used to test the theory. The predicted microstructure displayed accumulation and depletion of pair density in the compressive and extensive quadrants as observed in particle scale simulations and the shear stress predicted from the microstructure exhibited yield stress and shear thinning. Though the theoretical predictions showed good qualitative agreement with the simulation and experimental data, the predicted stresses for a given shear rate were an order of magnitude higher. The initial particle mobility that was used in the theory was computed from simulations where a single particle was dragged through a jammed suspension where the other particles had no external stimuli but in a steady shear flow all the particles are sheared and the collective effect might increase the particle scale mobility. The theoretical predictions were then tested using a particle mobility 15 times higher than that obtained from microrheology and the results showed good qualitative and quantitative agreement with particle scale simulations. Thus, the pairwise theory can be extended to quantitatively predict the nonlinear rheology of these materials including yield stress and shear thinning when appropriate particle scale mobility is used.

Here, for the purposes of testing the theory with a higher mobility, the entire mobility obtained from microrheology which includes contributions from elastic, elastohydrodynamic and hindered stokes contributions were multiplied by 15. But if collective particle dynamics in shear flow gave rise to the increase in mobility their contribution to enhancing the mobility of elastic and elastohydrodynamic components might be different from that of the stokes drag component. Also, collective mobility enhancement effects will be stronger at larger volume fractions. Thus, determining appropriate particle scale mobility for particles under shear flow is crucial in developing the pairwise theory as a theoretical tool to quantitatively predict the nonlinear rheology of these materials under shear. A different kind of microrheology simulations where a tagged particle is held stationary as the suspension is sheared might be useful to compute the appropriate mobility. The force on the stationary tagged particle can be computed at different shear rates of the suspension around it to extract a particle-scale mobility.

SUPPLEMENTAL MATERIAL 7.A: NUMERICAL CONVERGENCE TESTS

7.A.1 Iterations towards self consistently determining average elastic energy

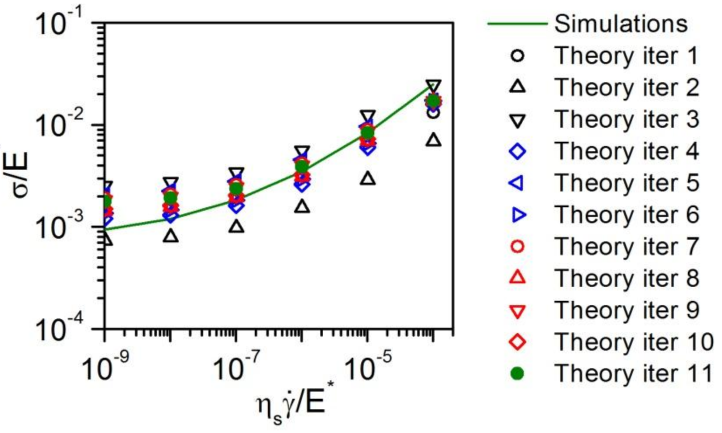

Figure 7.A.1 Convergence of stress iterations towards self consistently determining the average elastic energy for a volume fraction of 0.8 (higher mobility case).

After every iteration the value of *g*(**r**) at *r*=2*R* and average elastic energy are updated based on maintaining the number of contacts to the equilibrium value and self consistency respectively. Their evolution is shown below.

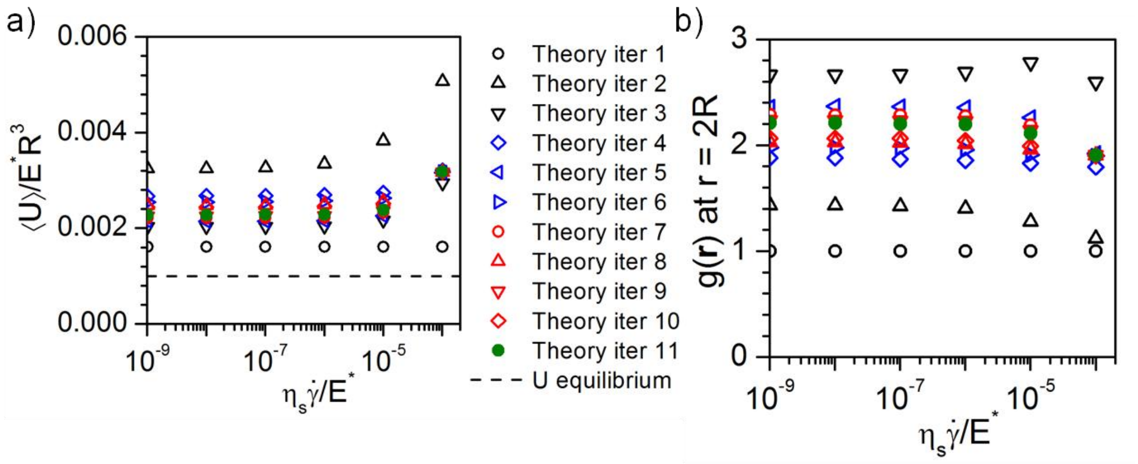

Figure 7.A.2 Convergence of average elastic energy (a) and boundary condition *g*(**r**) at *r*=2*R* for a volume fraction of 0.8 and using a higher mobility.

7.A.2 Insensitivity to number of terms in perturbation of elastic force, number of elements in domain and starting average elastic energy

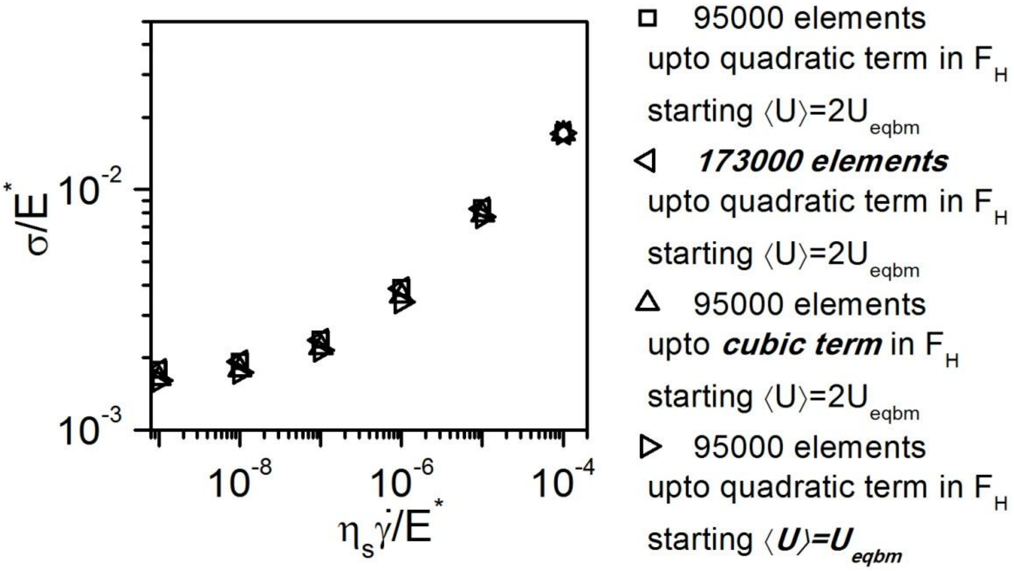

Figure 7.A.3 Insensitivity check in terms of number of elements in domain, number of perturbation terms in elastic force and starting average elastic energy for a volume fraction 0.8 (higher mobility case).

Note that using the equilibrium energy as the starting average elastic energy would require more iterations. Using too low or two high an energy (more than an order of magnitude than the equilibrium energy) will not converge to the right result. Using starting elastic energy as twice the average elastic energy at equilibrium was found to be optimal.

In terms of number of elements 95000 elements in the domain was sufficient for volume fractions 0.8 and higher whereas 135000 elements were used for volume fraction 0.75 to get converged results. This is because at lower volume fractions the range of compressions where particle pairs are found is smaller.

SUPPLEMENTAL MATERIAL 7.B: MESH AND SOLVER SETTING IN COMSOL

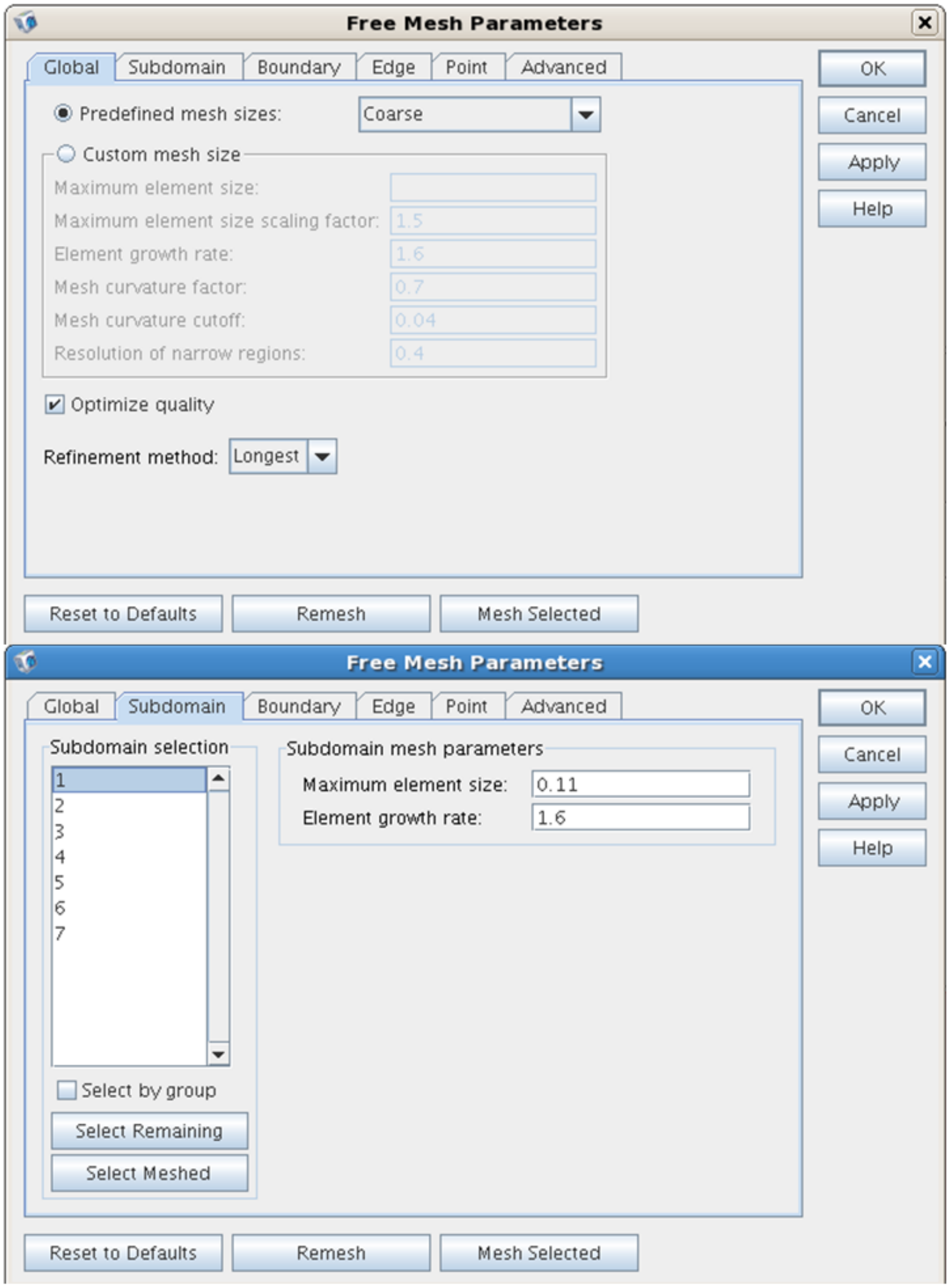

● Predefined mesh sizes: Coarse

○ Custom mesh size

Maximum element size:

Maximum element size scaling factor: 1.5

Element growth rate: 1.6

Mesh curvature factor: 0.7

Mesh curvature cutoff: 0.04

Resolution of narrow regions: 0.4

☑ Optimize quality

Refinement method: Longest

Subdomain selection

1
2
3
4
5
6
7

☐ Select by group

Subdomain mesh parameters

Maximum element size: 0.11

Element growth rate: 1.6

Figure 7.B.1: Mesh setting to generate 95000 elements. The subdomain 1 which is $r>1.8R$ was modified with the size shown above for a tighter mesh.

Solver: Direct (UMFPACK) linear system solver with automatic matrix symmetry

SUPPLEMENTAL MATERIAL 7.C: THEORY DATA TABLES

Table 7.C.1 Theoretical predictions using mobility from microrheology for ϕ=0.8

$\eta_s\dot{\gamma}/E^*$	σ/E^*	$\langle \mathrm{U} \rangle/\mathrm{E}^*\mathrm{R}^2$	***g(r = 2R)***
10^{-8}	0.017404	0.003286	1.795
10^{-7}	0.01807	0.003407	1.785
10^{-6}	0.020172	0.00373	1.76
10^{-5}	0.02518	0.004738	1.736
10^{-4}	0.037555	0.012601	2.02

Table 7.C.2 Theoretical predictions using higher mobility for ϕ=0.75

$\eta_s\dot{\gamma}/E^*$	σ/E^*	$\langle \mathrm{U} \rangle/\mathrm{E}^*\mathrm{R}^2$	***g(r = 2R)***
10^{-8}	0.000959	0.000887	2.73
10^{-7}	0.001063	0.000887	2.73
10^{-6}	0.001395	0.000887	2.73
10^{-5}	0.00233	0.000917	2.658
10^{-4}	0.005741	0.000965	2.55

Table 7.C.3 Theoretical predictions using higher mobility for ϕ=0.8

$\eta_s\dot{\gamma}/E^*$	σ/E^*	$\langle \mathrm{U} \rangle/\mathrm{E}^*\mathrm{R}^2$	***g(r = 2R)***
10^{-8}	0.001769	0.002278	2.2085
10^{-7}	0.001914	0.002278	2.2072
10^{-6}	0.002362	0.002288	2.203
10^{-5}	0.003861	0.002288	2.196
10^{-4}	0.008307	0.002379	2.11

Table 7.C.4 Theoretical predictions using higher mobility for ϕ=0.85

$\eta_s\dot{\gamma}/E^*$	σ/E^*	$\langle \mathrm{U} \rangle / \mathrm{E}^* \mathrm{R}^2$	***g(r = 2R)***
10^{-8}	0.002737	0.003629	1.3
10^{-7}	0.002919	0.003629	1.3
10^{-6}	0.003483	0.003629	1.295
10^{-5}	0.005255	0.003666	1.3
10^{-4}	0.010517	0.003831	1.32

Table 7.C.4 Theoretical predictions using higher mobility for ϕ=0.9

$\eta_s\dot{\gamma}/E^*$	σ/E^*	$\langle \mathrm{U} \rangle / \mathrm{E}^* \mathrm{R}^2$	***g(r = 2R)***
10^{-8}	0.004038	0.005847	0.99
10^{-7}	0.004247	0.005847	0.99
10^{-6}	0.004909	0.005847	0.99
10^{-5}	0.006941	0.005877	0.99
10^{-4}	0.012796	0.006048	1

Chapter 8: Concluding Remarks

8.1 CONCLUSIONS

This dissertation focused on the study of microstructure and rheology of soft particle glasses which are highly jammed suspensions of soft particles. Industrially, they are used as rheological additives in high-performance coatings, ceramic pastes, textured food and personal care products. Fundamentally, they serve as model systems to study the microstructure and dynamics of soft crowded systems in biology, such as tissues and intracellular cytoplasm, and geology, such as clays and slurries. Various aspects of the behavior of these glasses were investigated through theory, particle scale simulations and experiments. Their rheology was explained in terms of the constituent properties and the microstructural changes that occur during their deformation and flow. The different aspects investigated, the important findings and their impact are highlighted below.

Steady shear rheology

Particle scale simulations using a new micromechanical model including elastic and elastohydrodynamic particle contact interactions showed excellent quantitative agreement with experiments for both microgels and concentrated emulsions. This validated the micromechanical model and established its usefulness in describing and understanding different kinds of soft particle glasses. A constitutive equation that connects the constituent properties to the bulk steady shear rheology was established. The universality of the model was determined by the microstructure that developed during flow. Accumulation and depletion of particle density along the compression and extension axes respectively occurs during steady shear with an increased particle compression at high shear. This universal model is also useful in predicting hard to determine constituent properties like volume fraction or particle modulus from the macroscopic rheology which can be easily measured. Thus, a tool was developed to design materials using the right combination of solvent viscosity, particle concentration and modulus to exhibit the desired yield stress and steady shear viscosity.

Oscillatory shear rheology

The excellent quantitative agreement of macroscopic properties from particle simulations with experimental data further validated the micromechanical model. At small strain amplitudes the particles remain trapped in cages and at large amplitudes exceeding the yield strain the particles escape their cages. This transition is reflected in the appearance of a shear induced diffusion of constituent particles which is identified as the microscopic origin of yielding. Detailed study of the large amplitude oscillatory shear (LAOS) cycle established how this technique can be efficiently used to characterize soft particle glasses by capturing both their linear elastic and nonlinear flow properties.

Stress relaxation on flow cessation

The processing of soft particle glasses in many applications requires the material to be quenched to a solid state by flow cessation during which they develop internal stresses. Experiments using microgel suspensions with varying constituent properties showed that internal stress sensitively depends on the processing conditions and material properties. The larger the preshear stress, the smaller is the trapped internal stress. A universal scaling was developed between the internal stress, constituent properties and processing conditions. Simulations revealed the microscopic origin of the trapped internal stress to be residual flow induced angular distortion of microstructure. A two-step dynamics was identified for the relaxation on flow cessation. The first step corresponds to rapid initial stress decay on flow cessation through ballistic particle motion which depends on the preshear flow conditions. The second step corresponds to a slow long term relaxation of the trapped internal stress through local facet rearrangements. The rate of this long term relaxation was found to be independent of the preshear flow conditions.

Active Microrheology

Microrheological techniques offer many advantages over conventional rheometry. Soft particle glasses are athermal and Brownian forces are insufficient to produce a detectable response, thus active methods are necessary to characterize them. The microstructural rationale behind identifying yielding and flow using microrheology was determined based on the probe motion. A threshold force existed, beyond which the probe particle escaped its cage. A universal force-velocity curve for the probe motion for different solvent viscosities, particle modulus and concentration was developed. An analysis was established to use information from microrheology to quantitatively predict bulk rheological properties.

Pairwise theory to determine the static microstructure and elastic properties

A new method was developed to predict the static short ranged pair distribution function and mechanical properties of soft particle glasses. The theory was validated with comparison to particle scale simulations and experiments. The computational time required for the theory was much smaller than full particle scale simulations. Analytical models of the pair distribution function were developed using perturbation methods.

Pairwise theory to determine the sheared microstructure and flow properties

A new method was developed to predict the short range pair distribution function and flow curves of sheared soft particle glasses. The computational time for the theory was much smaller than full particle simulations. The predicted microstructure displays accumulation and depletion of pair density in the compressive and extensive quadrants similar to that observed in particle scale simulations. The pairwise theory can be used to quantitatively predict the yield stress and shear thinning when appropriate particle scale mobility is used.

8.2 SUGGESTED FUTURE WORK

The investigations performed in this dissertation and a review of relevant literature gave rise to many other interesting and important questions that are still open and the following future work is suggested based on it.

Effect of wall surfaces in microstructure and rheology of soft particle glasses

Soft particle glasses are known to slip when sheared with smooth surfaces [Meeker *et al.* (2004b)] and the rheology and flow heterogeneity is also known to be affected by the wall-particle interactions [Seth *et al.* (2012)]. Slip has a significant impact on material processing including introduction of surface defects and fracture during extrusion [Piau and Agassant (1996)] as well as increased mass flow rates in pumping and transportation due to plug flow before yielding [Lu and Zhang (2005)]. Rheology of soft particle glasses with walls of varying smoothness and chemical nature can be investigated through particle simulations. Microscopically the diffusivity of particles near these walls can be determined to explore their connection with the surface effects observed macroscopically. This will allow design of fluids with required slip characteristics and the study of modified surface interactions will help modify slip characteristics of existing fluids by just modifying the surfaces with which they interact.

Flow heterogeneities are observed when soft particle glasses flow on smooth or chemically modified surfaces. Flow induced segregation has been observed in multicomponent mixtures like blood and the effect of particle stiffness in confined flow of dilute soft particle suspensions has been recently investigated [Kumar and Graham (2012)]. It would be both interesting and useful to determine the surface effect in microstructure and rheology of soft particle glasses with heterogeneity in constituent particle size and/or softness.

Determination of appropriate particle mobility to be used in pairwise theory for sheared soft particle glasses

Intuitively, the mobility of a particle in sheared suspensions where all its neighbors are also sheared and want to move is larger than the particle mobility computed from microrheology where a single particle moves through a jammed suspension of particles. In Chapter 7, it was established that the determination of this higher mobility is crucial in developing a theoretical tool to quantitatively predict the nonlinear rheology of these materials under shear. A different kind of microrheology simulations where a tagged particle is held stationary as the suspension is sheared might be useful to compute the appropriate mobility. The force on the stationary tagged particle can be computed at different shear rates of the suspension around it to extract particle scale mobility.

Effect of heterogeneity in size of constituent particles

The effect of polydispersity in constituent particle size on the elastic properties of soft particle glasses has already been investigated by [Seth *et al.* (2006)]. No significant effect was observed in the low frequency storage modulus and osmotic pressure for up to 20% polydispersity (Gaussian standard deviation around average value) in particle radius. [Foudazi *et al.* (2012)] have recently compared the results presented in chapter 2 with experiments on highly concentrated emulsions with a bimodal particle size distribution and observed good agreement for size ratio upto 3 and deviations at larger size ratios of 6. Asymmetric caging at equilibrium and new solid-fluid transitions have been observed for soft glassy mixtures of large and small star polymers [Mayer *et al.* (2008)]. Simulations of steady and/or oscillatory shear using the current framework with packings of particles with a bimodal size distribution of varying size ratios would be useful to characterize the microstructure and rheology of soft particle glasses with large size heterogeneities.

Effect of heterogeneity in softness of constituent particles

Mixtures of hard and soft particles are used in many different applications. Latex blends are used in paints where the hard particles provide the required stability while the soft particles deform and fill the space to give a uniform finish [Eckersley and Helmer (1997)]. It has been shown that addition of hard nanoparticles to polymer glasses can be used to tune the fragility of the glass [Riggleman *et al.* (2007)]. Simulations of soft particle glasses with bimodal distribution of particle softness with varying softness ratios would be useful to characterize the rheology of such latex blends and other composite materials.

Effect of added attractive interactions between particles

Microgels are used as rheology modifiers in many applications and they can be used in conjunction with other additives like in the case of coatings [Boggs *et al.* (1996); Wolfe (1992)] or the surface chemistry of the microgel particles can be modified to suit the particular application as in the case of biopolymers used in drug delivery. These modifications can result in added attractive interactions and such interactions are known to have an effect on the behavior of other glassy systems such as hard sphere glasses [Kaufman and Weitz (2006); Pham *et al.* (2002); Pham *et al.* (2008)] and star polymers [Lo Verso *et al.* (2006)]. The particle-particle elastic contact interactions used in all the investigations in this dissertation were based on purely repulsive interactions and study of the microstructure and rheology of soft particle glasses with added tunable attractive interactions of varying magnitude would be both interesting and useful.

Effect of probe particle size, softness, and other directions in active microrheology

In Chapter 5 active microrheology was studied by pulling a random tagged particle in the suspension and tracking its response. It was also shown that experimentally, for soft jammed glasses, active magnetic methods are most suitable. On the simulations side, it would be useful and interesting to study the effect of probe size and particle softness. In the case of hard sphere suspensions it has been shown that the size of the probe particle can play a role in the measurements made [Meyer et al. (2006); Squires and Brady (2005)]. In soft particle glasses the number of contacts of the probe particle can change with the size of the probe and further investigations in this direction are required to determine the effect precisely. Similarly simulations of hard probe particles pulled through soft suspensions will allow determination of the probe particle softness effect. On the experiments side, it might be interesting to synthesize core-shell probe particles with a magnetic core and a soft shell to maintain the soft contact interactions in these glasses.

Other interesting future directions in active microrheology include using oscillatory pulling forces [Ziemann et al. (1994)] to determine if the oscillatory rheology of these glasses could be predicted using microrheology and the use of force pulses [Bausch et al. (1999); Ziemann et al. (1994)] to investigate the stress relaxation in these materials.

Bibliography

Abbas K. A., S. K. Khalil and A. S. Meor Hussin,"Modified Starches and Their Usages in Selected Food Products: A Review Study," J. Agricultural Science **2**, 90-100 (2010)

Abraham S. and P. Harrowell, "The origin of persistent shear stress in supercooled liquids," J. Chem. Phys. **137**, 014506 (2012)

Alting A. C., F. van de Velde, M. W. Kanning, M. Burgering, L. Mulleners, A. Sein and P. Buwalda, "Improved creaminess of low-fat yoghurt: The impact of amylomaltase-treated starch domains," Food Hydrocolloid **23**, 980-987 (2009)

Ancey C., "Plasticity and geophysical flows: A review," J. Non-Newton. Fluid. **142**, 4-35 (2007)

Andersen H. C., J. D. Weeks and D. Chandler, "Relationship between Hard-Sphere Fluid and Fluids with Realistic Repulsive Forces," Phys. Rev. A **4**, 1597-1607 (1971)

Angelini T. E., E. Hannezo, X. Trepat, M. Marquez, J. J. Fredberg and D. A. Weitz, "Glass-like dynamics of collective cell migration," P. Natl. Acad. Sci. USA **108**, 4714-4719 (2011)

Angell C. A., K. L. Ngai, G. B. McKenna, P. F. McMillan and S. W. Martin, "Relaxation in glassforming liquids and amorphous solids," J. Appl. Phys. **88**, 3113-3157 (2000)

Atapattu D. D., R. P. Chhabra and P. H. T. Uhlherr, "Creeping Sphere Motion in Herschel-Bulkley Fluids - Flow-Field and Drag," J. Non-Newton. Fluid. **59**, 245-265 (1995)

Ballauff M., J. M. Brader, S. U. Egelhaaf *et al.*, "Residual Stresses in Glasses," Phys. Rev. Lett. **110**, 215701 (2013)

Barnes H. A., "A Review of the Slip (Wall Depletion) of Polymer-Solutions, Emulsions and Particle Suspensions in Viscometers - Its Cause, Character, and Cure," J. Non-Newton. Fluid. **56**, 221-251 (1995)

Batchelor G. K., "Brownian Diffusion of Particles with Hydrodynamic Interaction," J. Fluid. Mech. **74**, 1-29 (1976)

Batchelor G. K., "Effect of Brownian-Motion on Bulk Stress in a Suspension of Spherical-Particles," J. Fluid. Mech. **83**, 97-117 (1977)

Bausch A. R., W. Moller and E. Sackmann, "Measurement of local viscoelasticity and forces in living cells by magnetic tweezers," Biophys. J. **76**, 573-579 (1999)

Ben-Amotz D. and G. Stell, "Hard sphere perturbation theory for fluids with soft-repulsive-core potentials," J. Chem. Phys. **120**, 4844-4851 (2004)

Beris A. N., J. A. Tsamopoulos, R. C. Armstrong and R. A. Brown, "Creeping Motion of a Sphere through a Bingham Plastic," J. Fluid. Mech. **158**, 219-244 (1985)

Boggs L. J., M. Rivers and S. G. Bike, "Characterization and rheological investigation of polymer microgels used in automotive coatings," J. Coating. Technol. **68**, 63-74 (1996)

Bonnecaze R. T. and M. Cloitre, "Micromechanics of Soft Particle Glasses," Adv. Polym. Sci. **236**, 117-161 (2010)

Borrega R., M. Cloitre, I. Betremieux, B. Ernst and L. Leibler, "Concentration dependence of the low-shear viscosity of polyelectrolyte micro-networks: From hard spheres to soft microgels," Europhys. Lett. **47**, 729-735 (1999)

Bower C., C. Gallegos, M. R. Mackley and J. M. Madiedo, "The rheological and microstructural characterisation of the non-linear flow behaviour of concentrated oil-in-water emulsions," Rheol. Acta. **38**, 145-159 (1999)

Brady J. F. and G. Bossis, "The Rheology of Concentrated Suspensions of Spheres in Simple Shear-Flow by Numerical-Simulation," J. Fluid. Mech. **155**, 105-129 (1985)

Brady J. F., "Model hard-sphere dispersions: Statistical mechanical theory, simulations, and experiments," Curr. Opin. Colloid. Interface Sci. **1**, 472-480 (1996)

Brady J. F. and J. F. Morris, "Microstructure of strongly sheared suspensions and its impact on rheology and diffusion," J. Fluid. Mech. **348**, 103-139 (1997)

Breuer K. S.,"Microscale diagnostic techniques,"xii, 259p. (2005)

Buitenhuis J. and S. Forster, "Block copolymer micelles: Viscoelasticity and interaction potential of soft spheres," J. Chem. Phys. **107**, 262-272 (1997)

Bursac P., G. Lenormand, B. Fabry, M. Oliver, D. A. Weitz, V. Viasnoff, J. P. Butler and J. J. Fredberg, "Cytoskeletal remodelling and slow dynamics in the living cell," Nat. Mater. **4**, 557-561 (2005)

Carbajal-Tinoco M. D., "Thermodynamically consistent integral equation for soft repulsive spheres," J. Chem. Phys. **128**, 184507 (2008)

Carpen I. C. and J. F. Brady, "Microrheology of colloidal dispersions by Brownian dynamics simulations," J. Rheol. **49**, 1483-1502 (2005)

Chandler D., J. D. Weeks and H. C. Anderson, "Van Der Waals Picture of Liquids, Solids, and Phase Transformations," Science, New Series **220**, 787-794 (1983)

Chen D. T., E. R. Weeks, J. C. Crocker, M. F. Islam, R. Verma, J. Gruber, A. J. Levine, T. C. Lubensky and A. G. Yodh, "Rheological microscopy: Local mechanical properties from microrheology," Phys. Rev. Lett. **90**, 108301 (2003)

Cheng Z. D., J. X. Zhu, P. M. Chaikin, S. E. Phan and W. B. Russel, "Nature of the divergence in low shear viscosity of colloidal hard-sphere dispersions," Phys. Rev. E **65**, 041405 (2002)

Cho K. S., K. Hyun, K. H. Ahn and S. J. Lee, "A geometrical interpretation of large amplitude oscillatory shear response," J. Rheol. **49**, 747-758 (2005)

Chung B., S. Ramakrishnan, R. Bandyopadhyay, D. Liang, C. F. Zukoski, J. L. Harden and R. L. Leheny, "Microscopic dynamics of recovery in sheared depletion gels," Phys. Rev. Lett. **96**, 228301 (2006)

Cianci G. C., R. E. Courtland and E. R. Weeks, "Correlations of structure and dynamics in an aging colloidal glass," Solid State Commun. **139**, 599-604 (2006)

Cicuta P. and A. M. Donald, "Microrheology: a review of the method and applications," Soft Matter **3**, 1449-1455 (2007)

Cipelletti L., S. Manley, R. C. Ball and D. A. Weitz, "Universal aging features in the restructuring of fractal colloidal gels," Phys. Rev. Lett. **84**, 2275-2278 (2000)

Cloitre M., R. Borrega and L. Leibler, "Rheological aging and rejuvenation in microgel pastes," Phys. Rev. Lett. **85**, 4819-4822 (2000)

Cloitre M., R. Borrega, F. Monti and L. Leibler, "Structure and flow of polyelectrolyte microgels: from suspensions to glasses," Cr. Phys. **4**, 221-230 (2003a)

Cloitre M., R. Borrega, F. Monti and L. Leibler, "Glassy dynamics and flow properties of soft colloidal pastes," Phys. Rev. Lett. **90**, 068303 (2003b)

Cohen-Addad S., H. Hoballah and R. Hohler, "Viscoelastic response of a coarsening foam," Phys. Rev. E **57**, 6897-6901 (1998)

Corte L., P. M. Chaikin, J. P. Gollub and D. J. Pine, "Random organization in periodically driven systems," Nat. Phys. **4**, 420-424 (2008)

Crassous J. J., M. Siebenburger, M. Ballauff, M. Drechsler, O. Henrich and M. Fuchs, "Thermosensitive core-shell particles as model systems for studying the flow behavior of concentrated colloidal dispersions," J. Chem. Phys. **125**, 204906 (2006)

Crassous J. J., M. Siebenburger, M. Ballauff, M. Drechsler, D. Hajnal, O. Henrich and M. Fuchs, "Shear stresses of colloidal dispersions at the glass transition in equilibrium and in flow," J. Chem. Phys. **128**, 204902 (2008)

Damman P., S. Gabriele, S. Coppee *et al.*, "Relaxation of residual stress and reentanglement of polymers in spin-coated films," Phys. Rev. Lett. **99**, 036101 (2007)

Dealy J. M. and K. F. Wissbrun,"Melt rheology and its role in plastics processing : theory and applications,"xix, 665 p.(1990)

Denkov N. D., V. Subramanian, D. Gurovich and A. Lips, "Wall slip and viscous dissipation in sheared foams: Effect of surface mobility," Colloid Surface A **263**, 129-145 (2005)

Denkov N. D., S. Tcholakova, K. Golemanov, K. P. Ananthapadmanabhan and A. Lips, "Viscous friction in foams and concentrated emulsions under steady shear," Phys. Rev. Lett. **100**, 138301 (2008)

Derec C., A. Ajdari and F. Lequeux, "Rheology and aging: A simple approach," Eur. Phys. J. E **4**, 355-361 (2001)

Derec C., G. Ducouret, A. Ajdari and F. Lequeux, "Aging and nonlinear rheology in suspensions of polyethylene oxide-protected silica particles," Phys. Rev. E **67**, 061403 (2003)

Dickinson E. and Royal Society of Chemistry (Great Britain). Food Chemistry Group.,"Food emulsions and foams : based on the proceedings of an international symposium organised by the Food Chemistry Group of the Royal Society of Chemistry at Leeds from 24th-26th March 1986,"Special publication viii, 290 p.(1987)

Dickinson E. and J. M. Rodríguez Patino,"Food emulsions and foams : interfaces, interactions and stability,"vi, 390 p.(1999)

Eckersley S. T. and B. J. Helmer, "Mechanistic considerations of particle size effects on film properties of hard/soft latex blends," J. Coating Technol. **69**, 97-107 (1997)

Erwin B. M., M. Cloitre, M. Gauthier and D. Vlassopoulos, "Dynamics and rheology of colloidal star polymers," Soft Matter **6**, 2825-2833 (2010)

Erwin B. M., D. Vlassopoulos, M. Gauthier and M. Cloitre, "Unique slow dynamics and aging phenomena in soft glassy suspensions of multiarm star polymers," Phys. Rev. E **83**, 061402 (2011)

Evans I. D. and D. R. Haisman, "Rheology of Gelatinized Starch Suspensions," J. Texture Stud. **10**, 347-370 (1980)

Evans I. D. and A. Lips, "Viscoelasticity of Gelatinized Starch Dispersions," J. Texture Stud. **23**, 69-86 (1992)

Ewoldt R. H., A. E. Hosoi and G. H. McKinley, "New measures for characterizing nonlinear viscoelasticity in large amplitude oscillatory shear," J. Rheol. **52**, 1427-1458 (2008)

Ewoldt R. H., P. Winter, J. Maxey and G. H. McKinley, "Large amplitude oscillatory shear of pseudoplastic and elastoviscoplastic materials," Rheol. Acta **49**, 191-212 (2010)

Fernandez-Nieves A.,"Microgel suspensions : fundamentals and applications,"xxi, 461 p.(2011)

Foffano G., J. S. Lintuvuori, K. Stratford, M. E. Cates and D. Marenduzzo, "Colloids in Active Fluids: Anomalous Microrheology and Negative Drag," Phys. Rev. Lett. **109**, 028103 (2012)

Foss D. R. and J. F. Brady, "Brownian Dynamics simulation of hard-sphere colloidal dispersions," J. Rheol. **44**, 629-651 (2000)

Foudazi R., I. Masalova and A. Y. Malkin, "The rheology of binary mixtures of highly concentrated emulsions: Effect of droplet size ratio," J. Rheol. **56**, 1299-1314 (2012)

Freidin A. S. and A. B. Sholokhova, "Internal stress relaxation in polymer systems," Mekhanika Polimerov **2**, 240-244 (1966)

Friberg S., K. Larsson and J. Sjöblom,"Food emulsions,"Food science and technology x, 640 p.(2004)

Fridrikh S., C. Raquois, J. F. Tassin and S. Rezaiguia, "Rheological behaviour of concentrated suspensions of soft spheres," J. Chim. Phys. Pcb **93**, 941-959 (1996)

Fuchs M. and M. E. Cates, "Theory of nonlinear rheology and yielding of dense colloidal suspensions," Phys. Rev. Lett. **89**, 248304 (2002)

Fuchs M. and M. E. Cates, "Schematic models for dynamic yielding of sheared colloidal glasses," Faraday Discuss. **123**, 267-286 (2003)

Fuchs M. and M. Ballauff, "Flow curves of dense colloidal dispersions: Schematic model analysis of the shear-dependent viscosity near the colloidal glass transition," J. Chem. Phys. **122**, 094707 (2005)

Fujii S. and W. Richtering, "Size and viscoelasticity of spatially confined multilamellar vesicles," Eur. Phys. J. E **19**, 139-148 (2006)

Gardel M. L., M. T. Valentine, J. C. Crocker, A. R. Bausch and D. A. Weitz, "Microrheology of entangled F-actin solutions," Phys. Rev. Lett. **91**, 158302 (2003)

Gazuz I., A. M. Puertas, T. Voigtmann and M. Fuchs, "Active and Nonlinear Microrheology in Dense Colloidal Suspensions," Phys. Rev. Lett. **102**, 248302 (2009)

Gnann M. V., I. Gazuz, A. M. Puertas, M. Fuchs and T. Voigtmann, "Schematic models for active nonlinear microrheology," Soft Matter **7**, 1390-1396 (2011)

Green D. J., R. Tandon and V. M. Sglavo, "Crack arrest and multiple cracking in glass through the use of designed residual stress profiles," Science **283**, 1295-1297 (1999)

Gurnon A. K. and N. J. Wagner, "Large amplitude oscillatory shear (LAOS) measurements to obtain constitutive equation model parameters: Giesekus model of banding and nonbanding wormlike micelles," J. Rheol. **56**, 333-351 (2012)

Habdas P., D. Schaar, A. C. Levitt and E. R. Weeks, "Forced motion of a probe particle near the colloidal glass transition," Europhys. Let.t **67**, 477-483 (2004)

Hanley H. J. M., J. C. Rainwater and S. Hess, "Shear-Induced Angular-Dependence of the Liquid Pair Correlation-Function," Phys. Rev. A **36**, 1795-1802 (1987)

Hansen J.-P. and I. R. McDonald,"Theory of simple liquids,"xi, 416 p.(2006)

Hasnain I. A. and A. M. Donald, "Microrheological characterization of anisotropic materials," Phys. Rev. E **73**, 031901 (2006)

Hebraud P., F. Lequeux, J. P. Munch and D. J. Pine, "Yielding and rearrangements in disordered emulsions," Phys. Rev. Lett. **78**, 4657-4660 (1997)

Hebraud P. and F. Lequeux, "Mode-coupling theory for the pasty rheology of soft glassy materials," Phys. Rev. Lett. **81**, 2934-2937 (1998)

Helfer E., S. Harlepp, L. Bourdieu, J. Robert, F. C. MacKintosh and D. Chatenay, "Microrheology of biopolymer-membrane complexes," Phys. Rev. Lett. **85**, 457-460 (2000)

Hodge I. M., "Physical Aging in Polymer Glasses," Science **267**, 1945-1947 (1995)

Hoye J. S. and A. Reiner, "Self-consistent Ornstein-Zernike approximation for molecules with soft cores," J. Chem. Phys. **125**, 104503 (2006)

Hyun K., S. H. Kim, K. H. Ahn and S. J. Lee, "Large amplitude oscillatory shear as a way to classify the complex fluids," J. Non-Newton. Fluid. **107**, 51-65 (2002)

Hyun K. and M. Wilhelm, "Establishing a New Mechanical Nonlinear Coefficient Q from FT-Rheology: First Investigation of Entangled Linear and Comb Polymer Model Systems," Macromolecules **42**, 411-422 (2009)

Hyun K., M. Wilhelm, C. O. Klein, K. S. Cho, J. G. Nam, K. H. Ahn, S. J. Lee, R. H. Ewoldt and G. H. McKinley, "A review of nonlinear oscillatory shear tests: Analysis and application of large amplitude oscillatory shear (LAOS)," Prog. Polym. Sci. **36**, 1697-1753 (2011)

Ikeda A., L. Berthier and P. Sollich, "Unified study of glass and jamming rheology in soft particle systems," Phys. Rev. Lett. **109**, 018301 (2012)

Ishikura S., "Preparation of microgels and their industrial application as fluidity controlling agents," Macromol. Symp. **101**, 115-122 (1996)

Jack R. L., D. Kelsey, J. P. Garrahan and D. Chandler, "Negative differential mobility of weakly driven particles in models of glass formers," Phys. Rev. E **78**, 011506 (2008)

Jacquin H. and L. Berthier, "Anomalous structural evolution of soft particles: equibrium liquid state theory," Soft Matter **6**, 2970-2974 (2010)

Jacquin H., L. Berthier and F. Zamponi, "Microscopic Mean-Field Theory of the Jamming Transition," Phys. Rev. Lett. **106**, 135702 (2011)

Jager-Lezer N., J. F. Tranchant, V. Alard, C. Vu, P. C. Tchoreloff and J. L. Grossiord, "Rheological analysis of highly concentrated w/o emulsions," Rheol. Acta **37**, 129-138 (1998)

Johnson K. L.,"Contact Mechanics,"(1985)

Jonason K., E. Vincent, J. Hammann, J. P. Bouchaud and P. Nordblad, "Memory and chaos effects in spin glasses," Phys. Rev. Lett. **81**, 3243-3246 (1998)

Jop P., J. R. Gomez-Solano, A. Petrosyan and S. Ciliberto, "Experimental study of out-of-equilibrium fluctuations in a colloidal suspension of Laponite using optical traps," J. Stat. Mech.-Theory E P04012 (2009)

Kaufman L. J. and D. A. Weitz, "Direct imaging of repulsive and attractive colloidal glasses," J. Chem. Phys. **125**, 074716 (2006)

Ketz R. J., R. K. Prudhomme and W. W. Graessley, "Rheology of Concentrated Microgel Solutions," Rheol. Acta **27**, 531-539 (1988)

Khair A. S. and J. F. Brady, "Single particle motion in colloidal dispersions: a simple model for active and nonlinear microrheology," J. Fluid. Mech. **557**, 73-117 (2006)

Khair A. S. and J. F. Brady, "Microrheology of colloidal dispersions: Shape matters," J. Rheol. **52**, 165-196 (2008)

Khan M. and A. K. Sood, "Out-of-equilibrium microrheology using optical tweezers to probe directional viscoelastic properties under shear," Epl-Europhys. Lett. **92**, 48001 (2010)

Klein C. O., H. W. Spiess, A. Calin, C. Balan and M. Wilhelm, "Separation of the nonlinear oscillatory response into a superposition of linear, strain hardening, strain softening, and wall slip response," Macromolecules **40**, 4250-4259 (2007)

Kobelev V. and K. S. Schweizer, "Strain softening, yielding, and shear thinning in glassy colloidal suspensions," Phys. Rev. E **71**, 021401 (2005)

Kumar A. and M. D. Graham, "Mechanism of Margination in Confined Flows of Blood and Other Multicomponent Suspensions," Phys. Rev. Lett. **109**, 108102 (2012)

Lacasse M. D., G. S. Grest, D. Levine, T. G. Mason and D. A. Weitz, "Model for the elasticity of compressed emulsions," Phys. Rev. Lett. **76**, 3448-3451 (1996)

Lado F., "Choosing the Reference System for Liquid-State Perturbation-Theory," Mol. Phys. **52**, 871-876 (1984)

Lang A., C. N. Likos, M. Watzlawek and H. Lowen, "Fluid and solid phases of the Gaussian core model," J. Phys.-Condens. Mat. **12**, 5087-5108 (2000)

Larson R. G., "The elastic stress in "film fluids"," J. Rheol. **41**, 365-372 (1997)

Larson R. G.,"The structure and rheology of complex fluids,"Topics in chemical engineeringxxi, 663 p.(1999)

Lau A. W. C., B. D. Hoffman, A. Davies, J. C. Crocker and T. C. Lubensky, "Microrheology, stress fluctuations, and active behavior of living cells," Phys. Rev. Lett. **91**, 198101 (2003)

Le Grand A. and G. Petekidis, "Effects of particle softness on the rheology and yielding of colloidal glasses," Rheol. Acta **47**, 579-590 (2008)

Lieleg O., J. Kayser, G. Brambilla, L. Cipelletti and A. R. Bausch, "Slow dynamics and internal stress relaxation in bundled cytoskeletal networks," Nat. Mater. **10**, 236-242 (2011)

Likos C. N., "Soft matter with soft particles," Soft Matter **2**, 478-498 (2006)

Liu A. J., S. Ramaswamy, T. G. Mason, H. Gang and D. A. Weitz, "Anomalous viscous loss in emulsions," Phys. Rev. Lett. **76**, 3017-3020 (1996)

Liu K. K., D. R. Williams and B. J. Briscoe, "The large deformation of a single micro-elastomeric sphere," J. Phys. D Appl. Phys. **31**, 294-303 (1998)

Lo Verso F., C. N. Likos, C. Mayer and L. Reatto, "Effect of attraction on the dynamical arrest of soft colloids," Mol. Phys. **104**, 3523-3534 (2006)

Lopez-Barron C. R., L. Porcar, A. P. R. Eberle and N. J. Wagner, "Dynamics of Melting and Recrystallization in a Polymeric Micellar Crystal Subjected to Large Amplitude Oscillatory Shear Flow," Phys. Rev. Lett. **108**, 258301 (2012)

Louis A. A., P. G. Bolhuis and J. P. Hansen, "Mean-field fluid behavior of the Gaussian core model," Phys. Rev. E **62**, 7961-7972 (2000)

Lu P. and M. Y. Zhang, "Rheology of coal-water paste," Powder Technol. **150**, 189-195 (2005)

Lubachevsky B. D. and F. H. Stillinger, "Geometric-Properties of Random Disk Packings," J. Stat. Phys. **60**, 561-583 (1990)

Lubrizol,"http://www.lubrizol.com/PersonalCare/Products/Carbopol/default.html,"

Macosko C. W.,"Rheology : principles, measurements, and applications,"Advances in interfacial engineering series xviii, 550 p.(1994)

Mansoori G. A. and F. B. Canfield, "Variational Approach to Equilibrium Thermodynamic Properties of Simple Liquids I," J. Chem. Phys. **51**, 4958-4967 (1969)

Marshall L. and C. F. Zukoski, "Experimental Studies on the Rheology of Hard-Sphere Suspensions near the Glass-Transition," J. Phys. Chem.-Us **94**, 1164-1171 (1990)

Mason T. G., J. Bibette and D. A. Weitz, "Elasticity of Compressed Emulsions," Phys. Rev. Lett. **75**, 2051-2054 (1995)

Mason T. G., J. Bibette and D. A. Weitz, "Yielding and flow of monodisperse emulsions," J. Colloid. Interf. Sci. **179**, 439-448 (1996)

Mason T. G., M. D. Lacasse, G. S. Grest, D. Levine, J. Bibette and D. A. Weitz, "Osmotic pressure and viscoelastic shear moduli of concentrated emulsions," Phys. Rev. E **56**, 3150-3166 (1997)

Mason T. G., "New fundamental concepts in emulsion rheology," Curr. Opin. Colloid Interface Sci. **4**, 231-238 (1999)

Mason T. G., T. Gisler, K. Kroy, E. Frey and D. A. Weitz, "Rheology of F-actin solutions determined from thermally driven tracer motion," J. Rheol. **44**, 917-928 (2000)

Mattsson J., H. M. Wyss, A. Fernandez-Nieves, K. Miyazaki, Z. B. Hu, D. R. Reichman and D. A. Weitz, "Soft colloids make strong glasses," Nature **462**, 83-86 (2009)

Mayer C., E. Zaccarelli, E. Stiakakis *et al.*, "Asymmetric caging in soft colloidal mixtures," Nat. Mater. **7**, 780-784 (2008)

McClements D. J.,"Food emulsions : principles, practices, and techniques,"CRC series in contemporary food science 609 p.(2005)

McQuarrie D. A.,"Statistical mechanics,"xii, 641 p.(2000)

Meeker S. P., R. T. Bonnecaze and M. Cloitre, "Slip and flow in soft particle pastes," Phys. Rev. Lett. **92**, 198302 (2004a)

Meeker S. P., R. T. Bonnecaze and M. Cloitre, "Slip and flow in pastes of soft particles: Direct observation and rheology," J. Rheol. **48**, 1295-1320 (2004b)

Meyer A., A. Marshall, B. G. Bush and E. M. Furst, "Laser tweezer microrheology of a colloidal suspension," J. Rheol. **50**, 77-92 (2006)

Miyazaki K., H. M. Wyss, D. A. Weitz and D. R. Reichman, "Nonlinear viscoelasticity of metastable complex fluids," Europhys. Lett. **75**, 915-921 (2006)

Mohan L. and R. T. Bonnecaze, "Short-ranged pair distribution function for concentrated suspensions of soft particles," Soft Matter **8**, 4216-4222 (2012)

Mohan L., C. Pellet, M. Cloitre and R. Bonnecaze, "Local mobility and microstructure in periodically sheared soft particle glasses and their connection to macroscopic rheology," J. Rheol. **57**, 1023-1046 (2013)

Mon K. K., "Lower free energy bound for hard-sphere perturbation theory," J. Chem. Phys. **116**, 9392-9394 (2002)

Morris J. F. and B. Katyal, "Microstructure from simulated Brownian suspension flows at large shear rate," Phys. Fluids **14**, 1920-1937 (2002)

Morris J. F., "A review of microstructure in concentrated suspensions and its implications for rheology and bulk flow," Rheol. Acta **48**, 909-923 (2009)

Negi A. S. and C. O. Osuji, "Dynamics of internal stresses and scaling of strain recovery in an aging colloidal gel," Phys. Rev. E **80**, 010404(R) (2009)

Negi A. S. and C. O. Osuji, "Physical aging and relaxation of residual stresses in a colloidal glass following flow cessation," J. Rheol. **54**, 943-958 (2010)

NipponPaints,"http://www.nipponpaintusa.com/products_automobile.html,"

Nordstrom K. N., E. Verneuil, P. E. Arratia, A. Basu, Z. Zhang, A. G. Yodh, J. P. Gollub and D. J. Durian, "Microfluidic Rheology of Soft Colloids above and below Jamming," Phys. Rev. Lett. **105**, 175701 (2010)

Nott P. R. and J. F. Brady, "Pressure-driven flow of suspensions: simulation and theory," J. Fluid. Mech. **275**, 157-199 (1994)

O'Hern C. S., S. A. Langer, A. J. Liu and S. R. Nagel, "Random packings of frictionless particles," Phys. Rev. Lett. **88**, 075507 (2002)

O'Hern C. S., L. E. Silbert, A. J. Liu and S. R. Nagel, "Jamming at zero temperature and zero applied stress: The epitome of disorder," Phys. Rev. E **68**, 011306 (2003)

Pal R., "Slippage during the flow of emulsions in rheometers," Colloid Surface A **162**, 55-66 (2000)

Paruta-Tuarez E., V. Sadtler, P. Marchal, L. Choplin and J. L. Salager, "Making Use of the Formulation-Composition Map To Prepare Highly Concentrated Emulsions with Particular Rheological Properties," Ind. Eng. Chem. Res. **50**, 2380-2387 (2011)

Pearson D. S. and W. E. Rochefort, "Behavior of Concentrated Polystyrene Solutions in Large-Amplitude Oscillating Shear Fields," J. Polym. Sci. Pol. Phys. **20**, 83-98 (1982)

Pham K. N., A. M. Puertas, J. Bergenholtz *et al.*, "Multiple glassy states in a simple model system," Science **296**, 104-106 (2002)

Pham K. N., G. Petekidis, D. Vlassopoulos, S. U. Egelhaaf, W. C. K. Poon and P. N. Pusey, "Yielding behavior of repulsion- and attraction-dominated colloidal glasses," J. Rheol. **52**, 649-676 (2008)

Philippoff W., "Vibrational Measurements with Large Amplitudes " Trans. Soc. Rheol. **10**, 317-334 (1966)

Physical Review Focus,"Toothpaste is a glass," **6**, 24 (2000)

Piau J. M. and J. F. Agassant,"Rheology for polymer melt processing,"Rheology series ix, 424 p.(1996)

Piau J. M., "Carbopol gels: Elastoviscoplastic and slippery glasses made of individual swollen sponges Meso- and macroscopic properties, constitutive equations and scaling laws," J. Non-Newton. Fluid. **144**, 1-29 (2007)

Pine D. J., J. P. Gollub, J. F. Brady and A. M. Leshansky, "Chaos and threshold for irreversibility in sheared suspensions," Nature **438**, 997-1000 (2005)

Plimpton S., "Fast Parallel Algorithms for Short-Range Molecular-Dynamics," J. Comput. Phys. **117**, 1-19 (1995)

Princen H. M. and A. D. Kiss, "Osmotic-Pressure of Foams and Highly Concentrated Emulsions .2. Determination from the Variation in Volume Fraction with Height in an Equilibrated Column," Langmuir **3**, 36-41 (1987)

Princen H. M. and A. D. Kiss, "Rheology of Foams and Highly Concentrated Emulsions .4. An Experimental-Study of the Shear Viscosity and Yield Stress of Concentrated Emulsions," J. Colloid Interf. Sci. **128**, 176-187 (1989)

Ramos L. and L. Cipelletti, "Ultraslow dynamics and stress relaxation in the aging of a soft glassy system," Phys. Rev. Lett. **87**, 245503 (2001)

Ramos L. and L. Cipelletti, "Intrinsic aging and effective viscosity in the slow dynamics of a soft glass with tunable elasticity," Phys. Rev. Lett. **94**, 158301 (2005)

Rapaport D. C.,"The Art of Molecular Dynamics Simulation "(2004)

Reichhardt C. J. O. and C. Reichhardt, "Viscous decoupling transitions for individually dragged particles in systems with quenched disorder," Phys. Rev. E **78**, 011402 (2008)

Rich J. P., J. Lammerding, G. H. McKinley and P. S. Doyle, "Nonlinear microrheology of an aging, yield stress fluid using magnetic tweezers," Soft Matter **7**, 9933-9943 (2011)

Riggleman R. A., J. F. Douglas and J. J. de Pablo, "Tuning polymer melt fragility with antiplasticizer additives," J. Chem. Phys. **126**, 234903 (2007)

Roberts G. P. and H. A. Barnes, "New measurements of the flow-curves for Carbopol dispersions without slip artefacts," Rheol. Acta **40**, 499-503 (2001)

Rogers S., J. Kohlbrecher and M. P. Lettinga, "The molecular origin of stress generation in worm-like micelles, using a rheo-SANS LAOS approach," Soft Matter **8**, 7831-7839 (2012)

Rogers S. A., B. M. Erwin, D. Vlassopoulos and M. Cloitre, "Oscillatory yielding of a colloidal star glass," J. Rheol. **55**, 733-752 (2011a)

Rogers S. A., B. M. Erwin, D. Vlassopoulos and M. Cloitre, "A sequence of physical processes determined and quantified in LAOS: Application to a yield stress fluid," J. Rheol. **55**, 435-458 (2011b)

Rogers S. A., "A sequence of physical processes determined and quantified in LAOS: An instantaneous local 2D/3D approach," J. Rheol. **56**, 1129-1151 (2012)

Rogers S. A. and M. P. Lettinga, "A sequence of physical processes determined and quantified in large-amplitude oscillatory shear (LAOS): Application to theoretical nonlinear models," J. Rheol. **56**, 1-25 (2012)

Rubinstein M., R. H. Colby, A. V. Dobrynin and J. F. Joanny, "Elastic modulus and equilibrium swelling of polyelectrolyte gels," Macromolecules **29**, 398-406 (1996)

Ruta B., Y. Chushkin, G. Monaco, L. Cipelletti, E. Pineda, P. Bruna, V. M. Giordano and M. Gonzalez-Silveira, "Atomic-Scale Relaxation Dynamics and Aging in a Metallic Glass Probed by X-Ray Photon Correlation Spectroscopy," Phys. Rev. Lett. **109**, 165701 (2012)

Saatweber D. and B. Vogt-Birnbrich, "Microgels in organic coatings," Prog. Org. Coat. **28**, 33–41 (1996)

Sarangapani P. S. and Y. X. Zhu, "Impeded structural relaxation of a hard-sphere colloidal suspension under confinement," Phys. Rev. E **77**, 010501(R) (2008)

Schmidt F. G., F. Ziemann and E. Sackmann, "Shear field mapping in actin networks by using magnetic tweezers," Eur Biophys J. Biophy. **24**, 348-353 (1996)

Schnurr B., F. Gittes, F. C. MacKintosh and C. F. Schmidt, "Determining microscopic viscoelasticity in flexible and semiflexible polymer networks from thermal fluctuations," Macromolecules **30**, 7781-7792 (1997)

Schosseler F., F. Ilmain and S. J. Candau, "Structure and Properties of Partially Neutralized Poly(Acrylic Acid) Gels," Macromolecules **24**, 225-234 (1991)

Seth J. R., M. Cloitre and R. T. Bonnecaze, "Elastic properties of soft particle pastes," J. Rheol. **50**, 353-376 (2006)

Seth J. R.,"On the rheology of dense pastes of soft particles," PhD Dissertation, Chemical Engineering, The University of Texas at Austin (2008)

Seth J. R., M. Cloitre and R. T. Bonnecaze, "Influence of short-range forces on wall-slip in microgel pastes," J. Rheol. **52**, 1241-1268 (2008)

Seth J. R., L. Mohan, C. Locatelli-Champagne, M. Cloitre and R. T. Bonnecaze, "A micromechanical model to predict the flow of soft particle glasses," Nat. Mater. **10**, 838-843 (2011)

Seth J. R., C. Locatelli-Champagne, F. Monti, R. T. Bonnecaze and M. Cloitre, "How do soft particle glasses yield and flow near solid surfaces?," Soft Matter **8**, 140-148 (2012)

Sierou A. and J. F. Brady, "Rheology and microstructure in concentrated noncolloidal suspensions," J. Rheol. **46**, 1031-1056 (2002)

Sollich P., F. Lequeux, P. Hebraud and M. E. Cates, "Rheology of soft glassy materials," Phys. Rev. Lett. **78**, 2020-2023 (1997)

Sollich P., "Rheological constitutive equation for a model of soft glassy materials," Phys. Rev. E **58**, 738-759 (1998)

Squires T. M. and J. F. Brady, "A simple paradigm for active and nonlinear microrheology," Phys. Fluids **17**, 073101 (2005)

Squires T. M. and T. G. Mason, "Fluid Mechanics of Microrheology," Annu. Rev. Fluid Mech. **42**, 413-438 (2010)

Sriram I., A. Meyer and E. M. Furst, "Active microrheology of a colloidal suspension in the direct collision limit," Phys. Fluids **22**, 062003 (2010)

Steeneken P. A. M., "Rheological Properties of Aqueous Suspensions of Swollen Starch Granules," Carbohyd. Polym. **11**, 23-42 (1989)

Stickel J. J. and R. L. Powell, "Fluid mechanics and rheology of dense suspensions," Annu. Rev. Fluid Mech. **37**, 129-149 (2005)

Struik L. C. E.,"Physical aging in amorphous polymers and other materials," xiv, 229 p.(1978)

Tighe B. P., E. Woldhuis, J. J. C. Remmers, W. van Saarloos and M. van Hecke, "Model for the Scaling of Stresses and Fluctuations in Flows near Jamming," Phys. Rev. Lett. **105**, 088303 (2010)

Trepat X., L. H. Deng, S. S. An, D. Navajas, D. J. Tschumperlin, W. T. Gerthoffer, J. P. Butler and J. J. Fredberg, "Universal physical responses to stretch in the living cell," Nature **447**, 592-595 (2007)

Valentine M. T., L. E. Dewalt and H. D. OuYang, "Forces on a colloidal particle in a polymer solution: A study using optical tweezers," J. Phys.-Condens. Mat. **8**, 9477-9482 (1996)

van der Vaart K., Y. Rahmani, R. Zargar, Z. B. Hu, D. Bonn and P. Schall, "Rheology of concentrated soft and hard-sphere suspensions," J. Rheol. **57**, 1195-1209 (2013)

van Hecke M., "Jamming of soft particles: geometry, mechanics, scaling and isostaticity," J. Phys.-Condens. Mat. **22**, 033101 (2010)

Velegol D. and F. Lanni, "Cell traction forces on soft biomaterials. I. Microrheology of Type I collagen gels," Biophys. J. **81**, 1786-1792 (2001)

Verlet L. and J. J. Weis, "Equilibrium Theory of Simple Liquids," Phys. Rev. A **5**, 939-952 (1972)

Vlassopoulos D. and G. Fytas, "From Polymers to Colloids: Engineering the Dynamic Properties of Hairy Particles," Adv. Polym. Sci. **236**, 1-54 (2010)

Wagner M. H., V. H. Rolon-Garrido, K. Hyun and M. Wilhelm, "Analysis of medium amplitude oscillatory shear data of entangled linear and model comb polymers," J. Rheol. **55**, 495-516 (2011)

Waigh T. A., "Microrheology of complex fluids," Rep. Prog. Phys. **68**, 685-742 (2005)

Wang S. Q., S. Ravindranath, P. Boukany, M. Olechnowicz, R. P. Quirk, A. Halasa and J. Mays, "Nonquiescent relaxation in entangled polymer liquids after step shear," Phys. Rev. Lett. **97**, 187801 (2006)

Weihs D., T. G. Mason and M. A. Teitell, "Bio-microrheology: A frontier in microrheology," Biophys. J. **91**, 4296-4305 (2006)

Weitz D. A., "Condensed matter - Memories of paste," Nature **410**, 32-33 (2001)

Weitz D. A., "Colloidal Glasses," Prog. Math. Phys. **61**, 25-39 (2011)

Wilhelm M., D. Maring and H. W. Spiess, "Fourier-transform rheology," Rheol. Acta **37**, 399-405 (1998)

Wilhelm M., "Fourier-Transform rheology," Macromol Mater. Eng. **287**, 83-105 (2002)

Wilking J. N. and T. G. Mason, "Optically driven nonlinear microrheology of gelatin," Phys. Rev. E **77**, 055101(R) (2008)

Williams S. R. and D. J. Evans, "Linear response domain in glassy systems," Phys. Rev. Lett. **96**, 015701 (2006)

Wilson L. G., A. W. Harrison, A. B. Schofield, J. Arlt and W. C. K. Poon, "Passive and Active Microrheology of Hard-sphere Colloids," J. Phys. Chem. B **113**, 3806-3812 (2009)

Wilson L. G. and W. C. K. Poon, "Small-world rheology: an introduction to probe-based active microrheology," Phys. Chem. Chem. Phys. **13**, 10617-10630 (2011)

Winter D., J. Horbach, P. Virnau and K. Binder, "Active Nonlinear Microrheology in a Glass-Forming Yukawa Fluid," Phys. Rev. Lett. **108**, 028303 (2012)

Winter D. and J. Horbach, "Nonlinear active micro-rheology in a glass-forming soft-sphere mixture," J. Chem. Phys. **138**, 12A512 (2013)

Wirtz D., "Particle-Tracking Microrheology of Living Cells: Principles and Applications," Annu. Rev. Biophys. **38**, 301-326 (2009)

Wolfe M. S., "Dispersion and Solution Rheology Control with Swellable Microgels," Prog. Org. Coat. **20**, 487-500 (1992)

Wyart M., L. E. Silbert, S. R. Nagel and T. A. Witten, "Effects of compression on the vibrational modes of marginally jammed solids," Phys. Rev. E **72**, 051306 (2005)

Yamada S., D. Wirtz and S. C. Kuo, "Mechanics of living cells measured by laser tracking microrheology," Biophys. J. **78**, 1736-1747 (2000)

Yziquel F., P. J. Carreau, M. Moan and P. A. Tanguy, "Rheological modeling of concentrated colloidal suspensions," J. Non-Newton. Fluid. **86**, 133-155 (1999)

Zaner K. S. and P. A. Valberg, "Viscoelasticity of F-Actin Measured with Magnetic Microparticles," J. Cell. Biol. **109**, 2233-2243 (1989)

Zhang Y., W. H. Wang and A. L. Greer, "Making metallic glasses plastic by control of residual stress," Nat. Mater. **5**, 857-860 (2006)

Zhang Z. X., N. Xu, D. T. N. Chen *et al.*, "Thermal vestige of the zero-temperature jamming transition," Nature **459**, 230-233 (2009)

Zia R. N. and J. F. Brady, "Stress development, relaxation, and memory in colloidal dispersions: Transient nonlinear microrheology," J. Rheol. **57**, 457-492 (2013)

Ziemann F., J. Radler and E. Sackmann, "Local Measurements of Viscoelastic Moduli of Entangled Actin Networks Using an Oscillating Magnetic Bead Micro-Rheometer," Biophys. J. **66**, 2210-2216 (1994)

Zwanzig R. and R. D. Mountain, "High-Frequency Elastic Moduli of Simple Fluids," J. Chem. Phys. **43**, 4464-4471 (1965)

Vita

Lavanya Mohan was born and raised in India in her hometown of Chennai. She graduated from her high school, S.B.O.A School and Junior College, Chennai in 2004 and completed her undergraduate degree in Chemical Engineering at National Institute of Technology, Tiruchirappalli, India in 2008. During her undergraduate studies she completed two summer research fellowships at Jawaharlal Nehru Center for Advanced Scientific Research, Bangalore which inspired her to pursue doctoral studies. She joined the PhD program in Chemical Engineering at The University of Texas at Austin in 2008 and completed her Master's degree in 2011.

She was married to Vivek Raja Raj Mohan in 2012 who also graduated from National Institute of Technology, Tiruchirappalli in 2008. Upon graduation, she has accepted employment at ExxonMobil Upstream Research Company in Houston, Texas.

Permanent email: lavamohan@gmail.com

This dissertation was typed by the author.